Hydrodynamics of Coral Forereef Spurs and Grooves

Lachlan Arthur Perris
ORCID: 0000-0003-2235-8671

A thesis submitted to fulfil the requirements of the degree of
Doctor of Philosophy

February 2026

Faculty of Science
School of Geosciences
The University of Sydney
Australia

Supervisor: Prof. Ana Vila-Concejo

Co-Supervisor: A/Prof Tristan Salles

Co-Supervisor: Dr. Ana Paula Da Silva

Co-Supervisor: Dr. Tommy Fellowes

Declaration

I, Lachlan Arthur Perris, certify that the intellectual content of this thesis is the product of my own work, and that all assistance received in preparing this thesis and all sources have been acknowledged. This thesis has not been submitted for any other degree or purpose.

Copilot was used for the purposes of text enhancement. The use of this generative AI tool includes spelling corrections, minor sentence restructuring, and clarity enhancement. I confirm that where text was modified by generative AI, the content was reviewed for possible errors, inaccuracies, and bias. I take full responsibility for the submitted thesis, confirm the work is my own, and have used generative AI in accordance with University guidelines and policies.

Lachlan Arthur Perris
27/02/2026

Acknowledgments

I have thoroughly enjoyed all aspects of the production of this thesis. I have also required a great deal of support to complete it. I would like to thank my supervisor, Professor Ana Vila-Concejo, who first showed me the world of coastal geomorphology and has continued to support me as a student and promote my research. Without Ana's efforts, this would not be possible.

I have also benefited from the mentorship of my co-supervisors, Associate Professor Tristan Salles, Dr. Thomas Fellowes and Dr. Ana Paula da Silva. Each have uniquely demonstrated an academic professionalism that I will continue to emulate throughout my career. I would also like to thank Professor Jody M. Webster for his unrelenting enthusiasm for geoscience, and Dr. Stephanie Duce for her kindness in response to my confusion about spurs and grooves.

To Grant, Linda, Bonnie and Lloyd, this would not be possible without your love of learning, and capacity for hard work. I am inspired by each of you every day. Thank you to my Grandfather, George Woods, who passed during the course of this thesis. His strength and generosity lives with all who knew him.

To Dr. Beatriz Hadler Boggiani, I am deeply grateful that you have been on this journey with me. We have stridden across the highs and lows of Ph.D. life and have arrived at the end together.

I also thank the many researchers and workers who have assisted me in the field, the lab and the pub. To fellow Ph.D. students, M.D. Gazi, Ratneel Deo and Kate Whitton, thank you for your enthusiasm for science and your composure following long days of field work in the tropics. Thank you, Mathew Kosnik and Amanda Sordes, for your expertise in the field. Thank you also to the station managers at One Tree Island, my good friends, Heinrich Breuer and Ruby Holmes.

Lachlan Perris, Summer 2026

This research reported in this thesis was supported by the award of a Research Training Program scholarship to the PhD Candidate. The research was partially funded by the Australian Research Council (ARC) Future Fellowship (FT100100215), the ARC Discovery Program (DP220101125), and Geoscience Australia funding through the Marine Studies Institute at the University of Sydney.

Authorship Attribution

This thesis is based on the following three articles:

ARTICLE 1: Perris, L.A., Salles, T., Fellowes, T. E., Duce, S., Webster, J., & Vila-Concejo, A. (2024). The Influence of Coral Reef Spur and Groove Morphology on Wave Energy Dissipation in Contrasting Reef Environments. Journal of Geophysical Research: Earth Surface, 129(8), 1–17. https://doi.org/10.1029/2023JF007424

ARTICLE 2: Perris, L., Salles, T., Fellowes, T. E., Da Silva, A. P., Duce, S., Webster, J. M., Thompson, A. M., & Vila-Concejo, A. (2026). Current flow in low-energy coral forereef spurs and grooves. Geomorphology, 493. https://doi.org/10.1016/j.geomorph.2025.110072

ARTICLE 3: Perris, L.A., Lindhart, M., Salles, T., Da Silva, A.P., Fellowes, T.E., Vila-Concejo, A. (2025): Hydrodynamic Controls on Spur and Groove Morphology: Flow Variability and Reef Structure (Submitted to *Coral Reefs* 25/09/2025).

Three co-authored articles are included in Appendix B for further reference:

Part I: Gazi, M. Y., Fellowes, T. E., Deo, R., Silva, A. P., Perris, L., & Vila-Concejo, A. (2025). A quantitative approach to classify the shape of beach profiles. Estuarine, Coastal and Shelf Science, 322. https://doi.org/10.1016/j.ecss.2025.109373

Part II: Duce, S., Mccarroll, R. J., Yiu, B., Perris, L. A., Yumba, B., Wales, S., & Melbourne, E. (2021). Field measurements from contrasting reefs show spurs and grooves can dissipate more wave energy than the reef crest. Earth and Space Science Open Archive ESSOAr, 413(June), 108365. https://doi.org/10.1016/j.geomorph.2022.108365

Part III: Vila-Concejo, A., Perris, L. A., Da Silva, A. P., Whitton, K., Meoded-Stern, L., Steilberg-Liu, W. Y., Holmes, R., Breuer, H., Byrne, M., Fellowes, T. E., Salles, T., Morris, B., & Bruce, E. (2025). Grooves in forereefs act as transport channels to deliver coral rubble during tropical cyclones. Cambridge Prisms: Coastal Futures. https://doi.org/10.1017/cft.2025.10019

In addition to the authorship attribution statements above, in cases where I am not the corresponding author of a published item, permission to include the published material has been granted by the corresponding author.
Lachlan Arthur Perris, February 2026

As supervisor for the candidature upon which this thesis is based, I can confirm that the authorship attribution statements above are correct.
Ana Vila-Concejo, February 2026

Abstract

Hydrodynamics govern many ecological and geological processes on a coral reef. Where reefs meet the open ocean, in the forereef zone, hydrodynamic energy, wave energy dissipation, coral growth and rubble production are greatest, typically producing spur and groove (SaG) morphology . Spurs are elongated coral mounds that extend seawards from the reef crest, separated by alternating channels (grooves), typically oriented perpendicular to the reef crest. Understanding the hydrodynamics in this critical zone is essential, as they underpin the ecological and geological stability of reefs and mediate the impact of disturbances, an urgency heightened by local human impacts and climate change . The central aim of this thesis is to quantify the hydrodynamic processes of the ubiquitous, yet poorly understood, SaG morphology.

Using numerical wave modelling with realistic forereef morphologies derived from light detection and ranging (LiDAR) from One Tree Island in the southern Great Barrier Reef (GBR), this thesis investigated the role of SaG morphology in wave energy dissipation and transmission at the reef crest. This thesis demonstrates that realistic forereef morphologies provided an extra 40% wave dissipation than when SaG were removed . Future climate scenarios showed that under the lowest emission scenario (RCP2.6), increased wave heights (+0.8 m) and water levels (+0.3 m) doubled dissipation rates across the forereef. The worst case (RCP8.5) and Total Disaster (TD) scenarios (i.e., a heavily degraded and smoothed reef) resulted in a 4-fold reduction in dissipation and increased wave transmission at the crest by up to 2.7 m relative to present conditions. This thesis is the first study to quantify wave dissipation over SaG under future climate change scenarios.

To complement the modelling work, this thesis incorporates two independent field experiments conducted at One Tree Reef (OTR; 23°30 S, 152°06 E), a lagoonal platform reef in the southern Great Barrier Reef. OTR is situated 84 km offshore, within the Marine Park's "Scientific Zone," and experiences semi-diurnal tides (mean spring range 3 m). Local hydrodynamics are dominated by southeast trade winds, generating mean offshore significant wave heights of 1.7 m, with occasional extremes exceeding 3 m during cyclones. The first campaign (6–8 October 2022) involved short-term deployments with high frequency (8 Hz) observations of currents in a low-energy and protected SaG system. The second campaign (25 November 2022–6 April 2023) was a long-term deployment during which the reef was exposed to a wide range of wave and tidal forcing, including high-energy events.

Fair weather conditions on the northern SaG yielded low wave conditions (mean significant wave height ($\overline{H_s}$) = 0.25 m), while currents reached up to 2 m/s with a dominant offshore component driven by surf zone processes and lagoonal outflow. These measurements represent the first in situ observations of water flow within reef spurs and grooves on the Great Barrier Reef. The data show that lagoon outflow creates persistent offshore-directed currents across the tidal cycle, even under low-energy wave conditions. Such steady outflows provide an effective mechanism for transporting sediment seaward of the forereef, consistent with hypotheses that constructional SaG development is sustained by offshore sediment transport. Stronger

outflow events are therefore likely to enhance sediment delivery and promote spur extension, reinforcing a lagoon-driven pathway for reef growth. Collectively, these findings demonstrate a direct link between forereef hydrodynamics and SaG morphology, providing new evidence for the role of lagoon–forereef exchanges in shaping reef structure and influencing coral reef resilience.

The second field campaign, spanning six months from November 2022 to April 2023, captured the first long-term hydrodynamic dataset across a high-energy SaG system on the eastern forereef. The results showed that alongshore tidal currents regularly outpaced wave-driven cross-shore flows, dominating 31.6% of the record. Despite their persistence, the geomorphic impact of these alongshore flows appeared limited, expressed only as a slight spur asymmetry aligned with the prevailing tidal current direction. By contrast, wave-driven sediment mobility was pervasive: near-bed orbital velocities and bed shear stresses on the upper forereef exceeded sediment mobility guides for 94% of the record, while across the entire SaG system, mobility thresholds were surpassed during storm events. These conditions indicate that sediment entrainment and abrasion are near-continuous on the upper forereef and episodically system-wide, supporting a model of SaG formation and maintenance driven primarily by wave-induced abrasion rather than direct current forcing. Taken together, these observations demonstrate how wave forcing interacts with tidal modulation to sustain SaG morphology, providing a mechanistic link between hydrodynamics and geomorphic structure that is critical for predicting reef response to hydrodynamic conditions.

In conclusion, the central aim of this thesis was achieved by quantifying the hydrodynamic processes shaped by SaG morphology that control their persistence in both low- and high-energy environments. The combined modelling and in situ observations demonstrated that SaG both significantly enhance wave energy dissipation and regulate sediment dynamics, playing a critical role in reef resilience under present and projected future conditions . These findings show that spur-and-groove structures are not only key geomorphic features but also essential components of reef function, underpinning coastal protection and ecosystem services. By linking SaG hydrodynamics to processes of reef growth, sediment transport, and wave energy regulation, this thesis demonstrates that the persistence of these structures will strongly influence reef health and the capacity of coral reef systems to sustain ecological goods and services in a changing climate.

Contents

1 | Introduction

1.1 Coral Reefs and Morphodynamics

Coral reefs are among the most productive and biologically diverse ecosystems on Earth, supporting diverse marine life and providing ecosystem services that benefit over half a billion people globally (Hoegh-Guldberg et al. 2019). In addition to their ecological value, reefs act as natural coastal barriers, attenuating wave energy and reducing coastal inundation and erosion risk (Beck et al. 2018; Ferrario et al. 2014; Hoegh-Guldberg et al. 2019). These functions translate into substantial economic and social benefits. For example, without coral reefs, global flood damages from centennial-scale storm events would increase by 91%, reaching an estimated US$272 billion annually (Beck et al. 2018). The socio-economic significance of reefs is perhaps most clearly illustrated by the Great Barrier Reef (GBR), valued at AU$56 billion and supporting over 64,000 jobs (O'Mahony et al. 2017). Beyond hazard mitigation and tourism, reefs stabilise tropical coasts through island formation, fisheries productivity, and carbonate sediment cycling.

Despite their ecological and socio-economic importance, coral reefs are undergoing rapid and widespread degradation because of anthropogenic climate change. Increasing sea surface temperatures (SST) have led to increasingly frequent and severe mass coral bleaching events (Hughes et al. 2017; McWhorter et al. 2022), while marine heatwaves have doubled in frequency since the 1980s (IPCC 2019). Ocean acidification weakens coral skeletons and slows accretion (Kleypas and Langdon 2006), undermining reef growth potential (Perry et al. 2018). Simultaneously, relative sea-level rise, projected to reach up to 1.1 m by 2100 under high-emissions scenarios (Pörtner et al. 2022), threatens to outpace coral accretion rates of many reef systems, increasing the likelihood of coral downing (falling below the photic zone) and island submergence (Perry et al. 2018). Storm intensity and wave energy are also increasing (Meucci et al. 2020), elevating the risks of coral breakage, sediment transport, and disruption of reef circulation patterns (Grimaldi et al. 2022; Madin and Connolly 2006). These environmental stressors often interact non-linear ways. Combined with direct human impacts, such as overfishing and nutrient pollution, they create feedback loops that accelerate reef degradation (Bozec and Mumby 2015; Hughes et al. 2017). As these compounding pressures intensify, it is increasingly clear that coral reef conservation alone will be insufficient to sustain reef structure and function beyond 2030 (Pörtner et al. 2022).

Geomorphology offers a powerful framework for diagnosing and anticipating the structural response of coral reefs to environmental change. Positioned between the ecological and geological timescales, geomorphological approaches capture physics-

based processes operating over decadal to centennial periods. These temporal scales align with the rate of contemporary climate forcing (Hopley et al., 2009; Molau, 2008). They also bridge contrasting perspectives of reef resilience: while geological records suggest long-term persistence under variable climates (Done 1992; Woodroffe and Webster 2014), ecological assessments highlight acute vulnerability to disturbance and collapse (Hughes 2000; Madin and Connolly 2006). The approach adopted in this thesis focuses on the morphodynamics of forereefs, with emphasis on the geomorphological responses to hydrodynamic forcing. This approach fills a critical gap in the current literature on forereefs by bridging ecological and geological understanding of these features. **By linking reef form to process, this thesis aims to improve our understanding of how forereef structures respond to climate-driven change and identify the conditions necessary to support their continued development and maintenance.**

1.2 Hydrodynamics of Forereefs and Spurs and Grooves

Hydrodynamic energy is the greatest on the forereef, where coral growth and reef morphological development are the most active. In this zone, incoming waves are transformed (shoaling, breaking) by shallow reef bathymetry and surface roughness, generating currents that circulate nutrients, disperse larvae, and transport sediment. These processes underpin the ecological productivity and carbonate accretion potential of forereef environments. The high coral growth rates on reef slopes were first recognised by (Darwin 1842), who noted the vertical development of coral structures in wave-exposed settings. Subsequent studies have confirmed that the forereef supports the most rapid coral accretion within the reef system (Duce et al. 2014; Munk and Sargent 1948; Kan et al. 1997; Odum and Odum 1955). The forereef is structurally complex across multiple spatial scales, with roughness features that influence wave attenuation and sediment transport (Harris et al. 2023; Monismith 2007). This structural complexity contributes to high biodiversity, with species richness on the reef slope often double that of the reef flat (Karlson et al. 2004). However, as forereefs are shallow areas with high wave energy, they are also the least accessible zone for scientific investigation, leading to a notable lack of field data. Ladd (1961) famously referred to forereef zones as *"Mare Incognitum"*, or Unknown Sea.

Spur and groove (SaG) structures are a dominant and widely observed feature of forereef zones. Spurs are ridges of consolidated carbonate reef framework that extend seaward from the reef crest, alternating with grooves, which are gaps in the forereef that act as sediment traps or hydrodynamic channels (Figure 2). SaG occur over a wide range of depths and morphologies (Duce et al. 2016). Their spur heights range from 0.5 to 10 m, with alongshore wavelengths typically between 5 and 150 m and groove widths from 1 to 100 m (Rogers et al. 2013). SaG morphologies are found on various reef types including fringing reefs, barrier reefs, and atolls, and have been documented across all major tropical ocean basins. SaG structures have been identified in the Pacific (Munk and Sargent 1948; Storlazzi et al. 2003), Caribbean (Blanchon and Jones 1997; Goreau 1959), Atlantic (Shinn et al. 1982), Indian Ocean (Sheppard 1981; Weydert 1979), and the Red Sea (Sneh and Friedman 1980). Munk and Sargent (1948) and Emery et al. (1949) were among the first to describe SaG structures in the western Pacific. Since then, SaG have attracted significant interest, with research focusing on their morphology (e.g. Duce et al. 2014; Duce et al. 2016;

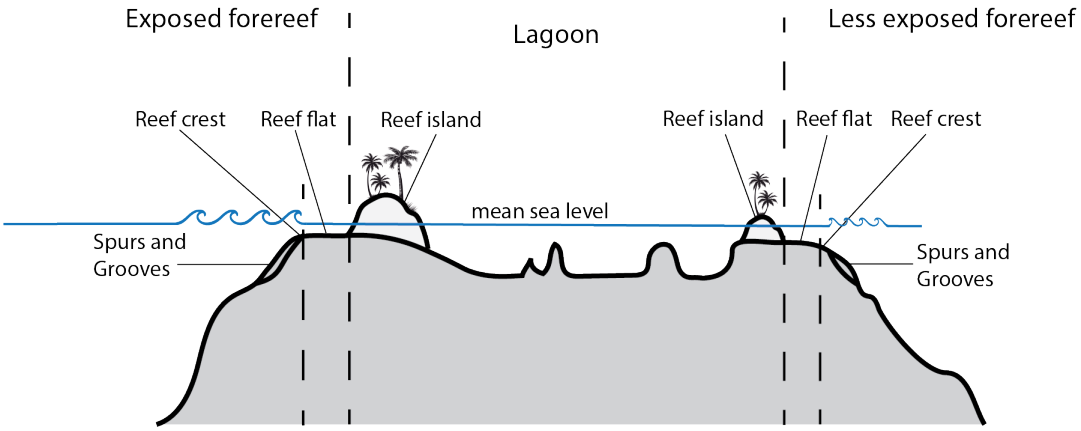

Figure 1: Illustration showing a cross-section of a platform lagoonal reef highlighting key geomorphic zones referenced in this thesis. Spurs and grooves (SaG) occur on both windward and leeward forereefs and typically extend seaward from the reef crest to depths of 20 m. Reef islands, where present, typically form on reef flats.

Sneh and Friedman 1980), hydrodynamic role (e.g. Rogers et al. 2013; Sartori et al. 2024; da Silva et al. 2020), and formation mechanisms (e.g. Duce et al. 2020; Gischler 2010; Kan et al. 1997).

The morphological structure of SaG (Figure 2) influences key reef hydrodynamic processes including wave transformation, circulation, and sediment dynamics. In some settings, the energy dissipated by SaG structures exceeds that of the reef crest (Acevedo-Ramirez et al. 2021; Duce et al. 2021), challenging the traditional view – based largely on field studies focused on reef crests and flats - that wave dissipation is the highest in those zones (e.g. Brander et al. 2004; Hardy and Young 1996; Harris et al. 2015; Jago et al. 2007; Kench and Brander 2006; Maticka et al. 2022; Rosenberger et al. 2020). The earlier studies often emphasised easily accessible reef flat and reef crest environments due to their lower hydrodynamic energy and logistical simplicity. As a result, there remains a considerable knowledge gap about wave transformation and energy dissipation processes occurring on the forereef. **This thesis seeks to address that gap, with Chapter 2 focusing specifically on how SaG zones contribute to wave energy attenuation.**

Wave and current flows over SaG structures drive water exchange between protected lagoons and the open ocean (Lindhart et al. 2021; Ludington 1979). This is of particular importance in platform reefs and atolls, where effective circulation helps regulate nutrient concentrations and prevents water stagnation – both essential for sustaining coral health and productivity (Callaghan et al. 2020; Green et al. 2018). Where previous studies have only investigated SaG in isolation from the broader reef platform (da Silva et al. 2020; Rogers et al. 2013), others have linked SaG hydrodynamics to the reef system (Duce et al. 2021), including some of the earliest interpretations of SaG hydrodynamics (Hoffmeister 1932).

Extreme wave events, especially tropical cyclones, are major drivers of geomorphic change on forereefs. These high-energy events can transport significant volumes of coral rubble onto the reef flat and lagoon bench, contributing to rapid reef growth and the development of low-lying islands/cays (Davies 1983; MacNeil 1954). Conversely, they can also destroy SaG systems altering reef edge topography (Stoddart

Figure 2: Coral forereef spurs and grooves at One Tree Island in the Southern Great Barrier Reef. Photo: Lachlan Perris

1962) and remobilise sediment within grooves, limiting coral settlement even during calmer conditions (Hopley et al. 2009). At larger scales, tropical cyclones have the capacity to both build and erode entire reef islands, underscoring their role as agents of sudden landscape change (Bramante et al. 2020). For example, hurricane waves on Grand Cayman in the Caribbean pruned branching corals and flushed sand from reef canyons, producing robust head coral assemblages on exposed buttresses. In contrast, more sheltered margins supported shallow, branching-coral-dominated ridges with minimal spur development. These patterns demonstrate how repeated storm wave impacts control reef-edge architecture and accretion over long timescales (Blanchon and Jones 1997). Extreme wave events also have important ecological implications for coral reefs. Fragmentation during storms provides an important asexual reproductive mechanism for many coral species and marine invertebrates (Bruno 1998). The dispersal distance of coral fragments is often greatest in shallow forereef environments, allowing fragments to colonise new areas and contributing to post-disturbance reef recovery (Bruno 1998). In this way, extreme wave events can be both destructive and constructive, reshaping reef morphology while also driving processes of coral regeneration (Vila-Concejo and Kench 2017).

Despite growing recognition of their importance, in situ field measurements of hydrodynamics over SaG morphology remain scarce. One key overlooked process is tidal truncation, common on platform reefs, where low tides isolate lagoon waters from the open ocean, creating persistent outflows across the reef rim (Lowe et al. 2015; Ludington 1979). These outflows can significantly influence circulation patterns at the reef edge but are often excluded from field studies focused on fringing reefs such as those in Molokai, Hawaii (Storlazzi et al. 2003) and Xanhauyxol, Mexico (Acevedo-Ramirez et al. 2021). Similarly, most numerical models do not incorporate this process (da Silva et al. 2020; Rogers et al. 2013).

Lagoonal outflow and alongshore currents, generated by wind or tide, can influence

the morphology of SaG. However, research has typically focused on shore normal waves, reflecting early observations of SaG orientation Munk and Sargent 1948. The exposed margins of platform reefs experience wave energy from multiple directions and support complex current systems modulated by the larger reef matrix (Burrage et al. 1996). Recent numerical models have shown that alongshore currents can eliminate lower forereef circulation cells and redistribute sediment along spur–groove boundaries, reducing the formation or persistence of SaG (da Silva et al. 2020). **To address these gaps, Chapter 3 assesses the connectivity of SaG with the broader reef platform-scale circulation and Chapter 4 evaluates the frequency, intensity, and directionality of flow events that contribute to sediment transport and SaG maintenance**

1.3 Formation Mechanisms of Spurs and Grooves

While the interaction of hydrodynamics with reef morphology is inherently site specific, there are consistent response features that emerge from common sets of environmental drivers (Roberts et al. 1980). SaG morphologies represent one such response (Blanchon 2011), While the interaction of hydrodynamics with reef morphology is inherently site specific, there are consistent response features that emerge from common sets of environmental drivers Early interpretations emphasised the influence of pre-existing grooves that were eroded into the Pleistocene substrate at times of low sea level (Newell et al. 1951; Purdy 1974). This process is also evident in non-coral reef settings, such as in oolite beds (Newell et al. 1951) or bedded sandstone substrates (Carling et al. 2018), suggesting that the complexity of hydrodynamic forcing, sediment transport and biological growth patterns on forereefs may be overlooked by this model. Later work highlighted this oversight, identifying SaG systems developing over beds of reef derived sediment with no pre-existing grooves in the antecedent substrate (Shinn et al. 1982).

Further exploration of SaG formation has proposed erosive mechanisms (Hoffmeister 1932). Here, the return flow of waves eroding the forereef are supported by observations of the Pleistocene substrate at the base of grooves (Shinn et al. 1982). Additionally, erosion of grooves may occur through indirect hydrodynamic forcing. Mobilisation of coral sediments by oscillatory waves may abrade grooves or inhibit organic growth in grooves (Blanchon and Jones 1997; Cloud Jr. 1959). Others have proposed that in some forereef environments, the removal of carbonate material is greater than coral growth rates, concluding that grooves must be erosional to support this balance (Davies 1983).

To reconcile these different views, Duce et al. (2016) proposed the most comprehensive classification of SaG morphotypes and formation mechanisms to date. Four classes of grooves morphologies were statistically defined, each with distinct formation mechanisms (reproduced in Fig 3, Duce et al. 2016; Duce et al. 2020)). This classification is particularly useful as it integrates the mechanisms of SaG formation while linking SaG development to the broader evolution of the reef platform (Dechnik et al. 2016; Duce et al. 2020). **Chapter 2 of this thesis further explores these morphotypes and assesses the hydrodynamic characteristics of each.**

SaG development was categorised by Duce et al. (2016) into three modes based on

reef morphology and wave exposure (Fig. 3). Mode 1 describes groove erosion and lagoonward accretion of the reef flat under high wave energy conditions. Mode 2 occurs in more protected settings, with lateral growth of the reef flat and shorter, less incised grooves. Mode 3, characteristic of moderate wave energy environments with episodic high-energy events, involves lateral accretion of the reef flat and forereef (Duce et al. 2020). Although this classification provides a useful morphological model, it was developed without access to detailed in situ hydrodynamic data from SaG zones. The absence of in situ data on wave transformation, flow routing, and sediment transport limits the ability to fully test formation theories or quantify the feedback between reef structure and reef function. **To address the gaps, this thesis assesses proposed SaG formation mechanisms using field data from both low energy (Chapter 3) and a high energy (Chapter 4) forereefs. By combining hydrodynamic observations with morphological analysis, it aims to better understand the dynamics of SaG formation and refine existing theories about their development.**

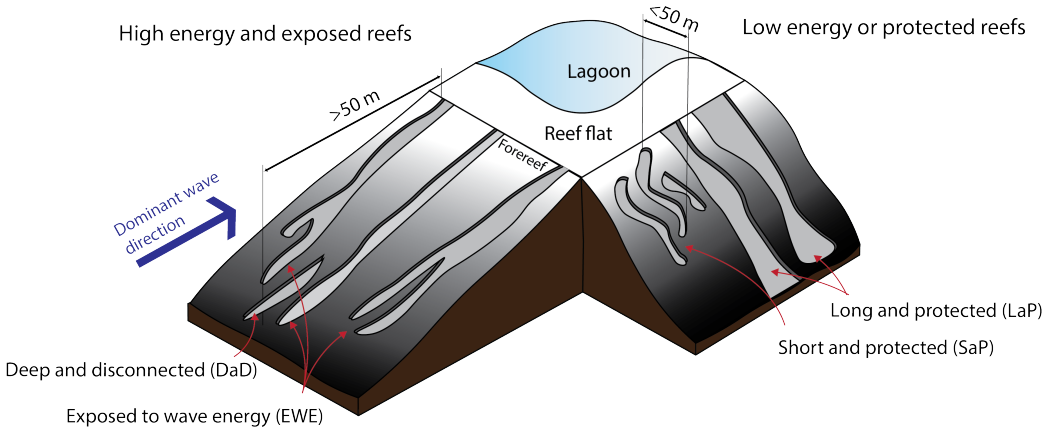

Figure 3: SaG morphotypes and relationship to relative wave exposure, reproduced from Duce et al. 2014.

1.4 Site Selection

One Tree Reef (OTR) (Fig 4) is an ideal study site located offshore in the southern Great Barrier Reef. It resides within a protected scientific zone that limits direct human pressures such as fishing, tourism and terrestrial runoff, ensuring that natural hydrodynamic and geomorphic processes can be studied without significant anthropogenic interference. The reef has also been the focus of more than fifty years of research through the One Tree Island Research Station (Davis et al. 2019), which has produced datasets that support new investigations. Among these is a high-resolution LiDAR-derived digital elevation model that captures the reef to a depth of 20 m, offering rare sub-metre resolution suitable for detailed morphological analysis (Harris et al. 2023; Purkis and Brock 2013).

OTR experiences semi-diurnal tides with a spring range of around 3 m, creating strong tidal flows that induce circulation through the lagoon (Ludington 1979). Trade winds dominate over much of the year and generate average significant wave

heights of 1.7 m, while cyclones and storms periodically deliver high energy conditions with waves exceeding 3 m (Jell and Webb 2012; Smith et al. 2023). These energetic processes combine to shape the reef's wave climate, influencing sediment transport, coral growth, and overall reef morphology. In addition, due to the relative elevation of the reef rim to the tide, the lagoon is isolated from the open ocean for 3-hours of the tidal cycle. In this time, the lagoon water level is up to 1.39 m higher than the surrounding ocean, and it drains through topographic low points in the reef crest and percolates through the porous framework of the reef flat. This process, known as tidal truncation creates water level gradients that drive circulation across the reef flat and forereef (Frith 1983; Ludington 1979; Wilson 1985).

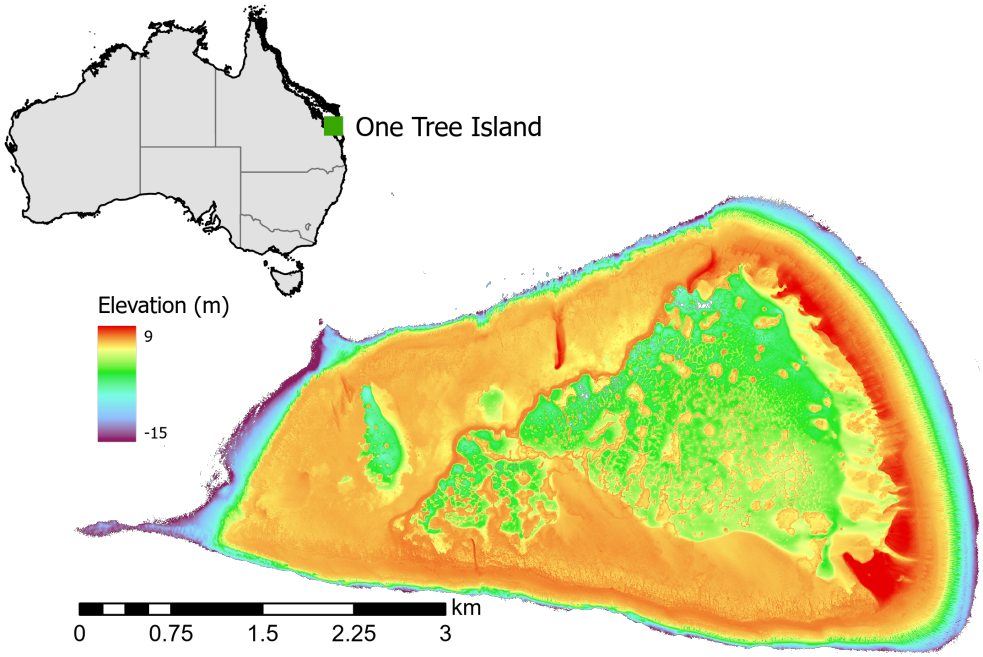

Figure 4: Location map of One Tree Reef (Capricorn Bunker Group, southern Great Barrier Reef, Australia). LiDAR-derived bathymetry of the entire reef platform; colours indicate depth (m) (Harris et al. 2023).

OTR is characterised by SaG systems that encircle the entire forereef and represent the full range of SaG morphological classes (Duce et al. 2016). The forereef, where this study is primarily focused, features spurs with high coral cover and coarse rubble-filled grooves (Figure 2), indicative of both ecological health and active geomorphic processes (Harris et al. 2023). Adjacent features shoreward of the forereef zone, such as storm-deposited rubble banks and reef-flat exposures during low tides, provide additional evidence of strong hydrodynamic forcing and storm-driven sediment transport (Davies 1983). **The combination of protected status, long-term research infrastructure, high-resolution datasets, energetic hydrodynamic conditions, and representative spur and groove morphology strongly justifies the selection of OTR for this study.**

Findings from OTR are relevant beyond this specific location, as the reef is representative of mid-shelf platform reefs in the Great Barrier Reef and other tropical

reef provinces. The reef may be representative of many reefs across the southwest Pacific due to its meso-tidal setting, exposure to persistent trade winds, and periodic cyclone influences (Harris et al. 2018; Hopley et al. 2007). Furthermore, the large, well-developed SaG systems encircling the forereef are typical of high-energy reef margins worldwide (Duce et al. 2016; Munk and Sargent 1948). Processes such as tidal truncation (Frith 1983), wave pumping (Harris et al. 2018), and storm-driven sediment transport (Vila-Concejo et al. 2013) documented at OTR are common on reefs in the Caribbean, Pacific, and Indian Oceans (Kench 1998; Roberts 1974). **Therefore, the insights gained from this site on the interaction between hydrodynamics, sediment mobility, and reef morphology can be applied to similar reef settings globally.**

1.5 Thesis Objectives

This thesis investigates the interaction between coral forereef spur and groove (SaG) hydrodynamics and morphology, with a focus on the feedbacks between wave energy dissipation, current regimes, and reef morphology across low and high-energy environments. By combining numerical wave modelling with field-based hydrodynamic measurements and high-resolution bathymetric data, the research aims to improve our understanding of the formation of SaG and the critical functions they have in sustaining critical eco-system services. This thesis provides new empirical and model-based insights into the physical processes that drive reef slope morphology and contribute to the persistence or transformation of coral reef ecosystems under climate stress.

The specific objectives of this thesis are to:

1. **Assess how different SaG morphotypes influence wave attenuation across contrasting reef settings.** To do this, Chapter 2 quantifies wave energy dissipation over spur-and-groove structures using numerical wave models run over high-resolution LiDAR-derived bathymetry.

2. **Evaluate the impact of climate change on SaG wave energy dissipation and reef hydrodynamics.** Chapter 2 models ecosystem functions change with projected sea level rise, forereef elevation and wave regime changes.

3. **Assess the connectivity of SaG with the broader reef platform-scale circulation.** Chapter 3 characterises with field measurements, by characterising current flow patterns and wave transformations across a low energy SaG system in low-energy conditions.

4. **Evaluate the frequency, intensity, and directionality of flow events that contribute to sediment transport and SaG maintenance.** Chapter 4 provides detailed analyses of in situ hydrodynamic measurements undertaken over 6 months on a high-energy reef slope.

5. **Establish links between the geological timescale of SaG formation with the hydrodynamic timescale** Chapter 4 analyses the feedback between instantaneous hydrodynamics and the long-term geological evolution. This chapter evaluates the eco-morphodynamics of SaG including sediment

transport thresholds, coral growth morphology and subsequent topographic steering of currents.

6. **Determine whether present-day hydrodynamic conditions are sufficient to sustain SaG morphology.** Chapters 3 and 4 assess the erosional and constructional mechanisms involved in SaG formation and explore their implications for reef resilience under changing environmental conditions.

1.6 Thesis Overview

The thesis contains six chapters:

Chapter 1 begins with a literature review that highlights the significance of SaG hydrodynamics and the known research gaps to be addressed here. It sets out the objectives of this thesis with relevant background information and the terminology used throughout the thesis.

Chapter 2 presents the publication 'The Influence of Coral Reef Spur and Groove Morphology on Wave Energy Dissipation in Contrasting Reef Environments'. In this chapter, I employ **hydrodynamic numerical models** with innovative use of realistic bathymetry to investigate the influence of SaG on wave energy dissipation. I compare wave dissipation between a realistic forereef and a forereef where SaG are removed. Additionally, I use the model to forecast how wave energy dissipation might change under projected future reef conditions. This chapter addresses the specific objectives 1 and 2.

Chapters 3 and 4 present **field measurements** that fill critical observational gaps in SaG hydrodynamic data, addressing the logistical and environmental challenges that have limited previous data collection in these environments. Both chapters use a high-resolution LiDAR derived bathymetry dataset to enhance the interpretation of the hydrodynamic measurements.

In **Chapter 3**, I focus on **SaG in a relatively low hydrodynamic energy environment**. I present the highest temporal resolution dataset ever recorded from SaG, offering critical insight into instantaneous flow dynamics through SaG morphology. I also investigate how SaG in this setting is hydrodynamically connected to the broader reef platform via tide-controlled lagoonal outflow. This chapter addresses the specific objectives 3 and 5.

In **Chapter 4**, a **high energy SaG environment** is examined, with emphasis on cyclone-induced extreme hydrodynamic disturbances. The frequency and intensity of high wave energy events that drive a fluctuation between cross-shore (groove-aligned) dominated flows and alongshore (perpendicular to grooves) dominated flows are analysed across the longest timeseries dataset of SaG ever reported. Sediment mobility parameters are derived from the hydrodynamic dataset to assess sediment motion in the groove. Additionally, feedback between SaG hydrodynamics and morphology is evaluated utilising a novel geomorphometric assessment of SaG morphology. This chapter addresses the specific objectives 4, 5 and 6.

Chapter 5 presents the overall discussion across the different objectives and findings, the broader implications of this research thesis, and the potential directions for future research in this field.

Chapter 6 concludes the thesis by explicitly addressing each research objective.

Appendix A includes supplementary material for Chapter 4

Finally, **Appendix B** presents publications arising from this thesis.

2| The Influence of Coral Reef Spur and Groove Morphology on Wave Energy Dissipation in Contrasting Reef Environments

Lachlan Arthur Perris[1, 2], Tristan Salles[1, 2], Thomas E. Fellowes[1, 4], Stephanie Duce[3], Jody Webster[1], Ana Vila-Concejo[1, 2],

[1]Geocoastal Research Group, School of Geosciences, The University of Sydney, NSW, 2006, Australia
[2]Marine Studies Institute, Faculty of Science, The University of Sydney, NSW, 2006, Australia
[3]College of Science and Engineering, James Cook University, Bebegu Yumba Campus, Townsville, Queensland, 4811, Australia
[4]Water Research Laboratory, School of Civil and Environmental Engineering, UNSW Sydney, Australia

- Accurate bathymetries (<1 m) in forereef wave energy dissipation models can include features such as spurs and grooves (SaG);
- SaG increase forereef wave energy dissipation when compared to similar bathymetries without SaG;
- Forereef dissipation shifts from bed friction to wave breaking in modeled environmental conditions based on future climate projections.

Abstract

Coral reefs protect coastlines from inundation and flooding, servicing over 200 million people globally. Wave transformation has previously been studied on coral reef flats with limited focus on forereef zones where wave transformation is greatest during high-energy conditions. This study investigates the role of forereef spur and groove (SaG) morphology on wave energy dissipation and transmission at the reef crest. Using XBeach on LiDAR-derived bathymetry from One Tree Island in the southern Great Barrier Reef, we reproduced dissipation rates comparable to SaG field studies. We examined how wave energy dissipation differs between realistic bathymetries and those with SaG features removed, demonstrating an up to 40% decrease in dissipation when SaG features are absent. We then investigated changes to wave energy dissipation and wave transmission at the reef crest based on IPCC AR5 emission scenarios (RCP2.6 and RCP8.5) and a total disaster scenario (TD) for the year 2100. For RCP2.6, an increase in wave heights of 0.8 m and an increase in water level of 0.3 m resulted in a two-fold increase in dissipation rates. For RCP8.5 and TD, with no increase in incident wave height, dissipation rates were 29% and 395% lower than RCP2.6. This resulted in increased wave transmission at the reef crest by 1.8 m and 2.7 m for RCP8.5 and TD based models, respectively, when compared to the RCP2.6 based model. The results from our novel modelling approach of using long-shore varying accurate bathymetries on forereefs show increased wave energy dissipation rates with implications for reducing coastal flooding and island inundation on reef-lined coasts.

Plain Language Summary

Coral reefs protect coastlines from floods and waves, benefiting over 200 million people globally. We studied how waves change over coral reefs, focusing on the forereef zone where wave transformation is most significant during high-energy conditions. The shape of the forereef, specifically the long comb-like grooves that cut through coral reefs, known as spur and grooves (SaG), modify wave energy transformation. Utilising digital representation of waves over accurate reef shapes (known at bathymetry), we simulated wave dissipation rates comparable to real-world SaG studies. By comparing high resolution, accurate bathymetries to smoothed bathymetries with SaG removed, we demonstrate a 40% decrease in wave energy dissipation. Next, we investigated how wave energy dissipation changes in different forereef environments. We considered low and high emission scenarios (RCP2.6 and RCP8.5) from the IPCC AR5 report and a total disaster scenario (TD) for the year 2100, considering changes to wave power, and water-level. We found that models based on high-emission scenarios (RCP 8.5) had decreased dissipation rates, resulting in more water passing the reef crest. Our study highlights the benefits of using accurate reef shapes in simulating wave energy dissipation on coral reefs. Accurate bathymetries can incorporate features such as SaG of different shapes, which increase wave dissipation.

1 Introduction

Coral reefs provide many ecosystem services including coastal hazard protection from ocean waves, with over 200 million people worldwide depending on the stability of this service (Ferrario et al. 2014). Coral reefs are topographically complex structures which contribute to the frictional dissipation of waves, however this has been studied in greater details on the reef crest and reef flat (Ferrario et al. 2014;/cite-Monismith2015, Péquignet et al. 2014, Yao et al. 2020) than on the high-energy environments of the forereef slope (Acevedo-Ramirez et al. 2021; Duce et al. 2014; Duce et al. 2016; Duce et al. 2022 Monismith et al. 2013, Sheppard 1981). Yet, wave breaking on the forereef slope is the dominant form of wave energy dissipation in high-energy conditions (Osorio-Cano et al. 2018) suggesting that it is a critical region for coastal protection by limiting wave transmission at the reef crest (Quataert et al. 2015). High dissipation rates on the forereef are controlled by forereef morphology such as spurs and grooves (SaG) (Monismith et al. 2013, Osorio-Cano et al. 2018). SaG are shore-normal elongate ridges (spur) and troughs (groove) on the forereef slopes of many coral reefs (Duce et al. 2016). Their size, spacing and orientation are typically aligned with incident waves and consequently the morphometric classification of SaG (Duce et al. 2016) reflects the influence of waves in their formation (Table 1). High energy forereefs feature more defined SaG than low-energy ones (Duce et al. 2016, Rogers et al. 2013). Recent research shows high-relief (up to 10 m) spurs in the Mexican Caribbean have a large influence over wave transformation, with dissipation in the SaG zone contributing 35% in wave energy flux. Wave energy flux on the forereef occurs mostly in the sea-swell frequency band (> 0.04 Hz), which is the focus of the research presented here. While infragravity waves (0.004-0.04 Hz) are important to wave transformation over reef flats and in lagoons (Cheriton et al. 2016), field measurements of waves over SaG have shown negligible energy in the infragravity bands (Duce et al. 2022). Further field investigations are required but have been limited by the difficulty of accessing highly exposed and turbulent forereef slopes (Sheppard 1981, Sous et al. 2022).

SaG morphologies are overlooked in 1D models of forereefs. SaG are also overlooked in both physical (e.g., Buckley et al. 2016) and numerical 2D models (e.g. Baldock et al. 2020, Monismith et al. 2013, Osorio-Cano et al. 2018) that do not include sufficient spatial resolution to include features at the spatial scale of SaG. Furthermore, numerical models that include SaG morphologies typically use idealised bathymetries (e.g. da Silva et al. 2020, Rogers et al. 2013) with simplified morphologies that overlook the irregularity and diversity of SaG. Consequently, the impact of SaG morphologies (Table 1) on wave attenuation is poorly understood (Duce et al. 2022, Monismith et al. 2013, da Silva et al. 2020).

Studies have shown that forereef morphologies including SaG will be impacted by climate change (Castillo et al. 2012, De'Ath et al. 2012, Hughes et al. 2018) likely resulting in reduced coastal protection (Baldock et al. 2014, Ferrario et al. 2014, Quataert et al. 2015, Sheppard et al. 2005) and increased wave overtopping (Amores et al. 2022, Beetham and Kench 2018). Most notably, a loss of structural complexity (roughness) in forereefs will reduce bed friction impacting wave attenuation (Baldock et al. 2014, Harris et al. 2018, Monismith et al. 2015, Rogers et al. 2016). These impacts are exacerbated by relative sea-level rise, changes in regional wave power

Deep and Disconnected (DaD)	Grooves are disconnected from the reef crest and appear in deeper water (> 5.5 m).
Exposed to wave energy (EWE)	Grooves are oriented toward the dominant wave direction.
Long and protected (LaP)	Grooves are longer (> 50 m) and not orientated toward the dominant wave direction.
Short and protected (SaP)	Groove lengths < 50 m and not orientated toward the dominant wave direction.

Table 1: Morphological categorisation of SaG Duce et al. (2016).

(Meucci et al. 2020, Reguero et al. 2019) and modification and intensification of storm climates (Knutson et al. 2015) which all modify wave transformation processes on forereefs.

The overall aim of this paper is to provide understanding of wave attenuation by SaG on contrasting coral reef environments. To achieve this, we first identify the benefits of high-resolution LiDAR-derived bathymetries in numerical wave models. Then we employ these models to determine how SaG of different morphological class affect the dissipation of wave energy. Finally, we investigate the effects of climate change on wave energy dissipation over SaG.

2 Methods

2.1 Study site

One Tree Reef (OTR) (23°30'S, 152°06'E) is located 84 km offshore of the NE Australian mainland in the Capricorn Bunker Group, in the southern Great Barrier Reef (GBR) (Figure 1a). OTR is a lagoonal platform reef with semi-diurnal tides with a mean spring tidal range of 3 m. The entire forereef of OTR features SaG (Duce et al., 2016). The mean significant offshore wave height, Hs,mean of 1.7 m (Smith et al. 2023) is typically generated from persistent SE trade winds that dominate the Coral Sea for over 70% of the year (Jell and Webb 2012). Consequently, the south-eastern forereef is the most exposed to ocean swells (Figure 1b). We considered two study sites featuring SaGs of varying morphological class (1) on the eastern and southern side of OTR (henceforth labelled OE and OS respectively) (Figure 1b, 1).

2.2 SaG morphometric analysis

We determined morphometric parameters for SAG in the two study sites including length, depth, width, and others (2) from analysis of LiDAR derived bathymetry and used them to classify the SAG following the categorical framework of Duce et al. (2016)(1).

2.3 Wave transformation modelling (XBeach)

We used XBeach (Roelvink et al. 2009) in Surf Beat mode due to its computational efficiency in solving short-wave amplitude variations. XBeach was selected as it has

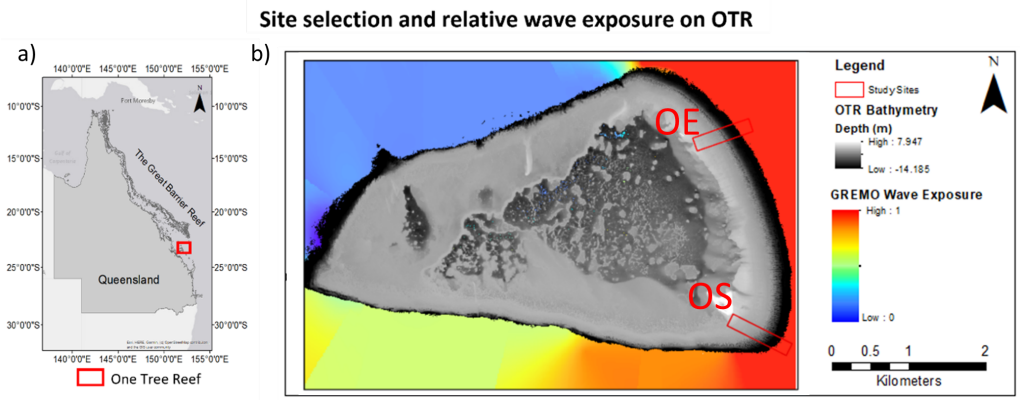

Figure 1: **A.** One Tree Reef (OTR) in the Southern Great Barrier Reef, and **B.** Study site locations for OTR East (OE) and OTR South (OS) and relative wave exposure Pepper and Puotinen (2009).

been extensively validated on complex coral reef bathymetries (Harris et al. 2018; Lashley et al. 2018; Quataert et al. 2015; Quataert et al. 2020, da Silva et al. 2020). XBeach has the capacity to include cross-shore currents and bed morphological changes, although those were not used in the present study. The lateral boundaries of all models were Neumann style boundaries which set the longshore gradients to zero, a recommended setting for Surf Beat modes to reduce the overestimation of longshore currents. For further details on the XBeach model parameters used see Perris (2024).

2.3.1 Bathymetric grids

We integrated data obtained from an Airborne LiDAR survey (Harris et al. 2023) with a spatial resolution of 0.5 x 0.5 m, to a depth of 14 m, and a bathymetry survey (Beaman 2017) with a resolution of 30 x 30 m, covering depths up to a maximum of 20 m (Figure 2). The mosaic was constructed by transforming both datasets to the Geocentric Datum of Australia 1994, zone 56. This allowed prioritisation of high-resolution dataset without averaging. The LiDAR derived bathymetry was modelled in XBeach at the same spatial resolution of 0.5 x 0.5 m, representing an 'accurate' bathymetry. The maximum depth at the offshore boundary, $h_{\max}$, was selected to capture all depth-limited wave breaking within the model and was based on historical wave heights for OTR considering:

$$h_{\max} = \frac{H_{\mathrm{rms}}}{\gamma} \tag{3.1}$$

where, γ is the breaker index, H_{rms} is the root mean square of the wave height. The breaker index was held constant across the reef at γ=0.55, reflecting the conservative estimation (γ=0.55) of Duce et al. (2022) and within the ranges determined by Harris et al. (2018). We created smooth bathymetric grids without the SaG morphologies (Figure 2 c) by resampling the grids using bilinear interpolation with cell size greater than γ_{SaG} (Table 2).

This method retained natural undulations in the forereef while removing the SaG.

Morphometric parameter	**Method**
Length (L)	Path distance along the groove (m).
Depth (h_G)	The vertical distance between the lowest point in the groove and the highest point on the neighbouring spur, calculated at four depths below sea level (-2, -4, -6, and -8 m).
Width (W)	Groove width measured as the horizontal distance between its walls at half the depth, along isobaths of -2, -4, -6 and -8 m.
Orientation (θ)	Azimuth of a straight line between the maximum onshore and offshore extents of the groove.
Sinuosity (S)	Ratio of straight-line distance (x) to path length (L), such that $S = x/L$.
Wavelength (γ_{sag})	The horizontal distance between the highest points of adjacent ridges, parallel to isobaths, measured at depths of -2, -4, -6, and -8 m below mean sea level.

Table 2: Morphometric parameters of SaG adapted from Duce et al. (2016).

Smoothed bathymetric grids were resampled to 0.5 m resolution to match the original grids.

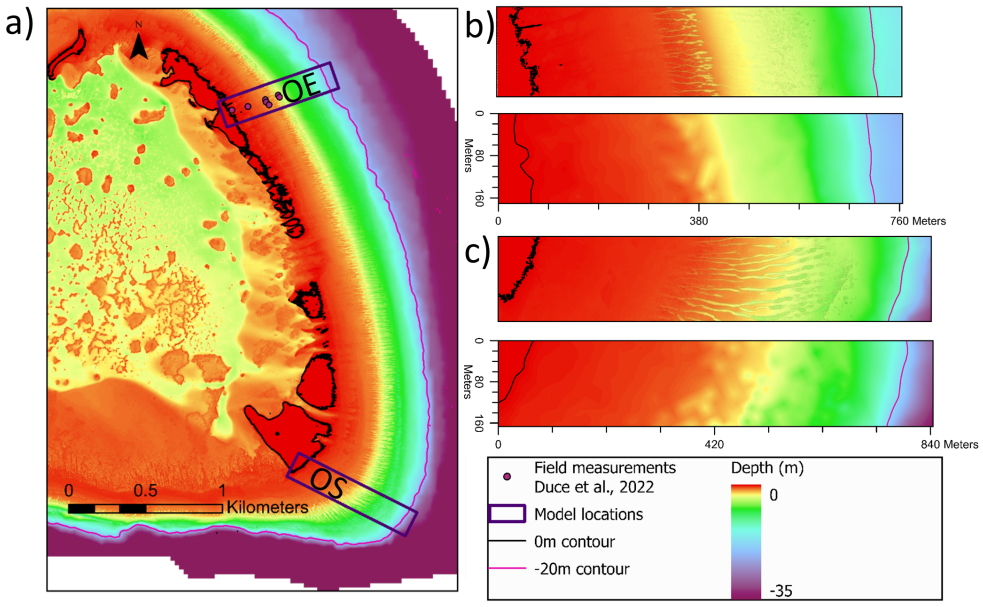

Figure 2: **a.** The bathymetric grids from LiDAR derived bathymetry of OTR (Harris et al. 2023) used in wave models from two study sites on the eastern (OE) and southern (OS) exposed forereefs of on One Tree Island. And **b.** the forereef bathymetries measured for site OE showing realistic and smoothed bathymetries. Smoothed bathymetries have retained the natural shape of the forereef with the removal of SaG Smoothed bathymetries have retained the natural shape of the forereef with the removal of SaG and **c.** for site OS.

The outer boundaries of the bathymetric grids were oriented to align mean groove headings with incident waves (Figure 2 b and c), following field observations (Duce et al. 2014, Munk and Sargent 1948, Shinn 1963) and other wave transformation models constructed over SaG (Rogers et al. 2013, da Silva et al. 2020) (Figure 2). Offshore boundaries were set beyond the maximum breaker depth for modelled wave heights (20 m: Equation 3.1) and the onshore boundaries at present-day 0 m MSL contour (Figure 2 b, c). Consequently, grids for each site are of different length and width (Figure 2 b).

We created smooth bathymetric grids without the SaGs morphologies by resampling the grids using bilinear interpolation with cell size greater than γ_{SaG} (Figure 2 c). Smoothed bathymetric grids were resampled to 1 m resolution to match the original grids. These smoothed grids were then run in XBeach under the defined four scenarios to quantify the influence of SaG presence on wave dissipation. The bed friction factor (f_w) was not changed between smoothed and realistic bathymetry models.

2.3.2 Contrasting forereef environmental models

We considered four conceptual differences in forereef environments, based on forecasted scenarios for the year 2100. We include critical climate impacts to wave energy dissipation on coral reefs: sea-level change, reef health and wave energy conditions. The climate change scenarios are based on IPCC AR5 and include (1) the present-day scenario considering no change to current environmental factors, (2) the *low* (RCP 2.6) and (3) *high* (RCP8.5) emission scenarios from the AR5 IPCC report (Shukla et al. 2019), and (4) a total disaster (TD) scenario included to represent an extrapolation from IPCC scenarios to demonstrate model sensitivity and to simulate non-climate drivers of reef degradation (Shukla et al. 2019) (Table 3).

2.3.3 Changes to sea level

We used IPCC AR5 sea-level rise (SLR) rate of 3 mm/yr (Shukla et al. 2019). Under the low and high emission scenarios (RCP2.6 and RCP8.5) SLR is expected to reach up to 10-20 mm/yr. Subsequently, we have included SLR of 0.43 m (RCP2.6) and 0.84 m (RCP8.5) for the year 2100 (Shukla et al. 2019). Human stressors (e.g., infrastructure development and human-induced habitat degradation) are also likely to contribute to increases in local SLR (Shukla et al. 2019). An additional 1 m of eustatic SLR was included for our total disaster (TD) scenario to reflect significant changes to climate conditions and non-climatic anthropogenic stressors (Shukla et al. 2019) (Table 3). The total sea-level increase in each of the models (Table 3) was determined by the sum of eustatic and local sea-level changes, and the vertical accretion and erosion of the reefs.

2.3.4 Reef morhological changes

Reef morphological changes have been simplified into three key characteristics, reef vertical accretion, erosion, and structural complexity. A forecasted vertical accretion rate of 2 mm/yr was used based on field measurements from coral reef cores from across the GBR (Dechnik et al. 2015; Sanborn et al. 2020), Western Australia

(Perry et al. 2018), Tahiti (Buddemeier and Smith 1988), the Maldives (Kench et al. 2022), Indo-Pacific averages compiled by Montaggioni (2005) and the Solomon Islands (Saunders et al. 2016). Alternatively, erosion of forereefs can occur due to the physical removal of coral and framework by storms and high wave energy (Madin and Connolly 2006). This is most evident on degraded coral reefs where erosion at the reef crest has been observed at 6 mm/yr (Eakin 1996; Sheppard et al. 2005). We used a conservative estimate of 2.6 mm/yr (0.2 m by 2100) of reef erosion for RCP 8.5 and a maximum of 6.4 mm/yr (0.5 m by 2100) of erosion under a TD scenario, modelled as a uniform decrease in elevation over the simulated domain, representing a simplified model of reef morphological transformation as spurs and grooves may respond to future reef transformation differently, however this has currently not been investigated. The resulting sea level was determined by combining projected rates of SLR with erosion and accretion values for each scenario (Table 3). To simulate a loss in forereef structural complexity, we altered the dimensionless wave friction factor (f_w) to replicate changes to coral structural complexity. To represent the healthy and rough forereef of OTR (Harris et al. 2023; Roelfsema et al. 2021), f_w were linearly interpolated between f_w=0.9 (healthy reef) to f_w=0.1 (degraded or smoothed reef). For the total disaster (TD) scenario, which represents a degraded reef and a shift to a carbonate sand substrate we used f_w=0.01 (Smyth and Hay 2002) (Table 3).

2.3.5 Wave input parameters

Mean offshore wave conditions were determined by satellite altimeter observations over 30 years (1985–2015) using RADWave (Smith et al. 2020) (Table 3). A small region (0.6° x 0.4°) representing dense altimeter data tracks was identified on the eastern, exposed side of OTR (Figure S1). We determined site-specific model input wave heights (H_model) by combining offshore wave conditions with a relative wave exposure model, GREMO (GIS-based generic model for estimating relative wave exposure; see Figure 1b) following Pepper and Puotinen (2009),

$$H_{\text{model}} = K_r \, H_{\text{offshore}} \tag{3.2}$$

where H_{offshore} is the offshore wave height obtained from RADWave (Figure 1b and Figure S1), and K_r is the relative exposure coefficient, normalised between 1 (most exposed) and 0 (least exposed). Finally, altimeter-derived wave heights for offshore swell ($H_{s,\text{mean}} = 1.3\,\text{m}$; Table 3) were compared with measured waves at the eastern forereef at OTR ($H_{s,\text{mean}} = 0.62\,\text{m}$ at the outer forereef) (Duce et al. 2022).

2.3.6 Changes to wave climate

We increased offshore model wave heights ($H_{offshore}$) to simulate contrasting forereef environments based on future climate change scenarios (Table 3), based on forecasted H_s estimates for the year 2100 by Shukla et al. (2019), with wave periods (T_{model}) determined for a fully developed sea-state from the Joint North Sea Wave Project (JONSWAP) spectrum (Young 1992). Storm waves were calculated from the maximum wave height observed in RADWave altimeter data. The final

model wave heights were dependent on forereef location and relative exposure to wave energy determined by equation 3.1.

Site	Climate scenario	Wave Condition	$H_{offshore}$ (m)	Exposure Factor	H model (m)	T_{model} (s)	Friction factor	SLR (m)	Vertical Accretion	Reef erosion (m)	Total change in MSL (m)
OS	Present day	Mean	1.34	0.985	1.3	5.74	0.9	0	0	0	0
	RCP 2.6		2.14				0.54	0.43	0.16	0	0.3
	RCP 8.5		2.14		2.1	7.26	0.1	0.84	0.1	0.2	0.99
	TD		2.14				0.01	1.84	0	0.5	2.34
	Present day	Storm	4.8		4.7	10.87	0.9	0	0	0	0
	RCP 2.6						0.54	0.43	0.16	0	0.3
	RCP 8.5		5.6		5.5	11.74	0.1	0.84	0.1	0.2	0.99
	TD						0.01	1.84	0	0.5	2.34
OE	Present day	Mean	1.34	0.9042	1.2	5.5	0.9	0	0	0	0
	RCP 2.6		2.14				0.54	0.43	0.16	0	0.3
	RCP 8.5		2.14		1.9	6.96	0.1	0.85	0.1	0.2	0.99
	TD		2.14				0.01	1.84	0	0.5	2.34
	Present day	Storm	4.8		4.3	10.42	0.9	0	0	0	0
	RCP 2.6		5.6				0.54	0.43	0.16	0	0.3
	RCP 8.5		5.6		5.1	11.25	0.1	0.84	0.1	0.2	0.99
	TD		5.6				0.01	1.84	0	0.5	2.34

Table 3: Model input parameters are presented for three study sites, two wave conditions and four forecasted climate outcomes for the year 2100. A total of 16 unique models were run.

2.3.7 XBeach model outputs

Each model was run for a total of 300 seconds to allow sufficient spin up time for wave propagation across the modelled domain. We analysed the outputs of XBeach for water surface elevation (z_s), total dissipation rate (D), and dissipation rate due to bed friction (D_f) to obtain wave energy dissipation rates and wave transmission over the reef crest. Total dissipation was used to compare XBeach results with field measurements and to determine dissipation by breaking (D_b) such that D_b=D-D_f . As models are two-dimensional (x, y spatial domains) and evolve through time (t), we calculated mean and peak total dissipation rates across t and x domains for the entire bathymetric grid. Mean total dissipation rates were also taken between two points where hydrodynamic data sampled by Duce et al. (2022). Wave transmission over the reef crest was calculated as the difference between the initial water level at the reef crest and the maximum water level at the reef crest during each model run.

3 Results

3.1 SaG morphometric analysis

SaG morphometrics were quantified for 123 grooves across the two study sites (Table 3). Grooves at the southern site (OS) were on average 3 times longer, 1.4 times deeper and 1.3 times wider than those at the eastern site (OE) (Table 3) Using the morphometric classification of Duce et al. (2016), the exposed to wave energy (EWE) grooves were the most common across three of the four sites (100 of 123 SaG) (Table 3). Deep and disconnected (DaD) grooves were present on the lower forereef platform of site OE.

	Mean SaG Morphometric Parameters					Quantity of SaG Classes by Site			
Site	**Length (m)**	**Sinuosity**	**Orientation (Deg)**	**Depth (m)**	**Width (m)**	**DaD**	**EWE**	**LaP**	**SaP**
OS (south)	187.12	0.99	116.73	1.95	4.02	0	40	0	0
OE (east)	63.18	0.99	71.5	1.38	3.12	23	60	0	0

Table 4: Morphometric parameters and classes of SaG at two study sites.

3.2 Wave transformation over accurate bathymetry

The peak dissipation rates under present day conditions, taken as the maximum dissipation across all axes (x, y, t), were 463.9 and 946.3 W/m^2 at sites OE and OS respectively (Figure 3). Wave energy dissipation due to bed friction was dominant in present day scenarios over dissipation due to wave breaking (Figure 4b and d). Between the two locations of field measurements conducted by Duce et al. (2022) (Figure 2 c) the mean dissipation rate was 10.6 W/m^2, the maximum dissipation rate of 463.9 W/m^2 occurred during this zone. Wave energy dissipation by bed friction contributed 78% of energy at the site OE before waves reached the reef crest, 67% at site OS in the upper forereef slope. The maximum wave energy dissipation due to wave breaking constituted 22%, and 32% of total dissipation at site OE and OS respectively (Figure 4b, d).

3.3 Comparison of realistic and smoothed bathymetry

Realistic bathymetries were compared to modified bathymetries with SaG removed. In all cases, removing SaG resulted in a decrease in both peak and mean wave energy

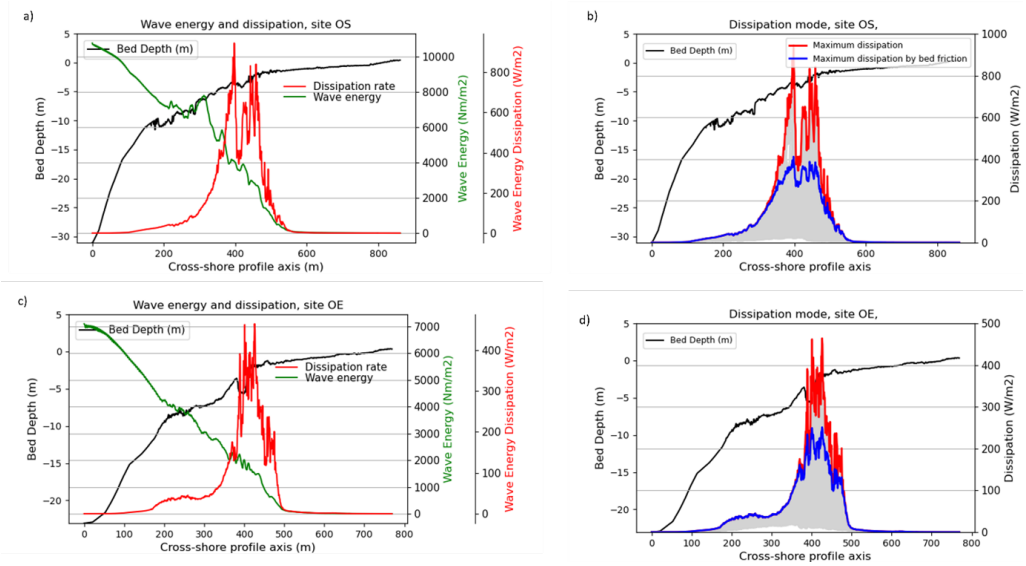

Figure 3: Alongshore-averaged wave energy (depicted in green) and corresponding maximum wave energy dissipation across the x-domain. Exemplary bathymetry profiles (illustrated by black lines) originate from the centre of the model (y/2) at Site OS (a) and site OE (c). Figure (b) and (d) represent the maximum dissipation and maximum dissipation attributed to bed friction (depicted in blue) for site OS and site OE, respectively. It is important to observe that distinct scale bars are applied for each respective site.

dissipation across the entire simulated domain. With SaG removed, peak dissipation at site OS was 92.56 W/m^2 and mean dissipation was 2.61 W/m^2. This represents a 90.2% reduction in peak wave energy dissipation, and a 40.06% reduction in mean wave energy dissipation across the entire profile. At site OE, removing SaG features from the bathymetry resulted in peak wave energy dissipation of 463.85 W/m^2 and a mean dissipation rate of 2.2 W/m^2. This represents a 16.6% decrease in peak wave energy dissipation and a 12.67% decrease in mean wave energy dissipation.

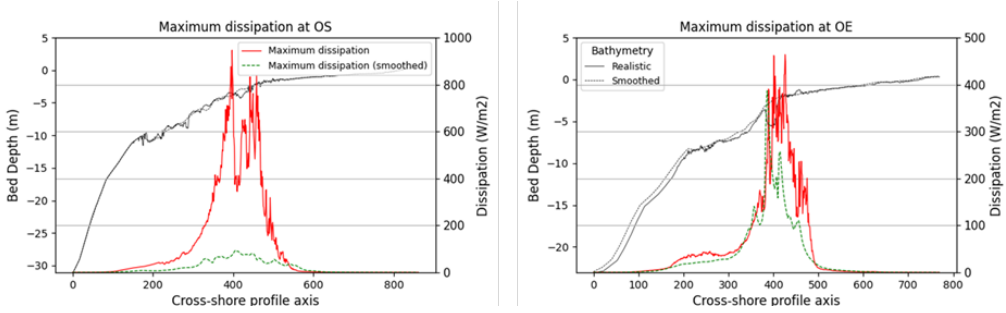

Figure 4: The maximum dissipation measured at site OS (a) and OE (b) for actual bathymetry and smoothed bathymetries.

The percentage of breaking versus frictional dissipation is also modified by the presence of SaG. Mean dissipation due to bed friction was 2.62 W/m^2 at site OS and 2.18 W/m^2 at site OE, representing 99.95% and 99.41% of total dissipation respectively (Figure 5). This contrasts to real bathymetry models (Figure 3 b,d) where dissipation by bed friction represented 78% and 67% at site OS and OE respectively. The

bed friction factor (f_w) was not changed between smoothed and realistic bathymetry models.

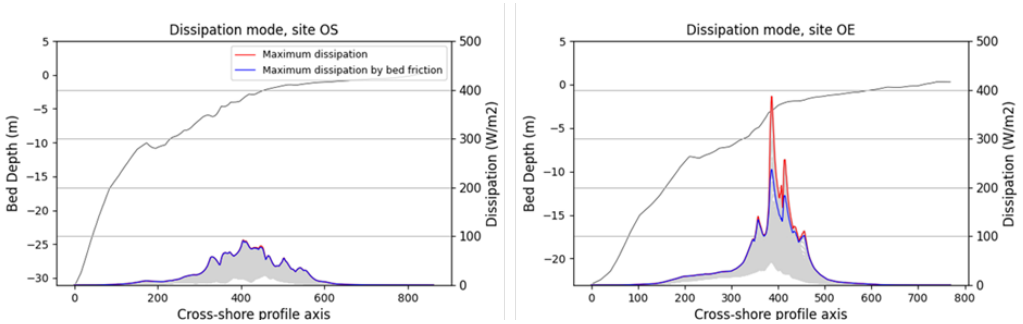

Figure 5: The maximum dissipation and maximum dissipation attributed to bed friction (depicted in blue) over smoothed bathymetries for site OS and OE. Exemplary bathymetry profiles (illustrated by black lines) originate from the central region of the model ($y/2$).

3.4 Wave transformation over contrasting forereef environments

Wave transformation was found to vary greatly among models depending on SaG morphology, wave exposure, mean water levels and reef structural complexity. These parameters are likely to change as climate changes (Amores et al. 2022; Castillo et al. 2012; Harris, Rovere, et al. 2018; Hughes et al. 2018). Total wave energy dissipation and dissipation due to bed friction changed at both sites for all modelled forereef environments (Table 3).

Mean and peak total dissipation rates were computed for each site across all three climate scenarios (Table 3, Figure 4). When comparing dissipation rates from present day to RCP2.6 for the year 2100, mean total dissipation increased by 187% at site OS (4.4 to 12.5 W/m^2) and maximum total dissipation increased by 59.7% (946.3 to 1511.4 W/m^2) (Figure 6a and b). At site OE, mean total dissipation rate increased by 208% (2.5 to 7.8 W/m^2) and maximum total dissipation increased by 217.7% (463.9 to 1473.4 W/m^2) (Figure 6d and e).

When comparing RCP2.6 to RCP8.5 we found a decrease in mean total dissipation across site OS of 18.1% (12.5 to 10.6 W/m^2) and an increase in the maximum total dissipation rate of 23.2% (1511.4 to 1966.9 W/m^2). Site OE retained at high mean total dissipation rate from RCP2.6 to RCP8.5, increasing a further 11.7% (7.78 to 8.81 W/m^2) and an increase of 19.3% to peak dissipation rate (1473.42 to 1824.70 W/m^2).

When comparing to RCP8.5, the TD scenario, mean total dissipation rates decreased by 66.2% (10.61 to 3.58 W/m^2) at site OS and a decrease in peak total dissipation of 31.8% (1966.89 to 1340.93 W/m^2) (Figure 3b and c). At site OE, mean total dissipation decreased by 86.2% (8.81 to 1.21 W/m^2) and peak total dissipation rate decreased by 75.4% (1824.7 to 448.24 W/m^2) (Figure 4 e and f).

Under present-day conditions, bed friction is dominant, contributing 98% and 99% of total wave energy dissipation (Figures 5 and 7). Comparing RCP 2.6 to RCP

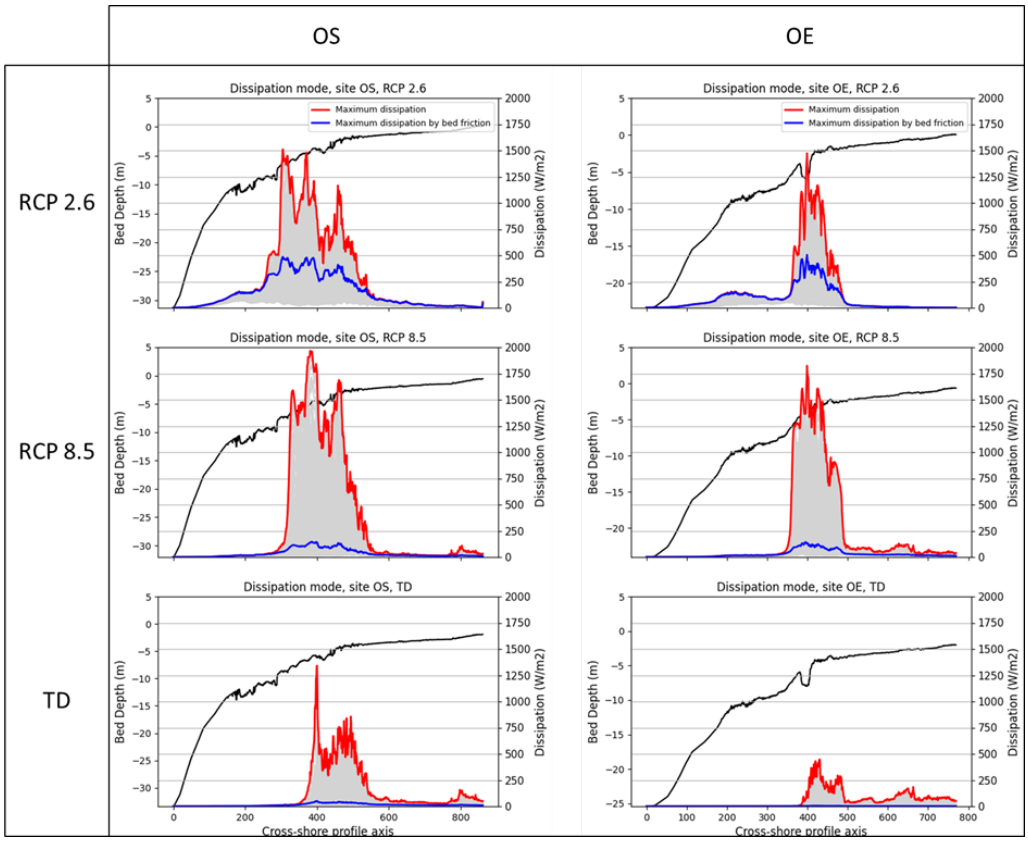

Figure 6: Maximum wave energy dissipation (red),dissipation due to bed friction (blue) and all dissipation profiles (grey) across the x and time domains, for Site OS under RCP 2.6, RCP 8.5 and TD forereef environments, for site OE under RCP 2.6, RCP 8.5 and TD forereef environments. Exemplary bathymetry profiles (illustrated by black lines) originate from the central region of the model ($y/2$). Note Y axis are unique for each study site to highlight relative differences in dissipation across contrasting forereef environments (Table 3).

8.5, site OS decreased in total dissipation by 15.3% and at site OE total dissipation increased by 13.2% (Figure 7). This can be attributed to a decrease in frictional dissipation by 57% at site OS and 42% at site OE.(Figure 6 and Figure 7). In this case, dissipation by wave breaking increased by an average of 659% for both sites. This results in a shift in the dominant form of wave energy dissipation (Figure 7). Comparing RCP2.6 to the TD scenario, mean frictional dissipation (Df) decreases by 82.5% at site OS and 95.8% at site OE while wave breaking remains marginally greater by 0.1% (OS) and 1.5% (OE) in the TD scenario. Despite this, mean total wave energy dissipation (the sum of frictional and wave breaking dissipation rates) decreases by 71.4% (OS) and 84.4% (OE).

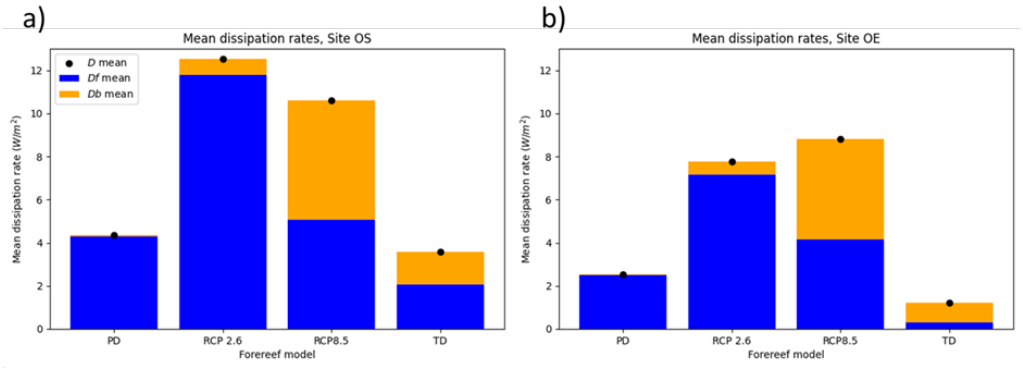

Figure 7: Mean total dissipation (D mean) for OS (a) and OE (b) study sites and mean dissipation by bed friction (Df mean) and wave breaking (Db mean) for each forereef model (see Table 3) under mean wave conditions.

We calculated maximum water levels at the reef crest for both sites under four forereef model environments, based on present day conditions and three climate change scenarios considering both mean and storm wave conditions (Table 2). For mean wave conditions, maximum reef crest water levels in the present-day model was near zero (0 and 0.1 m at site OS and OE, respectively). The maximum reef crest water levels increase for all simulated reef scenarios (Figure 7). We calculated a maximum excursion from mean water levels at the reef crest of 0.4 m at site OS and 0.1 m at site OE for RCP 2.6 with larger increases to 0.4 m (OS) and 0.7 m (OE) for RCP8.5. The high emissions scenario (TD) had the highest reef crest water levels of 2.1 m (OS) and 2.0 m (OE). Storm wave conditions increased reef crest water levels compared to mean wave heights in all cases (Figure 6; Table 2). Under present-day conditions, reef crest water levels were greater for mean wave conditions at 1.25 and 0.5 m for site OS and site OE respectively. Under forecast climate change scenarios, storm waves did not significantly impact reef crest wave transmission under RCP2.6 compared to present day conditions despite an increase in wave height of 3.5 m. Reef crest water levels, under RCP8.5, was 2.1 m at site OS and 1.4 m at site OE which increased significantly to 3.5 m and 3.9 m in TD models at each site respectively.

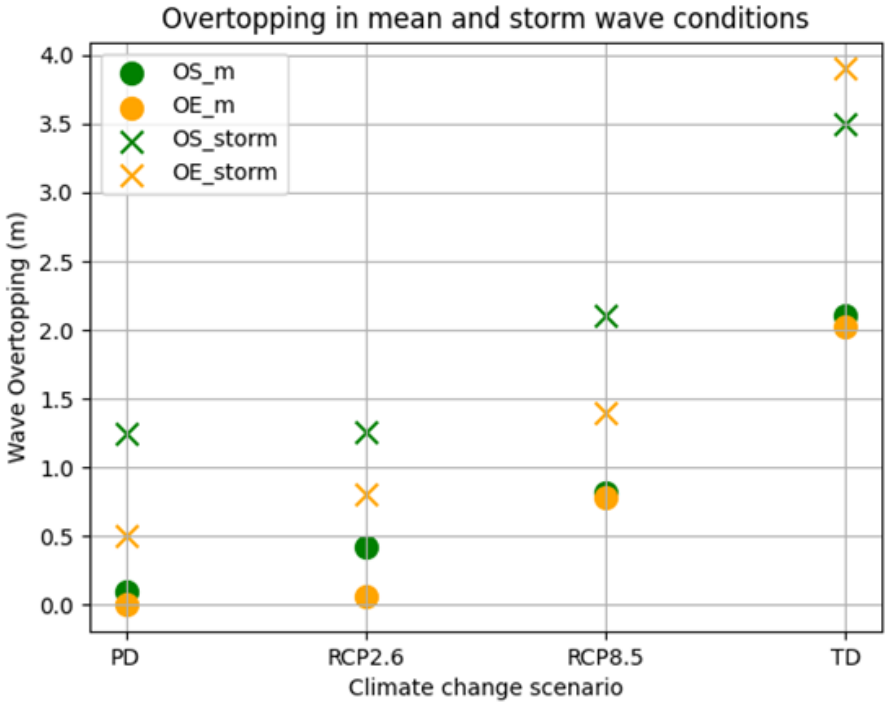

Figure 8: The maximum excursion from mean water levels at the reef crest (0 m contour) at both sites under mean (OS_m and OE_m) and storm (OS_storm and OE_storm).

4 Discussion

4.1 Benefits of accurate high-resolution bathymetries in numerical wave models

Our models of wave transformation over LiDAR-derived bathymetries focus on the influence of SaG morphology on wave energy dissipation and wave transmission over the reef crest. Under mean wave conditions we calculated average dissipation rates across the entire forereef profile of 3.61 W/m^2 at site OS and 2.52 W/m^2 at site OE for offshore wave heights of 1.3 m and 1.2 m respectively. This calculation is made across the entire reef profile representing 862 m and 770 m respectively (Figure 2b, c). Field measurements of wave energy dissipation conducted at OTR were taken at the same site as OE presented in this study (Figure 2) (Duce et al. 2022). We determined a mean dissipation rate of 10.6 W/m^2 across 60 m between the two instruments, almost entirely due to bed friction (Figure 3 d). Duce et al. (2022) recorded mean dissipation rates of 20 W/m^2 with wave heights of H_s = 0.78 m and T_p = 5 seconds. Differences in the recoded and modelled data at this site may be attributed to the incident wave direction (N-NE during the deployment period) which was not completely aligned with SaG as modelled here. These results compare with data obtained on a fringing reef in Ipan (Guam) which also featured SaG on the forereef (Péquignet et al. 2011). Between two sensors placed 55 m apart inside a 5 m deep groove, the dissipation rate was 25 W/m^2 for offshore wave heights of 1-2 m (Péquignet et al. 2011). Monismith et al. (2015) identified comparable dissipation

rates of 25 W/m^2 on a forereef in Palmyra (Kiribati) between instruments 50 m apart for incident wave heights of 1 m. Monismith et al. (2013) determined rates of 22 W/m^2 across a forereef at Mo'orea (French Polynesia) with instruments located 50 m apart and wave heights of 0.3 to 0.5 m. Dissipation rates for each of these studies are assumed to be due to bed friction with constant dissipation between the instruments. Our results produce comparable dissipation rates to field measurements in similar environments, demonstrating the successful application of realistic bathymetries to numerical modelling of forereef wave energy dissipation.

Using a real bathymetry, our study demonstrates the influence of groove sinuosity on wave energy dissipation by breaking. Our results show that shore-normal waves interact with spur walls that do not perfectly align with incoming swell. In our study, the mean groove heading was used to align the bathymetric grids to the oncoming waves (Figure 2 b), consistent with field observations (Duce et al. 2020; Munk and Sargent 1948). Despite this, variation in headings between grooves and the sinuosity of individual grooves produces steep irregularities in the forereef slope that have a large impact on the oncoming waves, playing a significant role on both dissipation by wave breaking and bed friction. The straight and shore normal SaG identified in this analysis (mean sinuosity of $S = 0.99$, where 1 is a perfectly straight groove) (Table 4) are representative of groove sinuosity across the southern Great Barrier Reef. For example, observations of 12,102 grooves in the GBR and South Pacific show a mean groove sinuosity of $S = 0.98$ (Duce et al. 2016). Despite the remarkable regional consistency in groove morphology, our results show that even small departures from shore-normal orientation can substantially alter wave transformation on the forereef (e.g. Figure 7), implying that the influence sinuous grooves on reef slope, rather than the presence of grooves alone, exerts a control on dissipation, consistent with Watanabe et al. (2023). These features would not be considered in 1D or idealised 2D bathymetries. The use of real bathymetries in modelling efforts can elucidate the heterogeneity of dissipation rates on forereefs.

4.2 Effects of SaG on wave energy dissipation

SaG morphology was found to increase wave energy dissipation. We compared forereefs featuring SaG to forereefs with SaG removed, while controlling for water level, wave height and bed friction (Figure 4). At both sites, the presence of SaG increased dissipation on the outer forereef (Figure 4). The frictional mode of dissipation was dominant in both smoothed (SaG removed) and realistic bathymetries. Dissipation by wave breaking was reduced in the smoothed models, despite similar model resolution and forereef geometry (Figure 5). At site OE, dissipation by breaking occurs in a similar location along the forereef (Figure 5, Figure 3 b,d), near the reef crest. However, the magnitude of wave breaking is reduced, as the mean bathymetric gradient at the reef crest is reduced by the removal of SaG features. This lends further support to the idea that SaG morphology can introduce steep bathymetric inclines to forereefs that can increase wave energy dissipation by breaking. Differences in SaG morphology similarly have an impact on wave transformation and dissipation. The most wave exposed site (southern site, OS) has the highest average dissipation rates of 71.5% over 300 m SaG zone due to bed friction (Figure 3 a). The long (mean length of 187.12 m) and deep (mean depth of 1.95 m) exposed to wave energy (EWE) grooves at this exposed site may explain how this high average

dissipation rate occurred (Table 1). The length of EWE SaG creates surfaces of high frictional drag that extend the zone of frictional dissipation and contribute to high average dissipation rates (Figures 4 a and 5). Shore normal currents occurring in the long and deep grooves have also been observed and facilitate high rates of dissipation (Rogers et al. 2013). We demonstrate under present-day conditions that bed frictional dissipation is dominant in dissipating wave energy before breaking occurs at the reef crest (Figure 3 a and c). Bed frictional dissipation represents 98.0% and 98.9% of total dissipation at site OS and OE respectively (Figure 3a and c). This is consistent with field research conducted at OTR (Duce et al. 2022) and in other high-energy settings (Lowe et al. 2005; Monismith et al. 2015; Rogers et al. 2017). For example, under mean wave conditions at Palmyra (Kiribati), a high bed friction coefficient (f_w =1.8) facilitated greater wave energy dissipation due to bed friction than from wave breaking (Monismith et al. 2015), which is consistent with field observations in Kaneohe Bay, Oahu, Hawaii (Lowe et al. 2005). Our results suggest that the modes of wave energy dissipation (frictional or breaking) are not only influenced by the wave conditions but also by the heterogenous morphology of the forereef slopes (Figure 6, 8).

SaG morphology and consequently the morphological classes of Duce et al. (2016) can provide further explanations for the mode of wave energy dissipation (Table 1). Where grooves are shorter, they play a critical role in creating steep bathymetric gradients that induce wave breaking (Figures 4 and 8). This differs from previous SaG research (Acevedo-Ramirez et al. 2021) that showed wave breaking being induced by the reef crest. Semi-exposed SaGs (represented here by site OE) are typically shorter (mean length of 71.5 m) and shallower (mean depth of 1.38 m) than the most exposed sites (site OS) and can include both exposed to wave energy (EWE) and deep and disconnected (DaD) classes (Table 1). The seaward extent of the EWE grooves at semi-exposed forereef sites (OE; Figure 3d) feature a steep bathymetric incline that produces the maximum wave energy dissipation by wave breaking rate observed across all present-day models (1824.7 W/m^2, Figure 6). As such, long spurs can facilitate frictional dissipation and short grooves can induce wave breaking by introducing steep bathymetric inclines within the breaker zone of incident waves.

The peak in wave energy dissipation shoreward of exposed to wave energy (EWE) grooves highlights the complex interaction between forereef morphological evolution and wave energy (Figure 3 e). The seaward extent of EWE grooves is at a depth of 3.5 m, coincident with the mean model wave height breaker depth for waves of 1.3 – 4.3 m (Figure 3, Table 2). As wave breaking imposes forces on the structure of the reef (Massel and Gourlay 2000; Storlazzi et al. 2005) the results presented here suggest that incident waves could be capable of modifying the EWE grooves in this zone, which is consistent with C14 and U-Th ages of SaG formations on the eastern forereef of OTR (Duce et al. 2020), suggesting an erosive origin for this grooves. Imposed climate change effects further elucidate the influence of grooves. Deep and disconnected (DaD) grooves at site OE exist below the typical wave base and have minimal interaction with present day wave energy. Supporting the previous findings that DaD grooves may be relict features, formed at an early stage during the Holocene transgression (Duce et al. 2016).

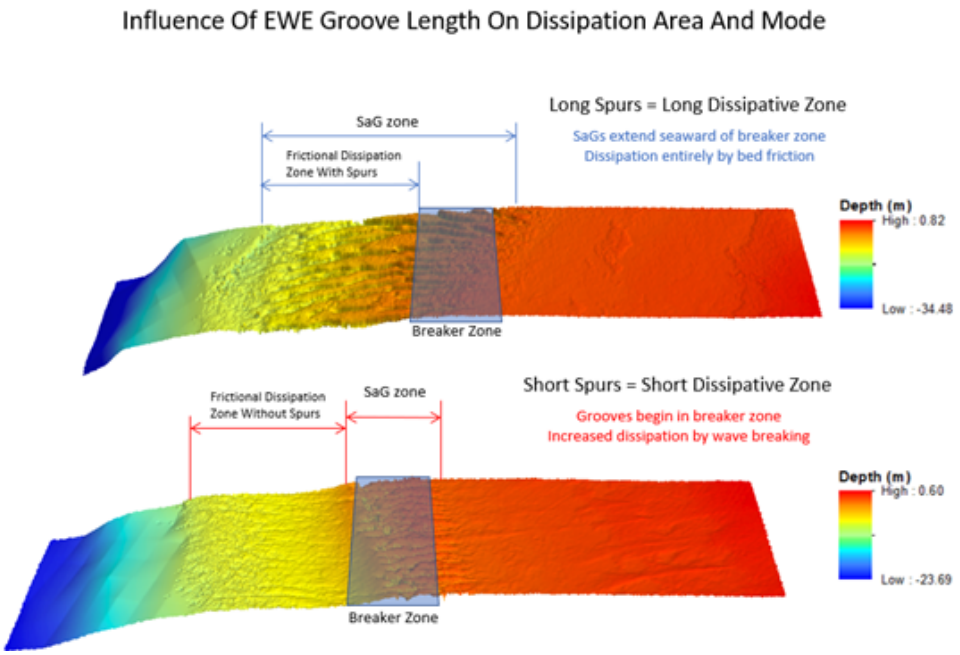

Figure 9: A comparison between exposed and semi-exposed bathymetric profiles (site OS and site OE) demonstrate the influence of the length of the SaG zone.

4.3 The impact of contrasting forereef environments on wave energy dissipation over SaG

Forecasted environmental changes decrease mean wave energy dissipation (Figure 6) which is consistent with other approaches (e.g., Quataert et al. 2015; Sheppard et al. 2005). In the simulations presented here, dissipation remains high between RCP 2.6 and RCP 8.5 as reduced dissipation by bed friction is balanced by an increase in dissipation by wave breaking (Figures 5 and 6). The difference between dissipation by bed friction and dissipation by wave breaking is the greatest at both sites for RCP 8.5, where water depth is still sufficient for wave breaking, yet the degradation of the reef reduces frictional effects (see Figure 8). A reliance on wave breaking dissipation is consistent with observations from high energy reefs of low structural complexity (Harris et al. 2018). Finally, dissipation is lowest where SLR is greatest (TD scenario) due to wave passing over the reef without breaking (Figure 8). Although the role of SLR is thought to be secondary in contributing to these changes (Harris et al. 2018), our models suggest that the combined impact of SLR and loss of structural complexity will lead to lowest dissipation rates (Figures 5 and 9) and highest waves at the reef crest(Figures 6 and 9) when climate change parameters (Table 3) were increased between the contrasting forereef environments. Sea-level rise (SLR) shifts the region of high energy dissipation toward the reef-crest (Figure 6 b, c and e, f). Bathymetric features that are submerged into the surf zone by rising relative sea level are likely to influence wave breaking and frictional dissipation (Figure 6). This is evident in the shoreward shifting dissipation zones (Figure 6) and as previous literature states (Massel and Gourlay 2000) is a threat to corals in this zone as wave breaking results in greater hydrodynamic forces on corals. Corals previously protected from wave energy are likely to be species of lower mechanical strength (Storlazzi et al. 2005). Under worse case scenarios (RCP 8.5) by

the year 2100 it is likely that corals of the same species may be weaker due to lower carbonate saturation in the water column (Eakin 1996) or high frequency bleaching events (Hughes et al. 2017). Coral breakage is likely to occur here and the corals that support a steep bathymetric incline with a high frictional coefficient responsible for this peak in wave energy dissipation may have lower structural resilience by 2100 (Eakin 1996).

High-energy SaG formations have been attributed to wave induced erosion, albeit at vastly different timescales to sedimentary swash-zone features such as rip channels (Duce et al. 2020). It is possible that climate change-driven increase in erosive forces promote further SaG development on forereefs, which contributes to the dissipation of wave energy.

4.4 Increased wave transmission at the reef crest

Wave transmission at the reef crest increases with increased climate change parameters due to the coupled effects of decreased bed friction and loss of dissipation due to breaking (Figure 6) Compared to mean wave conditions, the impact of storm waves results in increasingly greater excursion from mean water levels at the reef crest when climate projections are increased. (Figure 6). This effect is persistent despite the increased wave energy dissipation at the semi-exposed forereef (site OE) under RCP 8.5 (Figure 3 e). The primary control on wave height at the reef crest is sea-level rise, which incorporates eustatic and local sources. Future work should include tidal effects, which would contribute an additional 1.5 m of water level at mean spring high tide at OTR (Harris et al. 2015). The magnitude of wave height increase at the reef crest observed in the TD scenario at the exposed site (OS) of 4 m is sufficient to entirely flood all backreef environments at OTR, including the low-lying coral island. An increase in wave transmission at the reef crest of this magnitude would have significant impacts on coral reef islands and reef-lined shores(Fellowes et al. 2022; Storlazzi et al. 2015; Talavera et al. 2021). For example, 3.7 m of wave run up combined with sea surface elevation above a reef flat in Roi-Namur, Marshall Islands, was observed in flooding of inland area of the Island (Cheriton et al. 2016). Research elsewhere demonstrated that wave overtopping on reef islands in the year 2100 will be highly variable across due to variable reef vertical accretion and erosion rates (Beetham and Kench 2018, Kench et al. 2022), but also due to the vertical accretion of coral reef islands (Kench et al. 2019; Kench et al. 2022, Masselink et al. 2020) which is controlled by sediment availability.

The combined influence of coral reef degradation and sea-level rise amplifies the occurrence of wave transmission beyond the reef crest. Thereby, exposing communities protected by coral reefs to heightened risks of flooding (Harris et al. 2018, Quataert et al. 2015, Storlazzi et al. 2018). Notably, a maximum overtopping of approximately 4 m was measured here when the significant wave height reached 5.1 m. An examination of altimeter data reveals that within the 33-year data span, wave heights have not surpassed this threshold (95th percentile wave height = 3.1 m) (Figure S1, supplementary material). Consequently, further investigation is required to determine the frequency of significant overtopping events at OTR.

5 Conclusion

This study combined numerical modelling and LiDAR-derived bathymetry to demonstrate the importance of forereef spur and groove (SaGs) morphologies in modifying wave energy. Results indicate that high resolution digital elevation models (< 1 m) can provide morphometric data to examine wave transformation on forereefs comparable to field studies. We show that groove sinuosity plays a role in wave transformation and should be considered in future research on wave dissipation on SaG. This highlights the need for realistic bathymetries in future studies of forereef wave energy dissipation, as idealized bathymetries used in previous studies, using numerical or physical modelling overlook features such as SaG, which increase wave energy dissipation. By comparing bathymetries with and without SaG, we demonstrate that SaG morphologies can increase wave energy dissipation by inducing breaking and increasing bed friction. Additionally, SaG morphological classes exhibit distinct dissipation characteristics, with some showcasing higher frictional dissipation and others exhibiting greater breaking dissipation. Notably, spur length emerges as a critical factor in enhancing dissipation by bed friction. Among the SaG morphological classes, exposed to wave energy (EWE) grooves have demonstrated the greatest dissipation rates, while deep and disconnected (DaD) grooves contribute less to the dissipation process, particularly when climate change parameters like water level was increased and bed friction factor decreased between each model.

Analysing the climate change parameters included in each successive model demonstrated that changes in the mode of wave energy dissipation will likely occur. The most notable result was a decrease in dissipation by bed friction from 100% of dissipation under present day conditions to 48% under RCP 8.5. This is matched by a 52% increase in dissipation by wave breaking. Overall, we found a reduction in wave energy dissipation across contrasting forereef environments based on future climate change parameters such as increased water level and decreased bed friction factor. This leads to increased wave transmission at the reef crest, with the maximum transmission occurring where dissipation was lowest. Forereef morphological adjustment to increased dissipation by wave breaking may expose corals to erosion, a process which has been linked to the formation of SaG. The results highlight the critical role of forereef morphology in wave energy dissipation and the need for measures to promote coral growth to facilitate future dissipation.

Acknowledgments We acknowledge the Gadigal people of the Eora Nation, the traditional owners of the land and waters where this research was conducted, and pay respects to their elders past, present and emerging. We acknowledge the cultural significance of the Southern Great Barrier Reef, where we conduct fieldwork, to the Tarebilang Bunda, Bailai, Gooreng Gooreng and Gurang Traditional Owners. Lachlan Perris was supported by an RTP scholarship from The University of Sydney and the research was partially funded by ARC Future Fellowship (FT100100215), ARC Discovery Program (DP220101125), and Geoscience Australia funding through the Marine Studies Institute at The University of Sydney.

Open research XBeach version 1.22 (revision 4567) is used in this analysis (Roelvink et al. 2009). Python codes used to interpret bathymetry in XBeach and analyse outputs are available online (Perris 2024).

References

Acevedo-Ramirez, C. A., W. Stephenson, S. Wakes, and I. Mariño-Tapia (Sept. 2021). "Wave Transformation on a Fringing Reef System With Spur and Groove Structures". In: *Journal of Geophysical Research: Oceans* 126 (9). DOI: 10.1029/2020JC016910.

Amores, A., M. Marcos, G. L. Cozannet, and J. Hinkel (2022). "Coastal flooding and mean sea-level rise allowances in atoll island". In: *Scientific Reports* 12 (1), pp. 1–12. DOI: 10.1038/s41598-022-05329-1.

Baldock, T. E., A. Golshani, D. P. Callaghan, M. I. Saunders, and P. J. Mumby (June 2014). "Impact of sea-level rise and coral mortality on the wave dynamics and wave forces on barrier reefs". In: *Marine Pollution Bulletin* 83 (1), pp. 155–164. DOI: 10.1016/j.marpolbul.2014.03.058.

Baldock, T. E., B. Shabani, D. P. Callaghan, Z. Hu, and P. J. Mumby (2020). "Two-dimensional modelling of wave dynamics and wave forces on fringing coral reefs". In: *Coastal Engineering* 155. DOI: 10.1016/j.coastaleng.2019.103594.

Beaman, R. J. (2017). *High-resolution depth model for the Great Barrier Reef - 30 m*. DOI: 10.4225/25/5a207b36022d2.

Beetham, E. and P. S. Kench (2018). "Predicting wave overtopping thresholds on coral reef-island shorelines with future sea-level rise". In: *Nature Communications* 9 (1). DOI: 10.1038/s41467-018-06550-1.

Buckley, M. L., R. J. Lowe, J. E. Hansen, and A. R. V. Dongeren (2016). "Wave setup over a fringing reef with large bottom roughness". In: *Journal of Physical Oceanography* 46 (8), pp. 2317–2333. DOI: 10.1175/JPO-D-15-0148.1.

Buddemeier, R. W. and S. V. Smith (1988). "Coral reef growth in an era of rapidly rising sea level: predictions and suggestions for long-term research". In: *Coral Reefs*, pp. 51–56.

Castillo, K. D., J. B. Ries, J. M. Weiss, and F. P. Lima (2012). "Decline of forereef corals in response to recent warming linked to history of thermal exposure". In: *Nature Climate Change* 2 (10), pp. 756–760. DOI: 10.1038/nclimate1577.

Cheriton, O. M., C. D. Storlazzi, and K. J. Rosenberger (2016). "Observations of wave transformation over a fringing coral reef and the importance of low-frequency waves and offshore water levels to runup, overwash, and coastal flooding". In: *Journal of Geophysical Research: Oceans* 121 (9), pp. 6762–6778. DOI: 10.1002/2016JC012132.Received.

da Silva, R. F., C. D. Storlazzi, J. S. Rogers, J. Reyns, and R. McCall (2020). "Modelling three-dimensional flow over spur-and-groove morphology". In: *Coral Reefs*. DOI: 10.1007/s00338-020-02011-8.

De'Ath, G., K. E. Fabricius, H. Sweatman, and M. Puotinen (2012). "The 27-year decline of coral cover on the Great Barrier Reef and its causes". In: *Proceedings of the National Academy of Sciences of the United States of America* 109 (44), pp. 17995–17999. DOI: 10.1073/pnas.1208909109.

Dechnik, B., J. M. Webster, P. J. Davies, J.-c. Braga, and P. J. Reimer (2015). "Holocene " turn-on " and evolution of the Southern Great Barrier Reef : Revisiting reef cores from the Capricorn Bunker Group". In: *Marine Geology* 363, pp. 174–190. DOI: 10.1016/j.margeo.2015.02.014.

Duce, S., A. Vila-Concejo, R. J. McCarroll, B. Yiu, L. A. Perris, and J. M. Webster (Sept. 2022). "Field measurements show rough fore reefs with spurs and grooves

can dissipate more wave energy than the reef crest". In: *Geomorphology* 413. DOI: 10.1016/j.geomorph.2022.108365.

Duce, S., B. Dechnik, J. M. Webster, Q. Hua, J. Sadler, G. E. Webb, L. Nothdurft, M. Salas-Saavedra, and A. Vila-Concejo (2020). "Mechanisms of spur and groove development and implications for reef platform evolution". In: *Quaternary Science Reviews* 231. DOI: 10.1016/j.quascirev.2019.106155.

Duce, S., A. Vila-Concejo, S. M. Hamylton, J. M. Webster, E. Bruce, and R. J. Beaman (2016). "A morphometric assessment and classification of coral reef spur and groove morphology". In: *Geomorphology* 265, pp. 68–83. DOI: 10.1016/j.geomorph.2016.04.018.

Duce, S., A. Vila-Concejo, S. Hamylton, E. Bruce, and J. M. Webster (2014). "Spur and groove distribution, morphology and relationship to relative wave exposure, Southern Great Barrier Reef, Australia". In: *Journal of Coastal Research* 70, pp. 115–120. DOI: 10.2112/si70-020.1.

Eakin, C. M. (June 1996). "Where have all the carbonates gone? A model comparison of calcium carbonate budgets before and after the 1982–1983 El Nino at Uva Island in the eastern Pacific". In: *Coral Reefs* 15 (2), pp. 109–119. DOI: 10.1007/bf01771900.

Fellowes, T. E., F. Anggadi, M. Byrne, A. Vila-Concejo, E. Bruce, and E. Baker (2022). "Stability of coral reef islands and associated legal maritime zones in a changing ocean". In: *Environmental Research Letters* 17 (9). DOI: 10.1088/1748-9326/ac8a60.

Ferrario, F., M. W. Beck, C. D. Storlazzi, F. Micheli, C. C. Shepard, and L. Airoldi (2014). "The effectiveness of coral reefs for coastal hazard risk reduction and adaptation". In: *Nature Communications* 5, p. 3794. DOI: 10.1038/ncomms4794.

Harris, D. L., J. M. Webster, A. Vila-concejo, S. Duce, and J. X. Leon (2023). "Geomorphology Defining multi-scale surface roughness of a coral reef using a high-resolution LiDAR digital elevation model". In: *Geomorphology* 439 (September 2022), p. 108852. DOI: 10.1016/j.geomorph.2023.108852.

Harris, D. L., A. Rovere, E. Casella, H. Power, R. Canavesio, A. Collin, A. Pomeroy, J. M. Webster, and V. Parravicini (2018). "Coral reef structural complexity provides important coastal protection from waves under rising sea levels". In: *Science Advances* 4 (2). DOI: 10.1126/sciadv.aao4350.

Harris, D. L., A. Vila-Concejo, J. M. Webster, and H. E. Power (2015). "Spatial variations in wave transformation and sediment entrainment on a coral reef sand apron". In: *Marine Geology* 363, pp. 220–229. DOI: 10.1016/j.margeo.2015.02.010.

Hughes, T. P., K. D. Anderson, S. R. Connolly, S. F. Heron, J. T. Kerry, J. M. Lough, A. H. Baird, J. K. Baum, M. L. Berumen, T. C. Bridge, D. C. Claar, C. M. Eakin, J. P. Gilmour, N. A. Graham, H. Harrison, J. P. A. Hobbs, A. S. Hoey, M. Hoogenboom, R. J. Lowe, M. T. McCulloch, J. M. Pandolfi, M. Pratchett, V. Schoepf, G. Torda, and S. K. Wilson (2018). "Spatial and temporal patterns of mass bleaching of corals in the Anthropocene". In: *Science* 359 (6371), pp. 80–83. DOI: 10.1126/science.aan8048.

Hughes, T. P., J. T. Kerry, M. Álvarez-Noriega, J. G. Álvarez-Romero, K. D. Anderson, A. H. Baird, R. C. Babcock, M. Beger, D. R. Bellwood, R. Berkelmans, T. C. Bridge, I. R. Butler, M. Byrne, N. E. Cantin, S. Comeau, S. R. Connolly, G. S. Cumming, S. J. Dalton, G. Diaz-Pulido, C. M. Eakin, W. F. Figueira, J. P.

Gilmour, H. Harrison, S. F. Heron, A. S. Hoey, J. P. A. Hobbs, M. O. Hoogenboom, E. V. Kennedy, C. Y. Kuo, J. M. Lough, R. J. Lowe, G. Liu, M. T. McCulloch, H. A. Malcolm, M. J. McWilliam, J. M. Pandolfi, R. J. Pears, M. S. Pratchett, V. Schoepf, T. Simpson, W. J. Skirving, B. Sommer, G. Torda, D. R. Wachenfeld, B. L. Willis, and S. K. Wilson (2017). "Global warming and recurrent mass bleaching of corals". In: *Nature* 543 (7645), pp. 373–377. DOI: 10.1038/nature21707.

Jell, J. S. and G. E. Webb (2012). *Geology of Heron Island and Adjacent Reefs, Great Barrier Reef, Australia*. Tech. rep., p. 110.

Kench, P. S., E. P. Beetham, T. Turner, K. M. Morgan, S. D. Owen, and R. F. McLean (2022). "Sustained coral reef growth in the critical wave dissipation zone of a Maldivian atoll". In: *Communications Earth & Environment* 3 (1), pp. 1–12. DOI: 10.1038/s43247-021-00338-w.

Kench, P. S., M. R. Ford, and S. D. Owen (2019). "Patterns of island change and persistence offer alternate adaptation pathways for atoll nations". In: *Nature Communications* 9 (1). DOI: 10.1038/s41467-018-02954-1.

Knutson, T. R., J. J. Sirutis, M. Zhao, R. E. Tuleya, M. Bender, G. A. Vecchi, G. Villarini, and D. Chavas (Sept. 2015). "Global projections of intense tropical cyclone activity for the late twenty-first century from dynamical downscaling of CMIP5/RCP4.5 scenarios". In: *Journal of Climate* 28 (18), pp. 7203–7224. DOI: 10.1175/JCLI-D-15-0129.1.

Lashley, C. H., D. Roelvink, A. van Dongeren, M. L. Buckley, and R. J. Lowe (2018). "Nonhydrostatic and surfbeat model predictions of extreme wave run-up in fringing reef environments". In: *Coastal Engineering* 137 (October 2017), pp. 11–27. DOI: 10.1016/j.coastaleng.2018.03.007.

Lowe, R. J., J. L. Falter, M. D. Bandet, G. Pawlak, M. J. Atkinson, S. G. Monismith, and J. R. Koseff (2005). "Spectral wave dissipation over a barrier reef". In: *J. Geophys. Res* 110, p. 4001. DOI: 10.1029/2004JC002711.

Madin, J. S. and S. R. Connolly (2006). "Ecological consequences of major hydrodynamic disturbances on coral reefs". In: *Nature Letters* 444 (7118), pp. 477–480. DOI: 10.1038/nature05328.

Massel, S. R. and M. R. Gourlay (2000). "On the modelling of wave breaking and set-up on coral reefs". In: *Coastal Engineering* 39 (1), pp. 1–27. DOI: 10.1016/S0378-3839(99)00052-6.

Masselink, G., E. Beetham, and P. Kench (June 2020). "Coral reef islands can accrete vertically in response to sea level rise". In: *Science Advances* 6 (24), eaay3656. DOI: 10.1126/sciadv.aay3656.

Meucci, A., I. R. Young, M. Hemer, E. Kirezci, and R. Ranasinghe (2020). "Projected 21st century changes in extreme wind-wave events". In: *Science Advances* 6 (24), pp. 7295–7305. DOI: 10.1126/sciadv.aaz7295.

Monismith, S. G., J. S. Rogers, D. Koweek, and R. B. Dunbar (2015). "Frictional wave dissipation on a remarkably rough reef". In: *Geophysical Research Letters* 42 (10), pp. 4063–4071. DOI: 10.1002/2015GL063804.

Monismith, S. G., L. M. Herdman, S. Ahmerkamp, and J. L. Hench (2013). "Wave transformation and wave-driven flow across a steep coral reef". In: *Journal of Physical Oceanography* 43 (7), pp. 1356–1379. DOI: 10.1175/JPO-D-12-0164.1.

Montaggioni, L. F. (2005). "History of Indo-Pacific coral reef systems since the last glaciation: Development patterns and controlling factors". In: *Earth-Science Reviews* 71 (1-2), pp. 1–75. DOI: 10.1016/j.earscirev.2005.01.002.

Munk, W. and M. C. Sargent (1948). "Adjustment of Bikini Atoll to Ocean Waves". In: 29 (6), pp. 855–860.

Osorio-Cano, J. D., J. C. Alcérreca-Huerta, A. F. Osorio, and H. Oumeraci (2018). "CFD modelling of wave damping over a fringing reef in the Colombian Caribbean". In: *Coral Reefs* 37 (4), pp. 1093–1108. DOI: 10.1007/s00338-018-1736-4.

Pepper, A. and M. L. Puotinen (2009). "Gremo: A GIS-based generic model for estimating relative wave exposure". In: *18th World IMACS Congress and MODSIM 2009 - International Congress on Modelling and Simulation: Interfacing Modelling and Simulation with Mathematical and Computational Sciences, Proceedings*, pp. 1964–1970.

Péquignet, A. C., J. M. Becker, M. A. Merrifield, and S. J. Boc (2011). "The dissipation of wind wave energy across a fringing reef at Ipan, Guam". In: *Coral Reefs* 30 (SUPPL. 1), pp. 71–82. DOI: 10.1007/s00338-011-0719-5.

Péquignet, A. C., J. M. Becker, and M. A. Merrifield (Oct. 2014). "Energy transfer between wind waves and low-frequency oscillations on a fringing reef, Ipan, Guam". In: *Journal of Geophysical Research: Oceans* 119 (10), pp. 6709–6724. DOI: 10.1002/2014JC010179.

Perris, L. (Mar. 2024). *Lachie-Perris/XBeach_coral: v1.0*. Version XBeach. DOI: 10.5281/zenodo.10851163.

Perry, C. T., L. Alvarez-Filip, N. A. Graham, P. J. Mumby, S. K. Wilson, P. S. Kench, D. P. Manzello, K. M. Morgan, A. B. Slangen, D. P. Thomson, F. Januchowski-Hartley, S. G. Smithers, R. S. Steneck, R. Carlton, E. N. Edinger, I. C. Enochs, N. Estrada-Saldívar, M. D. Haywood, G. Kolodziej, G. N. Murphy, E. Pérez-Cervantes, A. Suchley, L. Valentino, R. Boenish, M. Wilson, and C. MacDonald (2018). "Loss of coral reef growth capacity to track future increases in sea level". In: *Nature* 558 (7710), pp. 396–400. DOI: 10.1038/s41586-018-0194-z.

Quataert, E., C. D. Storlazzi, A. van Dongeren, and R. McCall (2020). "The importance of explicitly modelling sea-swell waves for runup on reef-lined coasts". In: *Coastal Engineering* 160 (April), p. 103704. DOI: 10.1016/j.coastaleng.2020.103704.

Quataert, E., C. D. Storlazzi, A. V. Rooijen, O. Cheriton, and A. V. Dongeren (Aug. 2015). "The influence of coral reefs and climate change on wave-driven flooding of tropical coastlines". In: *Geophysical Research Letters* 42 (15), pp. 6407–6415. DOI: 10.1002/2015GL064861.

Reguero, B. G., I. J. Losada, and F. J. Méndez (2019). "A recent increase in global wave power as a consequence of oceanic warming". In: *Nature Communications* 10 (1), pp. 1–14. DOI: 10.1038/s41467-018-08066-0.

Roelfsema, C., E. M. Kovacs, J. Vercelloni, K. Markey, A. Rodriguez-Ramirez, S. Lopez-Marcano, M. Gonzalez-Rivero, O. Hoegh-Guldberg, and S. R. Phinn (2021). "Fine-scale time series surveys reveal new insights into spatio-temporal trends in coral cover (2002–2018), of a coral reef on the Southern Great Barrier Reef". In: *Coral Reefs* 40 (4), pp. 1055–1067. DOI: 10.1007/s00338-021-02104-y.

Roelvink, D., A. Reniers, A. van Dongeren, J. van Thiel de Vries, R. McCall, and J. Lescinski (2009). "Modelling storm impacts on beaches, dunes and barrier islands". In: *Coastal Engineering* 56 (11-12), pp. 1133–1152. DOI: 10.1016/j.coastaleng.2009.08.006.

Rogers, J. S., S. G. Monismith, F. Feddersen, and C. D. Storlazzi (2013). "Hydrodynamics of spur and groove formations on a coral reef". In: *Journal of Geophysical Research: Oceans* 118 (6), pp. 3059–3073. DOI: 10.1002/jgrc.20225.

Rogers, J. S., S. G. Monismith, O. B. Fringer, D. A. Koweek, and R. B. Dunbar (2017). "A coupled wave-hydrodynamic model of an atoll with high friction: Mechanisms for flow, connectivity, and ecological implications". In: *Ocean Modelling* 110, pp. 66–82. DOI: 10.1016/j.ocemod.2016.12.012.

Rogers, J. S., S. G. Monismith, D. A. Koweek, and R. B. Dunbar (Jan. 2016). "Wave dynamics of a Pacific Atoll with high frictional effects". In: *Journal of Geophysical Research: Oceans* 121 (1), pp. 350–367. DOI: 10.1002/2015JC011170.

Sanborn, K. L., J. M. Webster, G. E. Webb, J. C. Braga, M. Humblet, L. Nothdurft, M. A. Patterson, B. Dechnik, S. Warner, T. Graham, R. J. Murphy, Y. Yokoyama, S. P. Obrochta, J. xin Zhao, and M. Salas-Saavedra (2020). "A new model of Holocene reef initiation and growth in response to sea-level rise on the Southern Great Barrier Reef". In: *Sedimentary Geology* 397, p. 105556. DOI: 10.1016/j.sedgeo.2019.105556.

Saunders, M. I., S. Albert, C. M. Roelfsema, J. X. Leon, C. D. Woodroffe, S. R. Phinn, and P. J. Mumby (2016). "Tectonic subsidence provides insight into possible coral reef futures under rapid sea-level rise". In: *Coral Reefs* 35 (1), pp. 155–167. DOI: 10.1007/s00338-015-1365-0.

Sheppard, C. (1981). "The groove and spur structures of Chagos atolls and their coral zonation". In: *Estuarine, Coastal and Shelf Science* 12 (5), pp. 549–560. DOI: 10.1016/S0302-3524(81)80081-3.

Sheppard, C., D. J. Dixon, M. Gourlay, A. Sheppard, and R. Payet (Aug. 2005). "Coral mortality increases wave energy reaching shores protected by reef flats: Examples from the Seychelles". In: *Estuarine, Coastal and Shelf Science* 64 (2-3), pp. 223–234. DOI: 10.1016/j.ecss.2005.02.016.

Shinn, E. (June 1963). "Spur and Groove Formation on the Florida Reef Tract". In: *SEPM Journal of Sedimentary Research* Vol. 33 (2), pp. 291–303. DOI: 10.1306/74d70e34-2b21-11d7-8648000102c1865d.

Shukla, P., J. Skea, R. Slade, R. van Diemen, E. Haughey, J. Malley, M. Pathak, and J. P. Pereira (2019). *IPCC, 2019: Technical Summary*. Tech. rep. IPCC, pp. 35–74.

Smith, C., A. Vila-Concejo, and T. B. Salles (2020). "RADWave: Python code for ocean surface wave analysis by satellite radar altimeter." In: *Journal of Open Source Software* 1 (5), p. 46. DOI: https://doi.org/10.21105/joss.02083.

Smyth, C. and A. A. Hay (2002). "Wave friction factors in nearshore sands". In: *Journal of Physical Oceanography* 32 (12), pp. 3490–3498. DOI: 10.1175/1520-0485(2002)032<3490:WFFINS>2.0.CO;2.

Sous, D., S. Maticka, S. Meulé, and F. Bouchette (2022). "Bottom drag coefficient on a shallow barrier reef". In: *Geophysical Research Letters*, pp. 1–12. DOI: 10.1029/2021gl097628.

Storlazzi, C. D., E. K. Brown, M. E. Field, K. Rodgers, and P. L. Jokiel (Mar. 2005). "A model for wave control on coral breakage and species distribution in the Hawaiian Islands". In: *Coral Reefs* 24 (1), pp. 43–55. DOI: 10.1007/s00338-004-0430-x.

Storlazzi, C. D., E. P. Elias, and P. Berkowitz (Sept. 2015). "Many Atolls May be Uninhabitable Within Decades Due to Climate Change". In: *Scientific Reports* 5 (1), pp. 1–9. DOI: 10.1038/srep14546.

Storlazzi, C. D., S. B. Gingerich, A. V. Dongeren, O. M. Cheriton, P. W. Swarzenski, E. Quataert, C. I. Voss, D. W. Field, H. Annamalai, G. A. Piniak, and R. McCall (2018). "Most atolls will be uninhabitable by the mid-21st century because of sea-level rise exacerbating wave-driven flooding". In: *Science Advances* 4 (4), pp. 1–10. DOI: 10.1126/sciadv.aap9741.

Talavera, L., A. Vila-Concejo, J. M. Webster, C. Smith, S. Duce, T. E. Fellowes, T. Salles, D. Harris, J. Hill, W. Figueira, and J. Hacker (2021). "Morphodynamic controls for growth and evolution of a rubble coral island". In: *Remote Sensing* 13 (8), pp. 1–23. DOI: 10.3390/rs13081582.

Watanabe, M., H. Kan, K. Toguchi, Y. Nakashima, V. Roeber, and T. Arikawa (2023). "Effect of the structural complexity of a coral reef on wave propagation: A case study from Komaka Island, Japan". In: *Ocean Engineering* 287 (P1), p. 115632. DOI: 10.1016/j.oceaneng.2023.115632.

Yao, Y., Y. Liu, L. Chen, Z. Deng, and C. Jiang (2020). "Study on the wave-driven current around the surf zone over fringing reefs". In: *Ocean Engineering* 198. DOI: 10.1016/j.oceaneng.2020.106968.

Young, I. R. (1992). "The Determination of Spectral Parameters from Significant Wave Height and Peak Period". In: *Ocean Engineering* 19 (5), pp. 497–508.

3| Current Flow in Low-energy Coral Forereef Spurs and Grooves

Lachlan Arthur Perris[1, 2], Tristan Salles[1, 2], Thomas E. Fellowes[1, 5], Ana Paula Da Silva [1, 2] Stephanie Duce[4], Jody Webster[1], Alisha M Thompson [3] Ana Vila-Concejo[1, 2],

[1]Geocoastal Research Group, School of Geosciences, The University of Sydney, NSW, 2006, Australia
[2]Marine Studies Institute, Faculty of Science, The University of Sydney, NSW, 2006, Australia
[3]Wenona School, North Sydney, NSW, 2060, Australia
[4]College of Science and Engineering, James Cook University, Bebegu Yumba Campus, Townsville, Queensland, 4811, Australia
[5]Water Research Laboratory, School of Civil and Environmental Engineering, UNSW Sydney, Australia

Abstract

Coral forereef hydrodynamics, driven by waves and currents, play a critical role in controlling the distribution of nutrients, sediments and corals across platform reefs. These processes drive the formation of reef systems and are critical to determining the future of coral reef environments in a changing global climate. Despite this, limited in-situ research from the Great Barrier Reef (GBR) into the interactions between spurs and grooves (SaG) and forereefs currents is available. Here we analyse the first dataset of current measurements from a coral forereef SaG system in the GBR and assess forereef currents adjacent to a large reef lagoon that is isolated from the open ocean during low tides. We find that under prevailing weather conditions, waves are low (H_s = 0.25 m) and oblique to forereef isobaths. Currents in SaG under low wave exposure exhibit high velocity (2 m/s) with a dominant offshore component driven by surf zone processes and lagoonal outflow. This is consistent with postulated mechanisms of constructional development of SaG whereby offshore flow transports sediments seaward of the forereef, providing a substrate for coral larvae and living coral fragments to attach. These in-situ observations provide the first evidence from the GBR linking prevalent hydrodynamic conditions to the morphological evolution of coral forereef spur and groove systems.

1 Introduction

Hydrodynamic forcings dictate the transport and availability of sediments and nutrients therefore controlling all aspects of life on coral reef systems (Odum and Odum 1955) across all spatial and temporal scales (Monismith 2007). The outer forereef of platform reefs serves as the interface between open ocean hydrodynamics and the reef processes (Munk and Sargent 1948). Consequently, on undisturbed platform reef systems, lagoon systems fill and drain based on the interplay of tides, waves and currents around the reef rim. This dynamic, in turn, is influenced by the morphology of the forereef and reef flat (Grimaldi et al. 2022; Lowe et al. 2015). The feedback between hydrodynamics and morphology across these reef zones offers valuable insights into the long-term geomorphic evolution of coral reefs. In this study, we investigate a ubiquitous, yet under-studied, morphological feature of forereefs known as spurs and grooves (SaG). Spurs are elongate finger-shaped formations of carbonate material that stretch seaward from the reef flat. Grooves are channels or troughs that intermittently separate the spurs (Duce et al. 2016; Munk and Sargent 1948). SaG have been documented across different reef types including platform reefs, fringing reefs, barrier reefs and atolls, with SaG morphology varying considerably in response to local conditions (Cloud Jr. 1959; Duce et al. 2014). They have been observed through all coral-rich seas including the Red Sea (Sneh and Friedman 1980), the Atlantic Ocean (Shinn 1963), the Indian Ocean (Sheppard 1981; Weydert 1979), the Caribbean Sea (Blanchon and Jones 1997; Goreau 1959), and the Pacific Ocean (Munk and Sargent 1948; Storlazzi et al. 2003). Despite comprehensive documentation of SaG presence, in-situ measurements of current regimes in platform reef SaG systems are scarce. This paucity of hydrodynamic field measurements is likely due to the challenging turbulent surf zones of forereefs where SaG typically develop (Duce et al. 2020; Duce et al. 2014; Munk and Sargent 1948), making access

difficult. Remotely sensed data has provided the greatest insight into SaG morphology to date, with four classes of SaG defined in the Southern Great Barrier Reef based on morphometrics and relative exposure to wave energy (Figure 1) (Duce et al. 2016). Numerical modelling over remote-sensed SaG bathymetries has demonstrated that grooves of different classes exhibit distinct hydrodynamic regimes (Perris et al. 2024). Consequently, accounting for SaG morphological classifications is essential in any hydrodynamic analysis involving these systems.

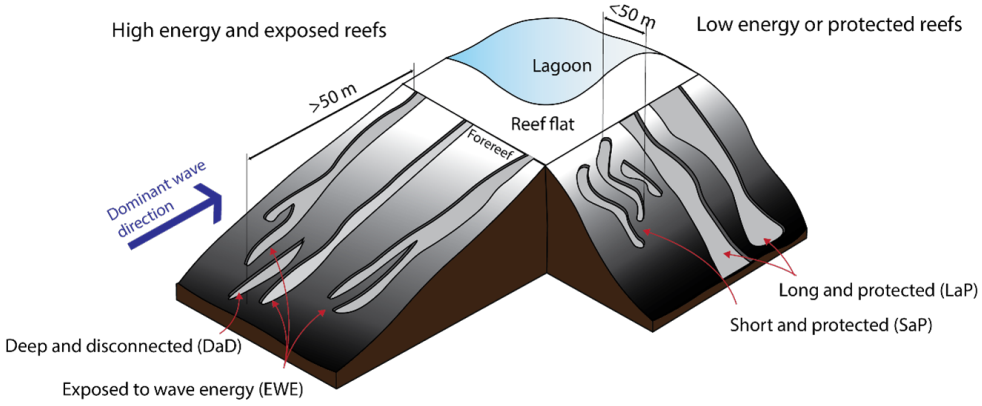

Figure 1: A schematic of SaG morphotypes modified after Duce et al. (2016). High energy SaG morphotypes, 'Exposed to wave energy' and 'Deep and Disconnected' face the dominant wave direction (blue arrow), bifurcation of 'exposed to wave energy' grooves is common. Low energy morphotypes, 'short and protected' and 'long and protected', typically occur in less exposed areas of a reef, such as the area being investigated here.

Early reports of waves in SaG zones by Munk and Sargent (1948) at Bikini Atoll, Republic of the Marshall Islands, inferred a relationship between wave direction and the orientation of forereef grooves. This was later supported by (Sneh and Friedman 1980) in the Red Sea with SaG perpendicular to refracted waves. This has led to numerical modelling efforts that consider waves perpendicular to the primary groove axis (da Silva et al. 2020; Perris et al. 2024; Rogers et al. 2013). In nature, exposed platform reefs can receive incident waves from a wide range of directions depending on the offshore wave parameters, fetch distance and refraction/diffraction around the reef. SaG in low-energy regions differ morphologically from their high-energy counterparts (Duce et al. 2016, modified in Figure 1), leaving a gap in our understanding of how these systems persist under predominantly low-energy and oblique wave settings.

Direct measurements of currents in SaG have only been reported in five reefs worldwide: Molokai in Hawaii (Storlazzi et al. 2004), Moorea in French Polynesia (Monismith et al. 2013), Palmyra Atoll in the central Pacific (Rogers et al. 2015), at Xahauyxol Reef in the Mexican Caribbean (Acevedo-Ramirez et al. 2021) and Ngederrak reef in Palau, Western Pacific (Sartori et al. 2024). Notably, to our knowledge no current measurements have ever been published from SaG in the Great Barrier Reef (GBR). Of the studied reefs, Molokai and Xanhauyxol are fringing reefs, and Moorea is a barrier reef—each exhibiting hydrodynamic regimes that differ significantly from those of platform reefs. Palmyra atoll has a large engineered navigational

channel cut through its forereef and reef flat, which alters lagoon circulation patterns (Gardner et al. 2011) and obfuscates the natural processes of lagoon-seawater exchange. Therefore, additional studies are needed to understand the characteristics of current flows through a platform reef SaG system.

With limited in-situ data across the wide range of reef morphologies, numerical models have so far provided the most significant insights into forereef SaG currents. (Rogers et al. 2013) proposed that SaG induce counter-rotating Lagrangian circulation cells by creating alongshore variations in depth and friction. This concept was further expanded upon by (da Silva et al. 2020), who used a comprehensive set of numerical models over idealised SaG bathymetry to identify vertical Lagrangian circulation cells under various wave conditions and water levels. Across all simulations, currents within the groove were directed onshore. However, in low-wave energy SaG, there is a relative reduction on the role of wave induced currents compared to the effects of high tidal ranges and reef lagoon outflow. Lagoon waters experience greater temperature fluctuations and increased salinity due to evaporation when isolated from the comparatively fresh water of the surrounding ocean (Silverman et al. 2012). The mixing of lagoonal and ocean waters around the forereef are critical to coral health in these regions. Numerical models have shown that lagoon waters can enter the open ocean via undertows over the forereef (Lindhart 2022). Since grooves represent local bathymetric minima, they may serve as pathways for lagoonal outflow, potentially influencing longer term SaG morphological evolution. Yet, there has been no published investigation into the role of SaG morphologies in mediating lagoon-to-ocean exchanges, leaving a significant gap in the understanding of these processes.

Flows at forereef SaG are essential to understanding the mechanisms driving their formation. A comprehensive short-coring analysis of vertical and lateral progradation rates on coral forereefs in the southern GBR demonstrated three modes of SaG development (Duce et al. 2020). Mode 1 occurs in wave dominated environments, where erosion of the forereef likely exceeds accretion. In this mode, both the reef flat and the SaG were prograding toward the lagoon. Mode 2 develops in moderate or episodic wave energy environments, where SaG potentially develop over antecedent bathymetry featuring proto-spurs. And finally, Mode 3 arises in low wave energy conditions, providing a mechanism for the seaward accretion of both the reef flat and the forereef. In Mode 3, offshore flows from the lagoon supply reef sediments to the outer forereef, with reduced wave energy increasing sediment residency time. This creates a substrate conducive to the seaward accretion of the forereef and reef flat. This aligns with findings that relative wave energy influences the direction of reef flat lateral accretion (Dechnik et al. 2016), including oceanward accretion in lower hydrodynamic settings. These three modes offer a framework for understanding how varying hydrodynamic and sedimentary conditions drive SaG formation and contribute to reef platform evolution. Whilst this model of SaG formation relies on an interpretation of hydrodynamics in a SaG system, it was not based on in-situ hydrodynamic measurements of current, which have never been reported from the GBR.

This study addresses three key gaps in understanding the hydrodynamics of spur and groove systems in low-energy reef settings: (1) Can spurs and grooves persist under prevalent oblique wave conditions? (2) What are the characteristics of current flows

in these systems under such conditions? and (3) Do the observed hydrodynamics support a constructional model of SaG formation and reef platform evolution?

2 Methods

2.1 Study site

One Tree Reef (OTR) (23°30'S, 152°06'E) is a lagoonal platform reef located 84 km offshore in the southern Great Barrier Reef (GBR) (Figure 2). It benefits from limited anthropogenic impacts and is protected within the GBR Marine Park's "Scientific Zone." OTR experiences semi-diurnal tides, with a mean spring tidal range of 3 m. Offshore hydrodynamics at OTR are primarily influenced by southeast trade winds of the Coral Sea, which dominate over 70% of the year (Jell and Webb 2012). These winds result in an average significant wave height of 1.7 m (Smith et al. 2023). Periodically, the reef is impacted by extreme waves conditions associated with tropical storms and cyclones, during which significant wave heights exceed 3 m (Smith et al. 2023).

The reef crest at OTR is unbroken by channels, isolating lagoonal waters from the open ocean for six hours of the tidal cycle—a phenomenon known as tidal truncation (Silverman et al. 2012). During this period, the water level inside the lagoon can be up to 0.2 m higher than the surrounding ocean, and the maximum water level within the lagoon can exceed that of the external tide due to wave forcing around the reef (Wilson 1985). Prevailing E–SE swells push water onto the reef flat and into the lagoon, a process known as wave pumping, where waves on the exposed reef and wind shear over the lagoon drive water across the reef platform. This water subsequently drains on the leeward side of the reef, producing lagoon outflows that are commonly focussed at local topographic low points (Frith 1983). OTR is entirely encircled by SaG (Duce et al. 2016), with this study focusing on a SaG system on the northern forereef (Figure 2). Here, the reef flat is exposed for three hours during the tidal cycle, while adjacent upper forereef spurs are exposed only during the lowest astronomical tides. The spurs show high coral cover and surface roughness, indicative of a healthy reef (Harris et al. 2023), while groove beds are filled with coarse and rounded rubble. About 300 metres west of the study site is "The Entrance," a low point in the reef crest that roughly corresponds to the half-tide level (Wilson 1985) and provides vessel access for about three hours during each high tide (Ludington 1979). A prominent storm-deposited rubble bank lies across the reef flat (Figure 2), measuring approximately 350 m in length and 30 m in width. This feature reflects onshore transport of coral rubble during periodic storm-driven erosion of the adjacent forereef (Davies 1983). Its presence indicates that large volumes of sediment can be stored temporarily on the reef flat following high energy events, providing a potential source of material that may under high-energy conditions be transported seaward and channelled by strong offshore currents through the groove.

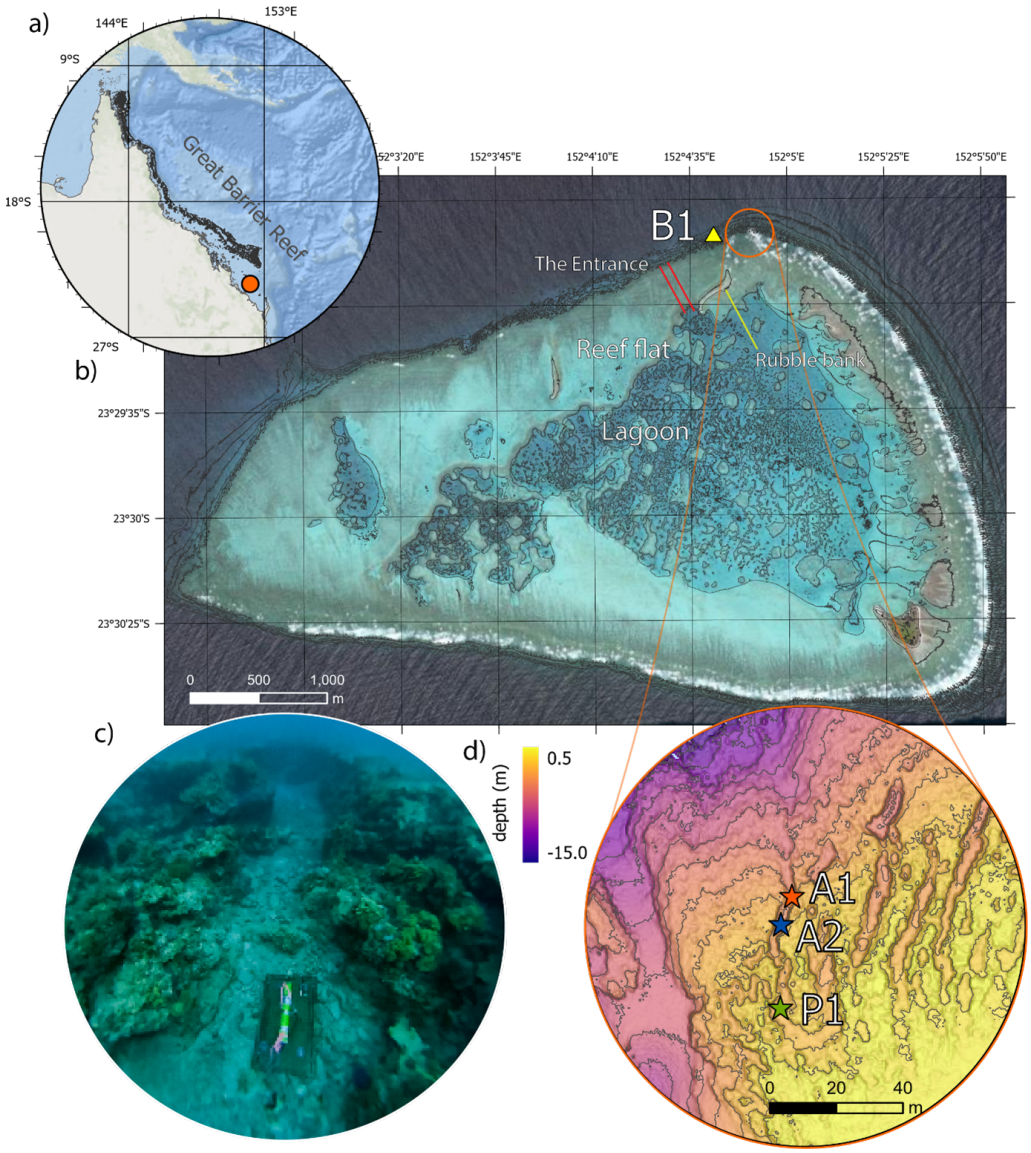

Figure 2: **a)** One Tree Reef (OTR) is in the southern Great Barrier Reef (orange circle). **b)** Study site and location of Spotter wave rider buoy (B1), the study site is located on the northern forereef of OTR, 400 m from 'The Entrance' (shown with red lines), the yellow line indicates the location of a storm-deposited rubble bank **c)** instrument A1 in place within a groove and, **d)** the location of the instruments in that groove, A1 and A2 are Nortek Velocimeters and P1 an RBR Virtuoso pressure transducer (Table 1).

2.2 Morphology

Morphological measurements of the coral forereef were derived from a 0.25 m × 0.25 m resolution airborne LiDAR digital elevation model (Figure 2) (Harris et al. 2023). SaG features were identified and classified according to the Duce et al. (2016) scheme (Figure 1). The following metrics were then computed for each SaG element: Spur height (h_{spur}) vertical distance from the groove floor to the crest of the adjacent spur. Groove length (L): the centre-line path length measured along the groove axis. Groove sinuosity (S): the ratio of straight-line distance (x) between groove endpoints to the path length L (i.e. $S = x/L$). Mean slope (θ): the average inclination of each spur or groove segment, calculated as the arctangent of elevation change over the horizontal extent. All measurements were extracted in GIS software (ArcGIS Pro v3.1) using custom scripted profiles perpendicular to isobaths at 1 m intervals. Elevations were referenced to mean sea level based on the AUSGeoid 2009 offset of the Australia Height Datum (Featherstone et al. 2011). Spur and groove endpoints were manually inspected to ensure correct feature pairing.

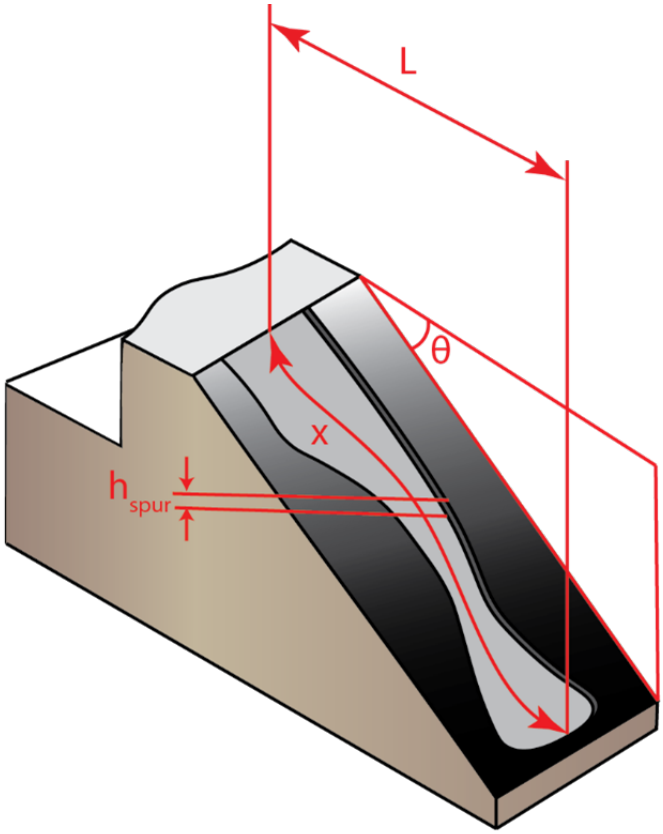

Figure 3: Schematic of a single groove with relevant dimensions, Spur height (h_spur) vertical distance from the groove floor to the crest of the adjacent spur, Groove length (L): the centre-line path length measured along the groove axis. Straight-line distance (x) between groove endpoints and mean slope (θ): the average inclination of the spur (shown in red) is also calculated for the groove bed.

2.3 Instrument deployment

We collected field data of waves and currents between 06/10/2022 and 08/10/2022 along a cross-shore transect in a forereef groove (Figure 2, Table 1). Two Nortek Vectors (A1 and A2) and an RBR Virtuoso3 pressure transducer (P1) were deployed, sampling continuously at 8 Hz. Nortek vectors (A1 and A2) include integrated inertial motion units which were calibrated in the deployment frame and clear of any other metallic disturbances, to remove any potential errors due to the presence of metals influencing the magnetic field. Additionally, data was recorded in XYZ coordinates which are based on the positioning of the instrument, rather than compass bearings. We aligned both A1 and A2 with the groove, so that the x-direction aligned with the western groove wall. By including both measurements (inertial motion unit and XYZ) we were able to determine any errors in the alignment of the instrument with compass bearings. We determined the mean deployment depth (Table 1) from pressure readings at each instrument. We measured the distance of each instrument from the reef crest, defined as the mean sea level contour derived from the LiDAR digital elevation model (Harris et al. 2023) and referenced to Australian Height Datum (AHD) using the AusGEOID09 model (Featherstone et al. 2011) (Table 1).

A second survey was conducted between 31/10/2023 and 27/03/2024 to assess hydrodynamic connectivity between the lagoon and the open ocean, as well as to provide an indication of representative offshore wave parameters at the study site. This array included a Sofar Spotter Buoy and Smart Mooring with a near-bed mounted RBR conda3, measuring temperature and pressure (B1, Table 1). To place both surveys in a broader seasonal context, conditions measured at B1 were compared with those from the first survey, together with local wind speed and direction obtained from the open-meteo API (Zippenfenig 2023) and offshore wave conditions derived from satellite radar-altimeter data using the RADWave Python package (Smith et al. 2020).

2.4 Local weather conditions

Local wind speed and direction during the deployment were derived from open-meteo API (Zippenfenig 2023). Offshore wave conditions were extracted from satellite radar-altimeter measurements using the RADWave Python package (Smith et al. 2020). RADWave (v 1.0.8) interfaces directly with THREDDS data services to access the Australian Ocean Data Network global altimeter archive (Ribal and Young 2019). Within our workflow, we specified a bounding-box region east of OTI from latitude 22S to 25S and longitude 152.1 to 156, then retrieved along-track measurements of sea surface elevation. RADWave subsequently computes standard wave parameters—significant wave height (H_s), peak period (T_p). Local weather conditions during the deployments (Table 1) were compared across surveys and against mean conditions for OTI.

2.5 Data processing

Field data of three-dimensional current vectors (recovered from the current meters A1 and A2) were processed using the Doppler Oceanography Library for Python

Table 1: Instrument deployment details

Name	Deployment period	Instrument	Sample rate (Hz)	Mean deployment depth (m)	Distance from bed (m)	Distance from crest (m)
A1	06/10/2022 – 08/10/2022	Nortek Vector	8	3.6	0.12	100.2
A2	06/10/2022 – 08/10/2022	Nortek Vector	8	3.3	0.24	92.4
P1	06/10/2022 – 08/10/2022	RBR Virtuoso	8	2.4	0.15	66.6
B1	31/10/2023 – 27/03/2024	Sofar Spotter Buoy with Smart Mooring (RBR Conda3)	3.84	10.5	1.5 (RBRConda 3), 10.5 (Spotter Buoy)	97

(DOLfYN) (Klise et al. 2020). To remove spikes caused by Doppler noise, aliasing of the Doppler signal or boundary interference, we implemented a phase-space threshold despiking algorithm (Goring and Nikora 2002). A block size of npt = 5000 points was employed throughout. Long runs of missing data (npt/10 = 500 points) were first identified and used to segment the time series so that each continuous "good" interval was processed independently. Within each block of 5000 samples, spikes were iteratively flagged if their velocity–derivative pair lay outside the expected phase-space envelope. Iteration continued until no additional spikes were detected (or a maximum of 100 cycles was reached). The resulting Boolean mask marked all despiked points, which were then omitted from further analysis.

Current meters A1 and A2 were deployed in alignment with the groove such that the positive x-direction was directed toward the western groove wall. Cross-shore and alongshore directions were defined based on the orientation of isobaths and the reef crest. Mean current directions were determined via circular mean calculations for each tidal phase (low and high). Tide induced currents were separated from wave induced currents by temporally averaging the time series at three-hour intervals.

2.5.1 Wave data analysis

Wave data was processed for pressure sensors on all three instruments (A1, A2 and P1) (Figure 2 c). We analysed raw pressure data with zero-crossing methods following (Karimpour and Chen 2017) (see Data Availability). We calculated wave parameters of significant wave height (H_s) and peak wave period (T_p) using linear

wave theory —an approach validated on steep and complex coral reef bathymetries (Monismith et al. 2013). We used spectral analysis in 15-minute intervals, that was found to be appropriate for long wave lengths at OTR (Harris et al. 2015). The one-sided bottom pressure spectrum is given by:

$$p_x(f_k) = \frac{2\,\Delta t}{n}\,|X_k|^2 \tag{3.1}$$

And only the spectral bin for all waves satisfying 0.0033 f_k<2.0Hz are retained. We then calculated the zeroth moment m_0 such that:

$$m_0 = \sum_k S_\eta(f_k)\;\Delta f \tag{3.2}$$

Where $\Delta f = \frac{1}{n\,\Delta t}$ for an n-point record with sampling interval Δt, and $S_\eta(f_k)$ is the power spectral density of the surface elevation at frequency f_k. Under linear wave theory, H_s is related to the zeroth moment (m_0) by:

$$H_s = 4\sqrt{m_0} \tag{3.3}$$

We calculated the peak period T_p such that:

$$T_p = \frac{1}{f_p} \tag{3.4}$$

Where f_p is the frequency at the maximum of the spectral density, $p_x(f_k)$. Wave power was calculated using linear wave theory:

$$P = C_g\,E \tag{3.5}$$

Where E is the wave energy density and c_g is the group speed determined for intermediate depths, such that:

$$c_g = \frac{c}{2}\left(1 + \frac{2kh}{\sinh(2kh)}\right) \tag{3.6}$$

Where c is the phase velocity, h is the water depth, and the wavenumber (k) and wave celerity (c) were derived using the Newton–Raphson method for the dispersion relation (Dean and Dalrymple, 1991). To investigate wave breaking over the instruments, we calculated:

$$\gamma = \frac{H_{\max}}{h} \tag{3.7}$$

Where $H_{\max}$ is derived from spectral analysis of the water-elevation time series, and γ is the wave-breaking parameter. Values for γ have been published for forereef environments varying from 0.83 (Rogers et al. 2016) to 0.98 (Monismith et al. 2013). We used a conservative estimate of $\gamma = 0.60$ to ensure that no waves were breaking over the instruments, as has been demonstrated on forereefs in similar studies (Duce et al. 2022). Finally, we did not compute dissipation rates and reflection coefficients because of the oblique nature of incident waves.

2.6 Temperature analysis

To further investigate the origin of currents in the forereef and determine the mean wave conditions at the study site, a secondary analysis was conducted with the Spotter Buoy (B1) and a near-bed mounted sensor (Table 1). The temperature gradient was calculated as the difference between the buoy-mounted temperature logger and the near-bed mounted temperature logger, with water depth measured by the co-located pressure sensor. A temperature inversion was identified when the water temperature at the bed was higher than at the surface. Spectral and time domain analyses were performed on displacement data collected by the wave buoy, following (Kinsela et al. 2024).

3 Results

3.1 Morphology

The study area (Figure 2) features SaG of varying morphologies. Following the morphological classification system of Duce et al. (2016) (Figure 1), we identified 'short and protected' grooves, which are located west of the study site in an area with lower exposure to the dominant south-easterly swell, and 'deep and disconnected' grooves on the lower forereef slope at the study site. The groove investigated here belongs to the 'long and protected' class (Figure 1), measuring 79 m in length, with a mean width of 5 m and a spur wall height reaching up to 2.2 m above the groove bed. Field observations show that spur walls overhang the groove, meaning that the groove width at the bed may be underestimated due to the constant scanning height and angle of airborne LiDAR. Groove sinuosity – the ratio of straight-line distance to path length – is 0.91. The forereef slope is consistent between the groove and the spurs, at 1.8°. Mean spur wall height adjacent to each instrument is 2.1 m.

3.2 Local weather conditions

A mean offshore wave height of 1.75 m was determined for the deployment period. Mean offshore wave heights at OTR were 1.7 m from 1985 to 2018 (Smith et al. 2023) (Figure 4 a). Consequently, the conditions measured in this analysis represent the prevalent wave conditions of OTR. The mean wind condition during the study period was 5.74 m/s from 92°N (easterly winds). Mean H_s at instrument B1 (Table 1) was 0.6 m with a mean wind speed of 4.2 m/s from 107°N (east-south-easterly winds).

3.3 Wave analysis

The deployment encompassed three full tidal cycles with an average tidal range of 2.41 m (Figure 5 a). The principal axis of flow for instruments A1 (furthest offshore) and A2 was found to be 93° and 61° respectively, indicating mostly oblique waves at the offshore instrument that refract toward the reef crest at instrument A2. The mean Hs at instrument A1 (farthest offshore) was 0.24 m (Figure 5 b), indicating a significant reduction in wave height occurred before reaching the survey site. Mean Hs at instrument A2 was the lowest at 0.21 m (Figure 5 c). The H_s at instrument P1, closest to the reef crest, were controlled by water level (0.87 Pearson correlation),

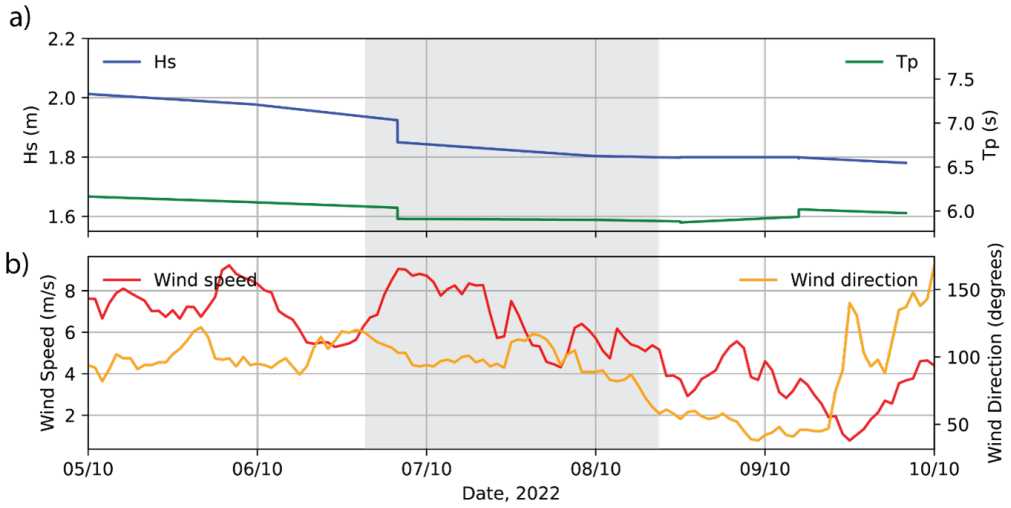

Figure 4: a) Offshore H_s (left y-axis) and T_p (right y-axis) derived from satellite altimetry (Smith et al. 2020), and b) wind speed (left y-axis) and direction (right y-axis) for the deployment period in October 2022 (highlighted in grey) (Zippenfenig 2023).

with mean H_s ranging from 0.16 m at low tide to 0.25 m at high tides (Figure 5 d). The analysis of wave breaking determined that waves were not breaking at any of the instruments, despite a conservative estimate of the wave breaking threshold, γ=0.6 (Eq. 3.7).

Table 2: Wave parameters averaged over the tidal period (high or low tide)

Instrument	$\overline{H_s}$ (low tide) (m)	$\overline{P}$ (low tide) (W/m^2)	$\overline{H_s}$ (high tide) (m)	$\overline{P}$ (high tide) (W/m^2)
P1	0.16	130	0.25	346
A2	0.19	208	0.23	331
A1	0.23	283	0.25	398

3.4 Current analysis

We quantified the maximum and mean velocities at each instrument. Measurements are taken as a point measurement sufficient to describe currents in the forereef groove, importantly, we do not extrapolate these results to the above water column. At instrument A1, the maximum current velocity was 2.25 m/s, directed at 150°N (offshore and to the west), with maximum offshore and onshore current velocity of 1.94 m/s and 2.06 m/s, respectively (Figure 7 b and Figure 8 a). The mean absolute velocity magnitude at instrument A1 was 0.12 m/s (Figure 6 d), and the mean cross-shore current velocity was directed offshore at 0.04 m/s (Figure 6 b). This cross-shore current decreased to 0 m/s at high tides but increased to 0.07 m/s offshore at low tide (Figure6b). Flow velocities were higher at the nearshore instrument, A2, with a maximum current velocity of 2.87 m/s directed at 39.8 °N (offshore and to the east). At A2 we recorded maximum offshore and onshore velocity components of 2.05 m/s and 1.45 m/s, respectively (Figure 7 c and b). The mean velocity magnitude measured at instrument A2 was 0.17 m/s, with the mean cross-shore current velocity indicating mean offshore current of 0.12 m/s (Figure

7 c). This offshore current was consistent across the full tidal cycle, with values decreasing to 0.03 m/s at high tide and increasing to 0.18 m/s during low tide (Figure 6 c). Isolated peaks in cross-shore directed velocity were recorded during low tides (Figure 7 b); we interpret this as likely caused by a short-term wave-breaking jet or localised flow convergence, rather than representing the prevailing flow regime.

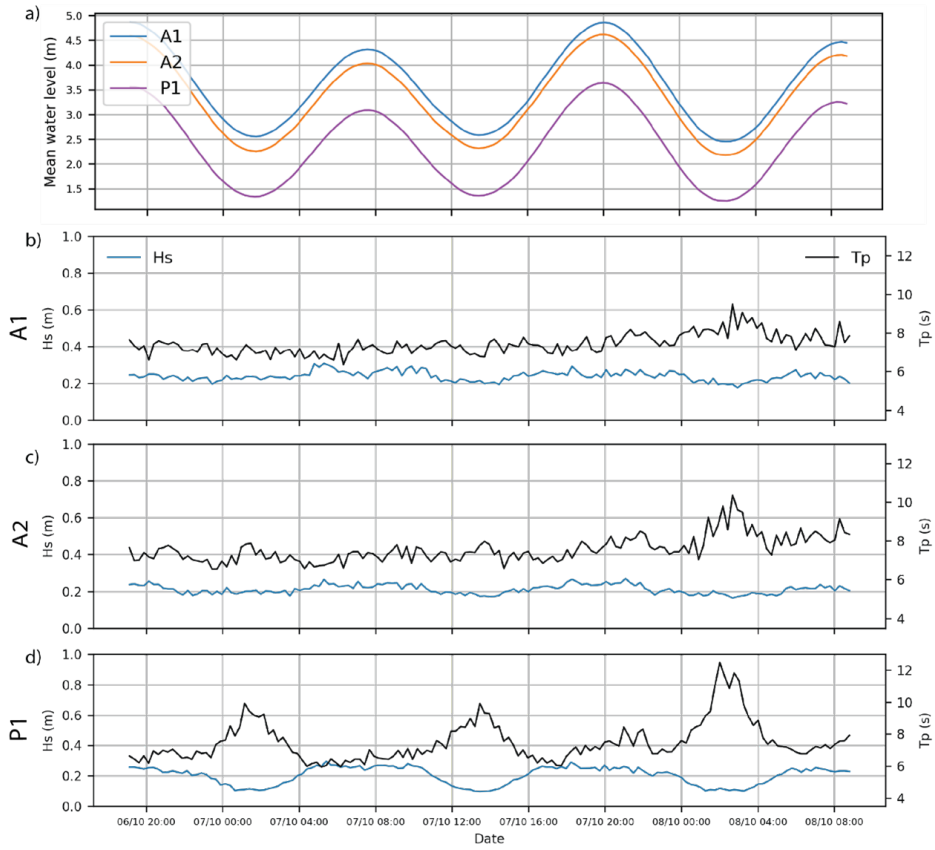

Figure 5: Hydrodynamic measurements from 6 to 8 October 2022. **(a)** Mean water levels indicating tide and spectral wave heights at each instrument. (**b**, **c**, and **d**) present the H_s and T_p at A1, A2 and P1 respectively, from the most offshore to the most shoreward instrument.

Wave power (P) at each instrument were controlled by tidal cycles with higher wave power observed during high tides. At instrument P1, the mean wave power at high tide was 166% greater than at low tides. At instrument A1 and A2, this increase was 59% and 40% respectively (Table 2). The influence of water level on wave power was most pronounced at instrument P1, located closest to the reef crest, where the Pearson correlation between intermediate wave power and water level was 0.92. At site A1 (furthest from the reef crest) the correlation was 0.86, and at site A2, it was 0.65.

3.5 Current analysis

We quantified the maximum and mean velocities at each instrument. Measurements are taken as a point measurement sufficient to describe currents in the forereef

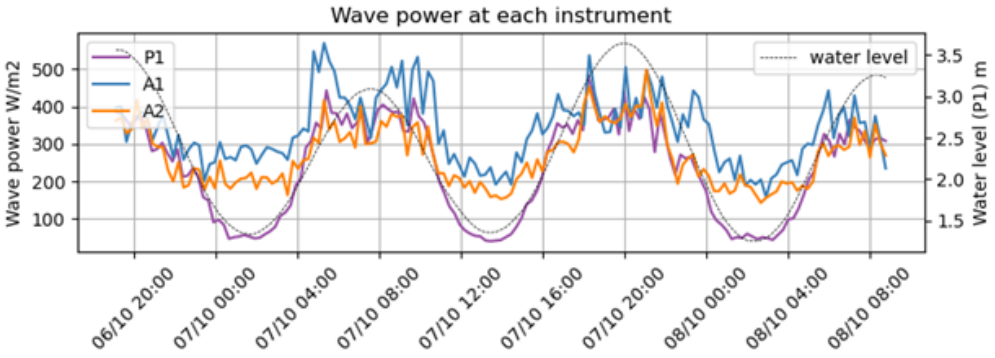

Figure 6: Wave power calculated at each instrument (A1, A2 and P1) and water level at instrument P1.

groove, importantly, we do not extrapolate these results to the above water column. At instrument A1, the maximum current velocity was 2.25 m/s, directed at 150°N (offshore and to the west), with maximum offshore and onshore current velocity of 1.94 m/s and 2.06 m/s, respectively (Figure 7 b and 8a). The mean absolute velocity magnitude at instrument A1 was 0.12 m/s (Figure 6 d), and the mean cross-shore current velocity was directed offshore at 0.04 m/s (Figure 6 b). This cross-shore current decreased to 0 m/s at high tides but increased to 0.07 m/s offshore at low tide (Figure 6 b). Flow velocities were higher at the nearshore instrument, A2, with a maximum current velocity of 2.87 m/s directed at 39.8 °N (offshore and to the east). At A2 we recorded maximum offshore and onshore velocity components of 2.05 m/s and 1.45 m/s, respectively (Figure 7 c and 7b). The mean velocity magnitude measured at instrument A2 was 0.17 m/s, with the mean cross-shore current velocity indicating mean offshore current of 0.12 m/s (Figure 7 c). This offshore current was consistent across the full tidal cycle, with values decreasing to 0.03 m/s at high tide and increasing to 0.18 m/s during low tide (Figure6c). Isolated peaks in cross-shore directed velocity were recorded during low tides (Figure 7 b); we interpret this as likely caused by a short-term wave-breaking jet or localised flow convergence, rather than representing the prevailing flow regime.

3.5.1 Current velocity and tidal controlled water levels

Current velocities within the grooves increased markedly during falling tides; however, the relationship with water level was non-linear. At instrument A1, a pronounced rise in velocity was observed when the water level dropped below 2.9 m (mean depth: 3.6 m), and at A2 when it fell below 2.6 m (mean depth: 3.3 m) (Figure 7). At these thresholds, water depths over the adjacent spurs were reduced to 0.4 m and 0.6 m, respectively. Importantly, at A2, the onset of increased current coincided with wave breaking on the adjacent spurs, which occurred once water depth fell below the estimated breaker depth (using a conservative $\gamma = 0.6$). In contrast, no breaking was observed within the deeper grooves at this stage of the tidal cycle. These observations suggest that wave breaking on spurs during low tide enhances along-groove currents, likely due to the lateral redirection of wave-driven momentum. The circular mean current direction at instrument A1 was 359.8°N, and at instrument A2, it was 346.5°N. In both cases, the mean current direction

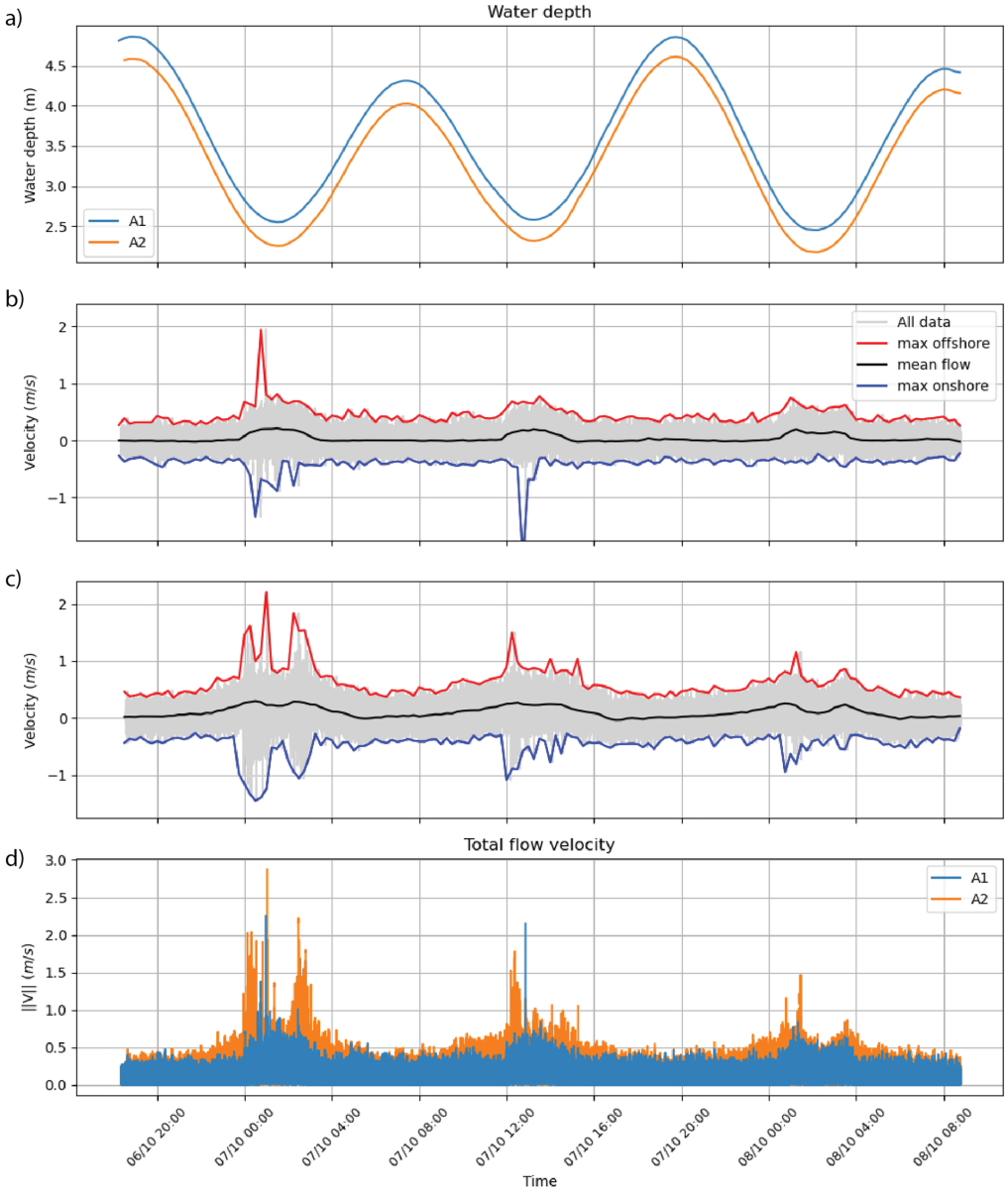

Figure 7: Field measurements of **(a)** water levels at instruments A1 and A2, **(b)** cross-shore current direction (offshore is positive) at instrument A1 and **(c)** at instrument A2. **(d)** shows the absolute magnitude of the current recorded at instrument A1 (orange) and A2 (blue).

was offshore (Figure 8). As water level increased, current direction became less constrained to the groove (Figure 8) and more oscillatory due to wave motion (Figure 7 b, c).

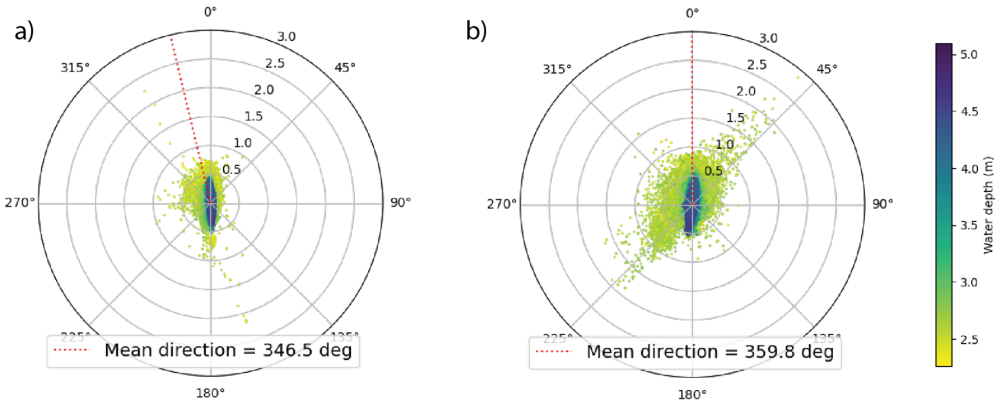

Figure 8: **(a)** Magnitude and direction of current velocity at instruments A1 and **(b)** A2 during the deployment period. Mean current direction is shown with a red dashed line. Water depth is shown with a colour bar.

3.6 Current direction analysis

Current direction was consistently offshore across all tidal levels at instrument A2, located nearest to the reef crest (u_{mean} =0.11 m/s). This current was greatest at low tides (u_{mean}, low tide = 0.18 m/s) (Figure 7, 8). Similarly, temperature gradient inversions, with cooler water at the surface and warmer water at the bed, occurred during the second deployment at instrument B1 in phase with tidal cycles (Figures 8 and 9), inferring the presence of internal waves or density driven flows. The temperature gradient was inverted for most of the deployment of instrument B1 (69%), likely due to constant outflow from the lagoon. On average, the mean temperature (26.5 °C) at the seafloor was similar to that at the surface (26.6 °C), but there were considerable oscillations in the temperature difference (ΔT) from the surface to near seafloor. The maximum temperature inversion recorded was 2.06 °C (Figure 8 a).

4 Discussion

4.1 Spurs and grooves can exist under prevailing oblique waves in low-energy settings.

Since early observations by (Munk and Sargent 1948), SaG systems are often considered to only exist under shore-normal incident high energy waves. Previous studies of SAG have only considered shore-normal waves, both in field observations (Acevedo-Ramirez et al. 2021; Rogers et al. 2013; Storlazzi et al. 2004) and numerical modelling (da Silva et al. 2020; Perris et al. 2024). For example, in a comprehensive numerical model utilising an idealised SaG bathymetry, (da Silva et al. 2020) predicted low magnitude flows in SaG of 0.01–0.1 m/s under wave heights of 0.5–6 m. Field studies in Palmyra Atoll with wave conditions of root-mean-square wave height (H_{rms})

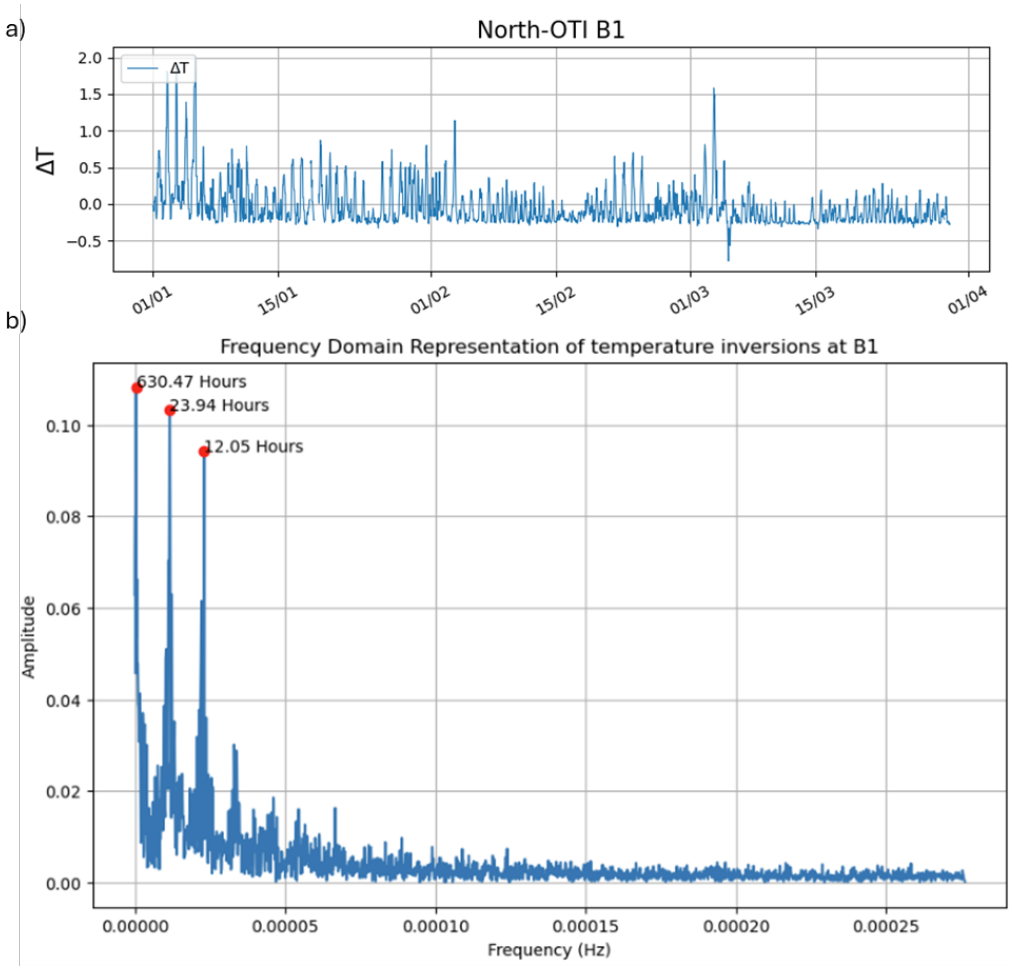

Figure 9: **(a)**Temperature difference between surface and near-bed sensors at site B1. Negative values indicate thermal inversions, where bottom waters were warmer than surface waters. The X-axis shows the date and month of records. **(b)** Frequency spectrum of temperature inversions at B1, highlighting dominant periodicities at 24 and 12 hours (red points), consistent with diurnal and semi-diurnal tidal forcing.

between 0.6 to 1.3 m in a microtidal (0.8 m) environment measured weak currents in a groove, up to 0.20 m/s (Rogers et al. 2015) directed offshore on the upper forereef.

However, during our study, we measured low-energy oblique waves ($P = 340.6\ W/m$ at A1, Figure 5 b, c) and offshore currents in the grooves likely driven by lagoon outflow (Figure 9). While we observe a similar direction of flow to that found by (Rogers et al. 2015), our observations include substantially higher current velocities of up to 1.45 m/s at the outer station (A1) during low tides, despite a maximum significant wave height of only 0.23 m ($P = 340.6\ W/m$, Figure 6, Table 2). This is probably related to the enhanced offshore currents due to the outflow of lagoon water, as discussed in Section 4.2.

We did not observe the Lagrangian circulation cells previously modelled under shore-normal waves, where current was offshore over the spurs and onshore in the grooves (da Silva et al. 2020; Rogers et al. 2013), as no current measurements were collected from over the spurs. The currents observed here were offshore in the grooves (Figure 7 b, c). We hypothesise that these circulation cells may emerge when wave power increases and dominates over the lagoon outflow, or when the direction of incoming waves becomes shore-normal and parallel to grooves for example, during tropical cyclone conditions (Woolsey et al. 2012). The studied low-energy SaG therefore exist under prevailing oblique incident waves, and their hydrodynamics are primarily driven by wave pumping and lagoon outflow, leading to offshore currents under prevailing low energy conditions (Figure 10).

This pattern is similar to currents observed in rip channels on open coast beaches, where shore-connected shoals exhibit higher current velocities compared to the seaward surf zone (MacMahan et al. 2004). However, in our case, given the thermal inversions observed at instrument B1, the offshore current at the inner groove (A2) is more likely driven by tidally induced lagoon outflow than by wave pumping i.e. the mass balance of the reef system, rather than surf zone dynamics.

4.2 The groove channelises the outflow of lagoon water during prevailing low-energy wave conditions

We found decreased wave power at low tides (Figure 6, Table 2), likely due to increased frictional dissipation of waves over the forereef slope. The low wave power conditions and non-shore-normal waves observed in this area had minimal impact on the offshore flows within the groove. We observed greater mean wave power at the outer groove (A1, $P = 283\ W/m$) than at the inner groove (A2, $P = 208\ W/m$). This reduction is consistent with shoaling transformations predicted by linear wave theory and with additional wave energy dissipation as waves propagate shoreward, particularly due to bottom friction and breaking over complex and steep forereef bathymetries (Monismith et al. 2013).

Additionally, from temperature inversions offshore of the grooves (instrument B1), we infer that hypersaline lagoon waters are sinking under the surface ocean water. This dense and warm hypersaline lagoon water has been observed in other atoll reefs (Gardner et al., 2011). The offshore currents measured at the study site therefore likely correspond to lagoon outflows of hypersaline warm water that are driven by wave pumping across the lagoon (sensu Callaghan et al. 2006) due to the

E–SE wave conditions. The lagoon outflow then sinks and travels offshore as bottom currents inside the groove, resulting in the warmer bed temperatures observed seaward of the SaG at B1 (Figure 9 a, b). Whilst seasonal variability likely influenced wave energy and lagoonal exchange, the mechanisms observed (e.g., lagoon outflow driving offshore currents through grooves) are not dependent on season but on relative tide–wave interactions, consequently, the temperature inversions were measured during in a period of lower wind speed and offshore wave height, which have been proposed to drive currents over the lagoon (Ludington 1979).

The observations of thermal inversions at the reef rim are consistent with observations of coral bleaching in the One Tree Reef lagoon (Byrne et al. 2025) and on the deep northern forereef (One Tree Island Research Station Managers Personal Communication) during the January 2024 bleaching event. While our observations suggest that offshore-directed currents are driven primarily by lagoon outflow, the short deployment window limits the ability to capture longer-term variability, including responses to high-energy events. Future studies should incorporate longer deployments and direct measurements of sediment flux to more conclusively link lagoon outflow with sediment transport.

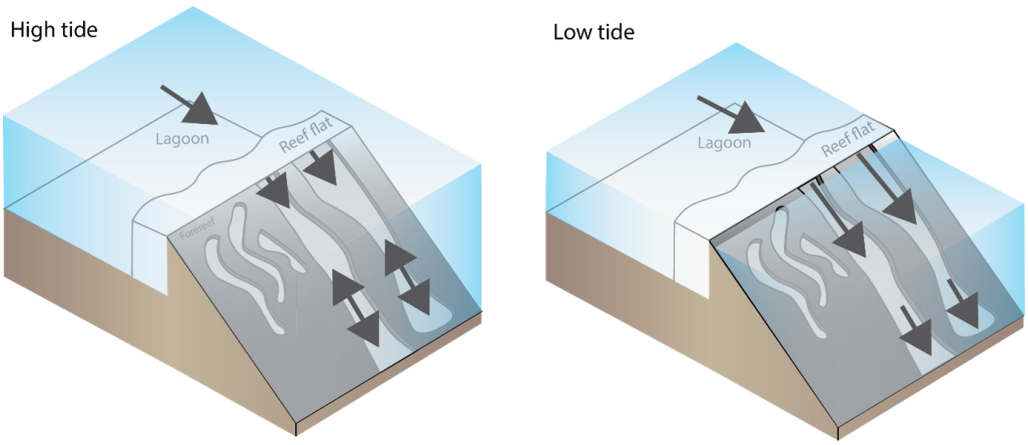

Figure 10: Conceptual diagram of the mean current velocities from measured hydrodynamics in long-and-protected SaG at OTR (Figure 2). Black arrows show current direction, and their length show relative current velocity in the grooves which is offshore for the full tidal cycle in the upper groove. Double headed arrows indicate no mean current and only wave induced oscillatory flow. The flow from the lagoon is always directed offshore.

4.3 Mechanistic interpretation of spur formation under observed current regimes

Wave and current measurements in the forereef groove align with the hydrodynamics expected for the long, protected groove classification (Duce et al. 2020), with higher instantaneous current velocity in the upper groove and offshore-directed current throughout the tidal cycle. These conditions, measured for the first time on the GBR in this study, closely aligned with the mechanisms of reef platform development under low wave energy (Duce et al. 2020). The constant outflow of nutrient-rich lagoon water would foster coral growth on the upper forereef. Additionally, given

the high instantaneous offshore velocities (Figure 7), we hypothesise that the current in the groove transports sediments offshore, fostering long-term spur development. Offshore currents were strongest near the reef crest (A2, Figure 7) and decreased seaward (A1, Figure 7), a pattern that supports the offshore transport and deposition of sediments. The ecological functioning of this process likely depends on current magnitude: when velocities remain within a moderate range, transported rubble and sediment can settle close enough to the spur-and-groove structure to facilitate colonisation and reef accretion. Conversely, if offshore currents become too strong, substrate may be carried beyond ecologically functional distances from the reef, reducing its potential to contribute to seaward reef growth. At Lizard Reef in the Central GBR, it was found that offshore currents, in the absence of extreme waves, transport 1.87 kg/yr of coral rubble offshore (Hughes, 1999). They proposed that this transport supports the seaward accretion of the forereef by providing an offshore substrate for corals to grow. Other studies at Looe Key Reef, Florida, (Shinn et al. 1982) and Ryuku Island, Japan (Kan 1995) have demonstrated spur development over carbonate reef sands. Evidence from U–Th dated cores taken from the forereef 560 m west of our study site reveals seaward lateral accretion of 231 m/ka on the reef flat and 24 m/ka on adjacent spurs (Duce et al. 2020). Similarly, cores have shown that reef flats have accreted seaward on the low-energy margins in OTR (Dechnik et al. 2016).

Although the dynamics of nutrients and sediments were not directly measured in this study, which focussed on groove hydrodynamics, our offshore currents align with (Duce et al. 2020) Mode 3 morphological model of SaG development, where lagoon outflow facilitates the seaward accretion of spurs and the reef flat in low-energy settings. Our findings provide the first hydrodynamic observations of a possible mechanism for this process, where offshore flow from the lagoon is focussed into grooves to support a constructional model of forereef development, driven by sediment accumulation and colonisation offshore of the reef crest.

Future research should examine the hydrodynamics of SaG systems across a range of reef exposures to better understand the current regimes that drive their development. In high-energy settings, where SaG features may be shaped by wave-driven erosion (Blanchon and Jones 1997; Cloud Jr. 1959), strong wave forcing is thought to enhance sediment transport towards the lagoon, with currents converging within grooves (Duce et al. 2020). To resolve the mechanisms driving these processes, long-term deployments are required that capture the full vertical structure of currents across a range of hydrodynamic conditions. Complementary sediment trap deployments would help quantify the relative magnitude of sediment dynamics under these conditions (Storlazzi et al. 2011). Such measurements are critical for identifying the frequency, direction, and intensity of onshore and offshore flows that shape not only SaG morphology but also influence the delivery of sediment to reef islands. This has broader relevance given the projected morphological changes of coral reefs under future climate scenarios (Talavera et al. 2021; Woodroffe et al. 1999). Future efforts to determine drivers of SaG morphodynamics should include simultaneous measurements over both spurs and grooves, with vertically resolved current profiles and direct observations of sediment and nutrient fluxes along the reef rim and through SaG systems.

5 Conclusions

In this study, we present the first field measurements of currents at forereef spurs and grooves (SaG) from the Great Barrier Reef, providing critical insights into their hydrodynamics and role in reef development. The studied SaG exist under prevailing conditions of low-energy oblique incident waves. Our findings demonstrate that the hydrodynamics of low-energy SaGs are influenced by the outflow of lagoonal waters, generating consistent mean offshore currents in the upper forereef groove throughout the tidal cycle. This outflow, with maximum values of 2.05 m/s are driven by wave pumping (i.e., larger waves on the opposite side of the reef push water into the lagoon generating an outflow on the low energy side), potentially transports sediment along the groove elongating the spurs and may contribute to the export of nutrients from the lagoon. These findings provide the first field-based support for the hypothesised Mode 3 of SaG development in the GBR, wherein lagoonal outflow sustains offshore groove currents and promotes the seaward accretion of spurs and the reef flat. This study highlights the importance of in-situ hydrodynamic measurements for understanding reef platform evolution and sets the stage for future long-term and multi-site investigations that would directly link sediment transport, deposition and reef accretion.

Acknowledgments Lachlan Perris was supported by an RTP scholarship from The University of Sydney and the research was partially funded by Australian Research Council (ARC) Future Fellowship (FT100100215), ARC Discovery Program (DP220101125), and Geoscience Australia funding through the Marine Studies Institute at The University of Sydney. Field assistance provided by STEM students from Wenona School. Conceptual figure was produced with assistance by Tessa Chong.

References

Acevedo-Ramirez, C. A., W. Stephenson, S. Wakes, and I. Mariño-Tapia (Sept. 2021). "Wave Transformation on a Fringing Reef System With Spur and Groove Structures". In: *Journal of Geophysical Research: Oceans* 126 (9). DOI: 10.1029/2020JC016910.

Blanchon, P. and B. Jones (1997). "Hurricane control on shelf-edge-reef architecture around Grand Cayman". In: *Sedimentology* 44 (3), pp. 479–506. DOI: 10.1046/j.1365-3091.1997.d01-32.x.

Byrne, M., A. Waller, M. Clements, A. S. Kelly, M. J. Kingsford, B. Liu, C. E. Reymond, A. Vila-Concejo, M. Webb, K. Whitton, and S. A. Foo (2025). "Catastrophic bleaching in protected reefs of the Southern Great Barrier Reef". In: *Limnology and Oceanography Letters*. DOI: 10.1002/lol2.10456.

Callaghan, D. P., P. Nielsen, N. Cartwright, M. R. Gourlay, and T. E. Baldock (June 2006). "Atoll lagoon flushing forced by waves". In: *Coastal Engineering* 53 (8), pp. 691–704. DOI: 10.1016/j.coastaleng.2006.02.006.

Cloud Jr., P. E. (1959). "Geology of Saipan, Mariana Islands, Part 4: Submarine topography and shoal-water ecology". In: *U. S. Geological Survey Professional Paper* (280-K), pp. 361–445.

da Silva, R. F., C. D. Storlazzi, J. S. Rogers, J. Reyns, and R. McCall (2020). "Modelling three-dimensional flow over spur-and-groove morphology". In: *Coral Reefs*. DOI: 10.1007/s00338-020-02011-8.

Davies, P. J. (1983). "Reef growth". In: *Perspectives on coral reefs*. Ed. by Barnes, D. J. Clouston Publisher, Manuka, Australia, pp. 69–106.

Dechnik, B., J. M. Webster, L. Nothdurft, G. E. Webb, J. xin Zhao, S. Duce, J. C. Braga, D. L. Harris, A. Vila-Concejo, and M. Puotinen (2016). "Influence of hydrodynamic energy on Holocene reef flat accretion, Great Barrier Reef". In: *Quaternary Research (United States)* 85 (1), pp. 44–53. DOI: 10.1016/j.yqres.2015.11.002.

Duce, S., A. Vila-Concejo, R. J. McCarroll, B. Yiu, L. A. Perris, and J. M. Webster (Sept. 2022). "Field measurements show rough fore reefs with spurs and grooves can dissipate more wave energy than the reef crest". In: *Geomorphology* 413. DOI: 10.1016/j.geomorph.2022.108365.

Duce, S., B. Dechnik, J. M. Webster, Q. Hua, J. Sadler, G. E. Webb, L. Nothdurft, M. Salas-Saavedra, and A. Vila-Concejo (2020). "Mechanisms of spur and groove development and implications for reef platform evolution". In: *Quaternary Science Reviews* 231. DOI: 10.1016/j.quascirev.2019.106155.

Duce, S., A. Vila-Concejo, S. M. Hamylton, J. M. Webster, E. Bruce, and R. J. Beaman (2016). "A morphometric assessment and classification of coral reef spur and groove morphology". In: *Geomorphology* 265, pp. 68–83. DOI: 10.1016/j.geomorph.2016.04.018.

Duce, S., A. Vila-Concejo, S. Hamylton, E. Bruce, and J. M. Webster (2014). "Spur and groove distribution, morphology and relationship to relative wave exposure, Southern Great Barrier Reef, Australia". In: *Journal of Coastal Research* 70, pp. 115–120. DOI: 10.2112/si70-020.1.

Featherstone, W. E., J. F. Kirby, C. Hirt, M. S. Filmer, S. J. Claessens, N. J. Brown, G. Hu, and G. M. Johnston (2011). "The AUSGeoid09 model of the Australian

Height Datum". In: *Journal of Geodesy* 85 (3), pp. 133–150. DOI: 10.1007/s00190-010-0422-2.

Frith, A. C. (1983). "Circulation at One Tree Reef, Southern Great Barrier Reef". In: *BMR Journal of Australian Geology and Geophyscs* 8, pp. 211–221.

Gardner, J. P., D. W. Garton, and J. D. Collen (2011). "Near-surface mixing and pronounced deep-water stratification in a compartmentalised, human-disturbed atoll lagoon system". In: *Coral Reefs* 30 (1), pp. 271–282. DOI: 10.1007/s00338-010-0701-7.

Goreau, T. F. (1959). "The Ecology of Jamaican Coral Reefs I. Species Composition and Zonation". In: *Ecology* 40 (1), pp. 67–90. DOI: 10.2307/1929924.

Goring, D. G. and V. I. Nikora (2002). "Despiking Acoustic Doppler Velocimeter Data". In: *Journal of Hydraulic Engineering*, pp. 117–126. DOI: 10.1061/ASCE0733-94292002128:1117.

Grimaldi, C. M., R. J. Lowe, J. A. Benthuysen, R. H. Green, J. Reyns, H. Kernkamp, and J. Gilmour (2022). "Wave and Tidally Driven Flow Dynamics Within a Coral Reef Atoll off Northwestern Australia". In: *Journal of Geophysical Research: Oceans* 127 (3). DOI: 10.1029/2021JC017583.

Harris, D. L., J. M. Webster, A. Vila-concejo, S. Duce, and J. X. Leon (2023). "Geomorphology Defining multi-scale surface roughness of a coral reef using a high-resolution LiDAR digital elevation model". In: *Geomorphology* 439 (September 2022), p. 108852. DOI: 10.1016/j.geomorph.2023.108852.

Harris, D. L., A. Vila-Concejo, J. M. Webster, and H. E. Power (2015). "Spatial variations in wave transformation and sediment entrainment on a coral reef sand apron". In: *Marine Geology* 363, pp. 220–229. DOI: 10.1016/j.margeo.2015.02.010.

Jell, J. S. and G. E. Webb (2012). *Geology of Heron Island and Adjacent Reefs, Great Barrier Reef, Australia*. Tech. rep., p. 110.

Kan, H. (1995). "Typhoon Effects on Sediment Movement on Reef Edges and Reef Slopes". In: *Recent Advances in Marine Science and Technology*, pp. 191–201.

Karimpour, A. and Q. Chen (2017). "Wind wave analysis in depth limited water using OCEANLYZ, A MATLAB toolbox". In: *Computers and Geosciences* 106 (June), pp. 181–189. DOI: 10.1016/j.cageo.2017.06.010.

Kinsela, M. A., B. D. Morris, T. C. Ingleton, T. B. Doyle, M. D. Sutherland, N. E. Doszpot, J. J. Miller, S. F. Holtznagel, M. D. Harley, and D. J. Hanslow (2024). "Nearshore wave buoy data from southeastern Australia for coastal research and management". In: *Scientific Data* 11 (1), pp. 1–22. DOI: 10.1038/s41597-023-02865-x.

Klise, K., R. Pauly, K. M. Ruehl, S. Olson, T. Shippert, Z. Morrell, S. Bredin, C. Lansing, M. Macduff, T. Martin, C. Sivaraman, B. Gunawan, and F. Driscoll (Jan. 2020). *MHKiT (Marine and Hydrokinetic Toolkit) - Python*. DOI: 10.5281/zenodo.3924683.

Lindhart, M. (2022). "Loss of reef roughness increases residence time on an idealized coral reef". In: *Scientific Reports* 12 (1), pp. 1–13. DOI: 10.1038/s41598-022-24045-4.

Lowe, R. J., A. S. Leon, G. Symonds, J. L. Falter, and R. Gruber (2015). "The intertidal hydraulics of tide-dominated reef platforms". In: *Journal of Geophysical Research: Oceans* (2), pp. 2121–2128. DOI: 10.1002/jgrc.20224.

Ludington, C. A. (1979). "Tidal Modifications and Associated Circulation in a Platform Reef Lagoon". In: *Aust. J. Mar. Freshwater Res* 30, pp. 425–455.

MacMahan, J. H., A. J. Reniers, E. B. Thornton, and T. P. Stanton (2004). "Infragravity rip current pulsations". In: *Journal of Geophysical Research: Oceans* 109 (1), pp. 1–9. DOI: 10.1029/2003jc002068.

Monismith, S. G. (2007). "Hydrodynamics of coral reefs". In: *Annual Review of Fluid Mechanics* 39 (1), pp. 37–55. DOI: 10.1146/annurev.fluid.38.050304.092125.

Monismith, S. G., L. M. Herdman, S. Ahmerkamp, and J. L. Hench (2013). "Wave transformation and wave-driven flow across a steep coral reef". In: *Journal of Physical Oceanography* 43 (7), pp. 1356–1379. DOI: 10.1175/JPO-D-12-0164.1.

Munk, W. and M. C. Sargent (1948). "Adjustment of Bikini Atoll to Ocean Waves". In: 29 (6), pp. 855–860.

Odum, H. T. and E. P. Odum (1955). "Trophic Structure and Productivity of a Windward Coral Reef Community on Eniwetok Atoll". In: *Ecological Monographs* 25 (3), pp. 291–320. DOI: 10.2307/1943285.

Perris, L., T. Salles, T. E. Fellowes, S. Duce, J. Webster, and A. Vila-Concejo (2024). "The Influence of Coral Reef Spur and Groove Morphology on Wave Energy Dissipation in Contrasting Reef Environments". In: *Journal of Geophysical Research: Earth Surface* 129 (8), pp. 1–17. DOI: 10.1029/2023JF007424.

Ribal, A. and I. R. Young (2019). "33 Years of Globally Calibrated Wave Height and Wind Speed Data Based on Altimeter Observations". In: *Scientific Data* 6 (1), pp. 1–15. DOI: 10.1038/s41597-019-0083-9.

Rogers, J. S., S. G. Monismith, F. Feddersen, and C. D. Storlazzi (2013). "Hydrodynamics of spur and groove formations on a coral reef". In: *Journal of Geophysical Research: Oceans* 118 (6), pp. 3059–3073. DOI: 10.1002/jgrc.20225.

Rogers, J. S., S. G. Monismith, R. B. Dunbar, and D. Koweek (2015). "Field observations of wave-driven circulation over spur and groove formations on a coral reef". In: *Journal of Geophysical Research: Oceans* (1), pp. 145–160. DOI: 10.1002/2014JC010464.Received.

Rogers, J. S., S. G. Monismith, D. A. Koweek, and R. B. Dunbar (Jan. 2016). "Wave dynamics of a Pacific Atoll with high frictional effects". In: *Journal of Geophysical Research: Oceans* 121 (1), pp. 350–367. DOI: 10.1002/2015JC011170.

Sartori, G., E. L. Boles, S. G. Monismith, R. B. Dunbar, P. J. Mumby, A. Khrizman, and R. Capozzi (2024). "Morphologically driven sedimentation patterns on a coral reef". In: *Coral Reefs*. DOI: 10.1007/s00338-025-02629-6.

Sheppard, C. (1981). "The groove and spur structures of Chagos atolls and their coral zonation". In: *Estuarine, Coastal and Shelf Science* 12 (5), pp. 549–560. DOI: 10.1016/S0302-3524(81)80081-3.

Shinn, E. (June 1963). "Spur and Groove Formation on the Florida Reef Tract". In: *SEPM Journal of Sedimentary Research* Vol. 33 (2), pp. 291–303. DOI: 10.1306/74d70e34-2b21-11d7-8648000102c1865d.

Shinn, E. A., J. H. Hudson, D. M. Robbin, and B. H. Lidz (1982). "Spurs and grooves revisited: construction versus erosion, Looe Key Reef, Florida". In: *Proccedings of the Fourth International Coral Reef Symposium*. Marine Sciences Center, University of the Philippines, pp. 475–483.

Silverman, J., D. I. Kline, L. Johnson, T. Rivlin, K. Schneider, J. Erez, B. Lazar, and K. Caldeira (2012). "Carbon turnover rates in the One Tree Island reef: A

40-year perspective". In: *Journal of Geophysical Research: Biogeosciences* 117 (3), pp. 1–16. DOI: 10.1029/2012JG001974.

Smith, C., A. Vila-Concejo, and T. B. Salles (2020). "RADWave: Python code for ocean surface wave analysis by satellite radar altimeter." In: *Journal of Open Source Software* 1 (5), p. 46. DOI: https://doi.org/10.21105/joss.02083.

Smith, C., A. Vila-Concejo, and T. Salles (June 2023). "Offshore wave climate of the Great Barrier Reef". In: *Coral Reefs* 42 (3), pp. 661–676. DOI: 10.1007/s00338-023-02377-5.

Sneh, A. and G. M. Friedman (1980). "Spur and groove patterns on the reefs of the northern gulfs of the Red Sea." In: *Journal of Sedimentary Petrology* 50 (3), pp. 981–986. DOI: 10.1306/212F7B3F-2B24-11D7-8648000102C1865D.

Storlazzi, C. D., E. Elias, M. E. Field, and M. K. Presto (2011). "Numerical modeling of the impact of sea-level rise on fringing coral reef hydrodynamics and sediment transport". In: *Coral Reefs* 30 (SUPPL. 1), pp. 83–96. DOI: 10.1007/s00338-011-0723-9.

Storlazzi, C. D., J. B. Logan, and M. E. Field (2003). "Quantitative morphology of a fringing reef tract from high-resolution laser bathymetry: Southern Molokai, Hawaii". In: *Bulletin of the Geological Society of America* 115 (11), pp. 1344–1355. DOI: 10.1130/B25200.1.

Storlazzi, C. D., A. S. Ogston, M. H. Bothner, M. E. Field, and M. K. Presto (2004). "Wave-and tidally-driven flow and sediment flux across a fringing coral reef: Southern Molokai, Hawaii". In: *Continental Shelf Research* 24, pp. 1397–1419. DOI: 10.1016/j.csr.2004.02.010.

Talavera, L., A. Vila-Concejo, J. M. Webster, C. Smith, S. Duce, T. E. Fellowes, T. Salles, D. Harris, J. Hill, W. Figueira, and J. Hacker (2021). "Morphodynamic controls for growth and evolution of a rubble coral island". In: *Remote Sensing* 13 (8), pp. 1–23. DOI: 10.3390/rs13081582.

Weydert, P. (1979). "Direction de croissance des eperons sur le front d'un recif barriere - l'exemple du grand recif de tulear (madagascar)". In: *Marine Geology* 30 (30), pp. M9–M19.

Wilson, P. R. (1985). *Tidal Studies in the One Tree Island Lagoon*. Tech. rep., pp. 139–56.

Woodroffe, C. D., R. F. Mclean, S. G. Smithers, and E. M. Lawson (1999). "Atoll reef-island formation and response to sea-level change: ž / West Island, Cocos Keeling Islands". In: *Marine Geology* 160, pp. 85–104.

Woolsey, E., S. J. Bainbridge, M. J. Kingsford, and M. Byrne (2012). "Impacts of cyclone Hamish at One Tree Reef: Integrating environmental and benthic habitat data". In: *Marine Biology* 159 (4), pp. 793–803. DOI: 10.1007/s00227-011-1855-8.

Zippenfenig, P. (2023). *Open-Meteo.com Weather API*. DOI: 10.5281/zenodo.7970649.

4| Hydrodynamic Controls on Spur and Groove Morphology: Flow Variability and Reef Structure

Lachlan Arthur Perris[1, 2], Mathilde Lindhart[3], Tristan Salles[1,2], Ana Paula Da Silva[1, 2], Thomas E. Fellowes[1, 4], Ana Vila-Concejo[1,2]

[1]Geocoastal Research Group, School of Geosciences, The University of Sydney, NSW 2006, Australia
[2]Marine Studies Institute, Faculty of Science, The University of Sydney, NSW 2006, Australia
[3]University of Plymouth, School of Biological and Marine Sciences
[4]Water Research Laboratory, School of Civil and Environmental Engineering, UNSW Sydney, Australia

Abstract

Spur and groove (SaG) structures are a prominent feature of wave-exposed coral forereefs, yet their formation and persistence remain poorly constrained by in situ hydrodynamic observations. This study presents a six-month record of wave and current measurements across a well-developed SaG system on the wave-exposed eastern forereef of One Tree Reef, a high-energy carbonate platform in the southern Great Barrier Reef (Australia). The results show that wave induced cross-shore flows were regularly outpaced by alongshore tidal currents (31.6% of the time). Despite strong and persistent alongshore currents, the geomorphic influence is seemingly limited, and only evident in a slight asymmetry of spurs that align with the asymmetrical tidal currents of the region. Additionally, wave-driven sediment mobility is strongly modulated by tidal elevation and incident wave height, with the upper forereef experiencing consistently strong near-bed orbital velocities and bed shear stresses, exceeding guides for sediment mobility for 94% of the record on the upper forereef. These conditions promote sediment entrainment and abrasion, with guides of sediment mobility exceeded across the entire SaG system under storm wave forcing. Our findings support a model of SaG development driven by wave-induced sediment abrasion rather than direct current forcing. This work identifies key processes driving the formation and maintenance of SaGs, highlighting their sensitivity to hydrodynamic changes under future climate scenarios.

1 Introduction

Climate change is reshaping the morphology of coral reefs through rising sea levels, ocean warming (Hughes et al. 2003), and changes in storm frequency and intensity (Knutson et al. 2020). The impacts of these pressures are evident on reef slopes, where the structural complexity of forereefs plays a critical role in modulating wave energy (Duce et al. 2022; Perris et al. 2024), sustaining high rates of coral growth (Goreau 1959; Madin and Connolly 2006), and driving the production and redistribution of carbonate sediment (Blanchon and Jones 1995; Kenyon et al. 2023a). However, there is growing concern about the capacity of stressed or degraded reefs to continue performing these ecological and physical functions under projected climate and sea level scenarios (Perry et al. 2015; Woodroffe and Webster 2014), creating urgency in understanding forereef morphology and hydrodynamics under present day conditions (Bellwood et al. 2019).

One of the most distinctive and widely observed geomorphic features on wave-exposed forereefs is the spur and groove (SaG) system. Spurs are shore-normal ridges and grooves are channels that work to modulate wave energy (Duce et al. 2021; Perris et al. 2024), alter flow structure (da Silva et al. 2020), and influence patterns of sediment transport and coral colonisations around reef systems (Perris et al. 2026). SaG exist under a broad range of conditions, from high to low wave energy (Duce et al. 2016). Despite their broad distribution, the processes responsible for the formation and maintenance of SaG morphology remain unresolved. Early interpretations attributed groove development to the seaward return flow of water across reef platforms (Cloud Jr. 1959; Tracey et al. 1948), while others proposed that these features form through preferential coral accretion on spurs and inhibited

growth in grooves (Goreau 1959; Shinn 1976). Later studies have suggested that both erosion and construction act in tandem, with sediment dynamics and wave-driven abrasion suppressing coral colonisation in channels while promoting growth on adjacent ridges (Blanchon and Jones 1995; Kobluk and Lysenko 1992; Storlazzi et al. 2003). Despite the growing number of conceptual models, few studies have quantified the hydrodynamic processes shaping these morphological features.

Recent work has advanced the conceptual understanding of SaG development by incorporating reef slope, wave energy, and accretional patterns. Duce et al. (2020) identified three dominant modes of forereef development that reflect different balances of physical and biological processes. In the first mode, high wave energy over low gradient slopes limits coral growth in channels and promotes groove formation through scouring and sediment transport. A second mode, occurring on steeper slopes with moderate wave exposure, reflects a dynamic equilibrium between accretion and erosion. A third mode, associated with moderate slopes and lower wave energy, permits spur development with offshore-directed flow maintaining grooves through sediment bypass, which has been observed in previous work on low-energy forereefs (Perris et al. 2026). These conceptual models suggest that the morphology of reef slopes emerges from spatially and temporally variable feedback between wave forcing, reef growth, and sediment transport. However, understanding those feedbacks remains limited by the scarcity of in situ hydrodynamic measurements within active SaG systems. Field and experimental studies have recently provided key guides for sediment mobilisation and coral dislodgement under wave forcing. Kenyon et al. (2023b) demonstrated that near-bed orbital velocities exceeding 0.3 m/s initiate sediment movement and rubble overturning, while Deng et al. (2025) reported that velocities above 1.3 m/s are required to dislodge coral colonies from reef slopes. These guides suggest that both chronic and extreme wave events can influence sediment dynamics and ecological succession in spur and groove systems. The movement of coral rubble has been identified as a constraint on coral recruitment and a potential mechanism for SaG formation and morphological maintenance (Duce et al. 2014; Leung and Mumby 2024).

Tropical cyclones represent an important but irregular forcing mechanism in coral reef environments. Their influence on reef morphology may include coral fragmentation, the redistribution of rubble and sand, and the modification of reef topography through intense wave and current forcing (Harmelin-Vivien and Laboute 1986; Kan 1995; Torres-Garcia et al. 2018). Cyclone-induced disturbances can alter sediment budgets and affect SaG morphology by changing the location, volume, or stability of sediment deposits. However, few studies have directly assessed whether the hydrodynamic conditions associated with cyclones are sufficient to form, maintain, or erode spur and groove features.

On mesotidal reefs, the interaction between wave-driven flows and tidal currents exerts a strong control on nearshore circulation. Wave driven flows have been observed to generate Lagrangian circulation cells when interacting with SaG, that influence sediment transport pathways (da Silva et al. 2020; Wolanski and Kingsford 2024). Numerical models have demonstrated that relatively weak wind driven alongshore currents can suppress offshore-directed flows within grooves, potentially modifying sediment transport and deposition patterns (da Silva et al. 2020). These interactions suggest that the maintenance of SaG structures may be sensitive not only to wave

energy and reef slope, but also to the magnitude and variability of tidal currents. However, in situ measurements relating the relative influence of tidal and wave forcing on SaG are limited, and the focus of numerical models have previously relied on the dominance of cross-shore wave driven flows only, despite observations that alongshore currents are present in most forereef environments (da Silva et al. 2020; Rogers et al. 2015).

We present a six-month dataset of hydrodynamic observations collected from a spur and groove system on the eastern forereef of One Tree Reef, located in the southern Great Barrier Reef (Australia). Instruments included a pressure transducer, an acoustic Doppler current profiler, and a directional wave buoy. The measurements are analysed alongside 0.5 m resolution bathymetry derived from airborne LiDAR (Harris et al. 2023) to assess the relationships between local morphology, wave and current dynamics, and sediment mobility guides. This study aims to answer the following questions: (1) Do observed forereef hydrodynamics support existing conceptual models of spur and groove formation? (2) How do forereef current regimes vary under high and low energy conditions? (3) Are hydrodynamic conditions sufficient to maintain spur and groove morphology through sediment transport and coral growth suppression? By integrating hydrodynamic measurements with quantitative morphological data, this study provides new empirical evidence on the physical drivers of reef slope development and informs broader questions about the resilience and future of structurally complex reef systems under environmental change.

2 Methods

2.1 Field study

2.1.1 Study site

The eastern forereef of One Tree Reef (OTR) features an extensive SaG system that extends over 200 m seaward from the reef crest, across depths of 1–10 m (Figure 1). The hydrodynamic conditions at OTR are shaped by both wave and tidal forcing. The site is exposed to high-energy wave events, with storm wave conditions (mean significant wave heights H_s>3 m) occurring at a return frequency of 8.5% (Harris et al. 2015). Tropical cyclone activity is also a relevant influence (Blanchon and Jones 1997; Kan 1995), with cyclone tracks identified in the region via the International Best Track Archive for Climate Stewardship (IBTrACS) database (Kruk et al. 2010).

One Tree Island is a meso-tidal reef with semi diurnal tides and a spring-tide range of 3 m. Tidal dynamics are complex, with intermittent influence from the transient Capricorn Eddy (Weeks et al. 2010). In the nearby Swains reefs, satellite imagery has revealed strong tidal flows, with currents reaching up to 4 m/s during flooding tides (Marmorino 2022), highlighting the potential for substantial tidal forcing in this region, which influences hydrodynamic circulation around the entire reef (Perris et al. 2026).

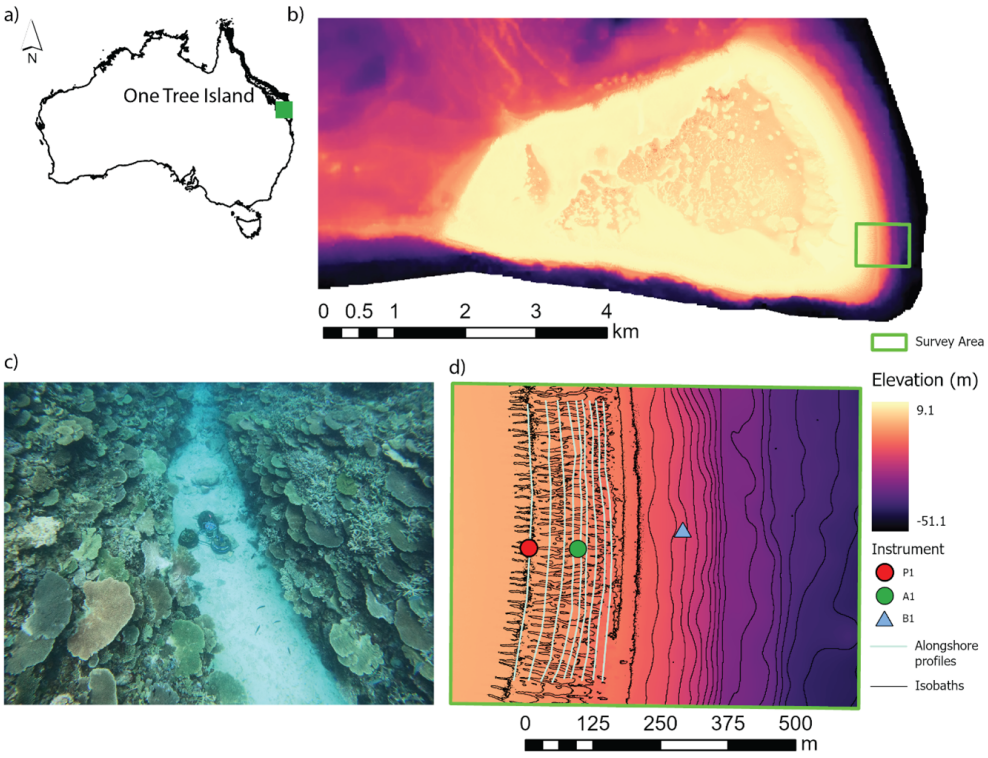

Figure 1: **(a)** One Tree Island (OTI) is in the Capricorn Bunker Group of the Southern Great Barrier Reef (GBR) **(b)** LiDAR elevation map, referenced to Australian Height Datum (AHD) using the AusGEOID09 model (Featherstone et al., 2011) showing the wave exposed forereef of OTI extends for 4 km of continuous spur and groove (SaG) morphologies **(c)** Acoustic Doppler Current Profiler (ADCP, Instrument A1) positioned within a SaG system, image taken by Lachlan Perris on 24 November 2022 **(d)** Location of instruments (P1: RBR Virtuoso^3, A1: Teledyne Instruments RDI Workhorse Sentinal (1200kHz) ADCP and B1: Sofar Spotter buoy, Table 1) inside a forereef groove and alongshore profiles extracted for morphological analysis, collected over each 1 m isobath.

2.1.2 Experimental set up

A 1200 kHz Teledyne RDI Workhorse Sentinel Acoustic Doppler Current Profiler (ADCP, Instrument A1, Figure 1 d) was deployed within a SaG channel on the forereef slope, at a depth of 9 m . The transducer head was mounted 0.6 m above the seabed on a custom-built frame deployed by a professional dive team. Instrument A1 operated in burst mode for both waves and currents, waves were recorded in 10-minute bursts every 3 hours. Each burst consisted of 1200 velocity profiles sampled at 2 Hz. Current measurements were collected in 1 m vertical bins and 30-min ensembles and subsequently aggregated to 3-hourly values to match the wave-burst sampling. The instrument's internal compass was calibrated on-site to account for potential magnetic interference from the steel and iron components of the deployment frame (Figure 1 c).

An RBR Virtuoso^3 pressure transducer (instrument P1, Figure 1 d) was secured in the same forereef groove with instrument A1, closer to the reef crest at a depth of 4.2 m. The instrument was secured to the substrate and configured to operate in burst mode, recording 15-minute bursts every hour at a sampling frequency of 8 Hz. Offshore wave parameters were derived from an ongoing deployment of a Sofar Spotter directional wave buoy (instrument B1, Figure 1 d) moored on the eastern forereef slope at a depth of 15.8 m (Figure 1 c, Table 1). The record spans from 22 November 2022 to 15 May 2023, with 174 days of valid data. The buoy records surface displacement at high frequency (4500 samples per 30-minute interval), from which significant wave height (H_s), peak period (T_p), and mean wave direction are derived (Kinsela et al. 2024).

Table 1: Instrument deployment details

Instrument name	Instrument model	Sample rate (Hz)	Data collection mode	Start date	End date	Mean depth (m)
P1	RBR Virtuoso^3	8	15 min burst per hour	25/11/2022 12:00	16/05/2023 8:00	4.2
A1	Teledyne Instruments RDI Workhorse Sentinal (1200kHz) ADCP	2	Waves: 10 min burst per 3 hour Currents: 30 min burst per hour	24/11/2022 6:00	6/04/2023 23:30	9.0
B1	Sofar Spotter buoy	3.84	Continuous	24/11/2022	15/05/2023	16

2.1.3 Morphological analysis

To quantitatively characterise spur and groove (SaG) morphology, alongshore and cross shore elevation profiles were extracted from 0.5 m resolution LiDAR of OTR (Harris et al. 2023). We extracted cross-shore profiles following groove beds across 500 m of forereef (Figure 1 d) to determine mean groove length and bearing. Alongshore profiles were extracted from successive 1 m isobaths (6-13 m isobaths) also extending 500 m along the forereef, centred on the instrument array (Figure 1 d). To process the alongshore profiles we used spectral methods derived for analysis of sea-surface spectra in oceanography (Srokosz and Longuet-Higgins 1986).

Each alongshore profile (Figure 1 d) was split into overlapping windows of length L_s= 100 m with 50% overlap. A Hann taper was applied to every window. Within each window we computed a one-sided spatial power spectral density $S_Y(f)$ (periodogram; units m^2 per $(cycles/m)$, where spatial frequency f is in cycles/m and the spatial sampling rate is $1/dx$. These window-level estimates yield a distribution of metrics per profile.

Spur height (h_{spur}) was determined for each window with the zeroth spectral moment,

$$m_0 = \int S_Y(f)\, df \tag{4.1}$$

To define the significant relief,

$$h_{\text{spur}} = 4\sqrt{m_0} \tag{4.2}$$

Spur wavelength (γ) was calculated for each window based on the spectral peak, and defined the dominant spur wavelength as

$$\gamma = \frac{1}{f_p} \tag{4.3}$$

This gives the characteristic along-profile spacing of the spur–groove field within that window. Finally, spur skewness was calculated to determine the symmetry of SaG, we computed the skewness of the local slope in each window, where $s(x) = dY/dx$. The slope skewness is given by the third standardised moment, following Srokosz and Longuet-Higgins (1986):

$$\text{Skew}(s) = \frac{1}{N}\sum_{n=1}^{N}\left(\frac{s_n - \mu_s}{\sigma_s}\right)^3, \tag{4.4}$$

where s_n are slope samples in the window, $\mu_s = \frac{1}{N}\sum s_n$ and $\sigma_s^2 = \frac{1}{N}\sum (s_n - \mu_s)^2$. Here, a value of zero reflects a symmetrical slope, positive values reflect a southward leaning slope and negative values show a northward leaning slope. All metrics were compiled for profiles (6–13 m isobaths) and analysed to evaluate spatial variability across the forereef slope. The use of a standardised detection and correction workflow across all profiles enabled consistent comparison of morphodynamic features and the identification of cross-shore trends in SaG geometry.

Spur height (h_{spur}) was determined for each window with the zeroth spectral moment,

$$m_0 = \int S_Y(f)\, df \tag{4.5}$$

To define the significant relief,

$$h_{\mathrm{spur}} = 4\sqrt{m_0} \tag{4.6}$$

Spur wavelength (γ) was calculated for each window based on the spectral peak, and defined the dominant spur wavelength as

$$\gamma = \frac{1}{f_p} \tag{4.7}$$

This gives the characteristic along-profile spacing of the spur–groove field within that window. Finally, spur skewness was calculated to determine the symmetry of SaG, we computed the skewness of the local slope in each window, where $s(x) = dY/dx$. The slope skewness is given by the third standardised moment, following Srokosz and Longuet-Higgins (1986):

$$\mathrm{Skew}(s) = \frac{1}{N}\sum_{n=1}^{N}\left(\frac{s_n - \mu_s}{\sigma_s}\right)^3, \tag{4.8}$$

where s_n are slope samples in the window, $\mu_s = \frac{1}{N}\sum s_n$ and $\sigma_s^2 = \frac{1}{N}\sum (s_n - \mu_s)^2$. Here, a value of zero reflects a symmetrical slope, positive values reflect a southward leaning slope and negative values show a northward leaning slope. All metrics were compiled for profiles (6–13 m isobaths) and analysed to evaluate spatial variability across the forereef slope. The use of a standardised detection and correction workflow across all profiles enabled consistent comparison of morphodynamic features and the identification of cross-shore trends in SaG geometry.

2.2 Hydrodynamic data processing

2.2.1 ADCP data processing

Raw data files from instrument A1 were imported into WAVESMON v2.4 (Teledyne RD Instruments). Beam-coordinate velocities were transformed to earth-coordinates, applying a magnetic variation correction of 9.68° and enabling the "correct for tilts" option to compensate for any fixed instrument tilt (<10°). A two-stage quality-control routine removed spurious data using default amplitude and correlation thresholds. Data were vertically binned at 1 m resolution and averaged into the prescribed 30 min ensembles. Spectral decomposition employed the VPS (Velocity–Pressure–Surface track) priority setting to capitalise on redundant measurements if one data source was screened. Ensembles of 128 s (1024 samples) were windowed with a Hann taper and 50% overlap. Spectra were computed over 256 frequency bands with 90 directional bins using the iterative maximum-likelihood

method, iterated three times to refine directional spreading. Bulk wave parameters were derived from spectral moments:

$$H_s = 4\sqrt{m_0},\ T_p = \frac{1}{f_p} \tag{4.9}$$

where m_0 is the zeroth moment and f_p the peak frequency. Mean wave direction and directional spread were also obtained for each 10 min record.

We quantified the relative influence of the cross-shore current component by normalising it to the total current magnitude. Specifically, we compared the absolute value of the cross-shore velocity (u) with the absolute current magnitude (V) at each depth bin. This was expressed as $|u/V|$. Where $|u/V| > 0.5$, the cross-shore component is dominant, and where $|u/V| < 0.5$, alongshore currents are dominant.

2.2.2 Pressure transducer data processing

We estimated wave parameters from pressure sensor (P1, Figure 1d) time series using spectral analysis. Records were divided into 30-min segments with linear detrending. Power spectral densities, S_{pp}, were computed for each segment using Welch's method with a Hann window. The segment length was set to the nearest power of two based on the sampling frequency (1024 points for 2 Hz data). A dynamic pressure transfer function was applied to account for sensor depth, following linear wave theory:

$$S_{\eta\eta}(f) = \left(\frac{\cosh kh}{\rho g}\right)^2 S_{pp}(f) \tag{4.10}$$

Where k is the wavenumber, h is the mean water depth, and z the sensor height above the bed. Wavenumbers were solved iteratively from the linear dispersion relation:

$$\omega^2 = gk\,\tanh(kh) \tag{4.11}$$

where ω is the angular frequency and g is gravitational acceleration. The significant wave height (H_s) was calculated from the zeroth spectral moment of the surface elevation spectrum, following Eq. 5 Wave periods were estimated from spectral moments and peak frequency. The mean period was defined as

$$T_m = \frac{m_0}{m_1} \tag{4.12}$$

where $m_0 = \int S_{\eta\eta}(f)$ and $m_1 = \int f S_{\eta\eta}(f)\,df$. The peak period ($T_p$) was determined directly from the frequency of maximum spectral density, as in Eq. 6.

2.2.3 Buoy data processing

Raw data derived from the wave buoy (B1) were processed following the spectral analysis framework described by Kinsela et al. (2024). Displacement records were segmented into regular half-hour intervals aligned to UTC and filtered to remove GNSS-related artefacts, using spike detection and a high-pass Butterworth filter (cut-off frequency: 0.029 Hz). Bulk parameters were computed from spectral moments following Eq. 4.5 and 4.6. Directional properties were estimated using co- and

quad-spectral methods. Only high-quality intervals (23% data completeness) were retained for analysis. From this filtered dataset, the full distribution of significant wave heights was used to compute descriptive statistics and percentile thresholds. The 5th and 95th percentiles of H_s were extracted to characterise background and extreme wave conditions, respectively. To visualise the distribution of wave heights, a histogram of H_s was generated and fitted with a Rayleigh distribution curve using maximum likelihood estimates for the mean and standard deviation (Longuet-Higgins 1952). This approach provided insight into the central tendency and spread of wave conditions over the deployment. This processed record constitutes the most temporally resolved *in situ* wave dataset for the region to date.

2.2.4 Derivation of relevant wave parameters

We calculated the peak period T_p following Eq. 6, Where f_p is the maximum of the spectral density S_{pp}. Wave power was calculated using linear wave theory:

$$P = c_g E \tag{4.13}$$

where, E is the wave energy density and c_g is the group speed determined for intermediate depths, such that:

$$c_g = \frac{c}{2}\left(1 + \frac{2kh}{\sinh 2kh}\right) \tag{4.14}$$

Bed shear stress and near-bed orbital velocities were estimated to assess bottom boundary layer forcing under waves. We estimated the amplitude of the near-bed orbital velocity and associated wave-induced shear stress following linear wave theory and (Storlazzi et al. 2003). The peak orbital velocity at the bed was estimated as:

$$U_{(s,\text{peak})} = \frac{H_s \omega}{2\sinh(kh)} \tag{4.15}$$

where, $\omega = 2\pi/T_p$ is the angular frequency and kh is the nondimensional relative depth.
The horizontal excursion amplitude was given by:

$$A_e = \frac{U_{\text{bed}}}{\omega} \tag{4.16}$$

Wave-induced peak bottom shear stress was estimated using a quadratic stress law:

$$\tau_b = \frac{1}{2}\rho_f f_w \left(A_e\,\omega\right)^2 \tag{4.17}$$

where, $\rho = 1020$ kg/m^3 is seawater density and f_w is the wave friction factor calculated from Nielsen (1992), which shows good agreement with frictional parametrisations on coral reefs (Rogers et al., 2016):

$$f_w = 0.04\left(\frac{A}{0.0025}\right)^{-0.25} \tag{4.18}$$

Values for the square root of shear stress τ_b with units N/m^2 were computed for comparison across wave conditions and measurement locations.

2.3 Sediment mobility

To screen for plausible sediment and coral motion under the observed waves, we used recent reef-specific datasets. For rubble and sand mobility we drew on (Kenyon et al. 2023b), who combined flume tests and in situ observations on a Maldivian reef to relate near-bed orbital velocity (U_s) to probabilities of movement. Their results indicate ∼50% movement around U_s ≈0.30 m/s and ∼90% around U_s ≈0.43 m/s, with rubble flipping near U_s ≈0.34 m/s (50%) and ≈0.50 m/s (90%). These estimates were averaged across rubble length, branchiness, and substrate. We employ these values as guides because the forereef SaG system studied here is in an area of high coral sediment productivity, where surrounding live corals produce a range of sediment grain sizes and forms, which influences mobility (Kench 1998). Additionally, grain size reflects mode and duration of transport (Krumbein 1941), which varies widely for sediments in a SaG system (Sartori et al. 2024). Sediment mobility is also enhanced over sandy beds rather than rubble beds (Kenyon et al. 2023b), which likely changed during the experiments. Consequently, we use these values as guides to identify periods when sediment motion on groove beds is plausible, noting that we did not measure sediment transport directly and instead apply established mobility guides as a proxy for potential sediment motion and its mechanical influence on groove morphology. Sediment grain sizes were not quantified; however, visual observations indicated that groove sediments spanned a wide range, from fine sand to boulders, and the relative proportions of these sizes likely varied over the long duration of the experiment. Accordingly, we emphasise that our analysis is based on mobility guides rather than direct transport measurements.

For live-coral dislodgement and breakage, we used values from Deng et al. (2025), who calibrated 3-D structural models with in situ measurements of Acropora muricata and Acropora hyacinthus at Heron Reef, 12 km from our site. Their results suggest indicative velocities for branch breakage of 1.3–1.7 m/s and for shallow-water colonies under surf forcing of 3.2–5.0 m/s. As with mobility, these values remain contingent on colony size, shape, health, bioerosion, and attachment, and are used as guides rather than transferable thresholds. We rely on these recent, reef-specific values to use them as guides to assess whether observed events could mobilise sediment or compromise colonies on the SaG forereef. They are used as context-appropriate guides for our setting, with applicability conditioned by local rubble geometry, grain-size distributions, settling velocities, and the instantaneous substrate state.

3 Results

3.1 Wave analysis

3.1.1 Offshore wave analysis

Mean offshore H_s (Instrument B1) was 1.3 m with a period of 8.9 seconds, with remarkable consistency from the easterly direction (101°, std = 17°, Figure 2 d). Offshore H_s ranged from 0.3 to 3.6 m, with a 5th percentile of 0.5 m and a 95th percentile of 2.4 m (Figure S1, Figure 2 a). We used this distribution to identify two events of continuously high and low wave energy where $H_s > 2.4$ and $H_s <$

0.5 m, respectively (Figure 2 a). The greatest wave heights (H_s = 3.6 m) occurred during the transit of Tropical Cyclone Gabrielle (Figure 3), with H_s > 2.4 m (95th percentile of H_s) for 2 consecutive days in February 2023 (Figure 2 c, Figure 3). The lowest wave heights were observed over a 2-day period during November 2022 ($\overline{H}_s$= 0.4 m, Figure 2 b).

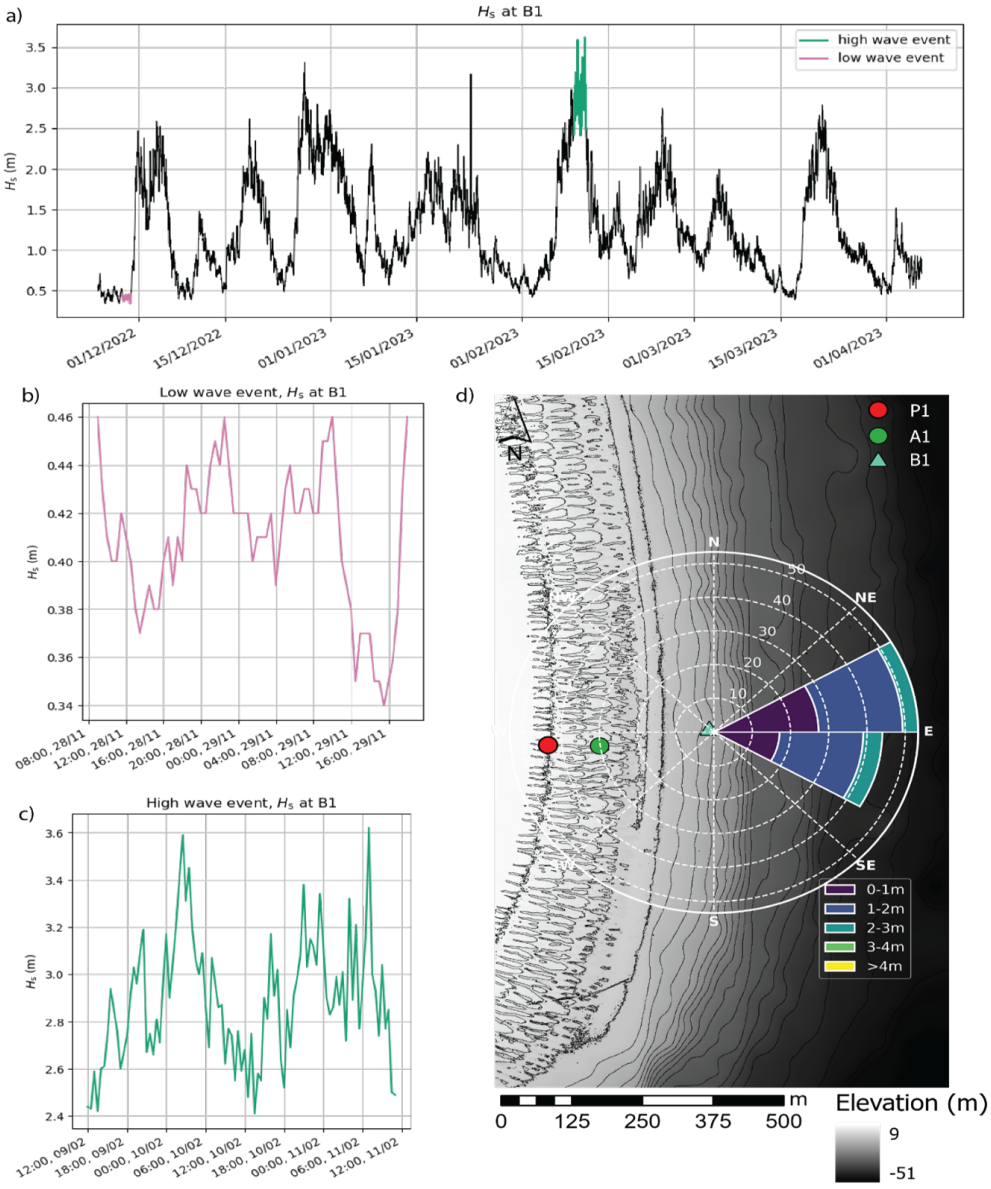

Figure 2: **(a)** Significant wave heights (H_s) derived from instrument B1 (Table 1) at approximately 16 m depth. Pink rectangle highlights a small wave event, representing a consecutive time series below the 5th percentile of H_s, and green rectangle shows a high wave event (during TC Gabrielle passage), representing a consecutive timeseries above the 95th percentile of H_s (Figure S1). b) and c) show the time series of H_s for both small and high wave events, respectively. d) a wave rose of all data recorded at B1, mean wave direction was 101°.

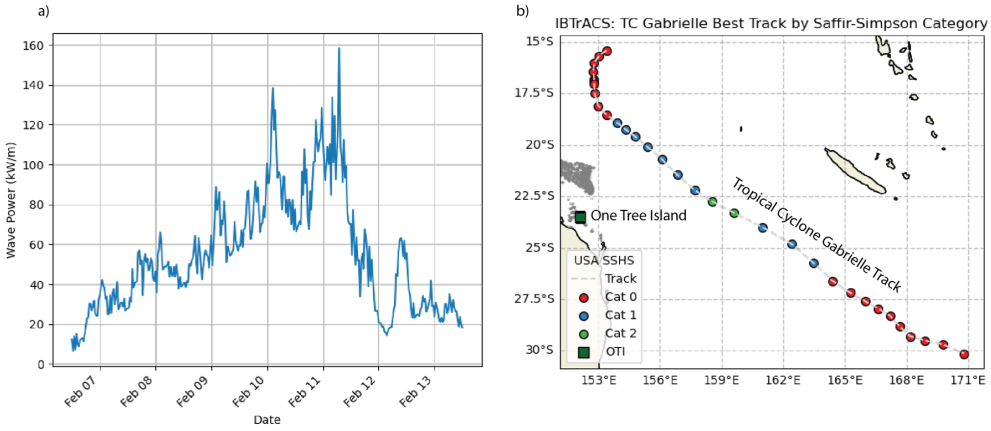

Figure 3: **(a)** TC Gabrielle produced a sustained H_s greater than the 95th percentile of wave heights (2.4 m, Figure 2 a, S1) for 2 consecutive days. **(b)** The track of TC Gabrielle through the Coral Sea from 08/02/2023 to 11/02/2023 and the Saffir-Simpson category, and location of OTR (green box).

3.1.2 Nearshore wave analysis

Mean wave conditions on the inshore instruments were modified by tidal water levels. At instrument P1, on the upper forereef slope (Figure 1), mean H_s at P1 was 1.3 m with mean peak bottom orbital velocity ($\overline{U}_{(s,\text{peak})}$), Eq. 4.11) of 0.75 m/s and a maximum of 1.7 m/s occurring during Tropical Cyclone Gabrielle (Figure 4 c). At this site there was a mean bed shear stress ($\overline{\tau}_b$) of 3.7 N/m^2, and a maximum of 14 N/m^2 (Figure 4 d). Near bed orbital velocities exceeded the guide for sediment motion ($U_{s,peak} = 0.3\ m/s$) for 95.6% of the record. At instrument A1, mean H_s was 1.2 m with $\overline{U}_{(s,\text{peak})}$ of 0.5 m/s and a maximum of 1.3 m/s occurring during Tropical Cyclone Gabrielle (Figure 4 c). At this site, $\overline{\tau}_b$ was 2.0 N/m^2, with a maximum of 9.3 N/m^2 (Figure 4 d). Here, near bed orbital velocities exceeded the guide for sediment motion $U_{s,peak} = 0.3\ m/s$) for 77.4% of the record. These values are comparable to observations in SaG on the southern shore of Molokai, Hawaii, where North Pacific winter waves generated high shear stresses ($\overline{\tau}_b > 1.5\ N/m^2$) (Storlazzi et al. 2003).

We identify high and low tidal peaks in the water surface elevation record to divide the timeseries and average over all observations that fall within each criterion. Mean water depths for high tides were +0.75 and -0.75 m below mean sea level for low tides. We also consider two high and low wave energy events (Offshore $H_s <$ 0.5 and $H_s >$ 2.4, Section 3.1.1, Figure 2 a).

Incident wave height had the greatest control over both U_s and τ_b (Figure 5 b, d). During the high energy event (Figure 5 c), $\overline{U}_{(s,\text{peak})}$, was 0.8 m/s and during the low wave energy event $\overline{U}_{(s,\text{peak})}$ was 0.16 m/s (Figure 5 b). Similarly, ranged from 6.8 N/m^2 during the high energy event, and 0.56 N/m^2 during the low energy event (Figure 5 b).

$\overline{U}_{(s,\text{peak})}$, was greatest during the high wave event led by TC Gabrielle passage and was the only time where the guide for coral colony dislodgement ($U_s = 1.3\ m/s$) was exceeded. Importantly, this value may be greater for robust coral morphologies of

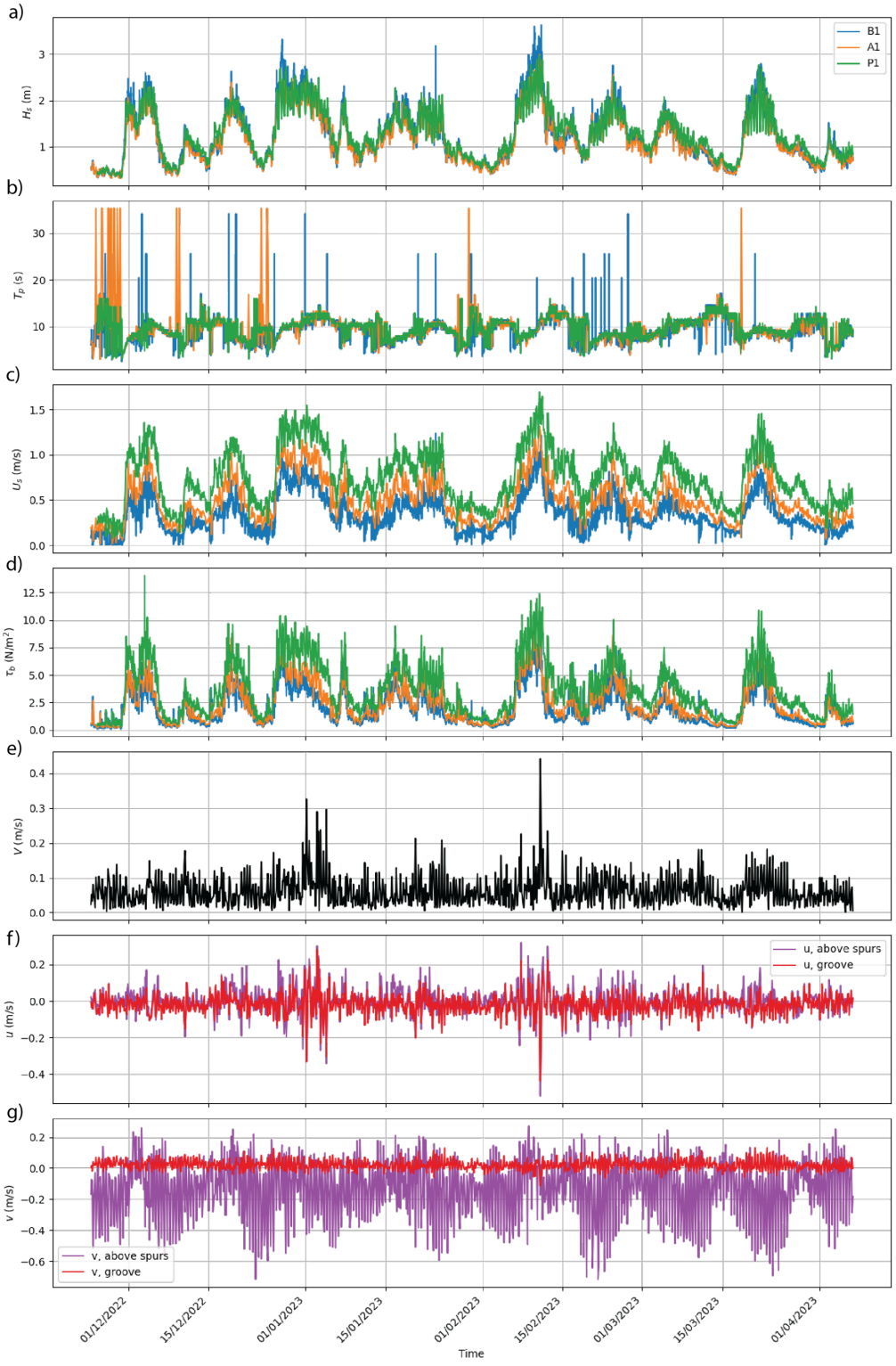

Figure 4: Timeseries of measured and computed variables **(a)** Significant wave height (H_s), **(b)** Peak wave period (T_p), **(c)** Near bed orbital velocity U_s, **(d)** Bed shear ($\overline{\tau}_b$), **(e)** Depth averaged current velocity (V), **(f)** depth averaged cross-shore flow velocity (u), measured at instrument A1 (Figure 1) for depth bins above the spur height (purple) and inside the groove (red), and g) depth averaged alongshore flow velocity (v), measured at instrument A1 (Figure 1) for depth bins above the spur height (purple) and inside the groove (red).

the forereef slope and represents a lower bound for dislodgement (Deng et al. 2025). This value was not exceeded at any of the other more offshore instruments.

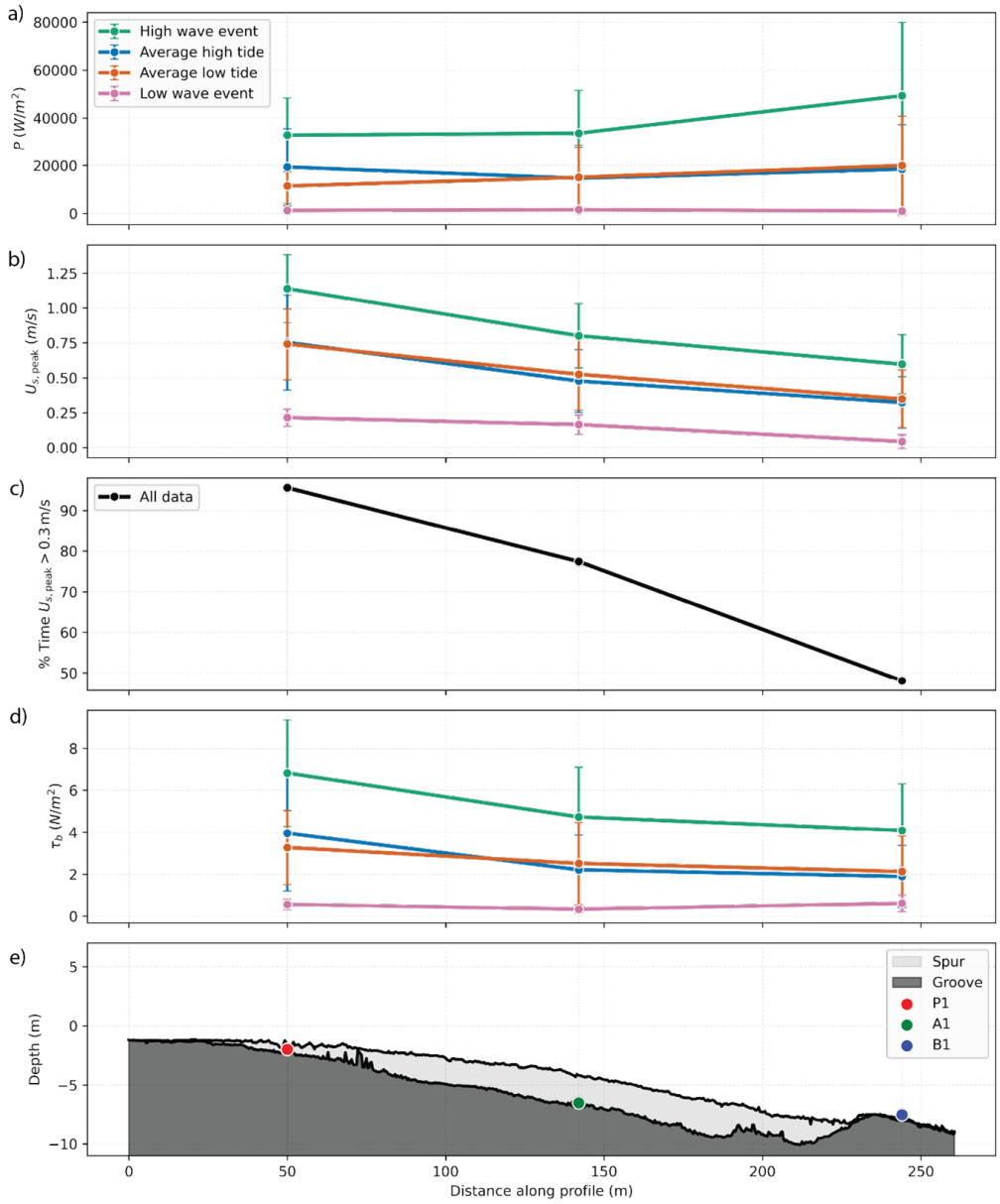

Figure 5: **(a)** Mean wave power, **(b)** peak near-bed orbital velocities ($U_{s,\text{peak}}$), **(c)** percentage of time $U_{s,\text{peak}}$ >0.3 m/s, and **(d)** bed shear stress (τ_b) at instrument locations along the spur and groove profile. Values are averaged across high-energy (green) and low-energy (purple) wave conditions, and across high tides (blue) and low tides (orange) (see Figure 2 for event identification and timeseries). **(e)** Cross-shore SaG morphology showing instrument locations. Vertical grey dashed lines indicate instrument positions across all subplots.

3.2 Current analysis

Persistent alongshore flows were observed throughout the deployment period, driven predominantly by tides. While tidal phase modulated the magnitude of the alongshore flow, the direction remained towards the south throughout the deployment

(Figure 6), likely due to regional tidal asymmetry. Alongshore velocities were strongest near the surface (0.4 m/s during high tide) and decreased with depth, reaching near-zero at a mean elevation of 2.4 m above the groove bed (Figure6). This elevation coincided with the mean height of adjacent spurs (2.8 m), indicating that the spur crest acts as an obstacle, creating flow separation in the grooves below. Analysis of the dimensionless ratio $|u|/V$, where $|u|$ is the absolute value of cross-shore velocity and $|V| = (u^2 + v^2)$ is the total velocity magnitude, revealed that currents were predominantly cross-shore directed inside the groove ($|u|/V$>0.5 for 81.3% of the record within the groove), despite alongshore flows dominating at depths greater than the spur height ($|u|/V$>0.5 for 25.8% of the record). This persistent reorientation of flow suggests that, despite the dominance of alongshore velocities in the upper water column (above the spurs height), near-bed circulation in the groove remains strongly aligned with groove axes. Under high-energy conditions, cross-shore flow became increasingly dominant from the surface to the top of spurs. When H_s exceeded 1.5 m, the vertically averaged ratio $\overline{(|u|)/V}$ exceeded 0.5, indicating a regime shift towards wave-driven cross-shore circulation (Figure 8). These conditions occurred during 31.6% of the observational period at instrument A1, highlighting the frequency and potential geomorphic significance of high-energy events. Under low energy conditions alongshore currents were dominant over cross shore flows (Figure 7), and it was found that for this site, the transition from alongshore dominant flows to cross-shore occurred where $H_s > 1.5$ m at instrument A1 (Figure 7), which occurred for 13% of the record.

3.3 Morphological analysis

The SaG zone is characterised by long, regularly spaced grooves, which slope seaward at a mean angle of 2.5°, intersecting an alongshore ridge at 11–13 m depth and producing abrupt elevation changes of up to 2 m (Figure 1). In contrast, adjacent spurs slope more gently at an average of 1.8°, consistent with observations from other high-energy reef systems (e.g., sartori2024). The mean groove direction in the survey area (Figure 1 d) was 93 (std =4.77) coinciding with the mean wave direction of 101° (std = 17°, Figure 2 d). Quantitative analysis of SaG morphology across nine cross-shore profiles (Figure 8) revealed systematic patterns in spur height (h_{spur}), wavelength (γ), and shape asymmetry (skew).

All metrics showed spatial variation across the forereef, with notably higher values observed at mid-slope positions. Spur height (h_{spur}, Figure 8 a) varied substantially across profiles, ranging from a mean of 0.95 m in the shallowest profile (6 m isobath) to a maximum of 2.15 m (8 m isobath) (Figure 8 a). Profiles at 7 to 10 m isobaths, located across the middle portion of the reef slope, consistently exhibited spur heights exceeding 1.7 m, while spur heights decreased toward the uppermost (6 m isobath) and lowermost (13 m isobath) profiles. The overall mean spur height across all profiles was 1.6 m, indicating that vertical relief was most strongly developed in the central reef zone. Mean spur skew (Eq. 4.4, Figure 8 c) was 0.06, indicating that spurs are near-symmetrical across the entire forereef, however this differed with depth. Profiles from the 7th to 10th isobath had negative skew, notably, the profile at the 9 m isobath, coinciding with the location of instrument A1 (Figure 8 d) had significant negative skew (Figure 8 c, Skew = -0.26) indicating a consistent trend of north-leaning spurs. Conversely, deeper spurs (profiles at 11,

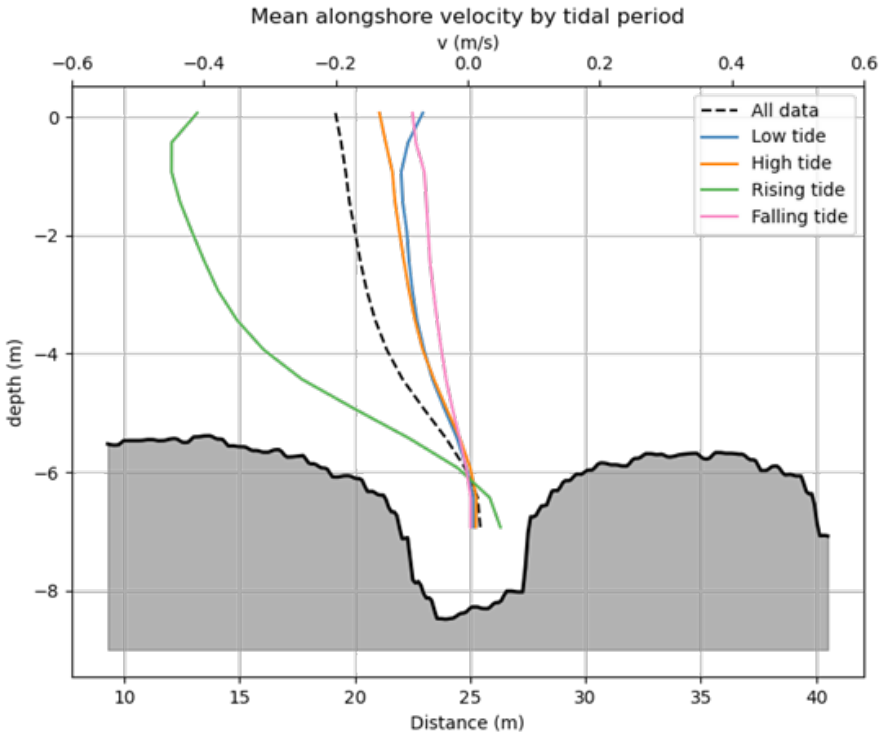

Figure 6: Mean alongshore current velocities by tidal phase for the entire six-month deployment (top x-axis) and alongshore SaG morphology (black line and grey infill). Alongshore currents were tidally controlled but always directed southward (negative values). Flow velocity (top x-axis) is greatest during rising tides (green line) but remains southward (negative values) for high tides (orange line) and low tide (blue line). Southward tidal currents are weakest during falling tides (pink line).

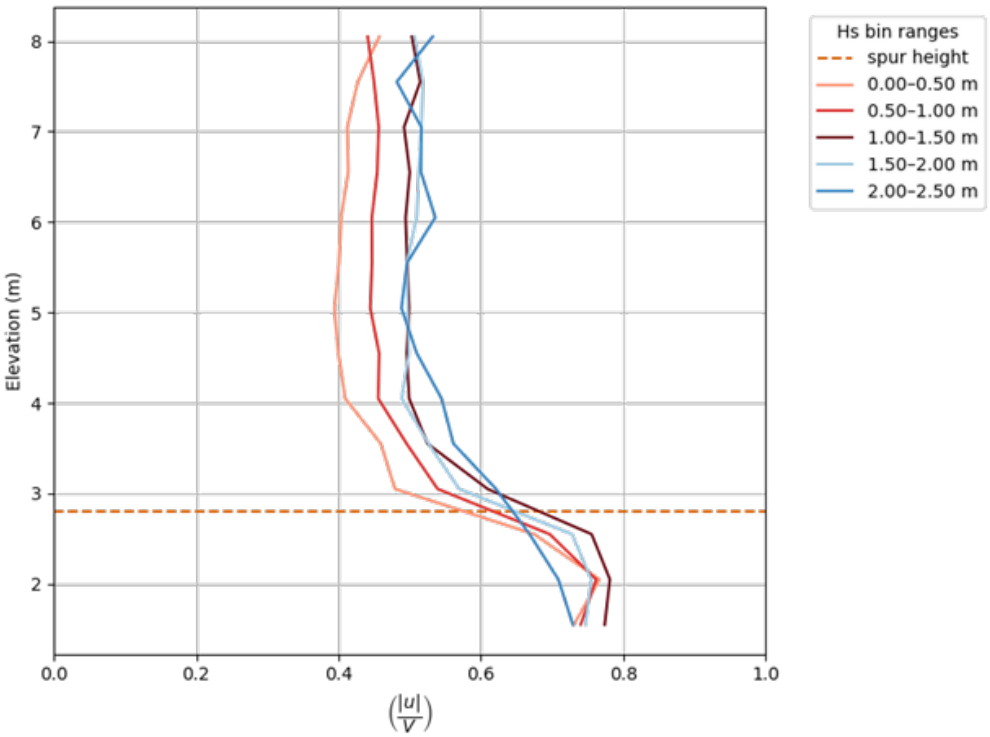

Figure 7: Strong alongshore tidally modulated currents dominated the forereef flows ($|u|/V$<0.5) for low significant wave heights ($H_s < 1.5$ m, shaded in red) but became cross-shore dominated ($|u|/V$>0.5), for larger significant wave heights ($H_s > 1.5$ m, shaded in blue). Notably, currents in the groove were always cross-shore.

12 and 13 m isobaths) had positive skew, indicating that slopes lean southwards. This suggesting that spur shape may be influenced by alongshore sediment transport processes or asymmetries in flow dynamics at shallower depths.

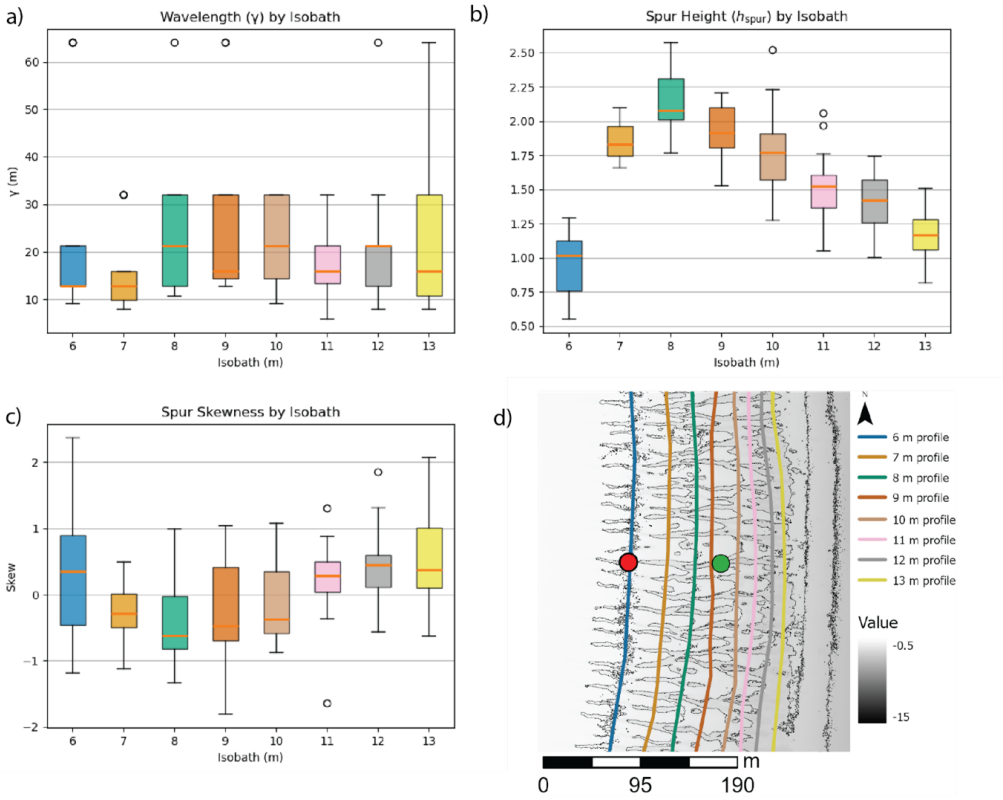

Figure 8: **(a)** Spur height (h_{spur}), **(b)** SaG wavelength (γ), **(c)** spur skewness and **(d)** subsection of the nine 500 m isobaths showing the complex bathymetry of the SaG formation in this zone.

4 Discussion

4.1 Do observed forereef hydrodynamics support existing conceptual models of spur and groove formation?

This study presents new observations of forereef current patterns which are useful to the assessment of models of spur and groove (SaG) development. Observations over a six-month period of velocity profiles on SaG show that above the spurs, mean currents were predominantly alongshore and tidally driven, and almost entirely unidirectional, running north to south. These currents were strongest during rising tides (Figure 6). Since Munk and Sargent (1954), most studies consider SaG characteristic of cross-shore wave dominated environments (da Silva et al. 2020; Rogers et al. 2013), including our own (Perris et al. 2024), where we only consider cross-shore wave driven flow on our process-based modelling. In the present study, however, there is evidence of alongshore currents having an influence on the SaG morphology development and evolution at this site. Spur structures at the location of measurement of alongshore currents (Figure 1 d) was asymmetrical (mean skew = -0.26, Figure 8 c) at the 7th to 10th Isobar, coinciding with the location of current measurements

(A1, Figure 1 d), Here, the current-facing spur wall was steeper on average than the leeward-current spur wall, meaning that the alongshore profile of the spurs typically leans toward the tidal current. This novel approach warrants further investigation, as spurs outside the location of currents measurements showed positive skew (Figure 8 c). As identified by previous modelling studies (e.g. daSilva2020), alongshore currents may remove sediment from the spurs where these currents are more intense, and deposit them in the grooves where the alongshore current approaches zero, this hydrodynamic response to SaG morphology is observable in our findings (Figure 6, 7). At our study site, spur height was greatest at the location of instrument A1 ($\overline{h_{spur}}$ = 1.6 m, Figure 8 a) and greater spur heights have been proposed to avoid sedimentation effects and likely promote coral growth (Storlazzi et al. 2003). As other researchers have noted, high spurs are free of sediment (Sartori et al. 2024). This process may support SaG development, and a more thorough investigation of this process is pertinent for future modelling efforts aimed at understanding SaG formation mechanisms and coral rubble transport.

Our results support a mechanism for groove maintenance based on abrasion. Bed-level orbital velocities on the upper forereef were above 0.3 m/s for 95.6% of the deployment. While direct measurements of sediment were transport were not taken, we found that this exceeds our guide for rubble mobilisation (Kenyon et al. 2023b). Sediment movement through the grooves likely causes abrasion along the base and spur walls. This supports earlier suggestions that abrasion plays a key role in SaG maintenance (Hopley et al. 1983; Kan 1995; Storlazzi et al. 2003).

Coral dislodgement was less common. Near-bed velocities exceeded the 1.3 m/s guide for coral breakage (Deng et al. 2025) only during cyclone-generated wave events. This event occurred only once in the six-month deployment (Figure 2 a). Additionally, coral species on the spur walls are well adapted to high-energy environments and produce strong growth forms that resist breakage (Hughes et al. 2012; Kaandorp and Sloot 2001). This suggests that rubble movement, rather than direct flow, is the more likely cause of coral damage, if it is occurring on spur walls. Impacts from mobile rubble may prune corals on the spur walls (Madin et al. 2014). Our findings are consistent with earlier studies that suggest, even in high energy events, sediment motion maintains groove form, rather than direct wave force (Kobluk and Lysenko 1992).

4.2 How do forereef current regimes vary under high and low energy conditions?

High-energy events produced strong near-bed flow. During Tropical Cyclone Gabrielle, wave heights and near-bed velocities exceeded the guides for rubble movement (Figure 3). Sediment mobilisation likely occurred along the full groove length during this event (Figure 5 b). Similar responses to storm waves have been reported in the Caribbean (Blanchon and Jones 1997; Hubbard et al. 1992), Japan (Kan 1995), and Hawaii (Storlazzi et al. 2003).

Under low-energy conditions flow in the upper water column was alongshore. However, within the grooves, flow was topographically steered cross-shore (Figure 7). As SaG morphology is likely driven by cross shore flows (da Silva et al. 2020; Rogers et al. 2013), it is possible that this topographic steering results in a feedback mech-

anism that supports the formation and maintenance of SaG by realigning currents into a cross-shore direction, suggesting that under low energy conditions, SaG morphology control current directions which further support SaG development. This feedbacks between flow and form require further investigation and may help sustain SaG morphology. Our findings confirm that SaG morphology does not rely solely on wave-driven events. Instead, it may be supported by ongoing feedbacks driven by SaG morphology.

4.3 Are hydrodynamic conditions sufficient to maintain spur and groove morphology through sediment transport and coral growth suppression?

Our results show that present-day hydrodynamic conditions seem sufficient to maintain SaG morphology. Sediment mobility guides suggest that sediment is frequently in motion on the upper forereef. Under high-energy conditions, sediment mobility extends across the entire SaG zone (Figure 7 c) suggesting that high-energy conditions play a long-term role in SaG maintenance. While we could not resolve all secondary flows in this study, the observed patterns suggest that alongshore and topographically steered flows both contribute to sediment transport. These flows may play a larger role than previously thought, with the system appearing more sensitive to wave height than to water level. Therefore, changes in wave climate may have greater impacts than changes in water level. For example, grooves in this study terminate at 13 m depth (Figure 1, 9), and that coincides with the depth of the Pleistocene basement, which terminates at a depth of between 9 m and 20 m (Jell and Webb 2012). Grooves are also aligned with present-day wave conditions (Figure 2 d), supporting the idea that SaG systems in this study were formed under Holocene sea-level conditions, in contrast to deeper relict grooves which likely formed during periods of lower sea level (Blanchon and Jones 1997; Cloud Jr. 1959; Duce et al. 2016).

Overall, this study sheds light on several new insights on SaG hydrodynamics and evolution from field measurements, but there are various limitations that warrant consideration. First, the long-term nature of the deployment required a compromise in sampling resolution (Table 1), meaning that high-frequency events or instantaneous peaks in flow velocity may have been underestimated. Such short bursts of elevated hydrodynamic stress may be particularly relevant for understanding coral dislodgement, which is governed by peak rather than average forces (Deng et al. 2025; Madin and Connolly 2006). The preferential settlement of coral larvae was not considered in this analysis, and as others have mentioned (Storlazzi et al. 2003), this may play an important role in the emergence of SaG on forereefs. Future studies may combine our findings with a model of preferential settlement of corals to further elucidate their influence on SaG development and maintenance. Finally, our findings indicate that present-day hydrodynamic conditions remain sufficient to maintain SaG morphology through sediment motion leading to the suppression of coral colonisation in high-energy grooves. Sediment mobility was found to respond to changes in wave conditions, more than changes in tidal water level (Figure 5 b, d), suggesting that anticipated changes to future wave climates (Knutson et al. 2020) will modify SaG morphology.

5 Conclusion

This study presents new field-based evidence linking hydrodynamic processes to the formation and maintenance of spur and groove (SaG) morphology on a high-energy forereef. Over a six-month deployment, tidally driven alongshore currents dominated the water column 71.5% of the time, with persistent southward flow due to regional tidal asymmetry. These flows influenced alongshore spur shapes, producing steeper current-facing (north) spur walls. Yet near-bed currents within grooves were consistently cross-shore directed due to morphological control of the groove axis ($|u|/V>0.5$ for 80.8% of the record at 1.55 m above groove bed).

Our findings confirm that wave-induced processes, particularly during high-energy events, are the primary driver of SaG maintenance by cross-shore currents. When significant wave height (H_s) exceeded 1.5 m, conditions that occurred during 28.5% of the record, cross-shore flows ($|u|/V>0.5$) dominated the entire water column, enhancing sediment entrainment within grooves. These events coincided with near-bed orbital velocities and shear stresses sufficient to mobilise sediment and rubble, especially on the upper forereef. During a tropical cyclone, guides of sediment and coral rubble movement were exceeded across the full groove depth, suggesting episodic yet intense reworking.

Our findings contribute to the growing understanding of the complex feedbacks between reef morphology and hydrodynamics. We identify that alongshore tidal currents have a geomorphic imprint on SaG morphology causing spur asymmetry (mean skew = -0.26, Figure 8 b). We highlight the importance of wave-induced bed shear stress and orbital velocity as a driver of groove abrasion and sediment transport that help maintain SaG morphology. Our observations support an eco-morphodynamic model of SaG formation and maintenance through sediment mobility. Importantly, the sensitivity of these processes to tidal water level suggests that future sea level rise will alter the zone of effective sediment transport, potentially reshaping forereef morphology and affecting the resilience of reef systems to climatic change.

Acknowledgments Lachlan Perris was supported by an RTP scholarship from The University of Sydney and the research was partially funded by Australian Research Council (ARC) Future Fellowship (FT100100215), ARC Discovery Program (DP220101125), and Geoscience Australia funding through the Marine Studies Institute at The University of Sydney. The authors would like to thank the dive team, Amanda Sordes, Mathew Kosnik, field campaign team, Eleanor Mawson and Chris Dagger and One Tree Island research station managers, Ruby Holmes and Heinrich Breuer. One Tree Island Research Station is a facility of The University of Sydney. We acknowledge the cultural significance of the Southern Great Barrier Reef, where we conduct fieldwork, to the Tarebilang Bunda, Bailai, Gooreng Gooreng and Gurang Traditional Owners.

References

Bellwood, D. R., R. P. Streit, S. J. Brandl, and S. B. Tebbett (June 2019). "The meaning of the term 'function' in ecology: A coral reef perspective". In: *Functional Ecology* 33 (6), pp. 948–961. DOI: 10.1111/1365-2435.13265.

Blanchon, P. and B. Jones (1995). "Marine-Planation Terraces on the Shelf Around Grand Cayman: A Result of Stepped Holocene Sea-Level Rise". In: *Journal of Coastal Research* (December 1993), pp. 1–33.

– (1997). "Hurricane control on shelf-edge-reef architecture around Grand Cayman". In: *Sedimentology* 44 (3), pp. 479–506. DOI: 10.1046/j.1365-3091.1997.d01-32.x.

Cloud Jr., P. E. (1959). "Geology of Saipan, Mariana Islands, Part 4: Submarine topography and shoal-water ecology". In: *U. S. Geological Survey Professional Paper* (280-K), pp. 361–445.

da Silva, R. F., C. D. Storlazzi, J. S. Rogers, J. Reyns, and R. McCall (2020). "Modelling three-dimensional flow over spur-and-groove morphology". In: *Coral Reefs*. DOI: 10.1007/s00338-020-02011-8.

Deng, W., T. Kenyon, K. Eigeland, D. P. Callaghan, and T. E. Baldock (2025). "Structural and hydrodynamic modelling of the probability of breakage of branching and plate coral colonies". In: *Coastal Engineering* 195 (October 2024), p. 104647. DOI: 10.1016/j.coastaleng.2024.104647.

Duce, S., R. J. Mccarroll, B. Yiu, L. A. Perris, and J. M. Webster (2021). "Field measurements from contrasting reefs show spurs and grooves can dissipate more wave energy than the reef crest". In: *Earth and Space Science Open Archive ESSOAr* 413 (June), p. 108365. DOI: 10.1016/j.geomorph.2022.108365.

Duce, S., A. Vila-Concejo, R. J. McCarroll, B. Yiu, L. A. Perris, and J. M. Webster (Sept. 2022). "Field measurements show rough fore reefs with spurs and grooves can dissipate more wave energy than the reef crest". In: *Geomorphology* 413. DOI: 10.1016/j.geomorph.2022.108365.

Duce, S., B. Dechnik, J. M. Webster, Q. Hua, J. Sadler, G. E. Webb, L. Nothdurft, M. Salas-Saavedra, and A. Vila-Concejo (2020). "Mechanisms of spur and groove development and implications for reef platform evolution". In: *Quaternary Science Reviews* 231. DOI: 10.1016/j.quascirev.2019.106155.

Duce, S., A. Vila-Concejo, S. M. Hamylton, J. M. Webster, E. Bruce, and R. J. Beaman (2016). "A morphometric assessment and classification of coral reef spur and groove morphology". In: *Geomorphology* 265, pp. 68–83. DOI: 10.1016/j.geomorph.2016.04.018.

Duce, S., A. Vila-Concejo, S. Hamylton, E. Bruce, and J. M. Webster (2014). "Spur and groove distribution, morphology and relationship to relative wave exposure, Southern Great Barrier Reef, Australia". In: *Journal of Coastal Research* 70, pp. 115–120. DOI: 10.2112/si70-020.1.

Goreau, T. F. (1959). "The Ecology of Jamaican Coral Reefs I. Species Composition and Zonation". In: *Ecology* 40 (1), pp. 67–90. DOI: 10.2307/1929924.

Harmelin-Vivien, M. L. and P. Laboute (1986). "Catastrophic impact of hurricanes on atoll outer reef slopes in the Tuamotu (French Polynesia)". In: *Coral Reefs* 5 (2), pp. 55–62. DOI: 10.1007/BF00270353.

Harris, D. L., J. M. Webster, A. Vila-concejo, S. Duce, and J. X. Leon (2023). "Geomorphology Defining multi-scale surface roughness of a coral reef using a

high-resolution LiDAR digital elevation model". In: *Geomorphology* 439 (September 2022), p. 108852. DOI: 10.1016/j.geomorph.2023.108852.

Harris, D. L., A. Vila-Concejo, J. M. Webster, and H. E. Power (2015). "Spatial variations in wave transformation and sediment entrainment on a coral reef sand apron". In: *Marine Geology* 363, pp. 220–229. DOI: 10.1016/j.margeo.2015.02.010.

Hopley, D., A. M. Slocombe, F. Muir, and C. Grant (1983). "Nearshore Fringing Reefs in North Queensland". In: *Coral Reefs* 1, pp. 151–160.

Hubbard, D. K., K. M. Parsons, J. C. Bythell, and N. D. Walker (1992). "The effects of Hurricane Hugo on the reefs and associated environments of St. Croix, US Virgin Islands - a preliminary assessment". In: *Journal of Coastal Research, Special Issue* 8 (8), pp. 33–48.

Hughes, T. P., D. R. Bellwood, M. Card, J. B. C. Jackson, J. Kleypas, J. M. Lough, P. Marshall, S. R. Palumbi, J. M. Pandolfi, B. Rosen, and J. Roughgarden (2003). "Climate change, Human impacts, and the Resilience of coral reefs". In: *Science* 301 (5635), pp. 877–1000.

Hughes, T. P., A. H. Baird, E. A. Dinsdale, N. A. Moltschaniwskyj, M. S. Pratchett, J. E. Tanner, and B. L. Willis (2012). "Assembly rules of reef corals are flexible along a steep climatic gradient". In: *Current Biology* 22 (8), pp. 736–741. DOI: 10.1016/j.cub.2012.02.068.

Jell, J. S. and G. E. Webb (2012). *Geology of Heron Island and Adjacent Reefs, Great Barrier Reef, Australia*. Tech. rep., p. 110.

Kaandorp, J. A. and P. M. Sloot (2001). "Morphological models of radiate accretive growth and the influence of hydrodynamics". In: *Journal of Theoretical Biology* 209 (3), pp. 257–274. DOI: 10.1006/jtbi.2001.2261.

Kan, H. (1995). "Typhoon Effects on Sediment Movement on Reef Edges and Reef Slopes". In: *Recent Advances in Marine Science and Technology*, pp. 191–201.

Kench, P. S. (1998). *A currents of removal approach for interpreting carbonate sedimentary processes*. Tech. rep., pp. 197–323.

Kenyon, T. M., C. Doropoulos, K. Wolfe, G. E. Webb, S. Dove, D. Harris, and P. J. Mumby (2023a). "Coral rubble dynamics in the Anthropocene and implications for reef recovery". In: *Limnology and Oceanography* 68 (1), pp. 110–147. DOI: 10.1002/lno.12254.

Kenyon, T. M., D. Harris, T. Baldock, D. Callaghan, C. Doropoulos, G. Webb, S. P. Newman, and P. J. Mumby (2023b). "Mobilisation thresholds for coral rubble and consequences for windows of reef recovery". In: *Biogeosciences* 20 (20), pp. 4339–4357. DOI: 10.5194/bg-20-4339-2023.

Kinsela, M. A., B. D. Morris, T. C. Ingleton, T. B. Doyle, M. D. Sutherland, N. E. Doszpot, J. J. Miller, S. F. Holtznagel, M. D. Harley, and D. J. Hanslow (2024). "Nearshore wave buoy data from southeastern Australia for coastal research and management". In: *Scientific Data* 11 (1), pp. 1–22. DOI: 10.1038/s41597-023-02865-x.

Knutson, T., S. J. Camargo, J. C. Chan, K. Emanuel, C. H. Ho, J. Kossin, M. Mohapatra, M. Satoh, M. Sugi, K. Walsh, and L. Wu (2020). "Tropical cyclones and climate change assessment". In: *Bulletin of the American Meteorological Society* 100 (10), pp. 1987–2007. DOI: 10.1175/BAMS-D-18-0189.1.

Kobluk, D. R. and M. A. Lysenko (1992). "Storm Features on a Southern Caribean Fringing Coral Reef". In: *Society of Sedimentary Geology: Research Letters* 7, pp. 213–221.

Kruk, M. C., K. R. Knapp, and D. H. Levinson (2010). "A technique for combining global tropical cyclone best track data". In: *Journal of Atmospheric and Oceanic Technology* 27 (4), pp. 680–692. DOI: 10.1175/2009JTECHA1267.1.

Krumbein, W. C. (1941). "Measurement and Geological Significance of Shape and Roundness of Sedimentary Particles". In: *SEPM Journal of Sedimentary Research* Vol. 11. DOI: 10.1306/D42690F3-2B26-11D7-8648000102C1865D.

Leung, S. K. and P. J. Mumby (2024). "Mapping the susceptibility of reefs to rubble accumulation across the Great Barrier Reef". In: *Environmental Monitoring and Assessment* 196 (2). DOI: 10.1007/s10661-024-12344-4.

Longuet-Higgins, M. S. (1952). "On the Statistical Distribution of the Wave Heights of Sea Waves". In: *Journal of Marine Research* 11.

Madin, J. S., A. H. Baird, M. Dornelas, and S. R. Connolly (2014). "Mechanical vulnerability explains size-dependent mortality of reef corals". In: *Ecology Letters* 17 (8), pp. 1008–1015. DOI: 10.1111/ele.12306.

Madin, J. S. and S. R. Connolly (2006). "Ecological consequences of major hydrodynamic disturbances on coral reefs". In: *Nature Letters* 444 (7118), pp. 477–480. DOI: 10.1038/nature05328.

Marmorino, G. (2022). "Investigation of Turbulent Tidal Flow in a Coral Reef Channel Using Multi-Look WorldView-2 Satellite Imagery". In: *Remote Sensing* 14 (3). DOI: 10.3390/rs14030783.

Munk, W. H. and M. C. Sargent (1954). "Bikini and nearby atolls, Marshall Islands; oceanography (physical) : Adjustment of Bikini atoll to ocean waves". In: *USGS Numbered Series* 260-B,C,D, pp. 275–280.

Nielsen, P. (1992). *Coastal bottom boundary layers and sediment transport*. World Scientific.

Perris, L., T. Salles, T. E. Fellowes, S. Duce, J. Webster, and A. Vila-Concejo (2024). "The Influence of Coral Reef Spur and Groove Morphology on Wave Energy Dissipation in Contrasting Reef Environments". In: *Journal of Geophysical Research: Earth Surface* 129 (8), pp. 1–17. DOI: 10.1029/2023JF007424.

Perris, L., T. Salles, T. E. Fellowes, A. P. D. Silva, S. Duce, J. M. Webster, A. M. Thompson, and A. Vila-Concejo (Jan. 2026). "Current flow in low-energy coral forereef spurs and grooves". In: *Geomorphology* 493. DOI: 10.1016/j.geomorph.2025.110072.

Perry, C. T., G. N. Murphy, N. A. Graham, S. K. Wilson, F. A. Januchowski-Hartley, and H. K. East (Dec. 2015). "Remote coral reefs can sustain high growth potential and may match future sea-level trends". In: *Scientific Reports* 5. DOI: 10.1038/srep18289.

Rogers, J. S., S. G. Monismith, F. Feddersen, and C. D. Storlazzi (2013). "Hydrodynamics of spur and groove formations on a coral reef". In: *Journal of Geophysical Research: Oceans* 118 (6), pp. 3059–3073. DOI: 10.1002/jgrc.20225.

Rogers, J. S., S. G. Monismith, R. B. Dunbar, and D. Koweek (2015). "Field observations of wave-driven circulation over spur and groove formations on a coral reef". In: *Journal of Geophysical Research: Oceans* (1), pp. 145–160. DOI: 10.1002/2014JC010464.Received.

Sartori, G., E. L. Boles, S. G. Monismith, R. B. Dunbar, P. J. Mumby, A. Khrizman, and R. Capozzi (2024). "Morphologically driven sedimentation patterns on a coral reef". In: *Coral Reefs*. DOI: 10.1007/s00338-025-02629-6.

Shinn, E. A. (1976). "Coral reef recovery in Florida and the Persian Gulf". In: *Environmental Geology* 1 (4), pp. 241–254. DOI: 10.1007/BF02407510.

Srokosz, M. A. and M. S. Longuet-Higgins (1986). "On the skewness of sea-surface elevation". In: *Journal of Fluid Mechanics* 164 (9), pp. 487–497. DOI: 10.1017/S0022112086002653.

Storlazzi, C. D., J. B. Logan, and M. E. Field (2003). "Quantitative morphology of a fringing reef tract from high-resolution laser bathymetry: Southern Molokai, Hawaii". In: *Bulletin of the Geological Society of America* 115 (11), pp. 1344–1355. DOI: 10.1130/B25200.1.

Torres-Garcia, L. M., P. S. Dalyander, J. W. Long, D. G. Zawada, K. K. Yates, C. Moore, and M. Olabarrieta (2018). "Hydrodynamics and Sediment Mobility Processes Over a Degraded Senile Coral Reef". In: *Journal of Geophysical Research: Oceans* 123 (10), pp. 7053–7066. DOI: 10.1029/2018JC013892.

Tracey, J. I., H. S. Ladd, and J. Hoffmeister (1948). "Reefs of Bikini, Marshall Islands". In: *Bulletin of the Geological Society of America* 59 (l), pp. 861–878.

Weeks, S. J., A. Bakun, C. R. Steinberg, R. Brinkman, and O. Hoegh-Guldberg (2010). "The Capricorn Eddy: A prominent driver of the ecology and future of the southern Great Barrier Reef". In: *Coral Reefs* 29 (4), pp. 975–985. DOI: 10.1007/s00338-010-0644-z.

Wolanski, E. and M. J. Kingsford (2024). *Oceanographic Processes of Coral Reefs*. Ed. by E, W. and Kingsford, M. Taylor & Francis Group. DOI: 10.1201/9781003320425.

Woodroffe, C. D. and J. Webster (2014). *Coral reefs and sea-level change*. DOI: 10.1016/j.margeo.2013.12.006.

5 | General Discussion

Chapters 2, 3 and 4 of this thesis correspond to published or submitted scientific papers, as such, each chapter presents a well-developed discussion on their specific objectives. The general discussion presented in this chapter synthesises the overall findings of the thesis to evaluate the relationship between spur and groove (SaG) morphology and reef hydrodynamics. While avoiding repetition from the scientific papers, it highlights how SaG enhance wave energy dissipation, and, in turn, how hydrodynamic processes influence the development and persistence of SaG morphology. The general discussion considers the limitations of this research and outlines directions for future work, with particular attention to the implications of changing hydrodynamic regimes under projected climate change scenarios.

1 Wave energy dissipation

This thesis demonstrates that SaG morphology significantly enhances wave energy dissipation on reef slopes through both bed friction and wave breaking. Models of wave propagation over the high-resolution seabed morphology showed that spur length and groove sinuosity influence the balance between frictional and breaking dissipation, with exposed-to-wave-energy SaG morphotypes exhibiting the highest frictional dissipation, while shorter grooves enhanced wave breaking (Chapter 2, Fig. 9). These findings are broadly consistent with dissipation values reported elsewhere on SaG forereefs in the Pacific and Caribbean (Péquignet et al. 2011 Monismith et al. 2013). Importantly, the model results in Chapter 2 take this further, suggesting that forereefs without SaG dissipate 40% less energy than those with SaG, highlighting the role of SaG morphological complexity in mediating wave transformation.

Chapter 4 shows that rubble is mobilised in the upper groove under low energy conditions, and that coral breakage or dislodgement may occur under high energy conditions, particularly during a Tropical Cyclone (TC Gabrielle in February 2023). Comparing to Chapter 2 findings – that decreased bed friction increases wave breaking forces at the reef crest (Chapter 2, Fig. 5) – it is assumed that forereef morphology down slope is improving dissipation and decreasing the impact of high energy events on coral breakage or dislodgement on the upper forereef. Similar observations have been made on coral reefs in the Pacific (Monismith et al. 2015), the Caribbean (Lugo-Fernández et al. 1998) and by others at OTR (Duce et al. 2021), whereby dissipation by bed friction across the forereef is far greater than by breaking on the reef crest. Consequently, SaG morphology is critical to the levels of wave energy dissipation on forereefs required to support reef growth. These results collectively

suggest that dissipation processes, and their influence on sediment and rubble dynamics, are fundamental to the persistence of SaG systems under contrasting wave regimes.

2 Current regimes and reef development

The combined results from this thesis provide new insights into the processes that form and maintain SaG structures. Chapter 2 shows that hydrodynamic behaviour differs across established SaG morphological classes, supporting the utility of morphotype classifications in interpreting reef hydrodynamics. Chapter 3 presents the first field evidence of a long-and-protected groove under modal low-energy wave conditions, where lagoon outflow generates consistent offshore currents. These findings support the constructional model of SaG development proposed by Duce et al. (2020), in which lagoonal flushing sustains offshore-directed flows that drive spur elongation.

In contrast, Chapter 4 examined an exposed-to-wave-energy groove where frequent sediment mobility and cyclone-driven reworking. Here, the hydrodynamic observations support the hypothesis that rubble abrasion and transport likely sustain groove incision. Cyclone generated wave conditions can move large volumes of rubble across forereefs (Kan 1995; Maragos et al. 1973). This rubble may impact spur walls and remove corals during high-energy events. The 6-month dataset also indicates that constructive processes may operate during periods of lower energy, allowing coral accretion and rubble stabilisation between disturbance events. While constructive models of SaG formation have been proposed (Kan 1995; Ladd 1961; Shinn et al. 1982), others have proposed erosion or construction based on regional differences in sea level curves (Gischler 2010), our results suggest a mixed model in which erosional and constructional mechanisms jointly contribute to the persistence of the same SaG system.

One of the most unexpected findings of this thesis is that both wave exposed and wave protected SaG were characterised by strong alongshore tidal currents. In Chapter 4, it is demonstrated that these currents influenced spur asymmetry, with spurs slightly leaning toward the prevailing current direction. Hence, it possible to infer that alongshore flows may contribute indirectly to SaG morphology by grooming spurs, clearing suspended sediments, and maintaining light availability for coral growth, such findings were also interpreted from modelling results of da Silva et al. (2020). The importance of alongshore currents in parallel channels in saltmarshes has been established (Zhou et al. 2024), and further investigations should be undertaken in SaG. For example, SaG may interact with oscillatory wave motions to generate eddies that increase sediment suspension and abrasion within grooves (da Silva et al. 2020). Such interactions could enhance sediment transport and play a secondary role in groove maintenance.

Finally, the observations of large wave events in Chapter 4 emphasise the importance of event-driven processes. Bed currents during storms were shore-normal, supporting the hypothesis that SaG incision is facilitated by high-energy events. However, modal conditions remain critical: under low energy the conditions would be conducive for spurs to accrete vertically, and tidal currents could promote coral

growth, while under high energy, growth rates on spurs are reduced (Gischler 2010) and grooves are maintained by sediment abrasion. As such, spurs may be growth features under low energy conditions, similar to our findings in Chapter 3, that are maintained by the movement of sediment along the grooves (Hopley et al. 2009). The persistence of SaG morphology across both sites suggests that constructive and erosive mechanisms are not mutually exclusive but instead operate over complementary temporal scales.

3 Climate Change

Thermal inversions in the water column identified in Chapter 3 highlight the importance of linking forereef morphology to processes occurring across the broader reef platform. Lagoon waters, which can be isolated from the open ocean due to tidal truncation, heat and cool more rapidly than offshore waters. Despite being warmer, their elevated salinity increases water density, causing them to flow as bottom currents (Chapter 3, Fig. 9). As a result, corals along the reef edge can be exposed to anomalously warm bottom flows spilling over the reef margin during low tide. These findings suggest that lagoon–ocean exchanges may exert a stronger influence on forereef communities than previously recognised.

The research presented in Chapter 2 highlights the importance of monitoring this exchange. Projected increases in ocean warming (Castillo et al. 2012; De'Ath et al. 2012; Hughes et al. 2018) and shifts in wave climate (Knutson et al. 2020) are expected to alter the frequency and magnitude of thermal inversions. Lagoon–seawater exchanges are primarily driven by wave set-up and wave pumping across the platform (Callaghan et al., 2006). However, regional wave modelling studies indicate a potential reduction in wave energy across the Australian tropics (Meucci et al. 2020) and fewer extreme wave events (Knutson et al. 2020). Ocean warming, combined with reduced wave-driven flushing may increase both salinity and thermal contrasts between lagoonal and oceanic waters, potentially intensifying thermal inversions and exposing forereef corals to greater thermal stress.

These processes interact with sea level rise , which is likely to shift the active SaG maintenance zone upslope (Chapter 2, Fig. 6). Results from Chapter 4 suggest that SaG maintenance decreases with depth, raising concerns for the persistence of these morphologies on deeper reef slopes. Whether platform reefs can sustain their protective function under future conditions will depend on whether corals can continue to keep pace with rising sea level, while simultaneously coping with climate change driven stresses.

The combined results of this thesis highlight that spur-and-groove morphology can emerge and persist under a wide range of hydrodynamic conditions. In low-energy settings, constructional processes associated with lagoon outflow support spur extension, while in high-energy environments, abrasion during storms maintains groove incision. Alongshore currents, although not primary drivers, may influence spur shape and sediment suspension. Together, these findings suggest that SaG formation is best explained by a combination of processes that vary with wave climate, reef setting, and timescale. Importantly, both erosive and constructive pathways contribute to the resilience of spur-and-groove systems, ensuring their persistence

under diverse and changing energy regimes.

4 Future Directions

This thesis provides innovative hydrodynamic modelling and the most comprehensive waves and currents datasets from SaG systems to date. In developing these methodologies, several future directions for research emerged from both the findings and limitations of this thesis. Firstly, the numerical models in Chapter 2 were based on the most accurate evaluations of relevant hydrodynamic and morphological changes anticipated from local and global scale human impacts (Chapter 2, Table 3). However, the morphological and hydrodynamic changes were not coupled in the model. As these systems operate in dynamic feedback, future research should develop coupled morphodynamic models to better predict the influence of SaG morphology on wave energy dissipation in future reef states.

In Chapter 3, this thesis advanced the field measurement of spur-and-groove (SaG) hydrodynamics on the Great Barrier Reef, providing some of the first direct current observations within grooves. These results establish a foundation for understanding the role of SaG morphology in regulating flow under typical wave and tidal conditions. Chapter 4 extended this by capturing hydrodynamic responses during extreme wave events, highlighting their importance for sediment transport and reef accretion. Building on these findings, future research should prioritise longer-term monitoring that spans a broader range of conditions, including extreme events, and incorporate direct sediment measurements such as traps on the reef flat to more robustly link flow dynamics to the processes of SaG construction. This thesis has shown that SaG can exist in areas with strong alongshore conditions, and that contrasts with most previous studies where only across-shore processes were considered. Future research should investigate the role, if any, that alongshore currents have in SaG formation and maintenance.

Finally, the findings of this thesis have direct relevance for the design of nature-based coastal protection strategies. This research shows that SaG morphology increases wave energy dissipation and reduces wave transmission at the reef crest. It also demonstrates that SaG can develop and persist across a wide range of hydrodynamic conditions, from low- to high-energy settings, including environments with strong alongshore currents and obliquely incident waves. Nature-based solutions for coastal defence have been proposed across broad ecological settings, yet coral reefs currently account for only 4% of such project (Paxton et al. 2024). Current coral restoration programmes (e.g., coral farming) rarely target moderate to high-energy reef environments. Restoration efforts typically focus on low-energy settings where stable conditions and high light availability support coral survival and growth (Harrison and Wallace 1990), and where the risk of physical damage to structures is reduced. Many projects are also designed primarily to enhance tourism and biodiversity rather than to improve wave attenuation and coastal protection (Boakes et al. 2022; Darkhal et al. 2025; McLeod et al. 2022; Scott et al. 2024).

The results presented here suggest that incorporating high-energy reef environments with well-developed SaG into restoration and management strategies could expand the protective capacity of nature-based defences. Recent developments in outplant-

ing mature corals may assist in overcoming the vulnerability of younger or smaller corals to the impact of wave energy (Cook et al. 2022; McLeod et al. 2022). Further developments to coral restoration in higher energy reef areas will have considerable benefits, as corals in SaG environments grow rapidly and contribute to wave energy dissipation, their restoration could yield both ecological and coastal protection benefits. Furthermore, as demonstrated in this thesis, changes to forereef morphology will have cascading effects on the wider reef system, reinforcing the need to integrate hydrodynamic and geomorphic considerations into future nature-based coastal defence planning.

6 | Conclusion

Across contrasting energy settings, spur and groove (SaG) morphology strongly structures forereef-slope hydrodynamics and thus wave energy dissipation, sediment motion, and morphological persistence. Using numerical models constrained by high-resolution LiDAR bathymetry and in situ observations, this thesis demonstrates that (i) SaG markedly enhance dissipation compared to forereefs with no SaG; (ii) future climate forcing shifts dissipation mechanisms and increases wave transmission; (iii) low-energy SaG connect dynamically to lagoonal circulation supporting a constructive mechanism of SaG formation through offshore elongation; and (iv) in high-energy settings, wave events periodically exceed mobility thresholds while morphology steers the vertical distribution of alongshore versus cross-shore flow. Overall, the thesis demonstrates that present-day conditions are sufficient to sustain SaG through erosional and constructional processes, although active maintenance is likely confined to the shallow areas and sensitive to sea-level rise.

1. Assess how different SaG morphotypes influence wave attenuation across contrasting reef settings.
    - The presence of SaG substantially increase wave dissipation: forereefs without SaG dissipate 40% less wave energy than those with SaG.
    - Dissipation varies by morphotype: exposed-to-wave-energy morphotypes are most effective; deep-and-disconnected grooves contribute less, especially under sea-level rise and reduced bed friction.
    - Realistic bathymetry is required to capture variations in SaG morphology including groove sinuosity, which increases wave energy dissipation.
2. Evaluate the impact of climate change on SaG wave energy dissipation and reef hydrodynamics. Under high emissions, bed-friction dissipation drops to roughly half its present-day potential, while breaking-related dissipation increases.
    - The net effect of climate change results in reduced total wave dissipation and greater wave transmission at the reef crest, elevating hydrodynamic exposure where once sheltered backreef environments may become dominated by wave breaking.
3. Assess the connectivity of SaG with the broader reef platform-scale circulation.
    - Overall, low-energy SaG exhibit offshore-directed groove currents up to 2 m/s throughout the tide. This is linked with continuous lagoonal outflow caused by windward setup.

- These flows imply capacity for sediment transport and seaward spur elongation and highlight the hydrodynamic connectivity between the forereef slope and the lagoon.

4. Evaluate the frequency, intensity, and directionality of flow events that contribute to sediment transport and SaG maintenance.

    - Alongshore tidal currents dominated the water column for 71.5% of the six months record. Alongshore currents were persistently southward from regional tidal asymmetry. Cross-shore currents were restricted to the grooves near the bed.

    - During high-energy events (including tropical cyclone Gabrielle, Feb 2023), flows on the entire water column became cross-shore, orbital velocities and bed shear stresses exceeded sediment-mobility thresholds, reworking coral rubble - particularly on the upper slope - and supporting wave-driven SaG maintenance.

5. Establish links between the geological timescale of SaG formation with the hydrodynamic timescale.

    - Consistent mean offshore flow through grooves in low energy settings supports constructive SaG formation through offshore elongation. On high-energy SaG, event-scale exceedance of sediment transport thresholds connect short-term forcing to longer-term morphological development. Both findings support geological evidence of the accretionary nature of SaG in low-energy conditions and their erosive nature in high-energy conditions.

6. Determine whether present-day hydrodynamic conditions are sufficient to sustain SaG morphology.

    - Contemporary conditions are adequate to sustain SaG via both erosional and constructional processes, but active maintenance observed to concentrate within the SaG zone, with diminished energy at depth limiting offshore formation.

    - In high energy settings, sediment is frequently mobilised in the upper forereef causing abrasion of the groove bed. High energy wave events mobilise sediment at the offshore extend of the SaG. Consequently, SaG formation is sensitive to wave climate and the frequency of large wave events.

    - Alongshore currents provide a consistent and asymmetrical impact on the studied SaG. These currents are dominant under low wave energy conditions and may assist in removing coral rubble from spurs and depositing it in grooves, a process that supports the self-organisation of SaG by promoting coral growth on spurs and prohibiting coral growth in grooves.

In summary, these statements reaffirm that SaG morphology is both a driver and a product of forereef slope hydrodynamics, central to present coastal protection and sensitive to future climate forcing. By employing novel methodologies, this

thesis demonstrates the efficacy of geomorphological approaches in understanding complex feedback on coral forereefs. Finally, this thesis situates the morphology of SaG within the context of the broader reef structure, with implications for reef health and the capacity of coral reef systems to sustain ecological goods and services, elucidating key knowledge gaps in the hydrodynamic and morphological responses of understudied reef zones to oceanic forcing.

1 Appendix A

1.1 Supplementary material for Chapter 4

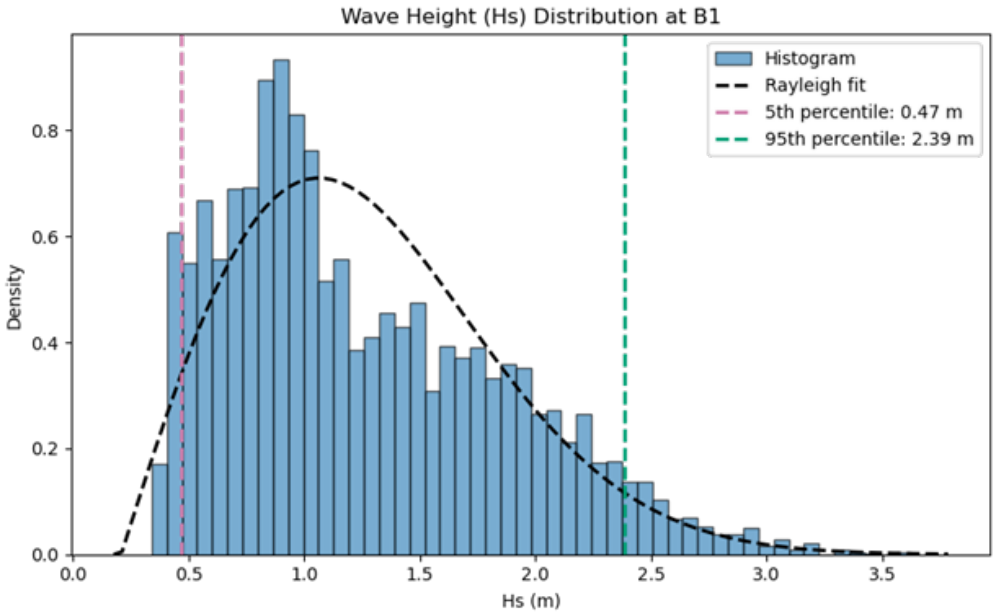

Figure S1: Distribution of significant wave height (H_s) recorded at One Tree Island between November 2022 and June 2024. The histogram is fitted with a Rayleigh distribution curve. Dashed lines indicate the 5th (0.47 m) and 95th (2.39 m) percentiles.

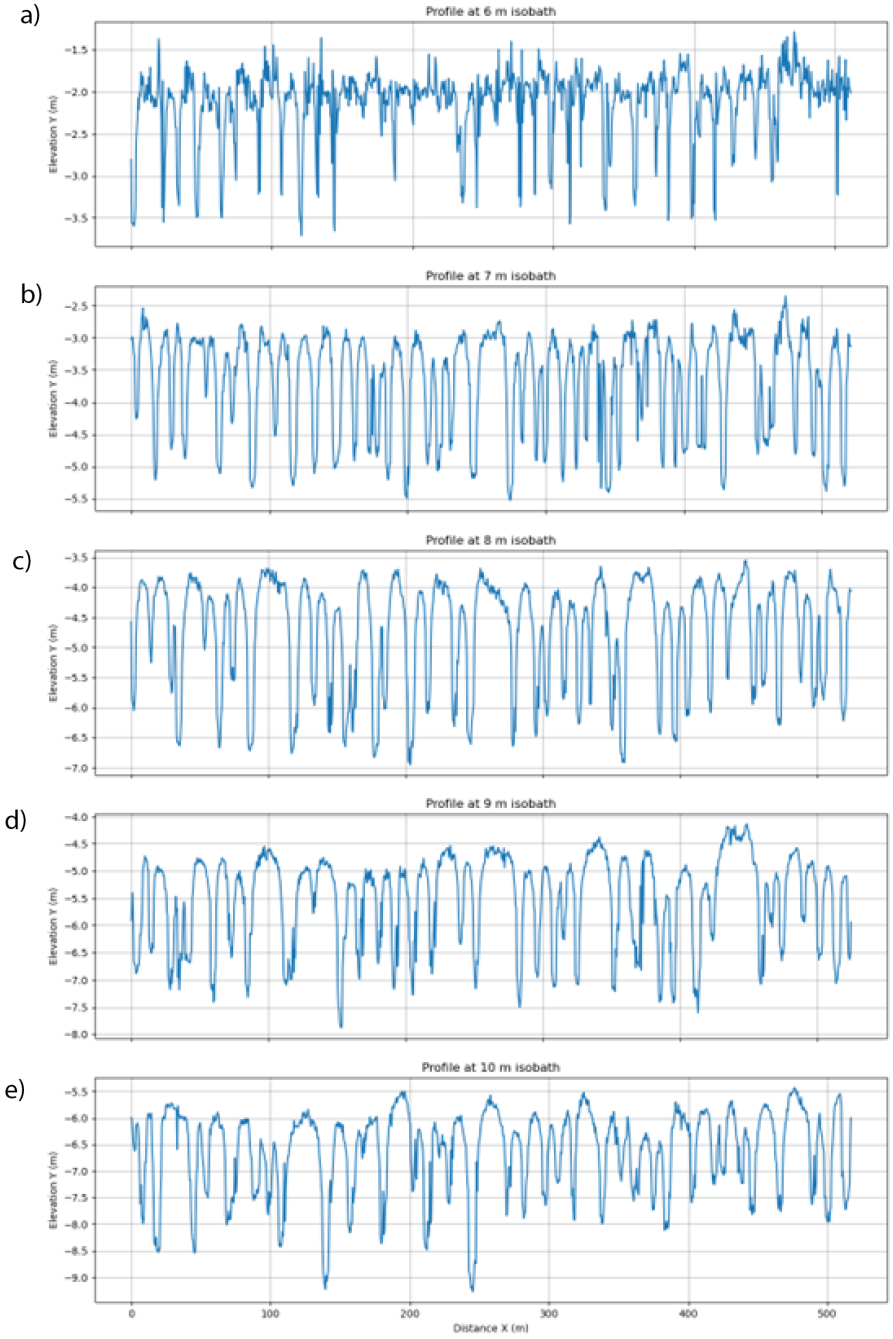

Figure S2: Bathymetry profiles at 6–10 m isobaths. Each plot shows elevation Y (m) against distance X (m), sampled every 0.5 m from LiDAR derived bathymetry of One Tree Reef. Lines are the raw (unsmoothed) data. The meter-scale undulations and spur and groove features. Differences in the height of the spurs and wavelength can be seen across isobaths.

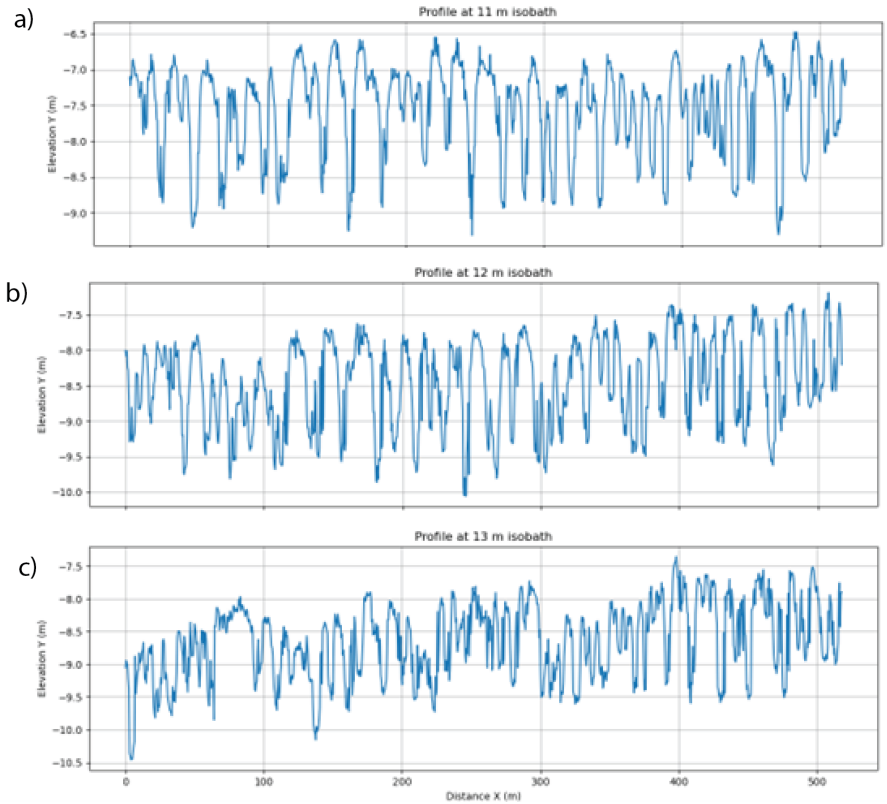

Figure S3: Bathymetry profiles at 10–13 m isobaths. Each plot shows elevation Y (m) against distance X (m), sampled every 0.5 m from LiDAR derived bathymetry of One Tree Reef. Lines are the raw (unsmoothed) data. The meter-scale undulations and spur and groove features. Differences in the height of the spurs and wavelength can be seen across isobaths.

Appendix B (Part I)| Field measurements from contrasting reefs show spurs and grooves can dissipate more wave energy than the reef crest

Duce, S., Vila-Conejo, A., Mccarroll, R. J., Yiu, B., Perris, L. A., Webster, J. M. (2021). Field measurements from contrasting reefs show spurs and grooves can dissipate more wave energy than the reef crest. *Earth and Space Science Open Archive ESSOAr*, 413(June), 108365. https://doi.org/10.1016/j.geomorph.2022.108365

Geomorphology 413 (2022) 108365

Contents lists available at ScienceDirect

Geomorphology

journal homepage: www.journals.elsevier.com/geomorphology

Field measurements show rough fore reefs with spurs and grooves can dissipate more wave energy than the reef crest

S. Duce [a,b], A. Vila-Concejo [b,*], R.J. McCarroll [b,c], B. Yiu [d], L.A. Perris [b], J.M. Webster [b]

[a] College of Science and Engineering, James Cook University, Bebegu Yumba Campus, Townsville, Queensland 4811, Australia
[b] Geocoastal Research Group, School of Geosciences, University of Sydney, Sydney, New South Wales 2006, Australia
[c] Department Environment, Land, Water and Planning, East Melbourne, Victoria, Australia
[d] Field Sampling & Testing, Sydney Water, 51 Hermitage Road, West Ryde, NSW 2114, Australia

ARTICLE INFO

Keywords:
Coral reef hydrodynamics
Wave energy dissipation
Spurs and grooves
Great Barrier Reef

ABSTRACT

Coral reefs are widely recognized as effective dissipaters of wave energy. Spurs and grooves (SAG) are common features of fore reefs worldwide and are thought to be particularly efficient at dissipating wave energy. However, very few studies have collected in-situ hydrodynamic data to verify this and understand SAG interactions with hydrodynamic forces. We present in-situ wave data from contrasting SAG sites at Moorea, French Polynesia, and One Tree Reef in the southern Great Barrier Reef, Australia. We measured high rates of wave energy dissipation (up to 0.1 kW/m^2) across the SAG zone. Interestingly, under the modal conditions measured, the SAG zones often dissipated wave energy at higher rates than the adjacent reef crest/flat zone. Rates of dissipation were the greatest at sites with high live coral cover in mesotidal environments (i.e., One Tree Reef sites), suggesting the structural complexity of live corals may increase bed friction and that tidal currents may also contribute to dissipation. Correlations between measured dissipation, wave height and depth allowed us to suggest that the SAG zone dissipates more energy under high wave conditions at low tides, while the reef crest/flat dissipates more energy at high tides under small wave conditions. Further study is required to better understand and model the hydrodynamics of SAG zones and the important role they play in reef dynamics and coastal protection.

1. Introduction

Waves can be a major hydrodynamic force acting on coral reefs and are a crucial driving factor in the formation, growth, and persistence of coral reefs across all spatial and temporal scales (Harris et al., 2015; Storlazzi et al., 2005). Reef hydrodynamics control the transport and deposition of spawn, larvae and recruits, the provision of nutrients, removal of wastes and the production and transport of biogenic sediments to form the reef and associated features such as reef islands (Masselink et al., 2020). Coral reefs have long been recognized as providing effective wave energy dissipation and protecting coastlines (e.g. Munk and Sargent, 1948). The value of reefs as natural breakwater systems has become particularly important with growing threats from rising sea levels and increased storm activity (e.g. Acevedo-Ramirez et al., 2021; Beck et al., 2018; Ferrario et al., 2014; Foley et al., 2014; Gallop et al., 2014; Van Zanten et al., 2014; Vila-Concejo et al., 2017; Woodhead et al., 2019).

Numerical modelling of wave dissipation across coral reefs has become a relatively common tool to inform coastal management and predict the likely effects of sea level rise (Baldock et al., 2019; Baldock et al., 2020; Bramante et al., 2020; Harris et al., 2018). Accurate and high-resolution field data are required to calibrate and validate numerical models and optimize their utility (e.g., Horstman et al., 2014; Storlazzi et al., 2011). However, the remote location of many coral reefs makes access difficult, and it is challenging to deploy instruments particularly in the high-energy fore reef zone. Nevertheless, field observations in fore reef environments are necessary to examine dissipation under complex natural conditions and to understand sediment production and transport in biogenic coral reef systems.

The majority of existing studies detailing wave dissipation by coral reefs measure dissipation across reef flats (e.g. Brander et al., 2004; Hardy and Young, 1996; Harris and Vila-Concejo, 2013; Harris et al., 2015; Huang et al., 2012; Kench and Brander, 2006) and around reef islands (e.g. Beetham and Kench, 2014; Kench et al., 2009; Mandlier, 2013; Samosorn and Woodroffe, 2008) or in model canopy arrays or flume experiments (e.g. Lowe et al., 2005a; Lowe et al., 2007; Buckley

* Corresponding author.
E-mail address: ana.vilaconcejo@sydney.edu.au (A. Vila-Concejo).

https://doi.org/10.1016/j.geomorph.2022.108365
Received 31 August 2021; Received in revised form 27 May 2022; Accepted 29 June 2022
Available online 5 July 2022

et al., 2016). Given the complexity of instrument deployments on reefs, some studies have measured wave dissipation across the reef crest based on a single instrument on the fore reef and another on the reef flat behind the reef crest (e.g. Lowe et al., 2005b; Lugo-Fernández et al., 1998a; Lugo-Fernández et al., 1998b; Pomeroy et al., 2012; Cheriton et al., 2016). These studies provide robust evidence of coral reefs' ability to dissipate wave energy but do not provide adequate spatial resolution to differentiate wave dissipation occurring on the forereef from that of the reef crest and reef flat. Notable exceptions are Monismith et al. (2015), Monismith et al. (2013), Péquignet et al. (2011) and Storlazzi et al. (2004), where wave measurements included at least two fore reef locations. On the fore reef of Palmyra Atoll, Monismith et al. (2015) calculated the highest friction factor (1.8) measured at any reef, with approximately 20 % wave energy dissipation over just 56 m (i.e., 3.57 % over 10 m) and suggested that healthy coral cover facilitated efficient wave dissipation.

Spurs and grooves (SAG) are a common geomorphic feature of many forereefs worldwide and their origin and formation mechanisms have been the subject of some debate (e.g., Gischler, 2010). They are characterized by parallel ridges of carbonate material (spurs), separated by channels (grooves) which are usually aligned perpendicular to the reef crest. The features show considerable variations in morphology which are thought to be predominantly driven by the prevailing hydrodynamic energy (Duce et al., 2020; Duce et al., 2014; Storlazzi et al., 2003; Roberts, 1974). Useful studies modelling flow over SAGs have confirmed the interdependency between SAG morphology and hydrodynamics (Rogers et al., 2013; da Silva et al., 2020). However, very few studies have collected in-situ hydrodynamic data to quantify and explain the mechanics and spatial variability of wave energy dissipation by fore reef SAG.

To our knowledge wave hydrodynamics across SAGs have only been directly measured at six reefs worldwide; Grand Cayman Island in the Caribbean (Roberts et al., 1975), Molokai, Hawaii (Storlazzi et al., 2004), Ipan, Guam (Péquignet et al., 2011), Moorea in French Polynesia (Monismith et al., 2013), Palmyra Atoll in the central Pacific (Rogers et al., 2015), and Xahauyxol Reef in the Mexican Caribbean (Acevedo-Ramirez et al., 2021). At Grand Cayman, Roberts et al. (1975) found that bottom friction over the fore reef SAGs modified deep water waves and currents reducing wave heights by ~20 % (i.e., 0.5 % per 10 m) and current speeds by ~60–70 % over the ~400 m between the outer instrument (21 m depth) and inner instrument (8 m depth). Storlazzi et al. (2004) measured <0.1 % dissipation in wave power per 10 m for small waves (Hs < 0.4 m) across the SAG zone (between 4 and 10 m depth) at Molokai, Hawaii. Péquignet et al. (2011) measured a 17 % decline in wave energy flux during a tropical cyclone over 55 m (i.e., 3.1 % per 10 m) between sensors at 7.9 and 5.7 m depth on the fore reef SAGs at Ipan fringing reef in Guam and found that the majority of energy was dissipated by wave breaking in the surf zone. Monismith et al. (2013) measured a 25 % reduction in wave energy flux across the SAG zone at Moorea from 6 m depth to the edge of the surf zone at 3 m depth. Rogers et al. (2015) measured a slight decrease in wave height and increase in wave period across the 115 m between their deep fore reef instrument (19 m depth) and their spur and groove instruments (8.6 to 10.7 m depths) at Palmyra Atoll during relatively low energy conditions (average H_{rms} 0.5–0.6 m). They found very little alongshore variation in wave characteristics between neighbouring spurs and grooves. Acevedo-Ramirez et al. (2021) presented a remarkable dataset over large spurs and grooves and found a high rate of wave dissipation (up to 0.077 kW/m^2) with the dissipation rate over the spur up to three times higher than on the adjacent groove.

In this paper, we quantify the wave energy dissipation across different fore reef SAG zones and compare the relative importance of two mechanisms by which energy dissipation can occur (i.e., wave breaking at the reef crest versus bottom friction across the fore reef). This paper presents measurements at the inner and outer parts of the SAG zone at five sites on two contrasting reefs under different tidal and wave energy regimes. These sites are Moorea in French Polynesia and One Tree Reef in the southern Great Barrier Reef (GBR), Australia. Importantly, our data capture wave characteristics at the shallow, inner end (<4 m depth) of the SAG zones. Our data provide insight into the geomorphic role of SAGs and the possible influence of other variables including offshore wave height, water depth, spur and groove morphology, tidal currents and coral cover on energy dissipation.

2. Study sites

We undertook 10 field experiments, five at One Tree Reef in the southern GBR, Australia, and five at Moorea, French Polynesia. The field experiments were conducted at sites on each reef with different degrees of wave exposure (Figs. 1 and 2). Wave measurements were undertaken across the SAG zone of the fore reef and on the outer reef flat. Each site is

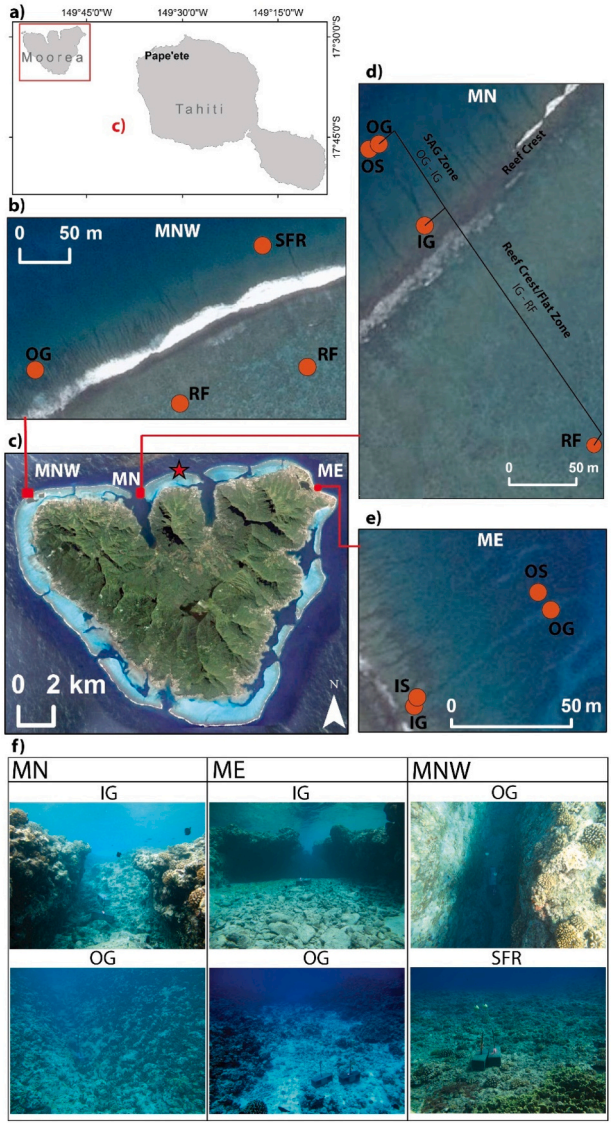

Fig. 1. The location of Moorea adjacent to Tahiti in the South Pacific Ocean (a). Panel (c) shows an overview of the island and location of the study sites where the star represents the location of the FOR01 wave mooring. Deployments at each study site are shown in, Moorea Northwest (MNW) (b); Moorea North (MN) (d) and Moorea East (ME) (e). The position of pressure sensors is shown and labelled IG (inner groove), OG (outer groove), OS (outer spur), IS (inner spur), SFR (smooth fore reef) and RF (reef flat). The two zones across which wave dissipation were calculated, the SAG zone and the reef crest/flat zone are labelled. Photographs of the deployment sites are shown (f).

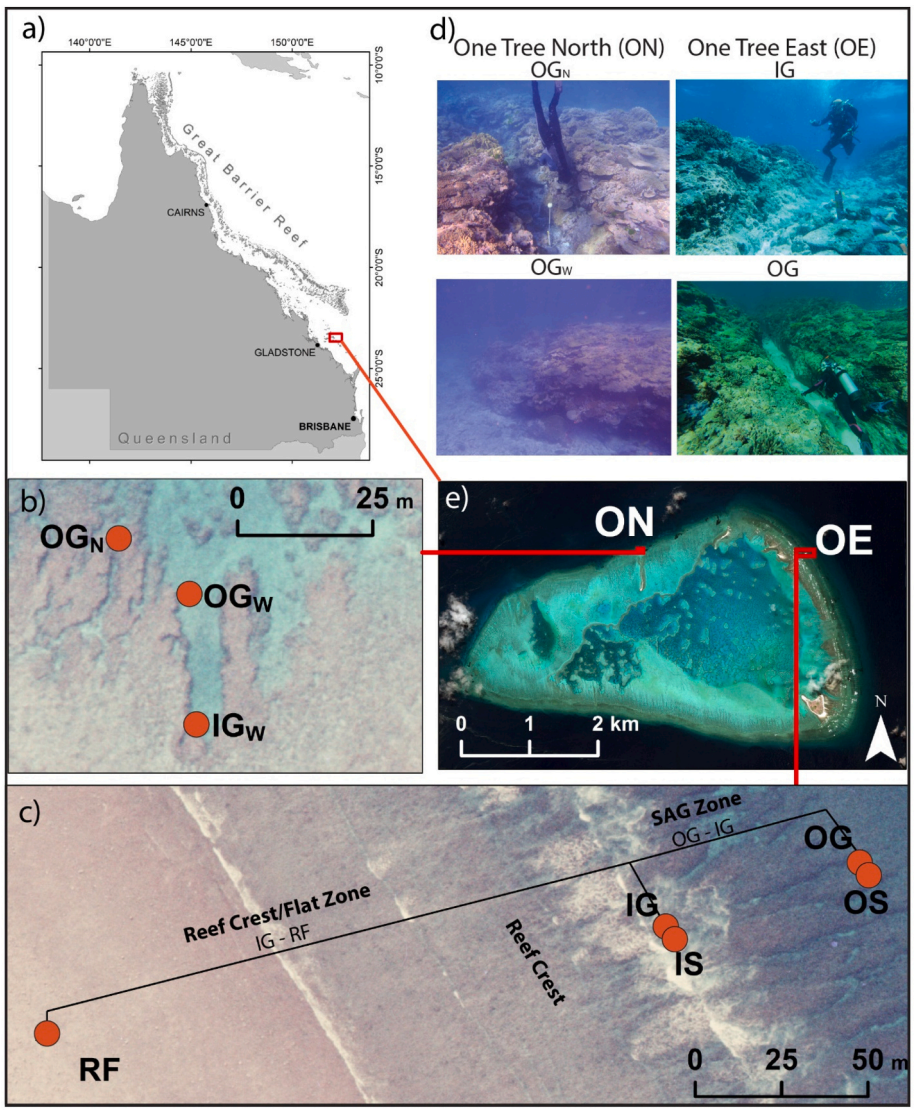

Fig. 2. Overview of One Tree Reef in the southern Great Barrier Reef (a) and the position of study sites around the reef (e). The position of pressure sensors at One Tree north (ON) (b) and One Tree east (OE) (c) are shown and labelled IG (inner groove), OG (outer groove), OS (outer spur), IS (inner spur) and RF (reef flat). The two zones across which wave dissipation were calculated, the SAG zone and the reef crest/flat zone are labelled. At ON (b) subscript $_N$ denotes narrow groove and $_W$ denotes wide groove. Photographs of the deployment sites are presented in (d).

described in detail in Supplementary Text S1-S5.

2.1. Moorea

Moorea (17°30′ S, 149°50′ W) is a high volcanic island in French Polynesia, in the central tropical South Pacific Ocean (Fig. 1). The island is surrounded by a barrier reef between 0.5 and 1 km from shore protecting an inshore lagoon (Leichter et al., 2012), with several passes connecting the inshore lagoon with the open ocean (Fig. 1b). SAGs are visible in satellite imagery around the entire forereef. Between 1 and 2 km offshore of the reef, water depths drop to >500 m (Leichter et al., 2013). Moorea is micro-tidal with a spring tidal range of 0.2 m (Hench et al., 2008). The dominant swell direction is from the southwest with significant wave heights between 1 and 2 m and seasonal oceanic swells from the north between October to April. Significant wave heights between 5 and 8 m, associated with storms and remotely generated swell, are not uncommon (Leichter et al., 2013). Waves are the dominant driver of currents over the reef crest as tides and wind-driven flows are relatively weak (Hench et al., 2008; Monismith et al., 2013).

Since the 1970s, Moorea reef has experienced a number of stressors in the form of recurrent bleaching events (Adjeroud et al., 2009), two major outbreaks of Crown-of-Thorns seastars (Trapon et al., 2011) and cyclones, particularly Cyclone Oli in 2010 (Etienne, 2012). These events caused coral cover on the fore reef to decline. By 2013, Scleractinian coral cover at Moorea fore reef (10 m depth) was approximately 20 % (Edmunds and Leichter, 2016).

2.2. One Tree Reef

One Tree Reef (OTR, 23°30′ S, 152°05′ E) is a lagoonal reef in the Capricorn-Bunker Group in the southern GBR (Hopley et al., 2007). The reef lies within a "Scientific Zone" of the GBR Marine Park, 80 km seaward of mainland Australia and hence has minimal anthropogenic influences. It is located only 20 km west of the edge of the continental shelf and is exposed to modal swell energy for most of the year (Frith and Mason, 1986). The average significant wave height is 1.54 m from a predominantly east southeasterly direction driven by trade winds (Talavera et al., 2021) with occasional tropical storms bringing higher energy wave conditions. The reef is mesotidal and has semidiurnal tides with a mean spring tidal range of 3 m (Vila-Concejo et al., 2014). The reef crest is mostly unbroken and the lagoon is isolated from swell and tides for approximately 5 h of each tidal cycle (Frith and Mason, 1986). There are high levels of live coral cover, particularly on the fore reef (Hamylton et al., 2013). SAGs are present around the entire fore reef with four distinct classes associated with the different levels of wave energy and antecedent topography (Duce et al., 2016, 2020). The

presence of a rubble cay on the southwest corner of the reef flat and several active rubble spits along the reef flats demonstrate active sediment transport from the forereef (Talavera et al., 2021; Bryson et al., 2016; Shannon et al., 2013).

3. Methods

3.1. Data collection

We deployed Aquistar INW PT2X pressure sensors at all sites, sampling continuously at 4 Hz to measure wave characteristics. The length of the deployments was typically short (<24 h) due to limited data storage in the instruments. The instruments were cable tied to purpose-

Table 1
Overview of the deployments at Moorea and One Tree reefs including the geomorphic characteristics of the site and the dates of each deployment. For further information on each site refer to S1-S5. (The following acronyms are used in this table: MN: Moorea North; ME: Moorea East; MNW: Moorea North West; OE: One Tree East; ON: One Tree North; IG: Inner Groove; OG: Outer Groove; RF: Reef Flat; IS: Inner Spur; OS: Outer Spur; SFR: Smooth fore reef; W: wide; N: narrow.)

Location	Deployment	Site	Depth (m)	Approx. width (m)	Approx. spur wall height (m)	Dist. from crest (m)	Dates	Site descriptions/comparisons
Moorea	Moorea North 1	MN1-IG	3.3	2	0.6	20	Aug to 9 Aug 2014	- Moderately exposed compared to other Moorea sites - SAG zone width ~100 m and gradient ~5° to a depth of ~12 m - Reef crest and flat submerged throughout the tidal cycle - Coral cover ~10–20 %
		MN1-OG	9.1	5	4	90		
		MN1-RF	1.9	–	–	180		
	Moorea North 2	MN2-IG	3.3	2	0.6	20	11 Aug 2014	- Bottom of grooves are bare or have large, rounded rubble grading to patches of coarse sand with depth
		MN2-OG	8.9	5	4	90		
		MN2-OS	4.7	20	4	90		
		MN2-RF	1.9	–	–	180		
	Moorea East 1	ME1-IG	3.8	4	1.5	15	19 Aug to 20 Aug 2014	- Least exposed of Moorea sites - SaG zone width ~100 m and gradient ~8° to a depth of ~16 m - Reef crest and flat submerged throughout the tidal cycle - Coral cover ~25 %
		ME1-IS	2.7	6	1.5	18		
		ME1-OS	7.0	20	3	85		
	Moorea East 2	ME2-IG	3.8	4	1.5	15	21 Aug 2014	- Bottom of grooves have large, rounded rubble grading to small angular rubble and sand with depth
		ME2-IS	2.7	6	1.5	18		
		ME2-OS	7.7	20	3	85		
	Moorea North West	MNW-OG	5.8	1.5	2.5	54	15 Aug to 16 Aug 2014	- Most exposed of Moorea sites (unable to deploy instruments at inner groove or on spur due to high energy waves breaking) - SaG zone width ~70 m and gradient ~6° to a depth of ~8 m - Reef crest and flat submerged throughout the tidal cycle - Coral cover ~40 %. - Bottom of grooves bare, with occasional large rounded coral boulders - A 150 m long area of smooth fore reef (SFR) between SAGS
		MNW-RF_{SAG}	1.1	–	–	50		
		MNW-SFR	3.6	–	–	56		
		MNW-RF_{SFR}	1.4	–	–	74		
One Tree	One Tree East	OE-IG	2.8	1.5	1	28	11 Oct to 13 Oct 2013	- Most exposed of One Tree sites - SAG zone width ~120 m with gradient of ~2° to a depth of 6 m - classified as “exposed to wave energy” (EWE) by Duce et al. (2016) - Reef crest and flat exposed and therefore disconnected from SAGs over low tides - Coral cover ~75 % - Bottom of grooves have large, smoothed rubble clasts transitioning to coarse rippled sand with depth
		OE-OG	5.4	2	2.5	88		
		OE-IS	1.9	7	1	28		
		OE-OS	2.5	10	2.5	88		
		OE-RF	0.6	–	–	156		
	One Tree North 1	ON1-IG_W	2.9	5.0	1.5	10	1 Dec 2014	- Least exposed of One Tree sites - SAG zone with ~200 m with gradient of ~4° to a depth of ~10 m - Outer groove narrow (OGN) classified as “short and protected” (SaP); neighbouring wide groove (IGW and OGW) classified as “long and protected” (LaP) by Duce et al. (2016)
		ON1-OG_W	2.9	8.5	2.0	34		
		ON1-OG_N	2.1	1.5	1.0	29		
	One Tree North 2	ON2-IG_W	3.0	5.0	1.5	10	2 Dec to 3 Dec 2014	- Reef crest and flat exposed and therefore disconnected from SAGs over low tides - -Coral cover ~85 % - Bottom of the narrow groove and the outer end of the wider groove have poorly sorted, angular coral rubble and little sediment. Inner end of the wide groove has sand with some angular rubble and occasional live corals.
		ON2-OG_W	3.2	8.5	2.0	34		
		ON2-OG_N	2.4	1.5	1.0	29		
	One Tree North 3	ON3-IG_W	3.5	5.0	1.5	10	5 Jan 2015	
		ON3-OG_W	3.6	8.5	2.0	34		
		ON3-OG_N	2.8	1.5	1.0	29		
	One Tree North 4	ON4-IG_W	3.5	5.0	1.5	10	7 Jan to 8 Jan 2015	
		ON4-OG_W	3.7	8.5	2.0	34		

built concrete blocks with protruding metal rods that were placed by SCUBA divers using lift bags. As shown by Duce et al. (2016, 2020), the same reef can support different SAG types, thus deployments were conducted at multiple sites on each reef to capture differing wave exposure regimes. Deployment locations included three sites on the forereef at Moorea – Moorea North West (MNW), Moorea North (MN) and Moorea East (ME) (Fig. 1); and two sites at One Tree Reef – One Tree East (OE) and One Tree North (ON) (Fig. 2). Detailed descriptions of each of these sites and the instrument deployment configuration are available in Table 1 and the supplementary materials (Supp. 1).

3.2. Data analysis

Spectral analysis of pressure sensor data was conducted using a Fourier transform algorithm for 15-minute intervals with 50 % overlap. The 15-minute interval allowed us to remove the tidal influence and assess for waves with periods up to 180 s (frequency 0.0055 Hz) and has been found to be appropriate at One Tree Reef (Harris et al., 2015). At Moorea previous studies revealed waves at the fore reef (our area of interest) to be dominated by gravity waves with significant wave periods up to 22 s (Hench et al., 2008; Monismith et al., 2013) thus, a 15-minute interval is also appropriate at this site. A Hanning window was applied with linear detrending. A dynamic pressure adjustment, based on Lee and Wang (1984), was performed to account for pressure attenuation with depth and convert the subsurface pressure record to surface waves. Significant wave height (H_s) and peak wave period (T_p) were calculated using spectral methods (Holthuijsen, 2010), taking wave power (energy flux), from linear wave theory, as

$$P = C_g E \tag{1}$$

with the group speed (C_g) determined for intermediate depths

$$C_g = \frac{c}{2}\left(1 + 2\frac{kh}{sinh2kh}\right) \tag{2}$$

where the wave number (k) and wave celerity (c) are derived using the dispersion relation, h is water depth, and wave energy density (E) is taken as

$$E = \frac{\rho g H_s^2}{8} \tag{3}$$

where ρ is sea-water density (1025 kg/m^3) and g is gravitational acceleration.

Given the considerable number of deployments (n = 10) and individual instrument records (n = 33) presented in this paper it is not practical to present the wave spectra or time series of wave parameters for each instrument here. Instead, and to allow for comparison, we made box plots showing the median, first and third quartile of H_s and P values recorded at each instrument during each deployment.

Rates of wave energy dissipation ($\in$) in kilowatts per square meter (kW/m^2) between outer and inner groove instruments (SAG zone) and between inner groove and reef flat instruments (reef crest/flat zone) were calculated using the following formula based on Monismith et al. (2015):

$$\in = \frac{\Delta P}{\Delta x} \tag{4}$$

where, ΔP is the change in wave power (kW/m) between the outer and inner instruments and Δx is the across reef distance in meters, between the two instruments. We chose to calculate dissipation rates in kW/m^2 for transparency and ease of comparison between sites and with other studies. Percent of total energy dissipated between instruments was calculated as ΔP divided by P at the outer groove instrument, multiplied by 100. Following the findings of Monismith et al. (2013), it was assumed that the direction of the incident wave field was perpendicular to groove orientation (indeed current data not presented here confirmed this to be the case, see Duce, 2017). For time series of $\in$, peak wave period is calculated using a moving 4-h average, to reduce noise. The effects of wave reflection were reported to be minimal at a similar forereef environment (Monismith et al., 2015) and therefore were not considered. This method assumes wave energy is dissipated at a uniform rate between the two instruments at which it was measured. While this is a reasonable assumption for unbroken waves on the fore reef SAG zone when dissipation is due to bottom friction alone, it does not hold when wave breaking occurs between two instruments. This is a limitation which must be considered particularly when interpreting the dissipation rates calculated across the reef crest/reef flat zone (IG-RF). Other processes such as refraction due to differential wave phase speeds on spurs versus grooves (e.g., Mandlier, 2013) and along-crest transport of wave energy may also influence wave height but fall beyond the scope of this analysis.

To assess whether wave breaking would have been a factor in dissipating wave energy between each instrument we defined the wave breaking parameter such that:

$$\gamma = H_{max}/h \tag{5}$$

where, H_{max} is double H_s and h is water depth. Published wave breaking parameters measured on coral fore reef environments vary from 0.83 (Rogers et al., 2016) to 0.98 (Monismith et al., 2013) up to 1.1 (Vetter et al., 2010). We chose a very conservative estimation (0.6) as we were interested in assessing the contribution of bottom friction to wave dissipation in the absence of breaking, thus we needed to be sure that waves would not have been breaking at our fore reef instruments.

4. Results

4.1. Wave conditions in the SAG zone

Measured mean H_s were relatively small (<1 m) during all deployments with wave conditions during each deployment varying across the SAG zone (Fig. 3). Spectral analysis revealed the dominant energy component to be the incident frequency band (3–25 s) for all deployments. Details of the offshore wind and wave conditions during all deployments are provided in the supplementary material (Supp. Figs. S1–S3). The conservative wave breaking parameter (0.6) was exceeded only at One Tree East during part of the first low tide. No other instruments showed wave breaking though it is assumed that breaking would have occurred at the reef crest between the inner SAG instruments and the reef flat instruments.

P was typically the greatest at the deepest and furthest seaward instruments (usually outer groove) for all deployments (Fig. 3). The largest waves (mean H_s = 0.86 m, P = 6.7 kW/m) were recorded at the outer groove at Moorea North West (Fig. 3e, o), followed by both spurs and grooves at One Tree East (Fig. 3f, p) and Moorea East deployment 2 (Fig. 3d, n). The smallest and least powerful waves for all deployments were recorded at the reef flat instruments. Regardless of wave height offshore, under modal conditions such as those recorded, virtually all power and height was dissipated by the time the waves reached the reef flat.

When comparing data from adjacent inner spur and inner groove instruments we found that at Moorea East H_s and P for both deployments were higher at the spur (P up to 4 kW/m) than the groove (P up to 3.1 kW/m, Fig. 3m, n), which could be related to increased shoaling over the spurs. Conversely, at One Tree East the inner groove had slightly higher H_s and P (3.2 kW/m) than the adjacent inner spur (2.6 kW/m) (Fig. 3p). These instruments were approximately 1 m shallower than at Moorea East (OE inner spur depth 1.9 m and groove 2.9 m vs 2.7 m and 3.8 m at ME) (Table 1), suggesting that as waves propagate further across the SAG zone, bottom friction influences waves at the spur more than the groove. At sites where we conducted more than one deployment (i.e.,

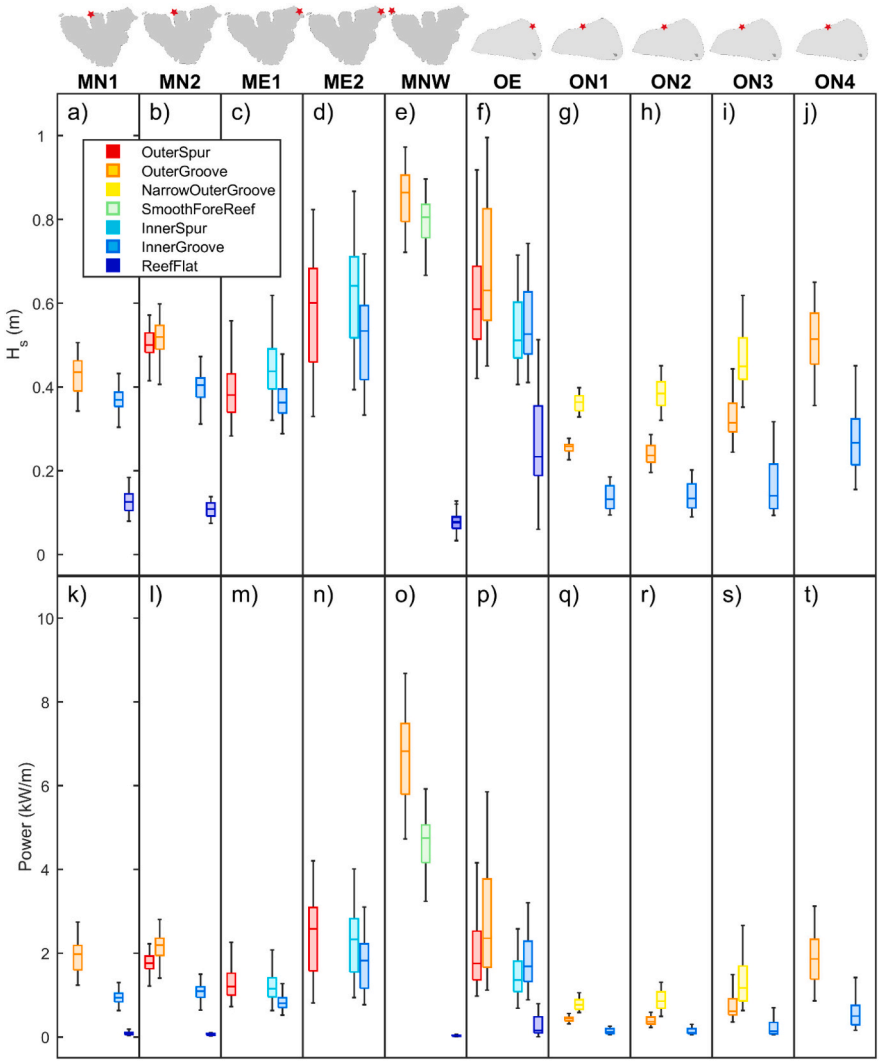

Fig. 3. Comparison of box plots showing the median, first and third quartile of H_s (a–j) and P (k–t) values recorded during each deployment as labelled across the top. Panels a) to e) and k) to o) are Moorea deployments while f) to j) and p) to t) are One Tree deployments. Boxes are arranged from outer to inner instrument (left to right) and the colour of each box plot denotes the location of the instrument as defined in the legend.

MN, ME and ON) despite changes in the magnitude of H_s and P the pattern of wave characteristics within the zone was consistent between deployments (e.g., at ME power was the highest at the outer spur, followed by the inner spur then the inner groove).

4.2. *Wave energy dissipation*

We found variation in dissipation rates both between and within deployments (Fig. 4). Here we present the wave dissipation across the SAG zone (between the outer and inner sensors in the SAGs) and compare that to the dissipation across the reef crest/flat zone from the inner SAG to the sensor on the reef flat. The dissipation rates across the SAG zone were higher at the One Tree sites (OE mean $\epsilon = 0.02$ kW/m^2; ON4 mean $\epsilon = 0.05$ kW/m^2) than the Moorea sites (MN1 mean $\epsilon = 0.01$ kW/m^2; MN2 mean $\epsilon = 0.02$ kW/m^2) (Fig. 4e–h). Interestingly, at both Moorea and One Tree, the rate of energy dissipation across the fore reef SAG zone was higher than across the reef crest/flat between the inner groove and the reef flat (Fig. 4e–g). The greatest difference was at Moorea North where the mean dissipation rate across the SAG zone (mean ϵ =0.01 kW/m^2) was 3.6 times higher than across the reef crest/flat zone (mean $\epsilon = 0.004$ kW/m^2).

Most of the time the percentage of energy dissipated across the SAG zone was greater than that dissipated across the reef crest from the inner groove to the reef flat (Fig. 4i–k). The maximum percentage of wave energy dissipated across the SAG zone was 86 % at One Tree North Deployment 4 (Fig. 4l) while the maximum dissipation across the reef crest was 75 % at One Tree East (Fig. 4k). Typically, the greatest percentage of energy dissipated by the SAG zone was during low tides with relatively high wave conditions.

Wave energy dissipation increased more notably with *Hs* across the SAG zone than across the reef crest (Fig. 5a–c), demonstrating the wave dissipation efficiency of this area of the fore reef. At Moorea North and One Tree East the percent dissipation across the SAG zone was positively correlated with *Hs* (Fig. 5e–g). Percent dissipation and *Hs* were negatively correlated at One Tree North (Fig. 5h). Across the SAG zone there is a negative correlation between percent dissipation and depth at all sites while across the reef crest from the inner groove to the reef flat it is positively correlated at Moorea North and negatively correlated at One Tree East (Fig. 5i–k).

We also compare the dissipation across a spur (from outer to inner sensor on the same spur) with the dissipation across the neighbouring groove (from the outer to the inner sensor in the same groove) with the assumption that changes due to alongshore variability in the wave field are small because the instruments were positioned very close together (Figs. 1e, 2c). One Tree East was the only site where direct comparison of dissipation across an adjacent spur and a groove was possible.

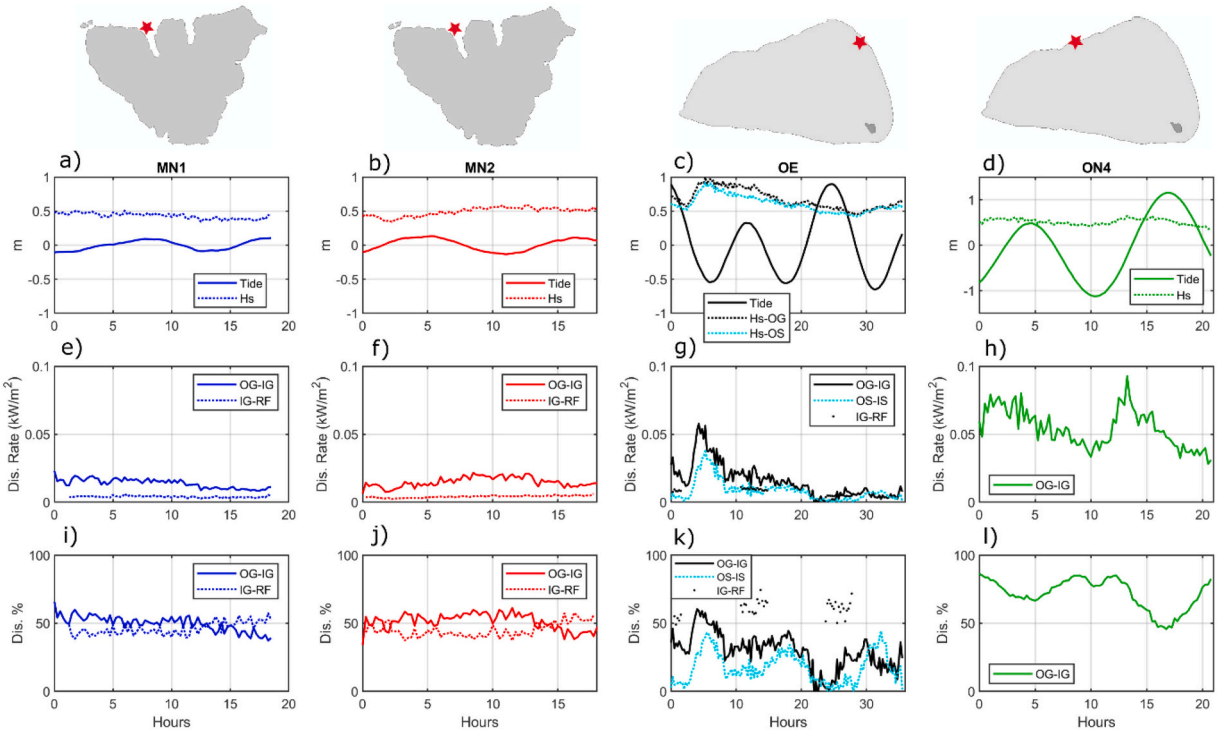

Fig. 4. Wave dissipation characteristics at Moorea North deployments 1 and 2 (MN1, MN2), One Tree East (OE) and One Tree North deployment 4 (ON4). Panels a) to d) show tidal stage and H_s at the outer instrument(s) in the array. The rates of wave power dissipation per meter across the SAG zone from the outer groove to the inner groove (OG – IG unbroken line) and across the reef crest from the inner groove to the reef flat (IG – RF dotted line) are shown in panels e) to h). Note that ON4 (h) does not have IG-RF as no instrument could be deployed on the reef flat. Panels i) to l) show the percentage of wave power dissipated across the SAG zone between the OG and IG (unbroken line) and across the reef crest from IG to RF (dotted line). The reef flat at OE is sub-aerially exposed over low tidal phases, therefore IG-RF calculations could only be made over high tides when waves could propagate across the reef crest. Note that deployments were not concurrent.

Surprisingly, the measured dissipation rate across a groove (mean ϵ = 0.02 kW/m^2) was double the rate across the adjacent spur (mean ϵ = 0.01 kW/m^2) (Fig. 4g). This is probably related to waves being larger on the grooves than on the spurs because of the deeper water (Fig. 3f, p).

5. Discussion

5.1. Wave energy dissipation across the SAG zone vs the reef crest

Our study showcases direct measurements of wave dissipation across the fore reef SAG zone and the reef crest/flat and compares the relative importance of bottom friction and wave breaking. We found that the fore reef SAG zones at both Moorea and One Tree Reef dissipated up to 86 % of wave energy at rates up to 0.1 kW/m^2 (Fig. 4e–g). We found rates of wave energy dissipation across the SAG zone, in the absence of wave breaking and therefore primarily due to bottom friction, were up to 3.6 times higher than across the reef crest where breaking likely contributed to energy dissipation (Fig. 4e–g). In addition, the percentage of energy dissipated across the SAG zone was often higher than across the reef crest/flat zone (Fig. 4i–j). These findings call into question the assumption that the vast majority of wave energy dissipation occurs due to wave breaking at the reef crest (e.g., Ferrario et al., 2014). The importance of dissipation at the fore reef was also reported by Monismith et al. (2015) who measured rates of wave energy dissipation up to 0.03 kW/m^2 on the fore reef SAG between 11.2 and 6.2 m depth at Palmyra Atoll and calculated an extremely high wave friction factor (1.80). A calibrated SWAN model for the same reef also found that the average wave dissipation rates at the fore reef due to bottom friction were larger than those due to wave breaking (Rogers et al., 2016).

We found significant positive correlations between percentage of energy dissipation and *Hs* across the fore reef SAG (Fig. 5e–g). The correlations between Hs and percent dissipation were negative at MN1 and virtually non-existent at MN2 and OE. This may suggest that, under the modal wave conditions measured, as wave heights increase bottom friction over the fore reef SAGs becomes increasingly important for energy dissipation. This is somewhat consistent with modelling by Lowe et al. (2005b) at Kaneohe Bay, Hawaii, which predicted that fore reef dissipation due to bottom friction would be greater than dissipation due to wave breaking under lower-than-average wave heights and approximately equal for average incident wave heights. For larger than average waves, their model predicted that wave breaking would become more important and dissipate energy at approximately double the rate of bottom friction. The wave heights during all our deployments were average or below average and we found mean rates of dissipation across the fore reef SAGs to be up to 3.6 times the rates of dissipation across the reef crest (Fig. 4e–g).

In addition to wave height, we found water depth (i.e., tidal stage) to be important in determining the proportion of wave energy dissipated across the fore reef SAG zone compared to across the reef crest/reef flat zone. We found that as water depth increased, the percentage of energy dissipated across the SAG zone decreased (Fig. 5i–l). Thus, even in micro-tidal Moorea (MN1 and MN2), tidal stage played a role in the relative percentage of energy dissipated across the SAG zone as compared to the reef crest/flat zone. Tidal modulation of the wave field at Moorea was also noted by Monismith et al. (2013). The decline in percent of energy dissipation with increasing water depth was particularly pronounced at One Tree North where half as much wave energy was dissipated at high tides compared to low tides (Fig. 5l). This agrees with previous findings on how propagation is controlled by tidal stage at One Tree Reef (Harris et al., 2015; Vila-Concejo et al., 2014).

The correlations we measured between percentage dissipation, *Hs* and water depth may provide some general insights into the functioning of the SAG zone. It suggests that typically, under high wave conditions and low tides, the proportion of dissipation is greater at the fore reef SAG

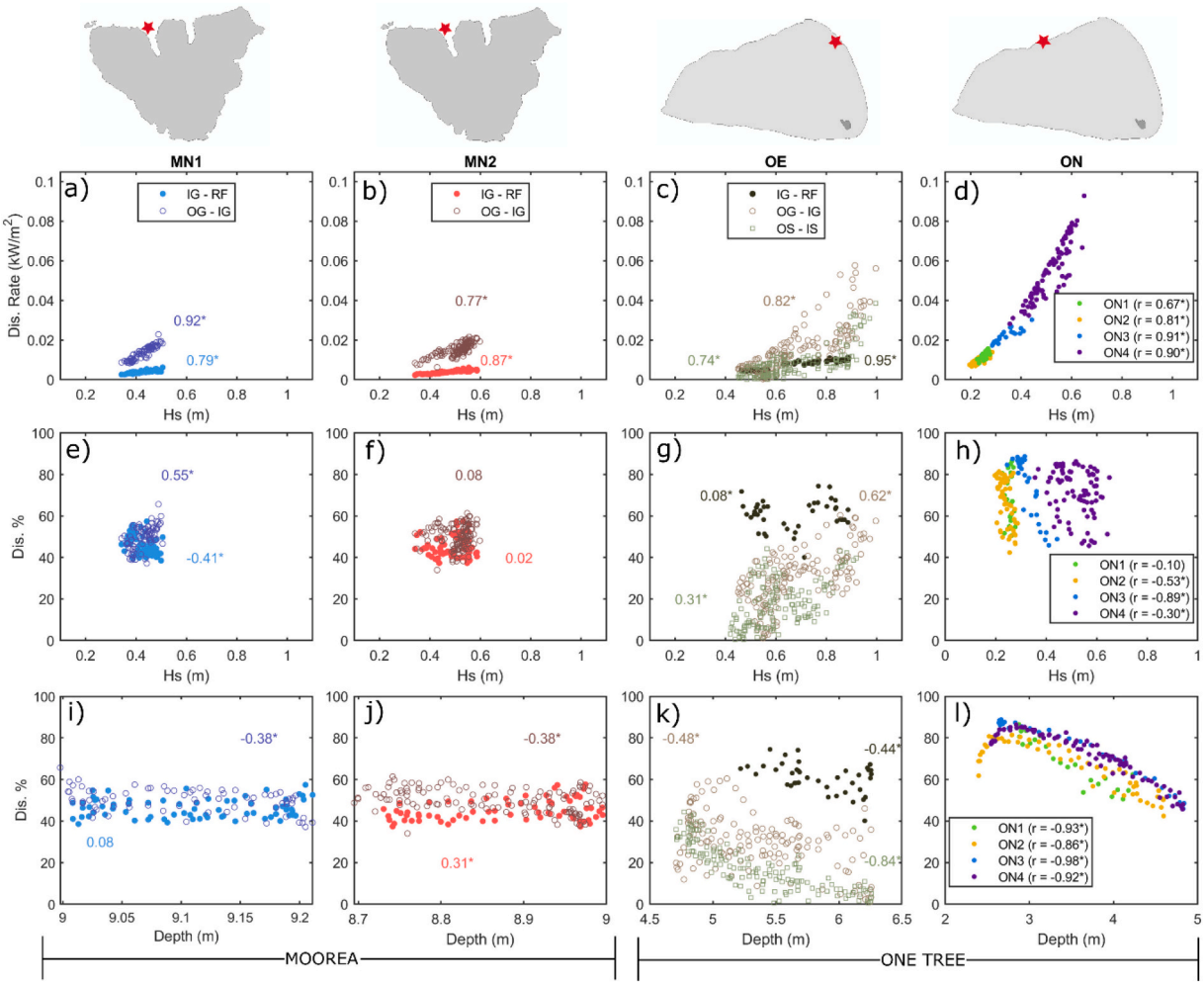

Fig. 5. Relationships between dissipation rate and *Hs* (a–d); percent of energy dissipated and *Hs* at the outer SAG zone instrument(s) in the array (e–h) and; percent of energy dissipated and depth (i–l) across the SAG zone from outer to inner groove (open symbols) and across the reef crest from inner groove to reef flat (filled symbols) at MN1, MN2, OE and ON4. Pearson's correlation r values are given with an asterisk denoting significance at the 95 % level and minus signs denoting a negative correlation. Note that the x-axes (depth) of plots i-l do not have the same scale.

zone than the reef crest/flat zone because the wave base interacts with the rough and topographically complex SAGs and dissipates the majority of its energy as bottom friction before it reaches the crest. Conversely, under low wave conditions with deeper water (i.e., at high tides) the wave base interacts less with the bed at the fore reef and more energy would be dissipated through wave breaking at the reef crest. Under high wave conditions and deep water, we suggest waves breaking across the SAG zone would be responsible for most energy dissipation as supported by Lowe et al. (2005b) and da Silva et al. (2020). Our findings that the percentage of energy dissipation at the fore reef SAG zone declines with increasing depth agree with studies linking sea level rise to an increased risk of wave attack and erosion for islands and coasts currently protected by coral reefs (e.g., Albert et al. (2016), Quataert et al. (2015), Storlazzi et al. (2015) and Storlazzi et al. (2011)). It is important to note, however, that our measurements did not extend to the coastline, and therefore we cannot discuss whether strong wave dissipation on the fore reef would result in lower wave energy at the coastline.

5.2. Global comparison of fore reef dissipation rates

An extensive literature review only found four other studies measuring wave conditions at more than one station on the fore reef allowing for calculation of fore reef wave dissipation rates (Monismith et al., 2013; Monismith et al., 2015; Pequignet et al., 2011; Storlazzi et al., 2004). The dissipation rates presented in our study are comparable to other reefs globally (Fig. 6). However, one should consider that mean dissipation rate is an imperfect metric as our results demonstrate that dissipation rates are highly spatially and temporally variable and dependent on offshore wave conditions during the deployment. The reason why it is displayed here is because it was the only comparable metric able to be gleaned from existing literature. The highest mean dissipation rate measured across the SAG zone in this study was at One Tree North Deployment 4, on the relatively shallow, leeward side (mean $\epsilon = 0.054$ kW/m^2). This is higher than previously published rates presented in the literature (Fig. 6) and occurred during a relatively high energy event with maximum offshore *Hs* reaching 3 m (Supp. Fig. S3). Monismith et al. (2015) suggested that the relatively high dissipation rate (~0.02 kW/m^2) and wave friction factor (1.8) measured at the relatively deep (11–6 m) fore reef in Palmyra Atoll were due to high levels of live, healthy coral cover. Our study provides initial evidence to support this. Generally, we measured higher rates of dissipation across the fore reef SAG zone at One Tree (ON and OE) than at Moorea (MN1 and MN2) and the levels of live coral cover between the spurs at both sites differed considerably (ON = ~85 %, OE = ~70 %, MN = 10–20 %). The spurs were higher at Moorea North than either of the One Tree sites (refer to Table 1) and the fore reef gradients at these sites were similar (ON = 4°, OE = 2° and MN = 5°) thus it is unlikely that slope drove the difference in dissipation rates. It is important to note that the ~3 m tidal

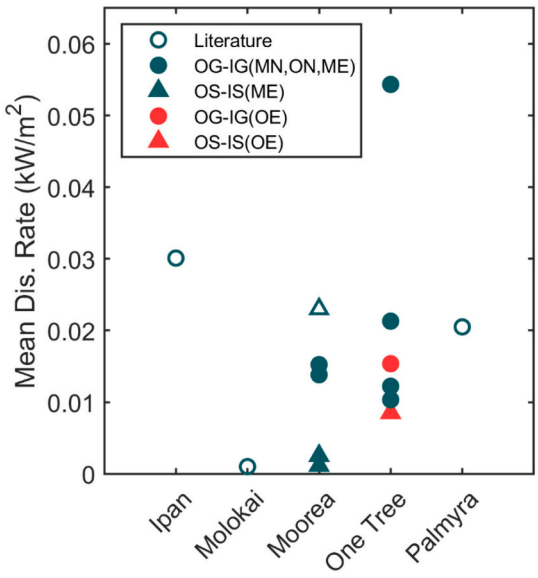

Fig. 6. Mean dissipation rates (kW/m^2) of wave energy across the fore reef SAG zone at different sites globally. Filled symbols are deployments Moorea north (MN), One Tree north (ON), Moorea east (ME) and One Tree east (OE) with circles representing measurements between the outer and inner groove (OG-IG) and triangles representing measurements between the outer and inner spur (OS-IS). Filled symbols represent measurements obtained in this study while open symbols represent values obtained from the literature. The reefs at which these rates were measured are shown on the x-axis with data derived from the following sources: Ipan, Guam (Pequignet et al., 2011); Molokai (Storlazzi et al., 2004); Moorea (this study and Monismith et al., 2013); One Tree (this study); Palmyra Atoll (Monismith et al., 2015).

range at One Tree and the associated tidal currents are also likely to play a role in wave dissipation. This implies that tidal currents are likely to be an important factor modulating wave energy dissipation in meso and particularly macro tidal environments.

One Tree North may also experience offshore currents driven by wave pumping of the type reported by Callaghan et al. (2006) and Nielsen et al. (2008) whereby waves on the exposed side of the reef push water into and across the lagoon and it drains out on the leeward side. Further research is warranted to assess the influence of tidal currents, wave pumping, and live coral cover at the fore reef on wave energy dissipation. More data is required from multiple fore reef instrument arrays to better understand the important role of this understudied geomorphic zone in dissipating wave energy.

5.3. *Comparison of wave dissipation with other ecosystems*

Coral reefs provide important ecosystem services in protecting the coasts from incoming wave energy (Ferrario et al., 2014). While direct comparison is not always possible due to different methods of calculating wave dissipation, authors have shown that mangroves in Vietnam could reduce wave energy between 1.7 and 6 % for every 10 m (Barbier et al., 2008). More recently, Gon et al. (2020) showed that a rock platform off Monterey Bay in California (USA) dissipated 32 % over 132 m (i.e., 2.4 % of the energy over 10 m). While most previous studies in reef environments presented wave dissipation over reef flats, this paper highlights the high wave dissipation that occurs across the fore reef SAG zone and underlines the importance of accounting for this in future numerical modelling studies. Our results show SAG maximum dissipation percentages over 10 m of 9 % in Moorea and 36 % at One Tree Reef this is considerably higher than the aforementioned ecosystems. While we did not obtain detailed bathymetric data to measure roughness or friction factors, our results demonstrate that coral reefs, and in particular SAGs, are amongst the most effective natural wave dissipaters on Earth. Temmerman et al. (2013) claimed that flood protection by ecosystem creation and restoration could provide a sustainable and cost-effective coastal engineering solution and called for implementation when possible. The coastal protection services provided by coral reefs demand global attention and conservation in light of ongoing climate change.

Numerical modelling has suggested that the structural complexity of coral reefs is more important than sea-level rise in determining the level of coastal protection provided by reefs under average wave conditions (Harris et al., 2018). An important future avenue for research includes coupling high spatial resolution (centimeter to meter scales) mapping of the 3D structure (rugosity) of reef environments (particularly the difficult to reach fore reef SAG zone) with closely spaced instrument transects to gain an in-depth understanding of local scale turbulence and friction induced by the interaction between coral reefs with differing benthic cover and hydrodynamic forces (waves and currents).

6. Conclusions

We measured waves across the fore reef spur and groove zone during a range of modal conditions at Moorea, French Polynesia, and One Tree Reef, southern GBR, Australia. The study sites chosen had contrasting tidal regimes (micro vs meso), wave regimes (exposed vs sheltered), broadscale reef type (barrier reef vs lagoonal platform reef), local fore reef SAG morphologies and levels of live coral cover. We found high rates of wave energy dissipation (up to 0.09 kW/m^2) across the fore reef SAG zone. Under the modal conditions measured, the percent of energy dissipated across the fore reef SAG zone was often higher than the percent dissipated across the reef crest/reef flat zone, calling into question the dominant assumption that the reef crest is the most important geomorphic zone for energy dissipation. Our results suggest that SAG zone dissipation is more important under high wave conditions at low tides, while reef crest/flat dissipation is more important with high tides and small waves. In general, higher rates of dissipation were measured across SAG zones at One Tree Reef than Moorea. This may support claims that high live coral cover produces greater bottom friction and wave dissipation though more research is required. It also suggests the importance of tidal currents in influencing wave energy dissipation. Longer deployments, capturing a range of hydrodynamic driving conditions, with instruments at inner and outer ends of both spurs and grooves are required to better understand the complex nature of morphodynamic feedbacks in this important zone.

Declaration of competing interest

The authors declare that they have no known competing financial interests or personal relationships that could have appeared to influence the work reported in this paper.

Acknowledgements

We gratefully acknowledge funding from a Tempe Mann Travelling Scholarship from the Australian Federation of Graduate Women (S.D.), an Australian Postgraduate Award (S.D.), a University of Sydney Merit Award (S.D), a Great Barrier Reef Marine Park Authority Science for Management Award (S.D. 9/1667(2)) an ARC Future Fellowship (A.V.C., FT100100215) and return to work grant for Women in Science at the University of Sydney (A.V.C.). We also thank staff at CRIOBE research station and One Tree Island Research Station. The help of field volunteers Russell Graham, Glen Shaw, Matt Kosnik, Andrew Irving, Pepe Brennen, Vetea Liao, Andrew Durrant, Selma Klanten, Jonathan Walsh and Aero Leplastrier is greatly appreciated. Offshore wave data sets were provided by the Moorea Coral Reef Ecosystem Long-Term Ecological Research (LTER) program, funded by the US National Science Foundation (OCE-0417412) and the Queensland Integrated Marine Observing System (Q-IMOS) operated by the Australian Institute of Marine Science

with the assistance of Craig Steinberg. Datasets for this research are available from Figshare: https://figshare.com/articles/dataset/SAG_Hydrodynamics_Datasets_Moorea_and_One_Tree/14036747.

Appendix A. Supplementary data

Supplementary data to this article can be found online at https://doi.org/10.1016/j.geomorph.2022.108365.

References

Adjeroud, M., Michonneau, F., Edmunds, P.J., Chancerelle, Y., de Loma, T.L., Penin, L., Galzin, R., 2009. Recurrent disturbances, recovery trajectories, and resilience of coral assemblages on a South Central Pacific reef. Coral Reefs 28 (3), 775–780. https://doi.org/10.1007/s00338-009-0515-7.

Acevedo-Ramirez, C.A., Stephenson, W., Wakes, S., Mariño-Tapia, I., 2021. Wave transformation on a fringing reef system with spur and groove structures. J. Geophys. Res. Oceans. https://doi.org/10.1029/2020jc016910.

Albert, S., Leon, J.X., Grinham, A.R., Church, J.A., Gibbes, B.R., Woodroffe, C.D., 2016. Interactions between sea-level rise and wave exposure on reef island dynamics in the Solomon Islands. Environ. Res. Lett. 11 (5), 1–9.

Baldock, T.E., Shabani, B., Callaghan, D.P., 2019. Open access Bayesian Belief Networks for estimating the hydrodynamics and shoreline response behind fringing reefs subject to climate changes and reef degradation. Environ. Model. Softw. 119 (June), 327–340. https://doi.org/10.1016/j.envsoft.2019.07.001.

Baldock, T.E., Shabani, B., Callaghan, D.P., Hu, Z., Mumby, P.J., 2020. Two-dimensional modelling of wave dynamics and wave forces on fringing coral reefs. Coast. Eng. 155 https://doi.org/10.1016/j.coastaleng.2019.103594.

Barbier, E.B., Koch, E.W., Silliman, B.R., Hacker, S.D., Wolanski, E., Primavera, J., Reed, D.J., 2008. Coastal ecosystem-based management with nonlinear ecological functions and values. Science 319 (5861), 321–323. https://doi.org/10.1126/science.1150349.

Beck, M.W., Losada, I.J., Menéndez, P., Reguero, B.G., Díaz-Simal, P., Fernández, F., 2018. The global flood protection savings provided by coral reefs. Nat. Commun. 9 (1) https://doi.org/10.1038/s41467-018-04568-z.

Beetham, E.P., Kench, P.S., 2014. Wave energy gradients and shoreline change on Vabbinfaru platform, Maldives. Geomorphology 209, 98–110. https://doi.org/10.1016/j.geomorph.2013.11.029.

Bramante, J.F., Ashton, A.D., Storlazzi, C.D., Cheriton, O.M., Donnelly, J.P., 2020. Sea-level rise will drive divergent sediment transport patterns on fore reefs and reef flats, potentially causing erosion on atoll islands. J. Geophys. Res. Earth Surf. https://doi.org/10.1029/2019jf005446.

Brander, R.W., Kench, P.S., Hart, D., 2004. Spatial and temporal variations in wave characteristics across a reef platform, Warraber Island, Torres Strait, Australia. Mar. Geol. 207 (1-4), 169–184. https://doi.org/10.1016/j.margeo.2004.03.014.

Bryson, M., Duce, S., Harris, D., Webster, J.M., Thompson, A., Vila-Concejo, A., Williams, S.B., 2016. Geomorphic changes of a coral shingle cay measured using Kite Aerial Photography. Geomorphology 270, 1–8. https://doi.org/10.1016/j.geomorph.2016.06.018.

Buckley, M.L., Lowe, R.J., Hansen, J.E., Van Dongeren, A.R., 2016. Wave setup over a fringing reef with large bottom roughness. J. Phys. Oceanogr. 46 (8), 2317–2333.

Callaghan, D.P., Nielsen, P., Cartwright, N., Gourlay, M.R., Baldock, T.E., 2006. Atoll lagoon flushing forced by waves. Coast. Eng. 53 (8), 691–704. https://doi.org/10.1016/j.coastaleng.2006.02.006.

Cheriton, O.M., Storlazzi, C.D., Rosenberger, K.J., 2016. Observations of wave transformation over a fringing coral reef and the importance of low-frequency waves and offshore water levels to runup, overwash and coastal flooding. J. Geophys. Res. Oceans 121.

da Silva, R.F., Storlazzi, C.D., Rogers, J.S., Reyns, J., McCall, R., 2020. Modelling three-dimensional flow over spur-and-groove morphology. Coral Reefs. https://doi.org/10.1007/s00338-020-02011-8.

Duce, S., 2017. The Form, Function and Evolution of Coral Reef Spur and Grooves. University of Sydney, Sydney, Australia (Unpublished PhD Thesis).

Duce, S., Dechnik, B., Webster, J.M., Hua, Q., Sadler, J., Webb, G.E., Nothdurft, L., Salas-Saavedra, M., Vila-Concejo, A., 2020. Mechanisms of spur and groove development and implications for reef platform evolution. Quat. Sci. Rev. 231, 106155 https://doi.org/10.1016/j.quascirev.2019.106155.

Duce, S., Vila-Concejo, A., Hamylton, S.M., Bruce, E., Webster, J.M., 2014. Spur and groove distribution, morphology and relationship to relative wave exposure, Southern Great Barrier Reef, Australia. J. Coast. Res. (70), 115–120.

Duce, S., Vila-Concejo, A., Hamylton, S.M., Webster, J.M., Bruce, E., Beaman, R.J., 2016. A morphometric assessment and classification of coral reef spur and groove morphology. Geomorphology 265, 68–83.

Edmunds, P.J., Leichter, J.J., 2016. Spatial scale-dependent vertical zonation of coral reef community structure in French Polynesia. Ecosphere 7 (5), 1–14. https://doi.org/10.1002/ecs2.1342.

Etienne, S., 2012. Marine inundation hazards in French Polynesia: geomorphic impacts of tropical cyclone oli in February 2010. Geochem. Soc. Spec. Publ. 361 (1), 21–39. https://doi.org/10.1144/SP361.4.

Ferrario, F., Beck, M.W., Storlazzi, C.D., Micheli, F., Shepard, C.C., Airoldi, L., 2014. The effectiveness of coral reefs for coastal hazard risk reduction and adaptation. Nat. Commun. 5, 3794. https://doi.org/10.1038/ncomms4794.

Foley, M., Stender, Y., Singh, A., Jokiel, P., Rodgers, K.U., 2014. Ecological engineering considerations for coral reefs in the design of multifunctional coastal structures. Coast. Eng. Proc. 1 (34) https://doi.org/10.9753/icce.v34.management.30, 30- 30.

Frith, C.A., Mason, L.B., 1986. Modelling wind driven circulation One Tree Reef, Southern Great Barrier Reef. Coral Reefs 4 (4), 201–211. https://doi.org/10.1007/BF00298078.

Gallop, S.L., Young, I.R., Ranasinghe, R., Durrant, T.H., Haigh, I.D., 2014. The large-scale influence of the Great Barrier Reef matrix on wave attenuation. Coral Reefs 33 (4), 1167–1178. https://doi.org/10.1007/s00338-014-1205-7.

Gischler, E., 2010. Indo-Pacific and Atlantic spurs and grooves revisited: the possible effects of different Holocene Sea-level history, exposure, and reef accretion rate in the shallow fore reef. Facies 56 (2), 173–177. https://doi.org/10.1007/s10347-010-0218-0.

Gon, C.J., MacMahan, J.H., Thornton, E.B., Denny, M., 2020. Wave dissipation by bottom friction on the inner shelf of a rocky shore. J. Geophys. Res. Oceans 125 (10). https://doi.org/10.1029/2019jc015963.

Hamylton, S., Silverman, J., Shaw, E., 2013. The use of remote sensing to scale up measures of carbonate production on reef systems: a comparison of hydrochemical and census-based estimation methods. Int. J. Remote Sens. 34 (18), 6451–6465. https://doi.org/10.1080/01431161.2013.800654.

Hardy, T.A., Young, I.R., 1996. Field study of wave attenuation on an offshore coral reef. J. Geophys. Res. Oceans 101 (C6), 14311–14326. https://doi.org/10.1029/96JC00202.

Harris, D.L., Rovere, A., Casella, E., Power, H.E., Canavesio, R., Collin, A., Parravicini, V., 2018. Coral reef structural complexity provides important coastal protection from waves under rising sea levels. Sci. Adv. 4 (2), 1–7. https://doi.org/10.1126/sciadv.aao4350.

Harris, D.L., Vila-Concejo, A., 2013. Wave transformation on a coral reef rubble platform. J. Coast. Res. 65, 506–510. https://doi.org/10.2112/si65-086.1.

Harris, D.L., Vila-Concejo, A., Webster, J.M., Power, H.E., 2015. Spatial variations in wave transformation and sediment entrainment on a coral reef sand apron. Mar. Geol. 363, 220–229. https://doi.org/10.1016/j.margeo.2015.02.010.

Hench, J.L., Leichter, J.J., Monismith, S.G., 2008. Episodic circulation and exchange in a wave-driven coral reef and lagoon system. Limnol. Oceanogr. 53 (6), 2681–2694. https://doi.org/10.4319/lo.2008.53.6.2681.

Holthuijsen, L.H., 2010. Waves in Oceanic and Coastal Waters. Cambridge university press.

Hopley, D., Smithers, S.G., Parnell, K.E., 2007. The Geomorphology of the Great Barrier Reef : Development, Diversity, and Change. Cambridge University Press, Cambridge.

Horstman, E.M., Dohmen-Janssen, C.M., Narra, P.M.F., van den Berg, N.J.F., Siemerink, M., Hulscher, S.J.M.H., 2014. Wave attenuation in mangroves: a quantitative approach to field observations. Coast. Eng. 94, 47–62. https://doi.org/10.1016/j.coastaleng.2014.08.005.

Huang, Z.C., Lenain, L., Melville, W.K., Middleton, J.H., Reineman, B., Statom, N., McCabe, R.M., 2012. Dissipation of wave energy and turbulence in a shallow coral reef lagoon. J. Geophys. Res. Oceans 117 (3), 1–18. https://doi.org/10.1029/2011JC007202.

Kench, P.S., Brander, R.W., 2006. Wave processes on coral reef flats: implications for reef geomorphology using Australian case studies. J. Coast. Res. 221, 209–223. https://doi.org/10.2112/05a-0016.1.

Kench, P.S., Brander, R.W., Parnell, K.E., O'Callaghan, J.M., 2009. Seasonal variations in wave characteristics around a coral reef island, South Maalhosmadulu atoll, Maldives. Mar. Geol. 262 (1-4), 116–129. https://doi.org/10.1016/j.margeo.2009.03.018.

Lee, D.-Y., Wang, H., 1984. Measurement of surface waves from subsurface gage. Coast. Eng. Proc. 1 (19), 271–286.

Leichter, J.J., Alldredge, A.L., Bernardi, G., Brooks, A.J., Carlson, C.A., Carpenter, R.C., Wyatt, A.S.J., 2013. Biological and physical interactions on a tropical island coral reef: transport and retention processes on Morea, French Polynesia. Oceanogr. Soc. 26 (3), 52–63.

Leichter, J.J., Stokes, M.D., Hench, J.L., Witting, J., Washburn, L., 2012. The island-scale internal wave climate of Moorea, French Polynesia. J. Geophys. Res. Oceans 117 (6), 1–16. https://doi.org/10.1029/2012JC007949.

Lowe, R.J., Koseff, J.R., Monismith, S.G., 2005a. Oscillatory flow through submerged canopies: 1. Velocity structure. J. Geophys. Res. Oceans 110 (C10).

Lowe, R.J., Falter, J.L., Bandet, M.D., Pawlak, G., Atkinson, M.J., Monismith, S.G., Koseff, J.R., 2005b. Spectral wave dissipation over a barrier reef. J. Geophys. Res. 110 https://doi.org/10.1029/2004JC002711, 4001-4001.

Lugo-Fernández, A., Roberts, H.H., Suhayda, J.N., 1998a. Wave transformations across a caribbean fringing-barrier Coral Reef. Cont. Shelf Res. 18 (10), 1099–1124. https://doi.org/10.1016/S0278-4343(97)00020-4.

Lugo-Fernández, A., Roberts, H.H., Wiseman, W.J., 1998b. Tide effects on wave attenuation and wave set-up on a Caribbean coral reef. Estuar. Coast. Shelf Sci. 47 (4), 385–393. https://doi.org/10.1006/ecss.1998.0365.

Mandlier, P.G., 2013. Field observations of wave refraction and propagation pathways on coral reef platforms. Earth Surf. Process. Landf. 38 (9), 913–925. https://doi.org/10.1002/esp.3328.

Masselink, G., Beetham, E., Kench, P., 2020. Coral reef islands can accrete vertically in response to sea level rise. Retrieved from Sci. Adv. 6 (June), 3656–3666. http://advances.sciencemag.org/.

Monismith, S.G., Herdman, L.M.M., Ahmerkamp, S., Hench, J.L., 2013. Wave transformation and wave-driven flow across a steep coral reef. J. Phys. Oceanogr. 43 (7), 1356–1379. https://doi.org/10.1175/jpo-d-12-0164.1.

Monismith, S.G., Rogers, J.S., Koweek, D., Dunbar, R.B., 2015. Frictional wave dissipation on a remarkably rough reef. Geophys. Res. Lett. 42 (10), 4063–4071. https://doi.org/10.1002/2015GL063804.

Munk, W.H., Sargent, M.C., 1948. Adjustment of Bikini Atoll to ocean waves. Trans. Am. Geophys. Union 29 (6). https://doi.org/10.1029/TR029i006p00855, 855-855.
Nielsen, P., Guard, P.A., Callaghan, D.P., Baldock, T.E., 2008. Observations of wave pump efficiency. Coast. Eng. 55 (1), 69–72. https://doi.org/10.1016/j.coastaleng.2007.07.003.
Pequignet, A.-C., Becker, J.M., Merrifield, M.A., Boc, S.J., 2011. The dissipation of wind wave energy across a fringing reef at Ipan, Guam. Coral Reefs 30, 71–82.
Péquignet, A.C., Becker, J.M., Merrifield, M.A., Boc, S.J., 2011. The dissipation of wind wave energy across a fringing reef at Ipan, Guam. Coral Reefs 30 (Suppl. 1), 71–82. https://doi.org/10.1007/s00338-011-0719-5.
Pomeroy, A., Lowe, R., Symonds, G., Van Dongeren, A., Moore, C., 2012. The dynamics of infragravity wave transformation over a fringing reef. J. Geophys. Res. Oceans 117 (11). https://doi.org/10.1029/2012JC008310.
Quataert, E., Storlazzi, C., van Rooijen, A., Cheriton, O., van Dongeren, A., 2015. The influence of coral reefs and climate change on wave-driven flooding of tropical coastlines. Geophys. Res. Lett. 42 (15), 6407–6415. https://doi.org/10.1002/2015GL064861.
Roberts, H.H., 1974. Variability of reefs with regard to changes in wave power around an island. In: Paper Presented at the Proceedings of the Second International Symposium on Coral Reefs, Brisbane, Brisbane, Australia.
Roberts, H.H., Murray, S.P., Suhayda, J.N., 1975. Physical processes in fringing reef system. J. Mar. Res. 33 (2), 233–260. Retrieved from ://WOS:A1975AL34800006.
Rogers, J.S., Monismith, S.G., Feddersen, F., Storlazzi, C.D., 2013. Hydrodynamics of spur and groove formations on a coral reef. J. Geophys. Res. Oceans 118, 1–15.
Rogers, J.S., Monismith, S.G., Dunbar, R.B., Koweek, D., 2015. Field observations of wave-driven circulation over spur and groove formations on a coral reef. J. Geophys. Res. Oceans 120, 145–160.
Rogers, J.S., Monismith, S.G., Koweek, D., Dunbar, R.B., 2016. Wave dynamics of a pacific atoll with high friction. J. Geophys. Res. Oceans 120, 1–18.
Samosorn, B., Woodroffe, C.D., 2008. Nearshore wave environments around a sandy cay on a platform reef, Torres Strait, Australia. Cont. Shelf Res. 28 (16), 2257–2274. https://doi.org/10.1016/j.csr.2008.03.043.
Shannon, A.M., Power, H.E., Webster, J.M., Vila-Concejo, A., 2013. Evolution of coral rubble deposits on a reef platform as detected by remote sensing. Remote Sens. 5 (1), 1–18. https://doi.org/10.3390/rs5010001.
Storlazzi, C.D., Brown, E.K., Field, M.E., Rodgers, K., Jokiel, P.L., 2005. A model for wave control on coral breakage and species distribution in the hawaiian Islands. Coral Reefs 24 (1), 43–55. https://doi.org/10.1007/s00338-004-0430-x.
Storlazzi, C.D., Elias, E., Field, M.E., Presto, M.K., 2011. Numerical modeling of the impact of sea-level rise on fringing coral reef hydrodynamics and sediment transport. Coral Reefs 30 (Suppl. 1), 83–96. https://doi.org/10.1007/s00338-011-0723-9.
Storlazzi, C.D., Elias, E.P.L., Berkowitz, P., 2015. Many atolls may be uninhabitable within decades due to climate change. Sci. Rep. 5 (1), 1–9. https://doi.org/10.1038/srep14546.
Storlazzi, C.D., Logan, J.B., Field, M.E., 2003. Quantitative morphology of a fringing reef tract from high-resolution laser bathymetry: Southern Molokai, Hawaii. Geol. Soc. Am. Bull. 115 (11), 1344–1355. https://doi.org/10.1130/b25200.1.
Storlazzi, C.D., Ogston, A.S., Bothner, M.H., Field, M.E., Presto, M.K., 2004. Wave-and tidally-driven flow and sediment flux across a fringing coral reef: Southern Molokai, Hawaii. Cont. Shelf Res. 24, 1397–1419. https://doi.org/10.1016/j.csr.2004.02.010.
Talavera, L., Vila-Concejo, A., Webster, J.M., Smith, C., Duce, S., Fellowes, T.E., Salles, T., Harris, D., Hill, J., Figueira, W., Hacker, J., 2021. Morphodynamic controls for growth and evolution of a rubble coral island. Remote Sens. 13 (8), 1582.
Temmerman, S., Meire, P., Bouma, T.J., Herman, P.M.J., Ysebaert, T., De Vriend, H.J., 2013. In: Ecosystem-based Coastal Defence in the Face of Global Change, Vol. 504, pp. 79–83.
Trapon, M.L., Pratchett, M.S., Penin, L., 2011. Comparative effects of different disturbances in coral reef habitats in Moorea, French Polynesia. J. Mar. Biol. 2011, 1–11. https://doi.org/10.1155/2011/807625.
Van Zanten, B.T., Van Beukering, P.J.H., Wagtendonk, A.J., 2014. Coastal protection by coral reefs: a framework for spatial assessment and economic valuation. Ocean Coast. Manag. 96, 94–103. https://doi.org/10.1016/j.ocecoaman.2014.05.001.
Vetter, O., Becker, J.M., Merrifield, M.A., Pequignet, A.C., Aucan, J., Boc, S.J., Pollock, C. E., 2010. Wave setup over a Pacific Island fringing reef. J. Geophys. Res. Oceans 115, 1–13. https://doi.org/10.1029/2010jc006455.
Vila-Concejo, A., Duce, S., Nagao, M., Nakashima, Y., Ito, M., Fujita, K., Kan, H., 2017. Typhoon waves on coral reefs. Coast. Dyn. 2017 (263), 697–701.
Vila-Concejo, A., Harris, D.L., Power, H.E., Shannon, A.M., Webster, J.M., 2014. Sediment transport and mixing depth on a coral reef sand apron. Geomorphology 222, 143–150. https://doi.org/10.1016/j.geomorph.2013.09.034.
Woodhead, A.J., Hicks, C.C., Norström, A.V., Williams, G.J., Graham, N.A.J., 2019. Coral reef ecosystem services in the Anthropocene. Funct. Ecol. 33 (6), 1023–1034. https://doi.org/10.1111/1365-2435.13331.

Appendix B (Part II)| A quantitative approach to classify the shape of beach profiles

Gazi, M. Y., Fellowes, T. E., Deo, R., da Silva, A. P., Perris, L., & Vila-Concejo, A. (2025). A quantitative approach to classify the shape of beach profiles. *Estuarine, Coastal and Shelf Science*, 322. https://doi.org/10.1016/j.ecss.2025.109373

Estuarine, Coastal and Shelf Science 322 (2025) 109373

Contents lists available at ScienceDirect

Estuarine, Coastal and Shelf Science

journal homepage: www.elsevier.com/locate/ecss

A quantitative approach to classify the shape of beach profiles

Md Yousuf Gazi [a,b,c,*], Thomas E. Fellowes [a,b,d], Ratneel Deo [a,b], Ana P. Silva [a,b], Lachlan Perris [a,b], Ana Vila-Concejo [a,b]

[a] Geocoastal Research Group, School of Geosciences, Faculty of Science, University of Sydney, Australia
[b] Marine Studies Institute, Faculty of Science, University of Sydney, Australia
[c] Department of Geology, University of Dhaka, Dhaka, Bangladesh
[d] Water Research Laboratory, School of Civil and Environmental Engineering, University of New South Wales Sydney, Australia

ARTICLE INFO

Keywords:
Beaches in estuaries and bays
Morphodynamics
Low energy beaches
Coastal erosion

ABSTRACT

Sandy beaches in estuaries and bays (BEBs) are common globally, and their existence relies on the complex interactions of regional and local waves, limited sediment input, tidal dynamics, and human interventions. BEB morphodynamics are poorly defined with only a few studies attempting to qualitatively relate different BEB profile shapes with relevant physical drivers. Here, we propose a novel Profile Morphotype Index (Γ) to quantitatively classify the shape of beach profiles in BEBs into distinct morphotypes to allow an objective analysis of changes in beach morphodynamic states. For this study, beach profiles in three swash-aligned and one drift-aligned BEBs in Gamay–Botany Bay (NSW, Australia) were measured periodically between 2016 and 2023, resulting in a total of 774 beach profile surveys. Based on this dataset, we defined equations that compute the profile shape assigning it to a specific morphotype. Ten unique morphotypes form the new morphometric index (Γ) varying gradually between *Concave* (Γ = −1.000) *and Convex* (Γ = 1.000) profile shapes, which indicate more erosive and accretive beach states, respectively. Our results show that those BEBs closest to the estuary entrance favoured the *Convex (Γ = 1.000)* morphotype, while BEBs farthest from the entrance and under erosive conditions were *Mostly Concave* (Γ = −0.570 to −0.950) morphotypes. The morphometric index also captured changes in profile shape due to high-energy storm waves propagating into the estuary. This new morphotype index (Γ) provides an objective classification of BEB profile shape allowing us to better predict beach state response to changes in coastal processes and hydrodynamics.

1. Introduction

Beaches in estuaries and bays (BEBs) are coastline features in semi-enclosed coastal environments including estuaries, bays, harbours, and lagoons (Nordstrom and Jackson, 2012; Vila-Concejo et al., 2020). They are historically considered sheltered from the influence of offshore swell waves, however, some receive swell waves that can propagate through the estuary entrance under certain offshore wave directions (Rahbani et al., 2022; Vila-Concejo et al., 2010). BEBs provide significant environmental and ecosystem services, such as coastal hazard protection, support critical estuarine habitats, and they have societal and recreational value (Kennedy et al., 2023; Largier and Taggart, 2006; Nordstrom and Jackson, 2012; Vila-Concejo et al., 2020, 2022). Many of the world's megacities (e.g., Shanghai, San Francisco, Sydney) are situated alongside estuarine and bay shores. BEBs have traditionally been considered sacrificial features in the planning of engineering works (Vila-Concejo et al., 2022, 2024), including dredging for land reclamation, seawalls and groins to counter erosion and river diversion to make way for high-value infrastructure such as ports and airports (Brand et al., 2022; Fellowes et al., 2021; Kennedy, 2002). These modifications can impact the stability of BEBs and change their morphodynamics (Austin et al., 2018; Carrasco et al., 2012; Dugan et al., 2011; Hughes et al., 2007). BEBs are therefore significant environments that may have commercial importance of which we have limited knowledge (Vila-Concejo et al., 2024).

BEBs shoreline dynamics are controlled by their geologic setting, sediment supply, location in relation to the estuary entrance and the flood-tide deltas, the estuary entrance width and orientation, as well as anthropogenic pressures (Gallop et al., 2020; Travers et al., 2010; Vila-Concejo et al., 2020). Tidal-range conditions and asymmetry of tidal currents are also important controls on the morphology of BEBs (Dronkers, 1986). Further, climate change plays a significant impact on

* Corresponding author. Geocoastal Research Group, School of Geosciences, Faculty of Science, University of Sydney, Australia
E-mail address: mdyousuf.gazi@sydney.edu.au (M.Y. Gazi).

https://doi.org/10.1016/j.ecss.2025.109373
Received 13 January 2025; Received in revised form 25 April 2025; Accepted 22 May 2025
Available online 22 May 2025

BEB morphodynamics through the modifications of modal wave climate (e.g., shift in storm wave direction), storm frequency (Gallop et al., 2020) and exposure to sea-level rise, which can lead to potential coastal recession and aggradation (Rosati et al., 2013).

BEBs that exist in low-energy settings typically have narrow beach widths, when compared to open-coast beaches, and are low-lying accumulations of sediment (Jackson et al., 2002). Early studies claimed that locally generated wind waves were the sole influencing factor on BEB morphodynamics (Inman and Filloux, 1960). Later, Nordstrom (1989) broadened this to include tidal and riverine currents along with locally generated wind waves and boat wakes. However, more recently, swell waves have been shown to be an important driver of BEB morphodynamics (Rahbani et al., 2022; Vila-Concejo et al., 2010). For instance, Gallop et al. (2020) found that extreme erosion along BEBs can occur due to swell energy propagating through the estuary entrance and onto BEBs shores. Therefore, BEBs morphology can depend on the relative contribution of different wave energy components, including local wind waves, swells, and long-period infragravity waves (Rahbani et al., 2022).

It is important to note that BEBs are not scaled-down versions of open coast beaches (Vila-Concejo et al., 2020), with previous studies highlighting the need to use the cross-shore shape of the beach profile to fully understand BEB morphodynamics. Hegge et al. (1996) described four morphotypes for low-energy beaches based on their overall profile shape (concave, moderately concave, moderately steep, and steeped) finding a substantial link between profile shape and sediment properties. In microtidal environments, Makaske and Augustinus (1998) identified three BEBs profile morphotypes: straight, concave, and convex-concave, based on the response to varying wave heights. Travers (2007) proposed a morphological model for low-energy beaches where the study identified four profile morphotypes based on wave exposure, including exponential, segmented, concave-curvilinear, and convex-curvilinear following the increasing wind wave energy. The above studies were able to classify profile morphotypes and link these with sediment characteristics, wave height, and exposure to wave energy. However, in these studies, the shapes of the profiles are defined qualitatively based on visual observations.

This study aims to develop a quantitative approach to classify profile shapes found on BEBs into morphotypes that represent various morphodynamic states. This is achieved by fulfilling the following objectives: (1) to develop a quantitative method and index to characterise beach profiles into profile morphotypes according to their shape, and (2) to determine the prevailing conditions under which these morphotypes exist. The new index proposed here provides the first quantitative characterisation of the BEB profile shapes. It can be applied globally and provides an objective and measurable tool to identify the BEB morphotypes and the changes over time. This information is relevant to inform management about beach stability and vulnerable areas, allowing us to take targeted measures to improve coastal protection strategies.

2. Study area

Gamay (Botany Bay) is 12 km south of the centre of Sydney in SE Australia. It occupies 39.6 km^2 (5 × 8 km) with a mean depth of 11.4 m (Roy et al., 2001) (Fig. 1). The BEBs in Gamay are economically and culturally significant (The First Nations people have lived in Gamay for tens of thousands of years), with historical sites and natural landmarks alongside human interventions, such as Sydney's port and airport. Since 1900, significant modifications have been made to the estuary (Fellowes et al., 2021), including river diversion, dredging and land reclamation for the construction and expansion of the port and airport, as well as the construction of groins along the adjacent BEB shores (Fig. 1) (Fellowes et al., 2021). These modifications have altered the shoreline position and wave conditions at some of the Gamay BEBs (Fellowes et al., 2021; Rahbani et al., 2022). In addition, the width of these BEBs has reduced due to the compound impacts of the dredging for the runways at Sydney Airport and the port navigation channel (Fellowes et al., 2021).

In this study, we consider four BEBs in Gamay: Congwong, Currewol (Frenchmans beach) and Yarra Bay, on the northeast shore adjacent (<3.5 km) to the estuary entrance (Fig. 1E and F), and Lady Robinsons on the western shore ~8 km from the entrance (Fig. 1D). There are two intermittently closed and open lakes and lagoons (ICOLLs) in the study area, one at the eastern end of Congwong and one at the midpoint alongshore at Yarra Bay, influencing the morphodynamic processes on these beaches (Gallop et al., 2020). Congwong, Currewol, and Yarra Bay are swash-aligned (waves arriving parallel to the shore) with the latter two BEBs having a central groyne constructed in 1976, following the notable 1974 storms (Fellowes et al., 2021). Lady Robinsons is drift-aligned (waves arriving at an angle to the shore) (Short, 1993) and in 1997 and 2005, groins were built along the central and southern parts of this beach to mediate the extensive modifications in Gamay (Cowell and Kannane, 2000) (Fig. 1D).

These four BEBs exhibit varied morphological states and morphodynamic responses due to their differing distances from the estuary entrance, exposure to swell waves, and fetch length for local wind wave generation (Table 1). Congwong, Currewol, Yarra Bay (post-groyne construction), and the northern part of the Lady Robinsons show limited decadal-scale shoreline changes and are classified as *quasi-stable* BEBs that recover sand lost between storm events. Conversely, the southern part of Lady Robinsons exhibits long-term erosional behaviour and is classified as a *relict* beach that does not recover lost sediment (Fellowes et al., 2021). Two river systems discharge in this area bringing sediment into the bay: the Cooks River in the NW corner, adjacent to the airport and the Tucoerah (aboriginal name for the Georges River) in the SW at the southern end of Lady Robinsons (Fig. 1).

Gamay experiences wind from all directions, with northeast winds during the summer days creating waves that can impact its southern shores. Additionally, strong southerly winds can produce waves that may still reach the northern shores in the summer afternoons and westerly winds that can last for up to a week in the winter (Rahbani et al., 2022). This region is micro-tidal with a mean spring tidal range of 1.25 m. The offshore wave climate is characterised by long-term mean significant wave heights (H_s) of 1.6 m, mean periods (T_z) of 6 s, and peak periods (T_p) of 10 s, with moderate to high wave energy that typically originates from the SSE (135°) (Shand et al., 2010).

The Sydney region regularly receives storm waves, defined as events with H_s over 3 m (95th percentile), that occur year-round with higher frequency in the Austral autumn and winter (March to August) due to weather systems that form offshore in the Tasman Sea east of NSW including East Coast Lows (ECLs) and mid-latitude depressions (Dowdy et al., 2013; Shand et al., 2010). These storms cause strong winds, and torrential downpours, and generate waves that can cause considerable erosion of the open coast and on exposed estuarine beaches (Pepler and Dowdy, 2021).

Recent research (Rahbani et al., 2022) shows that swell waves are the dominant energy signature inside Gamay contributing ~51 %, compared to locally generated wind waves and infragravity waves with ~31% and ~17 %, respectively. Swell waves are most prominent at Congwong Beach, accounting for 52 % of the total wave energy, with a mean significant wave height (H_s) of 0.17 m and a maximum height (H_{max}) of 0.39 m. In contrast, other BEBs exhibit a lower mean H_s of approximately 0.06 m and a maximum H_{max} of around 0.12 m (Table 2). Lady Robinsons has the highest wind waves (43 %) (Table 2). Infragravity waves are minimal at Congwong with the lowest mean H_s (0.02 m) at Lady Robinsons (Rahbani et al., 2022).

3. Data and methods

3.1. Beach profile surveys

The BEBs in Gamay were surveyed monthly from May 2016 to July 2018, then quarterly from August 2018 to March 2023. The surveys

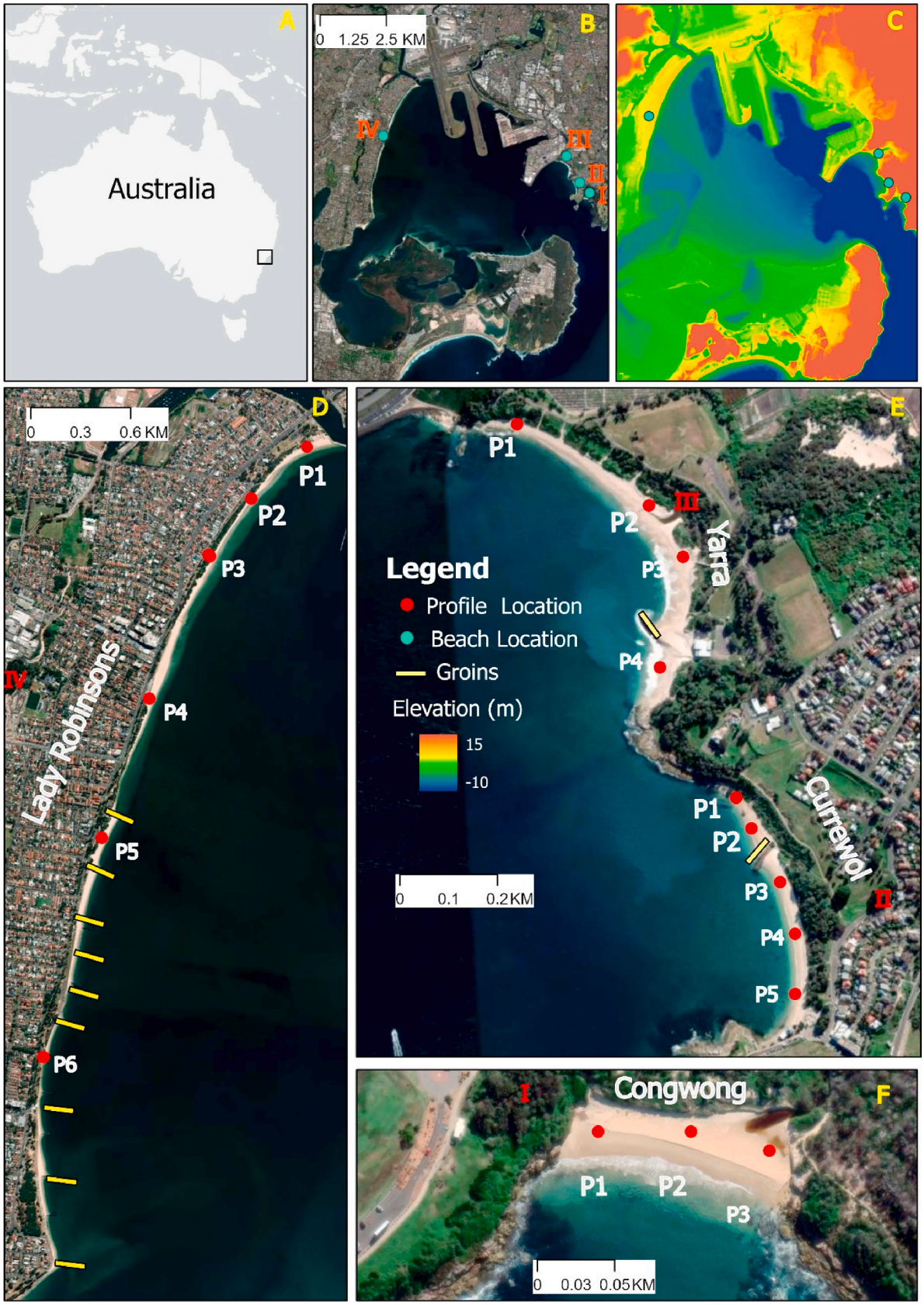

Fig. 1. (A) Study Area in Sydney, Southeastern Australia; (B) Gamay Bay and the location of the BEBs, I: Congwong, II: Currewol, III: Yarra, IV: Lady Robinsons; (C) Topo-bathymetric map of the region; (D) Lady Robinsons Beach with profile locations; (E) Profiles of Currewol and Yarra Beaches; (F) Congwong Beach Profiles. Digital elevation model (c) was downloaded from Wilson and Power (2018a) and satellite images from Google Earth (November 20, 2022).

Table 1
Geomorphological settings and survey information per beach in the study area, including beach length, distance from the estuary entrance, beach orientation, average sediment size, number of fixed beach transects, total number of surveyed profiles per beach.

BEBs	Beach Length (m)	Distance from the entrance (km)	Shoreline Orientation	D50 (μm)	Number of transects	Total number of surveyed profiles
Congwong	161	1.3	SE	333	3	129
Currewol	549	1.8	W	330	5	215
Yarra Bay	682	2.6	SW	288	4	172
Lady Robinsons	5501	8.2	E	280	6	258

Table 2
Local wave conditions representing the contribution of individual waves with mean H_s and maximum wave height (Rahbani et al., 2022).

Beach	Wind Wave			Swell Wave			Infragravity Wave		
	Total (%)	H_s	H_{max}	Total (%)	H_s	H_{max}	Total (%)	H_s	H_{max}
Congwong	35	0.16	0.39	52	0.17	0.39	13	0.05	0.06
Currewol and Yarra (same PTs)	16	0.04	0.09	51	0.06	0.14	33	0.03	0.05
Lady Robinsons	43	0.09	0.2	51	0.06	0.13	6	0.02	0.03

included measuring cross-shore profiles of the beach at low tide, starting at permanent landward benchmarks established by Gallop et al. (2020) at the back-beach dune or seawall, and finishing at a wading depth below 0 m mean sea level (MSL) (Australian Height Datum, AHD). Fixed cross-shore upper beach transects across all BEBs were measured using an RTK-GNSS (Real Time Kinematic–Global Navigation Satellite System) with vertical and horizontal uncertainties of 0.10 and 0.05 m, respectively (Table 1; Fig. 1).

In total, we used 774 beach profile measurements along 18 fixed transects, with individual transects being surveyed at least 43 times each, including pre-storm and post-storm events. We calculated the mean profile shape and standard deviation for each fixed transect along the study period to identify the overall shape of the upper beach and the extent of the changes along the profile and between different transects. To calculate linear profile volume (m^3/m), we used the trapezoid rule (Croft, 2014) that computes the cumulative area of a series of trapezoids that approximate the area beneath the measured cross-shore profile.

3.2. Profile Morphotype Index (Γ)

To quantitatively categorise the shape of the profiles into distinct profile morphotypes, the initial step involved drawing a 1:1 gradient line ***g(x)*** (straight line) atop the measured profile ***f(x)***, starting from the first point of the measured profile at the back of the beach, and extending cross-shore until the profile elevation reached 0 m MSL (Fig. 2). The function ***f(x)*** is the measured profile where the red line indicates the measured elevations at 1-m cross-shore intervals as well as gradient line ***g(x)***, depicted in dark blue (Fig. 2).

The measured profile ***f(x)*** was then divided into cross-shore segments. Segments were defined each time the profile's elevation intersected the gradient line ***g(x)***, indicating a change in the profile shape (e.g., from convex to concave). These inflection points were determined using the difference between ***f(x)*** and ***g(x)***.

$$\text{Let } D(x_i) = f(x_i) - g(x_i) \tag{1}$$

where x_i is any point in the gradient line (Fig. 2). A point is selected as an inflection point if the following criteria are met:

1. $D(x_i) = 0$ (when the profile lies on top of the gradient line)
2. $D(x_{i+1}) > 0$ and $D(x_i) < 0$ (profile is moving across gradient line (concave to convex))
3. $D(x_{i+1}) < 0$ and $D(x_i) > 0$ (profile is moving across gradient line (convex to concave))

Inflection points ≤1m from each other are merged into one segment, while those > 1m apart are treated as separate segments of the beach

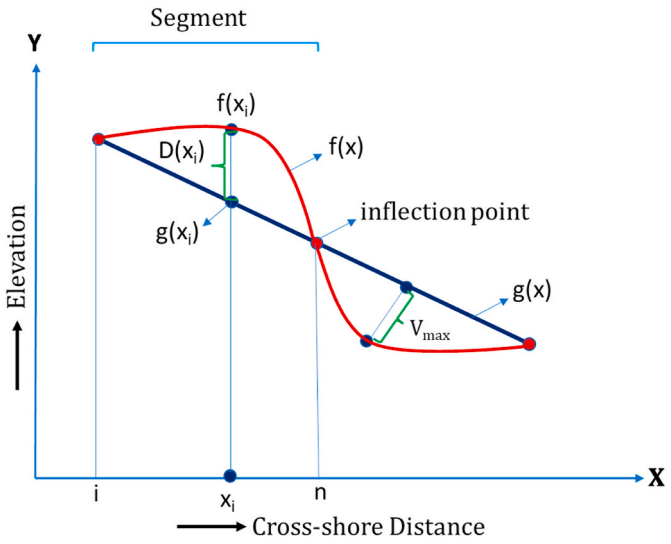

Fig. 2. Schematic view of the mathematically defined beach profile morphotype. The red curve is the beach profile, and the dark blue line connecting the profile is the gradient line. (For interpretation of the references to colour in this figure legend, the reader is referred to the Web version of this article.)

profile. Segments shorter than 1m in length are excluded to prevent misclassification of minor fluctuations. The primary inflection points are determined based on curvature magnitude and segment length. A flowchart detailing the process of inflection point selection is provided in Supplementary Fig. 1.

Given the inflection points, gradient line ***g(x)***, and profile ***f(x)***, we then calculate the curvature of each of the segments. The curvature on top of the gradient line is considered as positive and the curvature down the gradient line is regarded as negative. *D(x)* is calculated every 1 m interval in each segment to quantify the curvature. Curvature (representing one segment) is measured as the sum of the difference between the profile elevation and the gradient line within each segment.

$$Cur_{X_{i\ldots n}} = \sum_{t=i}^{t=n} D_{X_t}, where\ X_{i\ldots n} \tag{2}$$

where, the profile segment is considered convex when the following condition is met.

$$Cur_{X_{i\ldots n}} \geq 0.1 \tag{3}$$

Conversely, the profile segment is regarded as concave when the following circumstance occurs:

$$Cur_{X_{i...n}} \leq 0.1 \quad (4)$$

When considering profiles that have small curvatures, we classify them as linear if the curvature for a segment and the maximum vertical distance ***(V_{max})*** between the gradient line and profile segment is less than 0.10 m.

$$Cur_{X_{i...n}} \; and \; V_{max} \leq \pm 0.1 \quad (5)$$

Finally, the percentage of the individual profile segments was calculated. To determine the percentage of the individual profile segments (proportion of Concave, Convex, or Linear segments of the profile), we need to know the length of the entire profile as well as the length of the segment:

$$P_s = \frac{P}{L} \times 100 \quad (6)$$

where P is the length of the profile segment and L is the length of the entire profile.

The Profile Morphotype Index (Γ) (Eq. (7)) is a function of the percentage distribution of the individual profile segments and profile shape (Table 3 and Fig. 2):

$$\Gamma = \frac{S_{f1} \sum P_s E_f}{n S_{f2}} N_f \quad (7)$$

where, P_s is the profile segment percentage, E_f is the Elevation Factor, N_f = Normalization Factor, n = Number of Profile Segments, and S_{f1} = Sign Factor One, S_{f2} = Sign Factor Two.

The Elevation Factor (E_f) is 0 when the maximum vertical extent (V_{max}) is ≤ ±0.10 m and considered 1 when the maximum vertical extent (V_{max}) is > ±0.1m. On the other hand, the value of the Normalization Factor (N_f) is 1 except in the case when a cross-shore profile has a 60–89 % Convex or Concave portion, in all other cases, the Normalization Factor (N_f) *is 1.90*. Sign Factor-1 (S_{f1}) and Sign Factor-2 (S_{f2}) range between −1 and +1. The value of Sign Factor-1 (S_{f1}) is +1 when the percentage of concave segments of a profile is <40 % whereas the value is −1 when the percentage of concave segments of a profile is >40 %. Sign Factor-2 (S_{f2}) is −1 when the first segment is Convex and the second segment is Concave in a profile with two segments, and +1 for the remaining cases. Finally, considering all the surveyed profiles in Gamay and using the equation, we have identified a total of 10 profile morphotypes varying between 1.000 and −1.000 (Table 3).

The segment percentage thresholds used for morphotype classification were established through systematic testing, while the threshold for defining linear morphotypes was informed by the natural variability of beach profiles and measurement precision. A sensitivity analysis of the Γ index demonstrates its responsiveness to variations in segment percentages thresholds (Supplementary Fig. 4–10), linear classification thresholds (±0.05 m, ±0.10 m, ±0.15 m; Supplementary Fig. 2), and adjustments to the Normalization Factor (N_f = 1 and 1.9; Supplementary Fig. 3). The Γ index was more sensitive to changes in linear classification thresholds than to the Normalization Factor, whereas variations in profile segment percentages significantly influenced the classification and distribution of all morphotypes. Γ can be easily calculated using our open-source notebook (https://github.com/rvdeo/beb_morphotype_index).

Table 3
Percentage distribution of individual profile segments for calculating overall profile shape and Profile Morphotype Index (Γ) range.

Morphotypes	Percentage Distribution	Profile Morphotype Index (Γ)
Concave	≥90 % Concave (segment <10 % other)	−1.000
Mostly Concave	60–89 % Concave and 11–40 % Linear or Convex	−0.570 to −0.950
Concave-Convex	41–59 % Concave (first segment) and 41–59 % Convex	−0.500
Linear Concave	41–59 % Linear and 41–59 % Concave	−0.205 to −0.295
Linear	≥90 % Linear (segment <10 % other)	0.000
Mostly Linear	60–89 % Linear and 11–40 % Concave or Convex	0.055 to 0.200
Linear Convex	41–59 % Linear and 41–59 % Convex	0.205 to 0.295
Convex-Concave	41–59 % Convex (first segment) and 41–59 % Concave	0.500
Mostly Convex	60–89 % Convex and 11–40 % Linear or Concave	0.570 to 0.950
Convex	≥90 % Convex (segment <10 % other)	1.000

3.3. Hydrodynamic data

This study used offshore wave data from the Sydney Waverider buoy supplied by Manly Hydraulics Laboratory (NSW Government) and located in ~90 m water depth ~30 km north of the entrance to Gamay (01/01/2016–01/01/2023). These data include hourly significant wave height (H_s), maximum wave height (H_{max}), mean periods (T_z), peak period (T_p) and wave direction (θ). These hourly wave parameters were averaged into daily and 7-day moving averages to characterise the typical (non-storm) wave climate and storm wave climate. Next, we calculated deep-water wave power (P) following Komar (1998),

$$P = EC_g \quad (8)$$

where, wave energy (E) is expressed as

$$E = \frac{1}{8} \rho g H_s^2 \quad (9)$$

where, ρ is seawater density (1025 kg/m^3), g is gravitational acceleration (9.81 m/s); and wave group velocity (C_g), in Equation (1), is expressed as

$$C_g = \frac{g T_z}{2\pi} n \quad (10)$$

where, n is 0.5 for deep water waves.

We identified storms using the peaks-over-threshold method (Harley et al., 2017), considering a threshold of H_s > 3 m (95th percentile), a minimum storm duration of at least 6 h and an independence between storms of 24 h (Shand et al., 2010). Storm exposure for the BEBs in Gamay was determined by considering offshore storm wave direction against the estuary entrance orientation and calculated by counting storms with wave directions (95–175°) conducive to direct propagation into Gamay. We focused our analysis on two storm events from distinct offshore directions (SSE and ENE) to verify the changes in the shape of the upper beach profiles in terms of quantifiable morphotype variability due to storm waves.

4. Results

4.1. Dynamics of BEB profiles

The subaerial beach profiles from the four BEBs (n = 774) studied in Gamay had beach widths (i.e., back beach to 0 m MSL) ranging from 25 to 45 m (Fig. 3). Lady Robinsons and Yarra Bay had the widest beaches (mean 45 m) compared to Currewol (mean 25 m) and Congwong (mean 35 m). Alongshore all BEBs, profile shapes have presented noticeable changes during the study periods, indicating distinct levels of coastal exposure with interchange between periods of upper beach accretion and erosion. In Fig. 3, a higher standard deviation (SD) indicates the portion of each beach profile that is more dynamic.

At Congwong, the most active part of the beach was at the eastern end (P3), adjacent to the headland and closest to the entrance of the bay (Fig. 1F). Frequent changes were observed in the shape of P3 (Fig. 3), which is near a small ICOLL. The SD was higher (≥0.4 m) close to the beach face (shoreline) for all the profiles (P1, P2, and P3), indicating

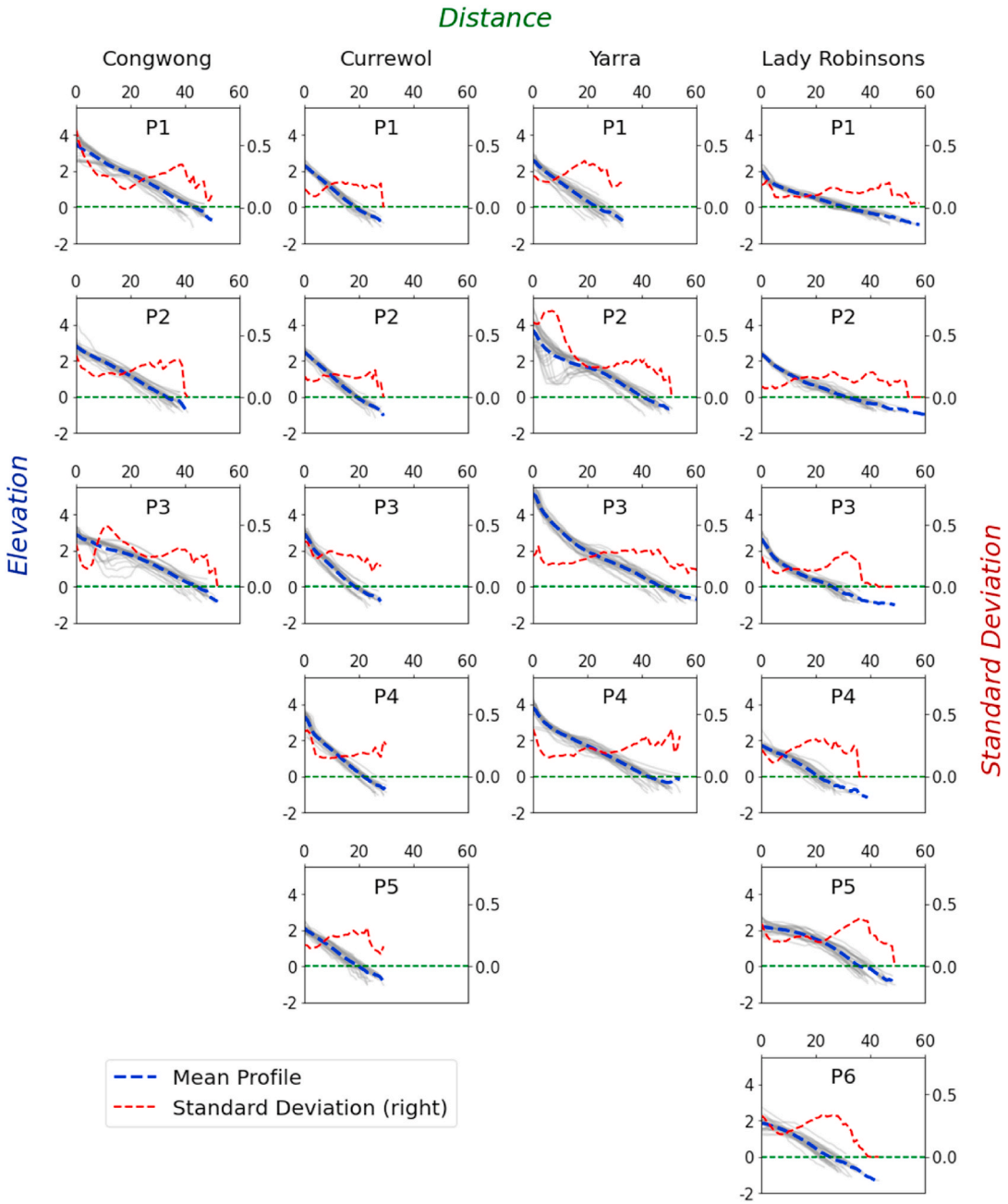

Fig. 3. Cross-shore beach profile plots. Each box shows the profile topography measurements (elevation presented in metres on the left y-axis) on a fixed transect (P1 and onwards) to each of the BEBs studied from May 2016 to March 2023. Beach profiles were measured from the back beach (distance 0 in the x-axis) to approximately 0 m MSL. Congwong, Currewol, Yarra, and Lady Robinsons are presented across the columns, respectively, from left to right. Grey lines show all elevation measurements for each specific transect, while the blue dashed line indicates the mean elevation (values on the left y-axis) and the red dashed line corresponds to the standard deviation (values on the right y-axis) along the profile. The green dashed line marks the 0 m MSL. (For interpretation of the references to colour in this figure legend, the reader is referred to the Web version of this article.)

large changes to the profile shape and shoreline position (Fig. 3).

At Currewol, the beach face morphology varied across all profiles (P1–P5) while there was minimal variability at the back beach part (SD 0.15 m) (Fig. 3). The area adjacent to the southern headland (P1) was the least active part of the beach (SD 0.2 m) while the most dynamic part (SD 0.35 m) was the exposed northern end (P5) (Fig. 3).

At Yarra Bay, profiles P1 and P2 at the exposed central region of the beach, away from the north headland and the south-central groyne, were the most dynamic with an SD of 0.56 m while the portion of the beach inside the south-central groyne (P4) was the least dynamic part with a SD of 0.25 m (Fig. 3). The beach (P3) to the south of the central groyne was highly dynamic (SD 0.5 m) and was also the location of an ICOLL.

On Lady Robinsons, the area (P4, P5 and P6) close to the southern groyne field presented more sediment deposition compared to the northern part of the beach (P1, P2 and P3) (Fig. 3). The beach face (elevation <1.5m) of all the profiles (P1–P6) had a higher SD (0.3–0.4 m) compared to the backshore (0.1–0.3 m). However, the beach face in the northern side (P1, P2 and P3) had a higher SD (0.4 m) compared to the beach face among the southern groyne field (P4, P5 and P6) (SD 0.3 m).

The shape of the profiles indicates decreasing sediment availability from Congwong, through Currewol and Yarra, to Lady Robinsons (Figs. 3 and 4). During the study period, the profile volume of Congwong

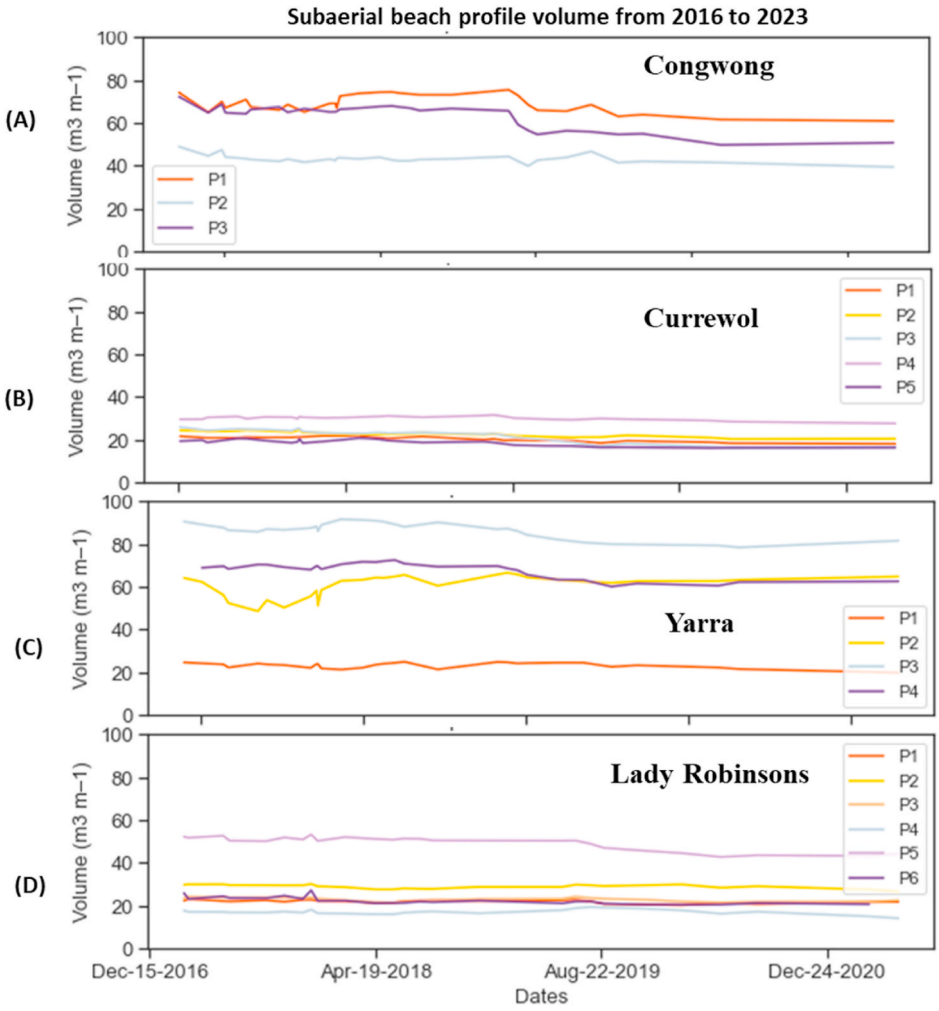

Fig. 4. Temporal changes of beach profile volume. The panel shows the fluctuation of the profile volume from 2016 to 2023 for all beaches. (A) Congwong (B) Currewol (c) Yarra and (D) Lady Robinsons.

fluctuated on average between 50 and 80 m^3/m, whereas Lady Robinsons' profile volume ranged from 20 to 30 m^3/m (Fig. 4). It should be noted that the southern groyne field in Lady Robinsons (i.e., P5) traps sediment and causes an increase in volume around those profiles. Furthermore, profile P3 at Yarra Beach was identified as a sediment-rich zone, with volumes ranging from 80 to 90 m^3/m, attributed to the influence of the adjacent central groyne (Fig. 4).

4.2. BEB morphotypes

The Profile Morphotype Index (Eq. (7)) indicated that the most common morphotypes at Congwong were *Convex* ($\Gamma = 1.000$) and *Mostly Convex* ($\Gamma = 0.570$ to 0.950) (Fig. 5). Around 40 % of the surveys along P1 and 50 % along P2 were *Mostly Convex* ($\Gamma = 0.570$ to 0.950), and 46 % of the surveys along P3 (were classified as *Convex* ($\Gamma = 1.000$) (Fig. 5).

At Currewol, 60 % and 63 % of P3 and P4 profiles, respectively, were classified as *Concave* ($\Gamma = -1.000$); however, it was not possible to determine a prevalent morphotype classification for the three other transects (P1, P2, and P5) due to the frequent transition among different morphotypes during the study period. For P1 and P5, the most frequent morphotype classification was *Mostly Convex* ($\Gamma = 0.570$ to 0.950) (24 % and 31 %, respectively). For P2, *Linear* ($\Gamma = 0.000$) (21 %) was the most frequent morphotype class (Fig. 5).

At Yarra Bay, all profiles were *Mostly Concave* ($\Gamma = -0.570$ to -0.950) to *Concave* ($\Gamma = -1.000$) with some temporal fluctuations (Fig. 5). P1 was 24 % of the time *Concave* ($\Gamma = -1.000$) and 18 % *Mostly Concave* ($\Gamma = -0.570$ to -0.950). For P2 and P3, these percentages were nearly 17 % and 70 % *Concave* ($\Gamma = -1.000$), and 30 % and 31 % *Mostly Concave* ($\Gamma = -0.570$ to -0.950), respectively. P4 is *Concave* ($\Gamma = -1.000$) 55 % of the time, followed by *Mostly Concave* ($\Gamma = -0.570$ to 0.950) for 28 % of the time.

Lady Robinsons shows two distinct regions according to the morphotype classification. The section of the beach with no human interventions (P1, P2, and P3) was *Concave* ($\Gamma = -1.000$) to *Mostly Concave* ($\Gamma = -0.570$ to -0.950); whereas the area with the groins (P4, P5, and P6) were *Mostly Convex* ($\Gamma = 0.570$ to 0.950) to *Convex* ($\Gamma = 1.000$). *Concave* morphotypes ($\Gamma = -1.000$) represent 70 %, 48 % and 80 % of the survey for the profiles in P1, P2, and P3, respectively, while *Mostly Concave* ($\Gamma = -0.570$ to -0.950) represent 30 %, 49 % and 19 % in P1, P2, and P3, respectively. In contrast, 39 % of the surveys of P4 represent *Convex* ($\Gamma = 1.000$) and 33 % *Mostly Convex* ($\Gamma = 0.570$ to 0.950). Similarly, P5 shows around 80 % of the total surveys along these transects are *Convex* ($\Gamma = 1.000$) and the remaining percentage are *Mostly Convex* ($\Gamma = 0.570$ to 0.950) (Fig. 5). The *Convex* ($\Gamma = 1.000$) and *Mostly Convex* ($\Gamma = 0.570$ to 0.950) morphotypes in P6 denote around 76 % and 16 % of the total measurements along this line.

4.3. Hydrodynamics

Between January 2016 and February 2023, the average wave energy offshore was moderate to high, predominantly reaching the wave buoy from SSE (137°) with significant wave height (H_s) of 1.56 m, peak

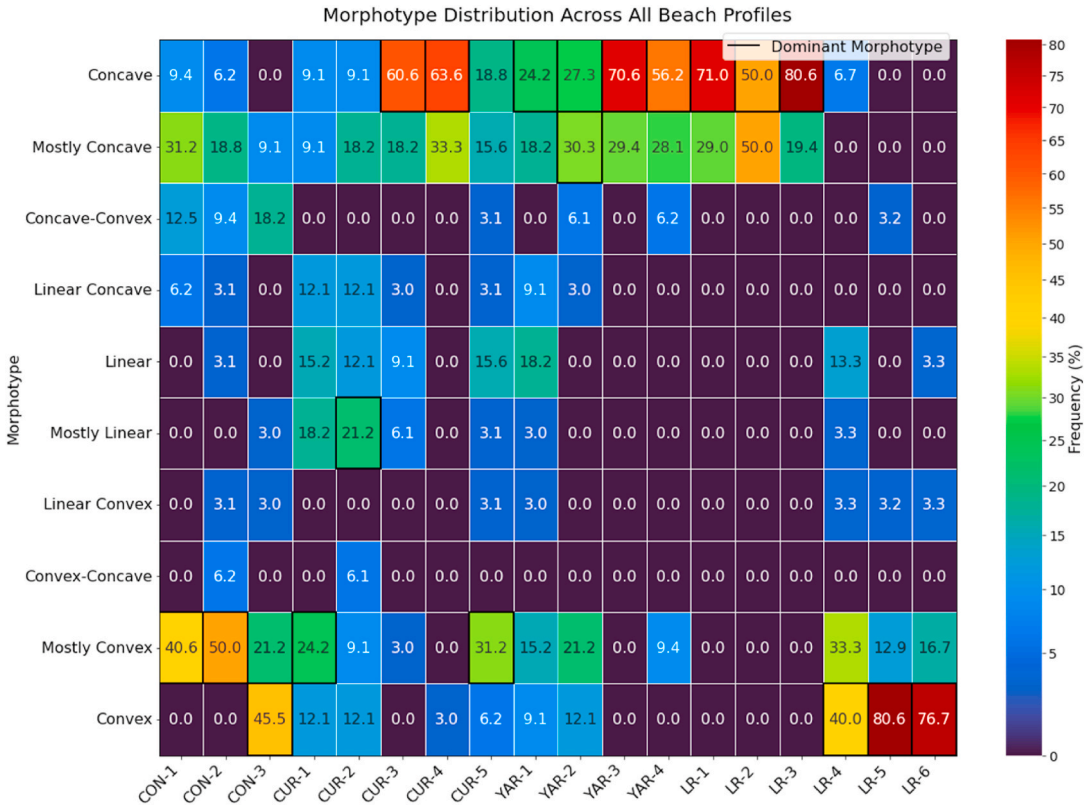

Fig. 5. Morphotype distribution across all surveyed beach profiles, represented as a heatmap of relative frequency (%). The x-axis indicates individual beach profiles, while the y-axis categorizes morphotypes from Concave to Convex. Warmer colours indicate a higher frequency of occurrence, with outlined cells highlighting the dominant morphotype for each profile. This percentage of occurrence is calculated by the total number of surveys along a transect divided by the number of individual morphotypes. Here, CON=Congwong, CUR=Currewol, YAR=Yarra, LR=Lady Robinson, and the number represent the profile. (For interpretation of the references to colour in this figure legend, the reader is referred to the Web version of this article.)

periods (T_p) of 9.56s, and mean periods (T_z) of 5.6s (Fig. 6). A total of 125 storms were observed, averaging 17 per year. Average storm conditions were a duration of 33 h, H_s of 3.58 m, T_p of 10.72 s, T_z of 7.6 s, θ of 167° and wave power (P) of 920 Kw/m (Fig. 6). The entrance to Gamay has a SE (about 135°) orientation and is 1.1 km wide, allowing wave propagation into the bay for 34 % of the storms (42 storms) which are from directions between 95 and 175° (Fig. 6). Throughout the study period, 28.8 % of the storms (36 storms) originated from the SSE, 62.4 % from the S (78 storms), 4 % from the ESE (5 storms), 3.2 % from the SSW (4 storms), and only 1.6 % from the E (2 storms) (Fig. 6).

The first storm considered in this study occurred in June 2016 and was a slow-moving East Coast Low (ECL) that generated waves (average H_s = 3.76 m) that reached up to 6.5 m offshore, and caused extensive erosion on the Gamay BEBs. Offshore H_s peaked on 5 June, and for the following 10 h, H_s was over 6 m, with mean periods of up to 12 s, and a directional range varying from NE to E. The average wave power for this storm was 516 kw/m. The second storm considered was in May–June 2018 with an average offshore H_s of 3.6 m, maximum H_s of 5.7 m, and mean periods of up to 7.5 s. The average wave power for this storm was 88 kw/m and the directional range varied from S to SE.

4.4. Profile morphotype response to storm waves

SSE storm: During the storm on 31 May – 3 Jun 2018 (Hs < 4m) SSE waves propagated into Gamay. Congwong experienced considerable change in the profile morphotypes across all transects. P1 and P3, adjacent to the headlands, shifted from *Concave-Convex* ($\Gamma = -0.500$) to *Mostly Concave* ($\Gamma = -0.570$ to -0.950) (P1) and *Convex* ($\Gamma = 1.000$) to *Mostly Concave* ($\Gamma = -0.570$ to -0.950) (P3), while the central part of the beach (P2) showed the largest shift in morphotype from *Mostly Convex* ($\Gamma = 0.570$ to 0.950) to the complete opposite *Mostly Concave* ($\Gamma = -0.570$ to -0.950) (Fig. 7B). Volume changes were evident (Fig. 7B) with profiles P1, P2, and P3 of Congwong losing about 4.6, 5.0, and 5.1 m^3 of sediment, respectively (Fig. 8).

At Currewol, the area adjacent to the southern headland (P1) (Fig. 7C) shifted from *Mostly Convex* ($\Gamma = 0.570$ to 0.950) to *Mostly Concave* ($\Gamma = -0.570$ to -0.950), while the profile at the mid-point between the south headland and the groyne (P2) and the exposed northern end (P5) changed from *Convex-Concave* ($\Gamma = 0.500$) to *Mostly Concave* ($\Gamma = -0.570$ to -0.950) and *Linear Concave* (-0.205 to -0.295) to *Mostly Concave* ($\Gamma = -0.570$ to -0.950) respectively. The associated loss of sediment volume in the profiles P1, P2, and P5 was around 3.1, 0.2, and 2.2 m^3, respectively (Fig. 8). Meanwhile, the profile in the lee of the central groyne (P4) and the exposed southern side of the groyne (P3) converted from *Concave* ($\Gamma = -1.000$) to *Mostly Concave* ($\Gamma = -0.570$ to -0.950) and *Concave* ($\Gamma = -1.000$) to *Mostly Concave* ($\Gamma = -0.570$ to -0.950) respectively (Fig. 7C), with sediment accretion (1.3 and 2.3 m^3, respectively) in these two profiles.

In Yarra Bay, the headland adjacent and exposed area of the beach (P1) and the exposed profile at the mid-point between the north headland and the south-central groyne (P2) remained unchanged as *Concave* ($\Gamma = -1.000$). Similarly, the central part of the beach inside the south-central groyne (P3, P4) remained *Concave* ($\Gamma = -1.000$) (Fig. 7D). Therefore, volume changes were small, Profile P1 and P4 of the Yarra experienced erosion (6.6 and 5.2 m^3) while P2 and P3 gained volume (1.1 and 2.8 m^3) due to the storm (Fig. 8).

At Lady Robinsons, which is the farthest from the entrance, very minor changes occurred in most of the profiles including those in the north area of the beach (P1, P3 and P4), and those in the southern groyne field (P5 and P6). In contrast, the only profile to change

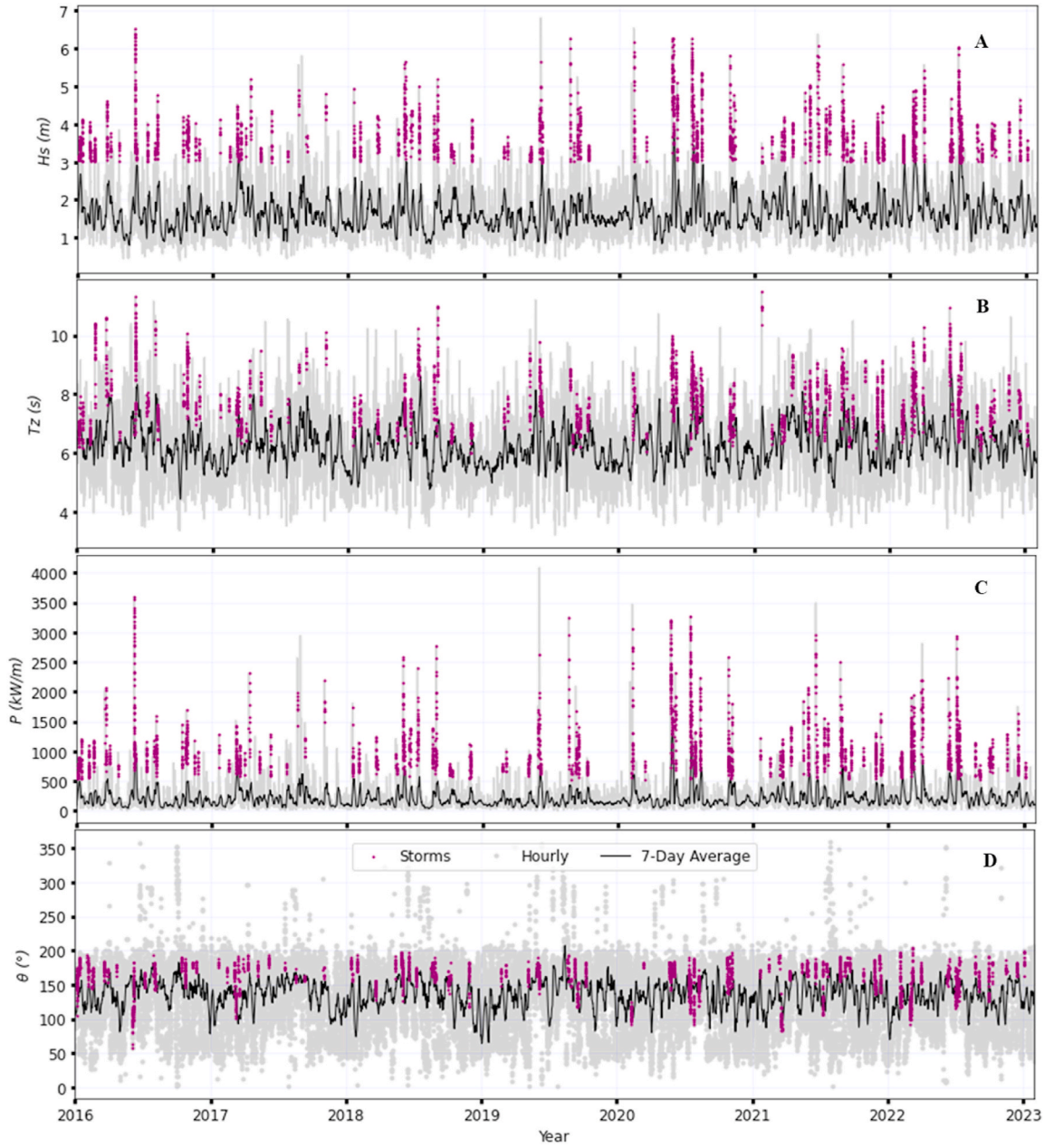

Fig. 6. Offshore wave parameters from 2016 to 2023, hourly (grey), 7-day average (black) and storms (purple) measurements. (a) Significant wave height (H_s), (b) average wave period (T_z), (c) wave power energy flux (P), and (d) wave direction (θ). (For interpretation of the references to colour in this figure legend, the reader is referred to the Web version of this article.)

morphotype because of this storm was at the north of the beach (P2), shifting from *Mostly Concave* (Γ = −0.570 to −0.950) to *Concave* (Γ = −1.000) (Fig. 7E). Almost all profiles of Lady Robinsons gained some sediment (7.6, 6.4, 4.9, 7.2, 6.3, and 6.9 m^3 in P1, P2, P3, P4, P5, and P6, respectively) due to this storm (Fig. 8).

ENE storm: At Congwong, the middle of the beach (P2) changed from *Mostly Convex* (Γ = 0.570 to 0.950) to *Linear* (Γ = 0.000) after this storm, while P1 and P3 were less impacted and remained *Mostly Convex* (Γ = 0.570 to 0.950) and *Convex* (Γ = 1.000) respectively (Fig. 7B). This morphotype shifting was associated with respective loss of sediment (13.5, 11, and 16.9 m^3) at all three profiles (Fig. 8).

At Currewol, profile P1 switched from *Mostly Convex* (Γ = 0.570 to 0.950) to *Linear* (Γ = 0.000), while the Profiles P2 and P3 changed from *Mostly Linear* (Γ = 0.055 to 0.200) to *Linear* (Γ = 0.000) and *Mostly Concave* (Γ = −0.570 to −0.950) to *Concave* (Γ = −1.000), respectively (Fig. 7C). Meanwhile, profile P4 remained *Concave* (Γ = −1.000), and P5 changed from *Mostly Concave* (Γ = −0.570 to −0.950) to *Concave* (Γ = −1.000) (Fig. 7C). Looking into the profile volume, all profiles of Currewol showed small erosion (4.9, 5.7, 7.9, 5.4, and 0.1 m^3 from P1, P2, P3, P4, P5, and P5, Fig. 7C and 8).

At Yarra, P1 and P2 switched from *Convex* (Γ = 1.000) to *Mostly Convex* (Γ = 0.570 to 0.950) (Fig. 7D). On the other hand, Profiles P3 and P4 switched from *Mostly Concave* (Γ = - 0.570 to −0.950) to *Concave* (Γ = -1.000) (Fig. 7D). The associated volume loss related to this morphotype shifting was 5.25, 16.1, and 4.1 m^3 for the P1, P2, and P3 profiles, while there were negligible changes for P4.

At Lady Robinsons, which is farthest from the entrance, the only profile to change because of the ENE storm was P3, which shifted from *Mostly Concave* (Γ = −0.570 to −0.950) to *Concave* (Γ = −1.000) (Fig. 7E). All other profiles did not change (Fig. 7E). Lady Robinson's profiles experienced severe erosion due to this storm (8.7, 9.2, 2.4, 4.3, 12.6, and 12 m^3 for P1, P2, P3, P4, P5, and P6). This was due to the

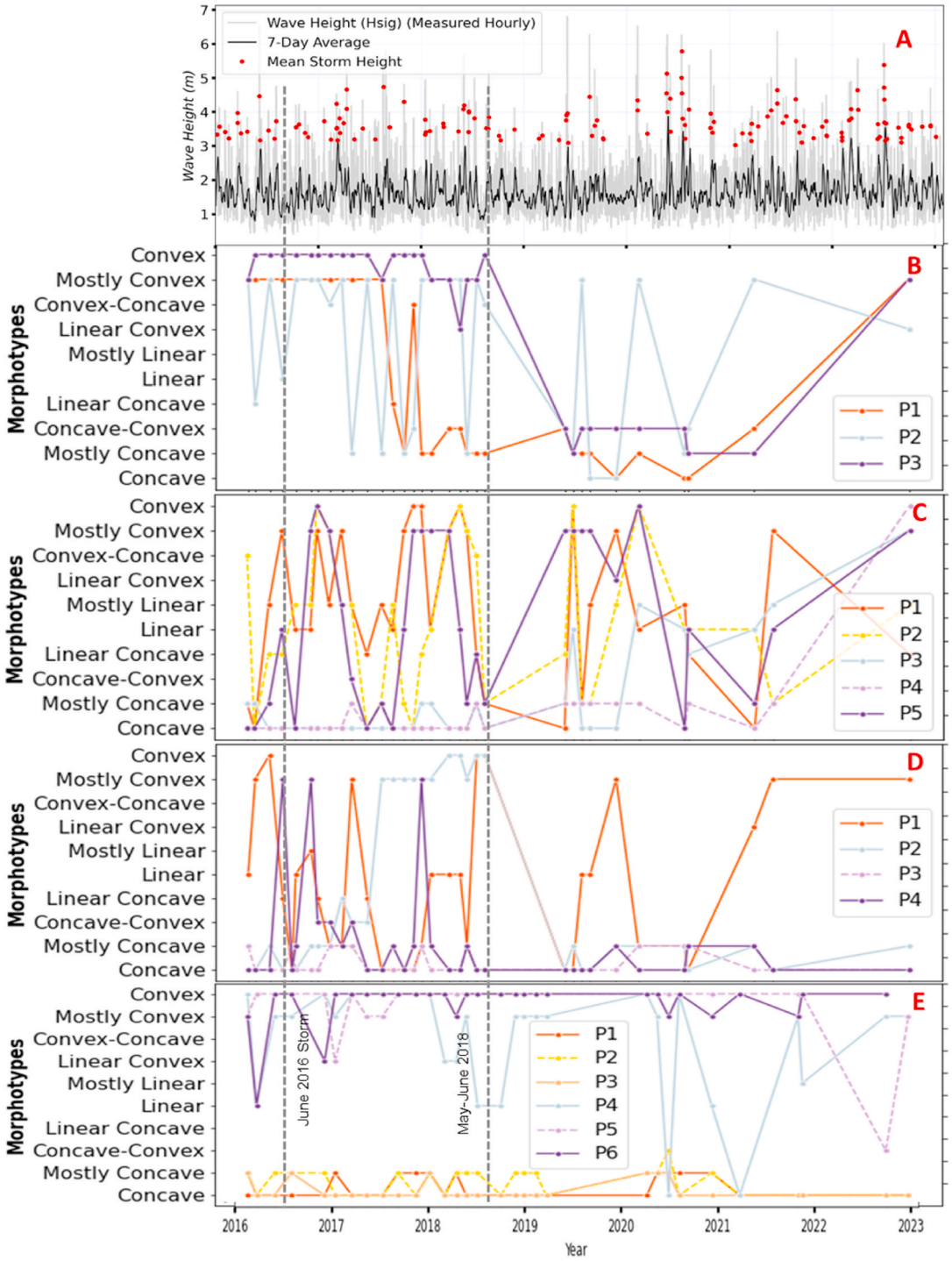

Fig. 7. Temporal dynamics of all profiles of the individual beaches and storm height. A. showing storm events with mean wave height and storm wave heights from 2016 to 2023. Dynamics of the beach profile, B. Congwong, C. Currewol, D. Yarra, E. Lady Robinsons.

impacts of locally generated wind waves in the distal part of the estuary associated with this storm.

5. Discussion

5.1. Quantitative classification of cross-shore profile morphotypes

This study proposes a new Profile Morphotype Index (Γ) that quantitatively classifies the cross-shore shape of BEBs (Eq. (10)). This index, tested on 774 profiles measured over 7 years at four BEBs in Gamay (SE Australia), is a step forward in quantifying the BEB morphodynamics. The method assigns profiles into 1 of 10 newly defined morphotypes (Fig. 9) with Γ values ranging from −1 to +1, varying from *Concave* (−1) through to *Linear* (0) through to *Convex* (+1) morphotypes. The proposed Profile Morphotype Index (Γ) (Equation (10)) successfully classified 99.5 % of all subaerial profiles (770 out of 774 profiles) with rare occurrence (0.5 %) of profiles with more than 3 cross-shore segments (combination), which occurred as a response to management interventions (e.g. artificial sand deposits) at Lady Robinsons; hence, due to the virtually negligible percentage of occurrence, the triple segment

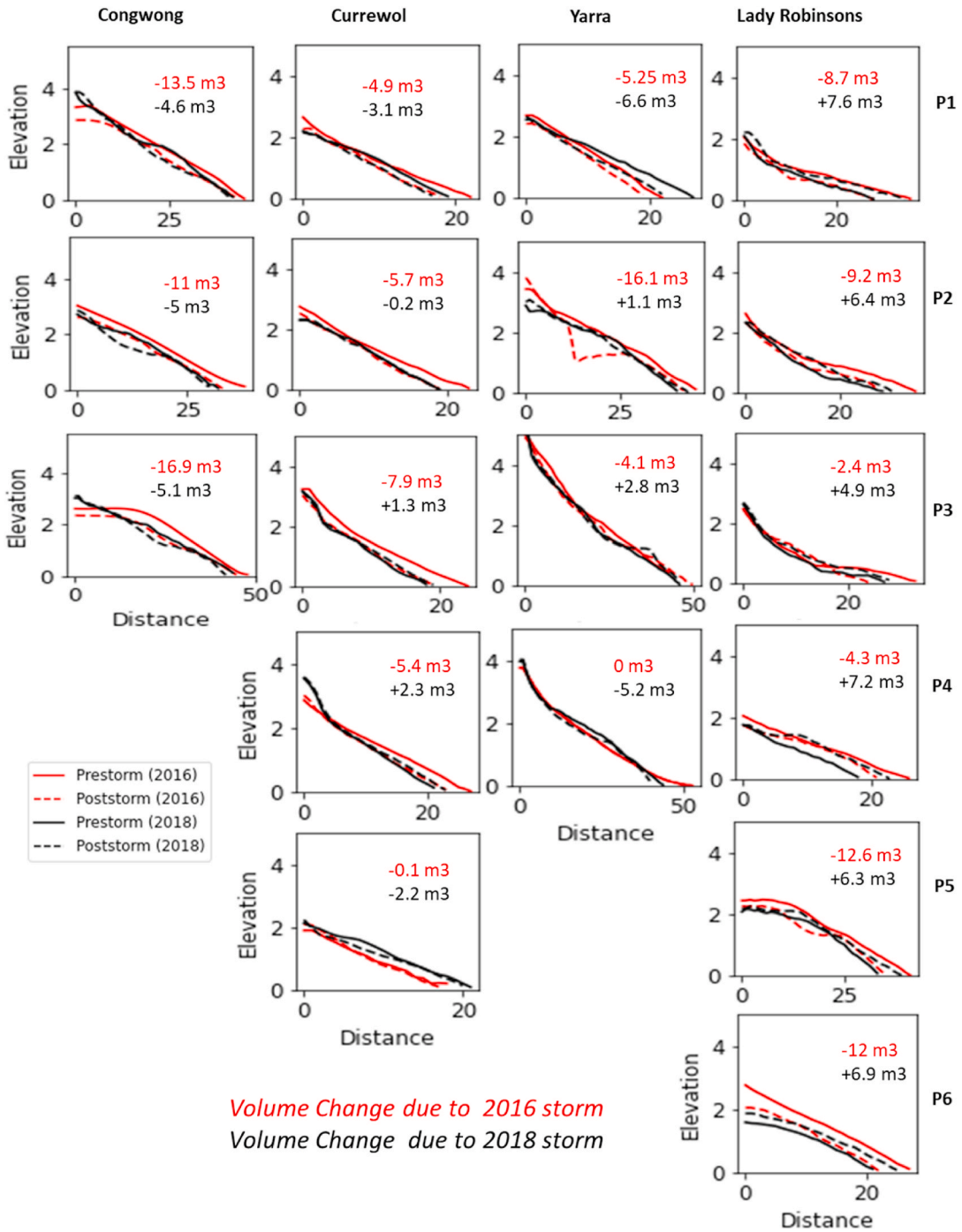

Fig. 8. Volume changes for each profile due to the 2016 and 2018 storms. Values in red indicate the net changes in profile volume before and after the 2016 storm, and values in black indicate the net changes in profile volume before and after the 2018 storm. (For interpretation of the references to colour in this figure legend, the reader is referred to the Web version of this article.)

combinations were not included in this morphotype index.

The Profile Morphotype Index is an extension of established qualitative and semi-quantitative methods that investigate cross-shore beach profile shapes on BEBs and low-energy beaches (Hegge et al., 1996; Makaske and Augustinus, 1998; Travers, 2007). Hegge et al. (1996) identified morphotypes based on the nearshore profiles, Makaske and Augustinus (1998) considered only the beach face portion of the profiles, and the morphotypes identified by Travers (2007) are based on both beach face and subtidal zones. In our approach, we measure the full subaerial part of the BEBs to classify the profile morphotypes. This study extends previous research, not by focusing on the coverage of the profile, but by transitioning from qualitative to quantitative classification. Focusing solely on the subaerial profile allows for consistent, repeatable analysis where subtidal data are often sparse or difficult to obtain, particularly in estuarine and embayed environments. This approach ensures practical applicability and standardization across a large dataset, offering a clear representation of beach morphology. Our method identifies more morphotypes, capturing subtle variations and enabling the detection of temporal changes.

Hegge et al. (1996) used cluster analysis to identify profile morphotypes and focused on the difference in morphotypes between low-energy and high-energy beaches. They identified four morphotypes

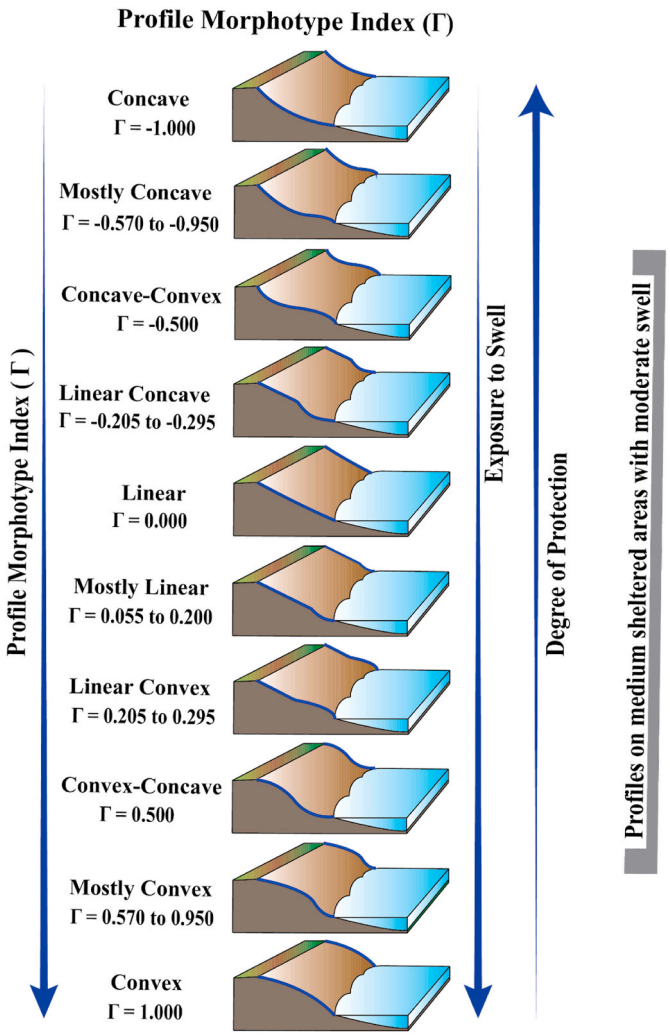

Fig. 9. Schematic 3D representation of profile morphotypes with morphotype index. This figure also shows the drivers responsible for morphotype variation. Here, the bold blue colour represents cross-shore profile morphotypes from (1) *Concave* to (10) *Convex*. Profile morphotypes index values represented as Γ ranging from −1 to +1. (For interpretation of the references to colour in this figure legend, the reader is referred to the Web version of this article.)

(concave, moderately concave, moderately steep, and steeped) for the low-energy beaches in a sheltered environment (Fig. 9). Morphotypes (concave, moderately concave, moderately steep) from Hegge et al. (1996)'s study are comparable to our study where moderately concave is *Mostly Concave* (Γ = −0.570 to −0.950) and moderately steep is considered *Linear* (Γ = 0.000) in our study (Fig. 9). Our comparison with their findings relies solely on the similarity in shape. However, while they associated the four morphotypes with sediment characteristics, they did not indicate which morphotype is sediment-starved and which one is sediment-enriched.

Makaske and Augustinus (1998) used a rapid semi-quantitative method for describing the shape of the beach profile with the help of a pantometer (an instrument for measuring angles of all kinds). They identified three morphotypes, namely "straight", "concave", and "convex-concave", which are comparable with the *Linear* (Γ = 0.000), *Concave* (Γ = −1.000), and *Convex-Concave* (Γ = 0.500) morphotypes defined here. They suggested that straight morphotypes form under low-energy conditions, whereas the convex-concave profile develops under higher energy conditions, with concave being intermediate. However, our study identified the Concave morphotype as having a low energy profile, the Convex as characteristic of high-energy settings (nearly open coast, e.g., Congwong), and the Linear morphotype as indicative of intermediate energy conditions. These differences likely arise from the methodological distinctions between the studies. Our approach incorporates a broader range of morphotypes and classifies beach profiles based on a more detailed, continuous index (Γ), whereas the previous study used a more simplified classification scheme with fewer morphotypes and different criteria for profile categorization.

Travers (2007) proposed morphotypes using curve-fitting techniques to define mean profile shapes. They identified four morphotypes, i.e., exponential, segmented, concave-curvilinear, and convex-curvilinear. In the context of this paper, exponential is comparable with *Concave* (Γ = −1.000), segmented with *Linear Convex* (Γ = 0.205 to 0.295), convex-curvilinear with *Convex* (Γ = 1.000), and concave-curvilinear with *Concave-Convex* (Γ = −0.500) based on the exposure in our study (Fig. 9). Here, exponential and segmented forms are associated with the lowest level of exposure, while concave-curvilinear and convex-curvilinear forms are related to higher levels of exposure.

The quantitative classification of the shape of the profiles allowed by computing Γ contributes to the understanding of BEB morphodynamics. For example, Γ can identify distinct patterns in the beach (morphotypes) related to erosion and depositional processes that are further related to wave forces including storms and tides. While our approach has the potential to be used for any beach profile, it is limited to classifying the shape of the profile only and should be used in combination with other quantitative parameters such as gradient and wave incidence. The beaches in the study area vary in aspect, orientation, distance from the estuary entrance, wave exposure, headland influence, and human intervention, demonstrating the index's versatility.

Open-coast beaches, though classified differently (Wright and Short, 1984; Short, 1993), may still be assessed using Γ. However, more extended profiles in open coast beaches increase the likelihood of multiple segments, potentially requiring profile length and segmentation adjustments. Open coasts are characterized by dynamic longshore processes, including bar-rip systems and significant sediment transport. Since the Γ index focuses on cross-shore shape, it may overlook features like bar migration, cusps, and megacusps. Regions with strong tidal currents or significant anthropogenic modifications may require adaptations.

5.2. Drivers of morphotype variability

The Profile Morphometric Index (Γ) accounts for BEB profiles that are exposed to a range of wave exposures, beach aspect, the presence/absence of headlands, and human interventions such as groins and adjacent dredging activities (Fig. 1). When comparing the profile morphotypes index with the wave signatures undertaken by Rahbani et al. (2022), the relationship between profile shape and wave climate becomes apparent. Our results indicate that BEBs far from the entrance, with small swell influence (Rahbani et al., 2022) (e.g., P1, P2, and P3 at Lady Robinsons) are typically characterised by *Concave* morphotypes (Γ = −1.000), whereas BEBs that are close to the entrance and dominated by swell (Rahbani et al., 2022) (e.g., P2 at Congwong) typically have *Convex* morphotypes (Γ = 1.000) (Fig. 9).

The morphotypes also vary depending on their alignment with the wave incidence angle. Swash-aligned beaches generally exhibit concave profiles due to minimal longshore transport and finer sediment accumulation (Masselink et al., 2006; Short, 1993). For example, profiles at Currewol and Yarra Bay are predominantly *Mostly Concave* (Γ = −0.570 to −0.950) to *Concave* (Γ = −1.000), reflecting their sheltered geomorphological settings. However, Congwong indicated predominantly *Mostly Convex* (Γ = 0.570 to 0.950) to *Convex* (Γ = 1.000) morphotypes, due to the exposure to higher wave energy as it is located close to the estuary entrance. Lastly, Lady Robinsons behaves as a drift-aligned beach, displaying different profile responses along its extension. The section unaltered by human interventions (P1–P3) remained *Mostly Concave* (Γ = −0.570 to −0.950) to *Concave* (Γ =

−1.000), likely due to reduced wave energy farther from the estuary entrance (Wright and Short, 1984). However, the highly modified section with hard coastal structures (P4–P6) exhibited *Mostly Convex* (Γ = 0.570 to 0.950) to *Convex* (Γ = 1.000) morphotypes, due to groin-induced sediment retention (Ranasinghe and Turner, 2006). This shows that while beach alignment influences the profile morphotypes, factors like wave exposure, sediment supply, and human modifications play a key role in shaping beach profiles.

Anthropogenic interventions such as groins, revetments, and seawalls impact the shape of the beach profiles, shifting the profile into different morphotypes. Morphotypes of BEBs with a history of anthropogenic intervention often differ from those of natural BEBs (Portz et al., 2024). In Gamay, human interventions have altered swell energy dynamics, causing diffraction, refraction, and reflection onto previously sheltered shorelines in Yarra Bay and Currewol. For instance, at Lady Robinsons, changes in the width are likely caused by dredging operations in the 1970s and 1990s to accommodate the Sydney Airport runways and the port navigation channel (Fellowes et al., 2021).

On the other hand, the introduction of groins created localized accretion hotspots. According to our findings, BEBs adjacent to groins are typically *Concave* morphotypes (Γ = −1.000) on the wave-exposed side and *Convex* morphotypes (Γ = 1.000) on the wave-protected (shadowed) side, which are indicative of erosive and accretionary conditions, respectively, on each side of the hard structure. For example, Profile 4, 5, and 6 of Lady Robinsons are located on the protected side of the groins (Fig. 1) and are *Mostly Convex* (Γ = 0.570 to 0.950) to *Convex* (Γ = 1.000) (Fig. 6). A higher accretion rate occurs (between +0.48 m/year and +0.61 m/year) particularly in the southern section (areas inside the groins) of Lady Robinsons, following the construction of multiple groins (1976–2022) (Fellowes et al., 2021). Similarly, Profile P1 and P2 (protected side of the groin) of the Yarra are *Mostly Convex* (Γ = 0.570 to 0.950) to *Convex* (Γ = 1.000), reflecting the sediment accumulation in this area. At Yarra Bay, the pre-groyne erosion rate (before 1976) was approximately −0.88 m/year. However, following groyne construction (1976–2017), the bay experienced accretion at rates ranging from +0.42 to +1.80 m/year, likely contributing to the observed *Convex (Γ = 1.000)* morphotypes. Local geomorphology also influences beach morphotypes by modifying wave energy and sediment dynamics. BEBs adjacent to rocky headlands (e.g., Profile P4 at Yarra) are typically *Concave* morphotypes (Γ = −1.000) (Fig. 9). This is related to the presence of headlands inducing wave attenuation and lowering the rate of deposition leading to *Concave (Γ = -1.000)* beach profiles (Short, 2010; Wright and Short, 1984).

Conversely, our results indicate that when wave exposure facilitates beach recovery following storms, or when sediment accumulation is enhanced by structures such as groins, as observed in sites like Congwong and Profile 3 of Yarra, the resulting beach morphotypes are typically *Convex (Γ = 1.000)* (Fellowes et al., 2021; Gallop et al., 2020) (Fig. 1). In contrast, sediment-starved BEBs that do not recover following typical open coast beach processes, for example, the relict beach of Lady Robinsons tend to display more *Concave (Γ = -1.000)* morphotypes (Fig. 1). Our results agree with Travers (2007) and Hegge et al. (1996), showing a consistent relationship between profile morphotype and exposure levels. Travers (2007) indicated that highly protected beaches typically exhibit exponential and segmented forms (similar to Concave profiles defined in this study), whereas more exposed beaches tend to show convex curvilinear profiles (like the Convex profiles in our study). Similarly, Hegge et al. (1996) noted that beaches with concave and moderately concave profiles are associated with higher levels of protection.

Finally, storm waves can cause morphotypes to change depending on their predominant direction. For example, the middle profile (P2) of the Congwong showed the largest shift in morphotype from *Mostly Convex* (Γ = 0.570 to 0.950) to *Mostly Concave* (Γ = −0.570 to −0.950) in response to the 31 May – 03 Jun 2018 storm, which generated waves from SSE direction. On the other hand, the same profile (P2) changed from *Linear* (Γ = 0.000) to *Mostly Convex* (Γ = 0.570 to 0.950) due to the 4–7 June 2016 storm that generated ENE waves. The orientation of the Congwong beach protects the embayment from waves coming from ENE. In addition to the direction, storm power alters beach morphotypes by increasing wave action, which reshapes beach profiles. For example, the impact of the ENE storm on the Gamay beaches was higher than the SSE probably due to the fact that the SSE storm gradually weakened as it approached the shore, while the ENE storm was more powerful and generated strong winds within Gamay, despite the storm's direction not aligning with the orientation of the Gamay entrance (BOM). This issue was also addressed by Hegge et al. (1996) stating that sometimes the profile morphotypes are misfitted to what we are expecting due to the characteristics of the storm event. Morphotype shifts during SSE and ENE storms indicate that differences in wave power, direction, and storm duration are key controlling factors.

6. Conclusion

This study presents a novel approach to quantitatively classify the subaerial cross-shore profile shape into ten distinct morphotypes using the proposed Profile Morphotype Index (Γ). The index uses the profile parameters to compute a unique value ranging from −1 (*Concave*) to +1 (*Convex*). This is an important step towards a quantitative morphodynamic classification of BEBs.

We calculated Γ for 774 profiles near Sydney (SE Australia) and found our index correctly classified 99.5 % of the profiles over 7 years. Profiles located in sediment-starved areas were correctly classified as *Concave (Γ = −1.000)* while profiles in areas with sufficient sediment supply were classified as *Convex (Γ = −1.000)*. Equally, Γ successfully explained erosion due to storm incidence, transitioning profiles from *Convex* (Γ = 1.000) to *Concave* (Γ = −1.000), and deposition, transitioning profiles from *Concave* (Γ = −1.000) to *Convex* (Γ = 1.000).

The quantitative characterisation of the shape of beach profiles is important to objectively compare profiles between different sites. Future research can use these morphotypes to develop a universal model of BEB morphodynamics that will facilitate a deep understanding of the variability in BEB profiles and the development of BEB-focused management tools.

CRediT authorship contribution statement

Md Yousuf Gazi: Writing – original draft, Validation, Software, Methodology, Formal analysis, Data curation, Conceptualization. **Thomas E. Fellowes:** Writing – review & editing, Supervision, Software, Resources, Project administration, Conceptualization. **Ratneel Deo:** Writing – review & editing, Software, Data curation. **Ana P. Silva:** Writing – review & editing, Supervision, Resources, Project administration. **Lachlan Perris:** Writing – review & editing, Resources, Data curation. **Ana Vila-Concejo:** Writing – review & editing, Supervision, Resources, Project administration, Funding acquisition, Conceptualization.

availability

The sample beach profile data and the Jupyter Notebook for calculating the Profile Morphotype Index (Γ), along with all relevant details, are available at the following link: https://github.com/rvdeo/beb_morphotype_index. Additionally, the results of the sensitivity analysis for linear thresholds, Normalization Factor, and profile segment percentage cutoffs used in the Profile Morphotype Index (Γ) calculation are provided in the supplementary information. A flowchart outlining the method for selecting inflection points is also included in the supplementary material.

Declaration of competing interest

We confirm there are no impediments to publication, including the timing of publication and presented data in the manuscript. Authors have no conflict with the submitted content. The authors have no financial interest.

Acknowledgements

We acknowledge and pay respect to the traditional custodians of the First Nations Lands and Sea Country on which this research was conducted. We are grateful for the funding from a Partnership Collaboration Award between The University of Sydney and The University of California, Davis. We also thank the Macquarie University New Staff Grant and Research Development Grant for funding fieldwork. Manly Hydraulics Laboratory for providing wave data used in this study. RTK data were collected with the use of a remote network academic subscription provided by HxGN SmartNet Australia. We extend our heartfelt gratitude to the University of Dhaka for providing the 'Bangabandhu Overseas Scholarship' and supporting MDG.

Appendix A. Supplementary data

Supplementary data to this article can be found online at https://doi.org/10.1016/j.ecss.2025.109373.

Data availability

Data will be made available on request.

References

Austin, T., Vila-Concejo, A., Short, A., Ranasinghe, R., 2018. A multi-scale conceptual model of flood-tide delta morphodynamics in micro-tidal estuaries. Geosciences 8 (9), 324. https://doi.org/10.3390/geosciences8090324.

Brand, E., Ramaekers, G., Lodder, Q., 2022. Dutch experience with sand nourishments for dynamic coastline conservation – an operational overview. Ocean Coast Manag. 217, 106008. https://doi.org/10.1016/j.ocecoaman.2021.106008.

Carrasco, A.R., Ferreira, Ó., Matias, A., Freire, P., 2012. Natural and human-induced coastal dynamics at a back-barrier beach. Geomorphology 159–160, 30–36. https://doi.org/10.1016/j.geomorph.2012.03.001.

Cowell, P.J., Kannane, A., 2000. Review of Changes to the Shores and Bed of Botany Bay: Past and Future. New South Wales Healthy Rivers Commission Occasional Paper 1005.

Croft, L.C., 2014. Interpolating Beach Profile Data Using Linear and Non-linear Functions.

Dowdy, A.J., Mills, G.A., Timbal, B., 2013. Large-scale diagnostics of extratropical cyclogenesis in eastern Australia. Int. J. Climatol. 33 (10), 2318–2327. https://doi.org/10.1002/joc.3599.

Dronkers, J., 1986. Tidal asymmetry and estuarine morphology. Neth. J. Sea Res. 20 (2), 117–131. https://doi.org/10.1016/0077-7579(86)90036-0.

Dugan, J.E., Airoldi, L., Chapman, M.G., Walker, S.J., Schlacher, T., 2011. Estuarine and coastal structures. In: Treatise on Estuarine and Coastal Science. Elsevier, pp. 17–41. https://doi.org/10.1016/B978-0-12-374711-2.00802-0.

Fellowes, T.E., Vila-Concejo, A., Gallop, S.L., Schosberg, R., de Staercke, V., Largier, J.L., 2021. Decadal shoreline erosion and recovery of beaches in modified and natural estuaries. Geomorphology 390, 107884. https://doi.org/10.1016/j.geomorph.2021.107884.

Gallop, S.L., Kennedy, D.M., Loureiro, C., Naylor, L.A., Muñoz-Pérez, J.J., Jackson, D.W. T., Fellowes, T.E., 2020. Geologically controlled sandy beaches: their geomorphology, morphodynamics and classification. Sci. Total Environ. 731, 139123. https://doi.org/10.1016/j.scitotenv.2020.139123.

Harley, M.D., Turner, I.L., Kinsela, M.A., Middleton, J.H., Mumford, P.J., Splinter, K.D., Short, A.D., 2017. Extreme coastal erosion enhanced by anomalous extratropical storm wave direction. Scientific Reports 7 (1), 6033.

Hegge, B., Eliot, I., Hsu, J., 1996. Sheltered sandy beaches of southwestern Australia. J. Coast Res. 12 (3), 748–760. https://www.jstor.org/stable/4298521.

Hughes, Z.J., FitzGerald, D.M., Howes, N.C., Rosen, P.S., 2007. The impact of natural waves and ferry wakes on bluff erosion and beach morphology in Boston harbor, USA. J. Coast Res. 497–501. https://www.jstor.org/stable/26481639.

Inman, D.L., Filloux, J., 1960. Beach cycles related to tide and local wind wave regime. J. Geol. 68 (2), 225–231. https://doi.org/10.1086/626655.

Jackson, N.L., Nordstrom, K.F., Eliot, I., Masselink, G., 2002. 'Low energy' sandy beaches in marine and estuarine environments: a review. Geomorphology 48 (1–3), 147–162. https://doi.org/10.1016/S0169-555X(02)00179-4.

Kennedy, D.M., 2002. Estuarine beach morphology in microtidal middle harbour, Sydney. Aust. Geogr Stud. 40 (2), 231–240. https://doi.org/10.1111/1467-8470.00176.

Kennedy, D.M., McCarroll, R.J., Fellowes, T.E., Gallop, S.L., Pucino, N., McSweeney, S.L., Vila-Concejo, A., Reef, R., Yuan, R., Carvalho, R., Quang, T.H., Ierodiaconou, D., 2023. Drivers of seasonal and decadal change on an estuarine beach in a fetch-limited temperate embayment. Mar. Geol. 463, 107130. https://doi.org/10.1016/j.margeo.2023.107130.

Komar, P.D., 1998. Beach Processes and Sedimentation. Prentice Hall.

Largier, J., Taggart, M., 2006. *Improving Water Quality at Enclosed Beaches: A Report on the Enclosed Beach Symposium Workshop (Clean Beaches Initiative)* (Clean Beaches Initiative). State of California State Water Resources Control Board.

Makaske, B., Augustinus, P.G.E.F., 1998. Morphologic changes of a micro-tidal, low wave energy beach face during a spring-neap tide cycle, rhône-delta, France. J. Coast Res. 14 (2), 632–645. https://www.jstor.org/stable/4298817.

Masselink, G., Kroon, A., Davidson-Arnott, R.G.D., 2006. Morphodynamics of intertidal bars in wave-dominated coastal settings—a review. Geomorphology 73 (1), 33–49. https://doi.org/10.1016/j.geomorph.2005.06.007.

Nordstrom, K.F., 1989. Downdrift coarsening of beach foreshore sediments at tidal inlets: an example from the coast of New Jersey. Earth Surf. Process. Landf. 14 (8), 691–701. https://doi.org/10.1002/esp.3290140804.

Nordstrom, K.F., Jackson, N.L., 2012. Physical processes and landforms on beaches in short fetch environments in estuaries, small lakes and reservoirs: a review. Earth Sci. Rev. 111 (1–2), 232–247. https://doi.org/10.1016/j.earscirev.2011.12.004.

Pepler, A., Dowdy, A., 2021. Intense east coast lows and associated rainfall in eastern Australia. J. Southern Hemisphere Earth Sys. Sci. 71 (1), 110–122. https://doi.org/10.1071/ES20013.

Portz, L.C., Villate-Daza, D., Bolívar-Anillo, H.J., Fontán-Bouzas, Á., Alcántara-Carrió, J., Manzolli, R.P., 2024. Impacts of anthropogenic structures in long- and short-term shoreline evolution of Santa Marta Bay (Colombian Caribbean). Geo Mar. Lett. 44 (2), 4. https://doi.org/10.1007/s00367-024-00768-3.

Rahbani, M., Vila-Concejo, A., Fellowes, T.E., Gallop, S.L., Winkler-Prins, L., Largier, J.L., 2022. Spatial patterns in wave signatures on beaches in estuaries and bays. Geomorphology 398, 108070. https://doi.org/10.1016/j.geomorph.2021.108070.

Ranasinghe, R., Turner, I.L., 2006. Shoreline response to submerged structures: a review. Coast. Eng. 53 (1), 65–79. https://doi.org/10.1016/j.coastaleng.2005.08.003.

Rosati, J.D., Dean, R.G., Walton, T.L., 2013. The modified Bruun Rule extended for landward transport. Mar. Geol. 340, 71–81. https://doi.org/10.1016/j.margeo.2013.04.018.

Roy, P.S., Williams, R.J., Jones, A.R., Yassini, I., Gibbs, P.J., Coates, B., West, R.J., Scanes, P.R., Hudson, J.P., Nichol, S., 2001. Structure and function of south-east Australian estuaries. Estuar. Coast Shelf Sci. 53 (3), 351–384. https://doi.org/10.1006/ecss.2001.0796.

Shand, T., Goodwin, I., Bracs, M., Carley, J., Browning, S., Coghlan, I., Harley, M., Peirson, W., You, Z.-J., Kulmar, M., 2010. NSW Coastal Storms and Extreme Waves.

Short, A.D., 1993. Beaches of the New South Wales Coast: A Guide to Their Nature, Characteristics, Surf and Safety. Sydney University Press.

Short, A.D., 2010. Role of geological inheritance in Australian beach morphodynamics. Coast. Eng. 57 (2), 92–97. https://doi.org/10.1016/j.coastaleng.2009.09.005.

Travers, A., 2007. Low-energy beach morphology with respect to physical setting: a case study from cockburn sound, southwestern Australia. J. Coast Res. 23 (2), 429–444. https://doi.org/10.2112/04-0275.1, 232.

Travers, A., Eliot, M.J., Eliot, I.G., Jendrzejczak, M., 2010. Sheltered sandy beaches of southwestern Australia. Geol. Soc. London, Special Pub. 346 (1), 23–42. https://doi.org/10.1144/SP346.3.

Vila-Concejo, A., Fellowes, T.E., Gallop, S.L., Alejo, I., Angnuureng, D.B., Benavente, J., Bosma, J.W., Brempong, E.K., Dissanayake, P., Gazi, M.Y., González-Villanueva, R., Guimarães, R., Kennedy, D.M., Largier, J.L., van der Lugt, M.A., Montes, J., Orescanin, M.M., Pattiaratchi, C.B., Pereira, C.C., et al., 2024. Morphodynamics and Management Challenges for Beaches in Modified Estuaries and Bays. Cambridge Prisms: Coastal Futures.

Vila-Concejo, A., Gallop, S.L., Fellowes, T.E., Rahbani, M., Kennedy, D.M., Largier, J.L., 2022. Storm morphodynamics and decadal evolution of beaches in modified estuaries and bays. Coastal Eng. Proceed. 37. https://doi.org/10.9753/icce.v37.sediment.47. Article 37.

Vila-Concejo, A., Gallop, S.L., Largier, J.L., 2020. Sandy beaches in estuaries and bays. In: Sandy Beach Morphodynamics. Elsevier, pp. 343–362. https://doi.org/10.1016/B978-0-08-102927-5.00015-1.

Vila-Concejo, A., Hughes, M.G., Short, A.D., Ranasinghe, R., 2010. Estuarine shoreline processes in a dynamic low-energy system. Ocean Dyn. 60 (2), 285–298. https://doi.org/10.1007/s10236-010-0273-7.

Wright, L.D., Short, A.D., 1984. Morphodynamic variability of surf zones and beaches: a synthesis. Mar. Geol. 56 (1), 93–118. https://doi.org/10.1016/0025-3227(84)90008-2.

Appendix B (Part III)| Grooves in forereefs act as transport channels to deliver coral rubble during tropical cyclones

Vila-Concejo, A., Perris, L. A., da Silva, A. P., Whitton, K., Meoded-Stern, L., Steilberg-Liu, W. Y., Holmes, R., Breuer, H., Byrne, M., Fellowes, T. E., Salles, T., Morris, B., & Bruce, E.(2025). Grooves in forereefs act as transport channels to deliver coral rubble during tropical cyclones. *Cambridge Prisms: Coastal Futures*, 3 e29, 1-5. https://doi.org/10.1017/cft.2025.10019

Cambridge Prisms: Coastal Futures

www.cambridge.org/cft

Rapid Communication

Cite this article: Vila-Concejo A, Perris LA, da Silva AP, Whitton K, Meoded-Stern L, Steilberg-Liu W-Y, Holmes R, Breuer H, Byrne M, Fellowes TE, Salles T, Morris BD and Bruce E (2025). Grooves in forereefs act as transport channels to deliver coral rubble during tropical cyclones. *Cambridge Prisms: Coastal Futures*, **3**, e29, 1–5
https://doi.org/10.1017/cft.2025.10019

Received: 18 August 2025
Revised: 26 November 2025
Accepted: 27 November 2025

Keywords:
spurs and grooves; coral island stability; sediment transport; coral reefs

Corresponding author:
Ana Vila-Concejo;
Email: ana.vilaconcejo@sydney.edu.au

Grooves in forereefs act as transport channels to deliver coral rubble during tropical cyclones

Ana Vila-Concejo[1,2], Lachlan A. Perris[1,2], Ana Paula da Silva[1,2], Kate Whitton[1,2], Liav Meoded-Stern[1,2], Wan-Yi Steilberg-Liu[1,2], Ruby Holmes[3], Heinrich Breuer[3], Maria Byrne[2,4], Thomas E. Fellowes[1,2,5], Tristan Salles[1,2], Bradley D. Morris[6] and Eleanor Bruce[1,2]

[1]Geocoastal Research Group, School of Geosciences, The University of Sydney Faculty of Science, Australia; [2]Marine Studies Institute, The University of Sydney Faculty of Science, Australia; [3]One Tree Island Research Station, The University of Sydney Faculty of Science, Australia; [4]Integrative Marine Biology Group, School of Life and Environmental Sciences, The University of Sydney Faculty of Science, Australia; [5]Water Research Laboratory, School of Civil and Environmental Engineering, UNSW Sydney, Manly Vale, NSW 2093, Australia and [6]Water, Wetlands and Coasts Science, Science and Insights Division, Department of Climate Change, Energy, the Environment and Water, NSW Government, Sydney, Australia

Abstract

The long-term stability of coral reef islands and associated reef top sedimentary landforms requires the delivery of sediment from the forereef, but the rates and pathways of sediment delivery to these systems remain unclear. Spurs and grooves (SAGs) are ubiquitous geomorphic features fringing coral reefs, characterised by shore-normal coral ridges (spurs) separated by channels (grooves) with either bare substrate or a relatively low sediment infill. SAGs dissipate wave energy, facilitate offshore sediment transport and enhance nutrient exchange. Here we present the first evidence that SAG can also act as channels for onshore transport of rubble during high-energy events, contributing to maintaining reef islands and rubble-based ecosystems.

Impact statement

This study documents a rare and consequential sediment transport event following a sequence of climate-related disturbances on the Great Barrier Reef. In the early months (Austral summer) of 2024, the reef experienced the ninth global bleaching event, with catastrophic impacts at One Tree Reef, a site of long-standing significance in Geoscience. One year later, in March 2025, Tropical Cyclone Alfred remobilised the resulting rubble and transported it onto the reef flat. While grooves (the channels of spur and groove systems) have long been suspected to play a role in sediment dynamics, the prevailing view has been that it is "impossible" for rubble to move upslope through them to the reef flat. Our study shows the first evidence that large volumes of coral rubble are delivered to the reef flat through these grooves. We present qualitative and quantitative drone surveys and field measurements of topography and bathymetry to document this process. These findings carry implications for sediment budgets, interpretations of past reef-building processes and forecasts of reef and shingle island evolution under climate change. These insights are especially timely given their relevance to increasingly used restoration strategies (*e.g.*, rubble stabilisation) and to global sustainability efforts, particularly United Nations Sustainable Development Goals related to Small Island Developing States, such as SDG13 (Climate action), SDG14 (Life below water) and SDG 11 (Sustainable cities and communities). These insights are important given the relevance to millions of people globally whose livelihoods are inextricably linked to coral reef ecosystems.

Introduction

Coral reef islands are dynamic environments that, by adjusting to the environmental conditions (Masselink et al., 2020), remain among the most climate-vulnerable ecosystems on Earth. Physical modelling of gravel islands has demonstrated that islands could build up and adapt to sea level rise (Tuck et al., 2019; Masselink et al., 2020). However, the pathways and rates of sediment supply, without which build-up cannot happen, are event-driven and remain poorly constrained (de Bakker et al., 2025). Islands composed of biogenic carbonate materials are built from sediments derived from the surrounding forereefs and reef flats. Consequently, the sediment supply is threatened by climate change disruptions such as increased marine heatwaves and intense tropical cyclones, which reduce overall reef productivity (de Bakker et al., 2025).

Here, we present new evidence of the pathways of sediment delivery from a bleached coral reef during a tropical storm.

Spurs and grooves (SAGs) act as living breakwaters (Munk and Sargent, 1948) on the forereef of coral reefs. Spurs are parallel ridges of living carbonate material (coral and algae) separated by regularly spaced channels (grooves) (Duce et al., 2016). SAGs are usually oriented perpendicular to the reef crest and/or the incoming waves. They form a "comb-tooth" pattern (6–8 m wide) extending from the reef crest to depths of 20 m (Gischler, 2010). SAGs show considerable variations in morphology predominantly driven by the prevailing hydrodynamic energy (Duce et al., 2020). SAG morphology has been documented across different reef morphologies, including fringing reefs, barrier reefs and atolls through coral-rich seas (Duce et al., 2016). While they have been studied since the mid twentieth century (Munk and Sargent, 1948), recent years have seen an increased focus on SAG research, including remote sensing (Duce et al., 2016), numerical modelling (Rogers et al., 2013; da Silva et al., 2020; Watanabe et al., 2023; Perris et al., 2024) and field measurements (Storlazzi et al., 2004; Monismith et al., 2013; Rogers et al., 2015; Duce et al., 2020, 2022; Acevedo-Ramirez et al., 2021; Sartori et al., 2025). These studies have confirmed that SAG morphology and hydrodynamics are linked to wave climate, from incident short waves to infragravity. They are important wave dissipaters protecting the areas behind reefs (Monismith et al., 2013; Duce et al., 2022; Watanabe et al., 2023; Perris et al., 2024).

SAGs exist under a broad range of wave energy settings and associated water flows (Duce et al., 2016, 2020). It is mostly through modelling that water flows in the SAG zone have been investigated, with research indicating the existence of counter-rotating Lagrangian circulation cells in the grooves (Rogers et al., 2013; da Silva et al., 2020). However, it is unclear whether the flows that occur in the grooves drive sediment transport onshore (towards the reef flat) or offshore. While numerical modelling studies (Rogers et al., 2013) mostly found gentle offshore flow over the shallow part of the grooves, others (da Silva et al., 2020) showed a gentle onshore current in most of their simulations. More recently, field measurements have shown offshore flow in shallow grooves under low wave energy conditions (Perris et al., 2025; Sartori et al., 2025). While Rogers (2013) posits that under strong wave forcing, the offshore transport on the grooves would be reduced or potentially reversed, such conditions have never been measured or observed. A study using tracers of the effects of Category 4 Typhoon Robyn in 1993 in Kume Island (Ryukyus, Southern Japan) showed that coral clasts could be transported from the forereef (up to 12 m depth) onto the reef flat, but those clasts were not located on the grooves (Kan, 1995). Other indications of onshore transport result from personal observations by the authors of the current manuscript of onshore imbrication of coral clasts witnessed while deploying instruments in the Maldives and the Great Barrier Reef.

One Tree Reef (OTR) is a wave-exposed mesotidal platform reef located on the southern Great Barrier Reef (GBR, Figure 1). Its eastern margin comprises a rubble-dominated reef flat containing an estimated 14 million tons of rubble derived from the reef front (Thornborough and Davies, 2011). It is one of the few reefs in the GBR containing a shingle island on its exposed margin. Coral rubble is the generic term used to denote sediments resulting from the fragmentation of calcifying organisms, including coral and molluscs. It refers to sediment larger than sand (>2 mm) and typically up to

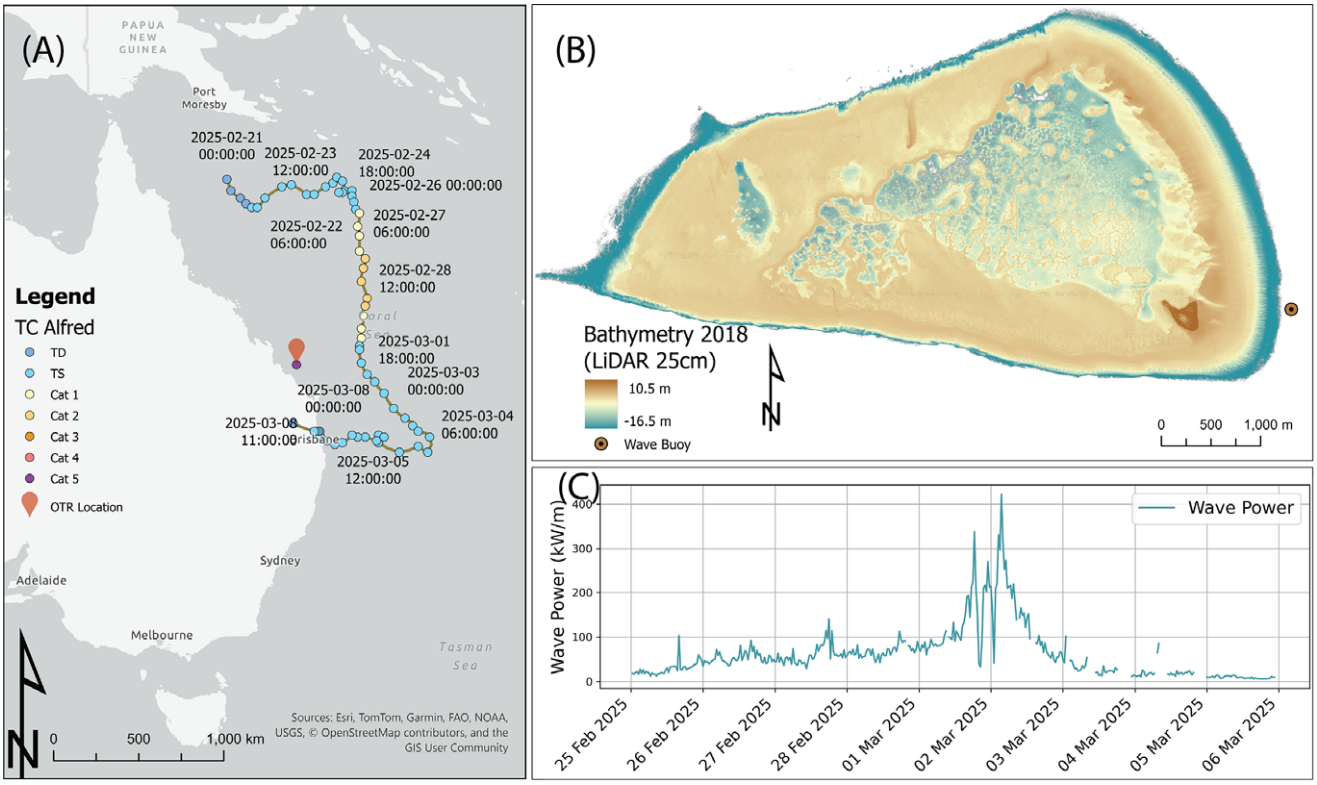

Figure 1. (A) Location of One Tree Island on the southern Great Barrier Reef off the coast of NE Australia and track and Saffir-Simpson category for Tropical Cyclone Alfred in March 2025, note in the legend, TD= Tropical Depression and TS= Tropical Storm (Source IBTrACS (Knapp et al. 2010)); (B) LiDAR Digital Elevation Model (Vertical datum is mean sea level, MSL) with 25 cm resolution of One Tree Reef (OTR) measured in 2018 (Harris et al. 2023) showing the location of the Spotter wave buoy; (C) Wave power from the southern One Tree Island Research Station (OTIRS) wave buoy on the east flank of One Tree Reef (see B for location) during TC Alfred.

https://doi.org/10.1017/cft.2025.10019 Published online by Cambridge University Press

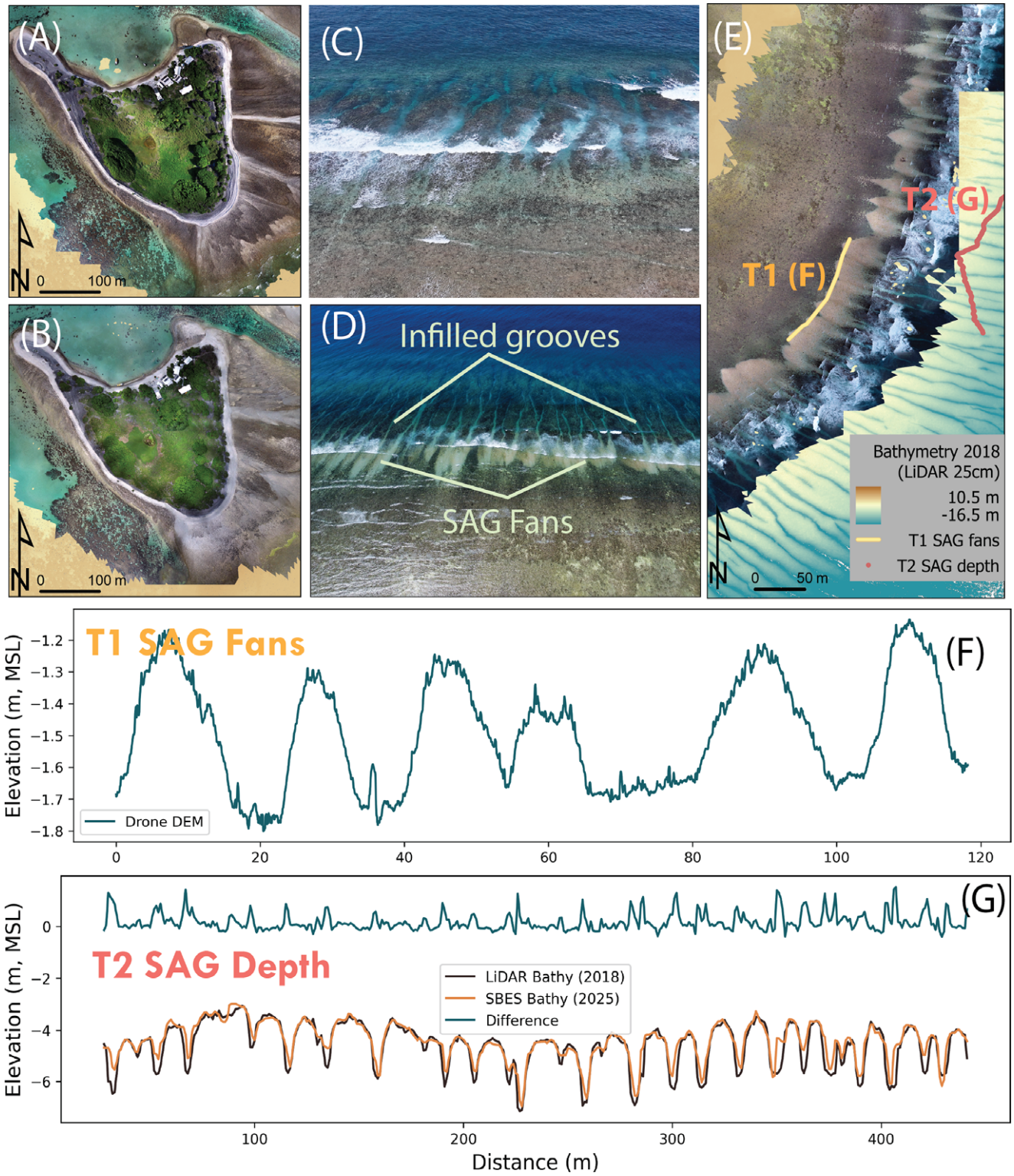

Figure 2. Orthomosaics of One Tree Island with adjacent rubble reef flat in November 2022 (A) and post TC Alfred in March 2025 (B); the grooves off the SE of One Tree Reef are clear of sediment in November 2024 (photo by Lachlan Perris, C) and infilled with coral rubble fans spilling sediment as SAG Fans onto the reef flat post TC Alfred in March 2025 (photo by One Tree Island Research Station, OTIRS, D); Orthomosaic of the SAG at One Tree Reef post TC Alfred (March 2025), showing the sediment fans delivered through the groove channels, and the locations of T1 and T2, the SAG bathymetry corresponds to data obtained with LiDAR in 2018(E); T1 shows a cross-section of the edges of the rubble fans extracted from the drone data (F); and, T2 demonstrates infilling of the grooves by comparing a LiDAR bathymetry from 2018 with a single beam bathymetry (T2) measured in 2025 post TC Alfred (G).

boulder size in the Udden-Wentworth scale (>256 mm), with a variety of morphologies ranging from branching to tabular (Rasser and Riegl, 2002). The coral rubble is dumped on the reef flat during a large, high-energy event and is then reworked (Thornborough and Davies, 2011) with some of it forming rubble spits or tracts (Shannon et al., 2013) that deliver rubble to the shingle island (Talavera et al., 2021). The SAGs on the eastern forereef of OTR (Figure 2) have spurs with ~90% coral cover and grooves with a "U"-shaped cross-section,

https://doi.org/10.1017/cft.2025.10019 Published online by Cambridge University Press

and at the base have a variable amount of large rubble clasts with occasional pockets of coarse sand (Duce et al., 2016). Rubble environments are ubiquitous in coral reefs (Blanchon et al., 1997; Thornborough and Davies, 2011), and previous ecosystem restoration studies have highlighted that rubble mobility hinders coral growth (Ceccarelli et al., 2020). On the other hand, recent studies suggest that rubble fields are important ecosystems that serve as potential targets for coral settlement (Heyward et al., 2024).

In February–March 2024, OTR underwent the worst bleaching in its history, causing up to 53% coral mortality (Byrne et al., 2025), more acute in areas of low hydrodynamic energy (Meoded-Stern et al., 2025). This event generated large amounts of coral rubble resulting from the dead coral collapse. One year after the bleaching, on 1 March 2025, Tropical Cyclone (TC) Alfred passed 340 km east of One Tree Island (Figure 1A). It was a slow-moving Category 1–2 cyclone (Saffir-Simpson Scale) that downgraded to Tropical Storm later that day, still sustaining strong winds. Our wave Spotter Buoy located on the SE off the reef (Figure 1B) recorded Significant Wave Heights (H_s) up to 7 m with associated Peak Periods (T_p) of 12 s. This led to wave power exceeding 250 kW/m sustained over nearly 12 h (Figure 1C). Fortunately, for One Tree Island Research Station, the largest waves occurred during the astronomical low tides.

As expected, TC Alfred delivered large volumes of rubble to the reef flat, modifying the overall morphology of the island (Figure 2A,B; see white rubble in 2B over the reef flat and on the northern tip). The mechanisms acting during these event-driven stochastic occurrences are not well established/studied, and scientists have debated for years whether SAGs could act as channels to deliver sediments to the reef flat under high-energy conditions. In March 2025, immediately after the passage of TC Alfred, we captured a photo showing grooves that are normally relatively empty of sediment (Figure 2C) were completely infilled with sediment and had newly formed sedimentary fans of rubble extending out from each groove on the eastern margin of OTR (Figure 2D). This is the first evidence showing the grooves acting as channels for rubble delivery onto the reef flat from decades of SAG research worldwide. Measurements from drone surveys post-Alfred show the distinct one-to-one spatial alignment between the rubble fans and the grooves, with each groove producing a single fan (Figure 2E). Bathymetric measurements show over 1 m of rubble infilling on the previously mostly bare grooves (Figure 2F).

Our observations and measurements establish, for the first time, grooves as channels transporting coral rubble onto the reef flat during high-energy conditions. This contrasts with the commonly accepted paradigm that rubble on the reef flats is transported from the spurs during high-energy conditions, and that rubble in the grooves remains trapped there or, under the right conditions, moves down the groove (Kan et al., 1997; Hubbard and Dullo, 2016; Duce et al., 2020; Sartori et al., 2025). The observed groove onshore transport occurred during extreme high-energy conditions, with TC Alfred being in the top 99th percentile of TC-generated waves for the study area. The threshold at which this onshore transport initiates is likely location dependent and deserves further investigation, as onshore rubble transport is crucial for the persistence of rubble islands, and TCs are expected to become more intense and less frequent in the Southern Hemisphere (Knutson et al., 2020). Finally, our observations highlight that the function of SAGs is not limited to the dissipation of wave energy but enables onshore rubble transport and contributes to coral environment dynamics essential for reef ecosystem health. While we have shown that rubble delivery plays an important role in the island stability of shingle islands, it has also been shown to influence sandy islands such as the Maldives (Gea-Neuhaus et al., 2025). Reef building is more than coral growth; it is a complex interplay of carbonate production, destruction and transport, as well as the reincorporation of sediment into the reef framework (Hubbard and Dullo, 2016). In the face of a changing climate, there is an urgent need to understand natural coral reef systems (Streit et al., 2024). Understanding rubble dynamics must precede rubble restoration as a management tool in natural systems.

Open peer review. To view the open peer review materials for this article, please visit http://doi.org/10.1017/cft.2025.10019.

Data availability statement. The data will be made available once processed and published in its entirety. In the meantime, colleagues can address data requests to the corresponding author.

Acknowledgements. The authors would like to acknowledge the First Nation peoples on whose land the One Tree Island Research Station stands, the Bailai, Gurang, Gooreng and Taribelang Bunda (FNBGGGTB) People. The authors would also like to acknowledge the Gadigal People from the Eora Nation, where the University of Sydney stands. This research has been partially funded by the Australian Research Council (ARC) Discovery Project DP220101125 and the Marine Resource Initiative (MRI) project with Geoscience Australia and the Australian Department of Foreign Affairs and Trade. Wave data from the spotter buoy was processed by the Coastal and Marine Science team, Department of Climate Change, Energy, the Environment and Water (DCCEEW), NSW Government, Australia. This work represents a contribution to the ARISE project (UKRI grant EP/X029506/1). We thank Jody Webster and the MARS5007 2025 cohort for supporting some of the measurements. Claudia Le Quesne and Lara Talavera contributed to the data processing for the November 2022 dataset.

Author contribution. AV-C led the research, processed data and wrote the manuscript. LAP, KW, W-YS-L, RH and HB obtained and processed field data. BDM processed the Spotter Buoy wave data. APdS, LM-S, MB, TEF, TS and EB contributed to data analysis. All authors contributed to writing and editing the manuscript.

Financial support. This research has been partially funded by the Australian Research Council (ARC) Discovery Project DP220101125 and the Marine Resource Initiative (MRI) project with Geoscience Australia and the Australian Department of Foreign Affairs and Trade. LAP was supported by an RTP scholarship. KW and APdS were supported by DP220101125.

Competing interests. The authors declare none.

References

Acevedo-Ramirez CA, Stephenson W, Wakes S and Mariño-Tapia I (2021) Wave transformation on a fringing reef system with spur and groove structures. *Journal of Geophysical Research: Oceans*. https://doi.org/10.1029/2020jc016910.

Blanchon P, Jones B and Kalbfleisch W (1997) Anatomy of a fringing reef around grand Cayman; storm rubble, not coral framework. *Journal of Sedimentary Research* **67**(1), 1–16. https://doi.org/10.1306/D42684D7-2B26-11D7-8648000102C1865D.

Byrne M, Waller A, Clements M, Kelly AS, Kingsford MJ, Liu B, Reymond CE, Vila-Concejo A, Webb M, Whitton K and Foo SA (2025) Catastrophic bleaching in protected reefs of the Southern Great Barrier Reef. *Limnology and Oceanography Letters*. https://doi.org/10.1002/lol2.10456.

Ceccarelli DM, McLeod IM, Boström-Einarsson L, Bryan SE, Chartrand KM, Emslie MJ, Gibbs MT, Rivero MG, Hein MY, Heyward A, Kenyon TM, Lewis BM, Mattocks N, Newlands M, Schläppy M-L, Suggett DJ and Bay LK (2020) Substrate stabilisation and small structures in coral restoration: State of knowledge, and considerations for management and implementation. *PLoS One* **15** (10), e0240846. https://doi.org/10.1371/journal.pone.0240846.

da Silva RF, Storlazzi CD, Rogers JS, Reyns J and McCall R (2020) Modelling three-dimensional flow over spur-and-groove morphology. *Coral Reefs* **39** (6), 1841–1858. https://doi.org/10.1007/s00338-020-02011-8.

de Bakker DM, Perry CT and Webb AE (2025) Quantifying coral reef accretion in a changing world: Approaches, challenges and emerging opportunities.

Cambridge Prisms: Coastal Futures **3**, e15. https://doi.org/10.1017/cft.2025.10005.

Duce S, **Dechnik B**, **Webster JM**, **Hua Q**, **Sadler J**, **Webb GE**, **Nothdurft L**, **Salas-Saavedra M and Vila-Concejo A** (2020) Mechanisms of spur and groove development and implications for reef platform evolution. *Quaternary Science Reviews* **231**, 106155. https://doi.org/10.1016/j.quascirev.2019.106155.

Duce S, **Vila-Concejo A**, **Hamylton SM**, **Webster JM**, **Bruce E and Beaman RJ** (2016) A morphometric assessment and classification of coral reef spur and groove morphology. *Geomorphology* **265**, 68–83. https://doi.org/10.1016/j.geomorph.2016.04.018.

Duce S, **Vila-Concejo A**, **McCarroll RJ**, **Yiu B**, **Perris LA and Webster JM** (2022) Field measurements show rough fore reefs with spurs and grooves can dissipate more wave energy than the reef crest. *Geomorphology* **413**, 108365. https://doi.org/10.1016/j.geomorph.2022.108365.

Gea-Neuhaus A, **Scott T**, **Masselink G**, **Lindhart M**, **Vila-Concejo A and Kench P** (2025) Coral rubble mobility on an intertidal reef flat Huvadhoo atoll, Maldives. In *Proceedings of Coastal Dynamics*. Aveiro, Portugal: Springer-Nature.

Gischler E (2010) Indo-Pacific and Atlantic spurs and grooves revisited: The possible effects of different Holocene Sea-level history, exposure, and reef accretion rate in the shallow fore reef. *Facies* **56**(2), 173–177. https://doi.org/10.1007/s10347-010-0218-0.

Harris DL, **Webster JM**, **Vila-Concejo A**, **Duce S**, **Leon JX and Hacker J** (2023) Defining multi-scale surface roughness of a coral reef using a high-resolution LiDAR digital elevation model. *Geomorphology* **439**, 108852. https://doi.org/10.1016/j.geomorph.2023.108852.

Heyward A, **Giuliano C**, **Page CA and Randall CJ** (2024) Rock and roll: Experiments on substrate movement and coral settlement. *Coral Reefs* **43** (5), 1417–1429. https://doi.org/10.1007/s00338-024-02547-z.

Hubbard DK and Dullo W-C (2016) The changing face of reef building. In Hubbard KD, Rogers SC, Lipps HJ and Stanley JDG (eds.), *Coral Reefs at the Crossroads*. Dordrecht: Springer Netherlands, pp. 127–153. https://doi.org/10.1007/978-94-017-7567-0_6.

Kan H (1995) Typhoon effects on sediment movement on reef edges and reef slopes. In Bellwood O (ed.), *Recent Advances in Marine Science and Technology '94*. Townsville: Pacon International and James Cook University, pp. 191–201.

Kan H, **Hori N**, **Kawana T**, **Kaigara T and Ichikawa K** (1997) The evolution of a Holocene fringing reef and island: Reefal environmental sequence and sea level change in Tonaki Island, the Central Ryukyus. *Atoll Research Bulletin* **443**, 1. https://doi.org/10.5479/SI.00775630.443.1.

Knapp KR, **Kruk MC**, **Levinson DH**, **Diamond HJ and Neumann CJ** (2010) The international best track archive for climate stewardship (IBTrACS): Unifying tropical cyclone best track data. *Bulletin of the American Meteorological Society* **91**, 363–376. https://doi.org/10.1175/2009bams2755.1.

Knutson T, **Camargo SJ**, **Chan JCL**, **Emanuel K**, **Ho CH**, **Kossin J**, **Mohapatra M**, **Satoh M**, **Sugi M**, **Walsh K and Wu L** (2020) Tropical cyclones and climate change assessment part II: Projected response to anthropogenic warming. *Bulletin of the American Meteorological Society* **101**(3), E303–E322. https://doi.org/10.1175/BAMS-D-18-0194.1.

Masselink G, **Beetham E and Kench P** (2020) Coral reef islands can accrete vertically in response to sea level rise. *Science Advances* **6**(24), eaay3656. https://doi.org/10.1126/sciadv.aay3656.

Meoded-Stern L, **Silva AP**, **Foo SA**, **Waller A**, **Byrne M and Vila-Concejo A** (2025) Reef geomorphology, hydrodynamic energy and coral morphology influence recovery after bleaching. *Marine Environmental Research* **212**, 107554. https://doi.org/10.1016/j.marenvres.2025.107554.

Monismith SG, **Herdman LMM**, **Ahmerkamp S and Hench JL** (2013) Wave transformation and wave-driven flow across a steep coral reef. *Journal of Physical Oceanography* **43**(7), 1356–1379. https://doi.org/10.1175/JPO-D-12-0164.1.

Munk WH and Sargent MC (1948) Adjustment of bikini atoll to ocean waves. *Eos, Transactions American Geophysical Union* **29**(6), 855–860. https://doi.org/10.1029/TR029I006P00855.

Perris LA, **Lindhart M**, **Salles T**, **da Silva AP**, **Fellowes TE and Vila-Concejo A** (2025) Hydrodynamic controls on spur and groove morphology flow variability and reef structure. *Geomorphology in review*.

Perris L, **Salles T**, **Fellowes TE**, **Duce SJ**, **Webster JM and Vila-Concejo A** (2024) The influence of coral reef spur and groove morphology on wave energy dissipation in contrasting reef environments. *Journal of Geophysical Research-Earth Surface* **129**(8), e2023JF007424. https://doi.org/10.1029/2023JF007424.

Rasser M and Riegl B (2002) Holocene coral reef rubble and its binding agents. *Coral Reefs* **21**(1), 57–72. https://doi.org/10.1007/s00338-001-0206-5.

Rogers JS, **Monismith SG**, **Dunbar RB and Koweek D** (2015) Field observations of wave-driven circulation over spur and groove formations on a coral reef. *Journal of Geophysical Research: Oceans* **120**(1), 145–160. https://doi.org/10.1002/2014JC010464.

Rogers JS, **Monismith SG**, **Feddersen F and Storlazzi CD** (2013) Hydrodynamics of spur and groove formations on a coral reef. *Journal of Geophysical Research: Oceans* **118**(6), 3059–3073. https://doi.org/10.1002/jgrc.20225.

Sartori G, **Boles EL**, **Monismith SG**, **Mumby PJ**, **Dunbar RB**, **Khrizman A**, **Tatebe L and Capozzi R** (2025) Morphologically driven sedimentation patterns on a coral reef. *Coral Reefs* **44**(2), 591–607. https://doi.org/10.1007/s00338-025-02629-6.

Shannon AM, **Power HE**, **Webster JM and Vila-Concejo A** (2013) Evolution of coral rubble deposits on a reef platform as detected by remote sensing. *Remote Sensing* **5**(1), 1–18. https://doi.org/10.3390/rs5010001.

Storlazzi CD, **Ogston AS**, **Bothner MH**, **Field ME and Presto MK** (2004) Wave- and tidally-driven flow and sediment flux across a fringing coral reef: Southern Molokai, Hawaii. *Continental Shelf Research* **24**(12), 1397–1419. https://doi.org/10.1016/j.csr.2004.02.010.

Streit RP, **Morrison TH and Bellwood DR** (2024) Coral reefs deserve evidence-based management not heroic interference. *Nature Climate Change* **14**(8), 773–775. https://doi.org/10.1038/s41558-024-02063-6.

Talavera L, **Vila-Concejo A**, **Webster JM**, **Smith C**, **Duce S**, **Fellowes TE**, **Salles T**, **Harris D**, **Hill J**, **Figueira W and Hacker J** (2021) Morphodynamic controls for growth and evolution of a rubble coral island. *Remote Sensing* **13**(8). https://doi.org/10.3390/rs13081582.

Thornborough KJ and Davies PJ (2011) Reef flats. In Hopley D (ed.), *Encyclopedia of Modern Coral Reefs*. Netherlands: Springer, pp. 869–876.

Tuck ME, **Kench PS**, **Ford MR and Masselink G** (2019) Physical modelling of the response of reef islands to sea-level rise. *Geology* **47**(9), 803–806. https://doi.org/10.1130/G46362.1.

Watanabe M, **Kan H**, **Toguchi K**, **Nakashima Y**, **Roeber V and Arikawa T** (2023) Effect of the structural complexity of a coral reef on wave propagation: A case study from Komaka Island, Japan. *Ocean Engineering* **287**, 115632. https://doi.org/10.1016/j.oceaneng.2023.115632.

https://doi.org/10.1017/cft.2025.10019 Published online by Cambridge University Press